

# DSE - The Manned Drone

*Provide a personal, autonomous, zero-emission aerial mode of transport as an alternative to conventional transport in highly congested urban environments*

J.C.M. van Beek  
P. de Heer  
M.J.L. de Jong  
J.B. Koelewijn  
T. Kuperus

4359038  
4360834  
4303229  
4400542  
4299795

R.F. Nostheide  
M.H. Schouten  
T.G. van Veldhoven  
S.P. Vermeijlen  
J.P. Watchorn

4011716  
4171233  
4298934  
4344707  
4351398

Final Report

Design Synthesis Exercise



**HyDrone**



---

# Preface

This is the fourth and final report of Design Synthesis Exercise (DSE) Group 19 in partial fulfilment of the requirements for the degree of Bachelor of Science in Aerospace Engineering. The purpose of this project is to design a personal, autonomous, zero-emission aerial mode of transport as an alternative to conventional transport in highly congested urban environments.

The final design concept was selected out of a choice of three, as presented in the previous report (the Midterm Report). The final design has been elaborated to the fullest extent, based on the knowledge acquired throughout the BSc Aerospace Engineering programme.

This report is intended for individuals and organisations with a background in aeronautical engineering, given that it contains technical language and theories that are specific to this field.

Group 19 would like to sincerely thank project tutor Dr. Marios Kotsonis, along with his assistants ir. Hemmo Koornneef and ir. Nando van Arnhem for the extensive help and guidance provided. The DSE Organising Committee has also provided much needed advice on many occasions, particularly by Dr.ir. Erwin Mooij.



# Nomenclature

## Acronyms

AF	Aramid Fibre
Al	Aluminium
AR	Aspect Ratio
ATR	Average Temperature Response
BEMT	Blade Element Momentum Theory
BoP	Balance of Plant
CF	Carbon Fibre
CFD	Computational Fluid Dynamics
CFRP	Carbon Fibre Reinforce Polymer
CORS	Continuously Operating Reference Station
DC	Direct Current
DSE	Design Synthesi Eercise
EMS	Environmental Management System
FAA	Federal Aviation Administration
FEM	Finite Element Method
GNC	Guidance Navigation Control
GPD	Gravimetric Power Density
GPS	Global Positioning System
GWP	Global Warming Potential
HFC	Hydrogen Fuel Cell
LIDAR	Light Detection and Ranging
MTOW	Maximum Take-Off Weight
PCU	Power Control Unit
PED	Primary Energy Demand
PEM	Proton Eichange Membrane
PMMA	PolyMethylMethaCrylate (Acrylic Glass)
PRD	Pressure Relief Device
QI	Quasi Isotropic
R&D	Research Development
RADAR	Radio Detection and Ranging
rCFRP	Recycled Carbon Fibre Reinforce Polymer
RoI	Return on Investment
RPM	Rotations per Minute
SGF	S-Glass Fibre
TI	Titanium
TRL	Technology Readiness Level
UD	Unidirectional
vCFRP	Virgin Carbon Fibre Reinforce Polymer
VPD	Volumetric Power Density
VTOL	Vertical Take-Off and Landing

## Requirement Acronyms

AERO	Aerodynamics
CLI	Client
COM	Communication
CONT	Control
MS	Materials and Structure
PERF	Performance
POW	Power
SFT	Safety
SOFT	Software
STK	Stakeholder
SUS	Sustainability
SYS	System
TECH	Technical

## Roman Symbols

$\%wt$	Gravimetric Density [%]
$\dot{m}$	Mass Flow [ $kg/s$ ]
$A$	Rotor Disk Area [ $m^2$ ]
$a$	Horizontal beam radius [ $cm$ ]
$a$	Speed of Sound [ $m/s$ ]
$A_c$	Cross-sectional area [ $m^2$ ]
$A_e$	Enclosed area [ $m^2$ ]
$a_x$	Acceleration in X-Axis [ $N$ ]
$A_{con}$	Contracted Wake Area [ $m^2$ ]
$B$	Boom area [ $m^2$ ]
$B$	Number of Blades [-]
$b$	Torque factor [ $Nm/(rad/s)^2$ ]
$b$	Vertical beam radius [ $cm$ ]
$b$	Wing Span [ $m$ ]
$c$	Blade Chord [ $m$ ]
$C_D$	Drag Coefficient [-]
$c_e$	External Complementary Energy [ $J$ ]
$c_i$	Internal Complementary Energy [ $J$ ]
$C_L$	Lift Coefficient [-]
$C_M$	Moment Coefficient [-]
$c_{body}$	Body Chord [ $m$ ]
$C_{D_0}$	Zero Lift Drag Coefficient [-]
$C_{D_i}$	Induced Drag Coefficient [-]
$C_{L_\alpha}$	Lift Curve Slope [ $1/rad$ ]
$C_{P,B}$	Blade Loading [ $N/m^2$ ]
$C_{P_u}$	Power Coefficient of Upper Rotor [-]
$C_{T_u}$	Thrust Coefficient of Upper Rotor [-]
$D$	Drag [ $N$ ]
$D$	Propeller Diameter [ $m$ ]
$D_b$	Drag in Body Frame [ $N$ ]
$d_x$	Desired Parameter Factor [-]
$di$	Incremental Value of i [-]
$e$	Span Efficiency Factor [-]
$E_i$	Required Energy for i [ $J$ ]
$e_i$	Emission [ $kg$ ]
$F_i$	Force of i [ $N$ ]
$H$	Flyover Distance to Observer [ $m$ ]
$h_d$	Diffuser Height [ $m$ ]
$h_s$	Shroud Height [ $m$ ]
$h_{lg}$	Landing Gear Height [ $m$ ]
$I$	Current [ $A$ ]
$i_d$	Desired Parameter i [-]
$I_{xx}$	Mass Moment of Inertia About X-Axis [ $kg \cdot m^2$ ]
$k_D$	Drag Factor [ $N/v^2$ ]
$k_L$	Lift Factor [ $N/v^2$ ]
$k_T$	Thrust Factor [ $N/(rad/s)^2$ ]
$K_{i,DD}$	Acceleration Controller Gain of i [-]
$K_{i,D}$	Velocity Controller Gain of i [-]
$K_{i,I}$	Integral Position Controller Gain of i [-]
$K_{i,P}$	Position Controller Gain of i [-]
$L$	Lift [ $N$ ]
$L'$	Thrust to Overcome Lift [ $N$ ]
$L_A$	Noise Level [ $dB$ ]
$l_{arm}$	Beam arm length [ $m$ ]
$l_{between}$	Skid Length between Landing Gear Struts [ $m$ ]
$l_{drone}$	Length of Drone [ $m$ ]
$l_{hind}$	Skid Length outside Landing Gear Struts [ $m$ ]

$l_{lg}$	Landing Gear Strut Length [m]	$v_l$	Induced Velocity of Lower Rotor [m/s]
$l_{tank}$	Tank Length [m]	$v_u$	Induced Velocity of Upper Rotor [m/s]
$M$	Moment [Nm]	$V_\infty$	Free Stream Velocity [m/s]
$M_H$	Helical Blade Tip Mach Number [-]	$W_i$	Weight of Component i [N]
$m_i$	Mass of Component i [kg]	$w_l$	Exhaust Velocity of Lower Rotor [m/s]
$N$	Propeller Rotational Speed [rpm]	$w_s$	Shroud Width [m]
$n$	Load factor [-]	$w_{drone}$	Width of Drone [m]
$n$	Number of Propellers [rpm]	$x_n$	Centre of Gravity of Component n on X-Axis [m]
$N_b$	Number of Blades [-]	$x_{cg}$	Centre of Gravity on X-Axis [m]
$P$	Power [W]	<b>Greek Symbols</b>	
$p$	Ambient Pressure [N/m <sup>2</sup> ]	$\alpha$	Angle of Attack [rad]
$p$	Beam growth factor [-]	$\alpha_x$	Angular Acceleration in X-Direction [rad/s <sup>2</sup> ]
$p$	Roll Rate [rad/s]	$\chi$	Beam angle [°]
$P_i$	Power Required for Phase i [W]	$\Delta T$	Thrust Difference [N]
$P_u$	Power of Upper Rotor [W]	$\Delta t$	Time Increment [s]
$P_{tank}$	Tank Pressure [N/m <sup>2</sup> ]	$\delta z$	Beam Element Length [cm]
$Q$	Torque [Nm]	$\delta$	Tip Clearance [m]
$q$	Pitch Rate [rad/s]	$\Delta_i$	Deflection [m]
$q$	Shear flow [A]	$\eta_i$	Efficiency of component i [%]
$r$	Fractional Rotor Radius [-]	$\lambda$	Advance Ratio [-]
$r$	Yaw Rate [rad/s]	$\lambda_d$	Diffuser Angle [rad]
$r_c$	Lower Rotor Radius Affected by Upper Rotor [m]	$\mu$	Dynamic Viscosity [Ns/m <sup>2</sup> ]
$r_i$	Inside Tank Radius [m]	$\Omega$	Rotational Velocity [rad/s]
$r_o$	Outside Tank Radius [m]	$\omega$	Angular Velocity [rad/s]
$r_R$	Rotor Radius [m]	$\phi$	Roll Angle [rad]
$R_e$	Shroud Exit Radius [m]	$\psi$	Yaw Angle [rad]
$R_i$	Shroud Inner Radius [m]	$\rho$	Air Density [kg/m <sup>3</sup> ]
$r_i$	Shroud Inlet Radius [m]	$\rho_i$	Density of material i [kg/m <sup>3</sup> ]
$R_o$	Shroud Outer Radius [m]	$\sigma$	Normal Stress [N/m <sup>2</sup> ]
$Re$	Reynolds Number [-]	$\sigma$	Rotor Solidity [-]
$S$	Surface Area [m <sup>2</sup> ]	$\sigma_{axial}$	Axial stress [N/m <sup>2</sup> ]
$S_x$	Shear Force in X-Axis [N]	$\sigma_{hoop}$	Hoop stress [N/m <sup>2</sup> ]
$T$	Temperature [K]	$\tau$	Shear Stress [N/m <sup>2</sup> ]
$T$	Thrust [N]	$\tau_x$	Torque about X-Axis [Nm <sup>2</sup> ]
$t$	Skin thickness [mm]	$\theta$	Pitch Angle [rad]
$T'$	Thrust to Overcome Drag [N]	$\theta_u$	Upper Blade Pitch Angle [rad]
$T_b$	Thrust in Body Frame [N]	<b>Constants</b>	
$t_i$	Time of Phase i [s]	$\gamma$	Isentropic Expansion Factor [1.4 -]
$T_O$	Time Interval [s]	$\mu$	Unit Average Temperature Response [5.77·10 <sup>-15</sup> K/kg]
$T_u$	Thrust of Upper Rotor [N]	$g$	gravitational acceleration [9.80665 m/s <sup>2</sup> ]
$t_{tank}$	Tank Thickness [m]	$P_0$	Reference Sound Pressure [20 μPa]
$U$	Number of Flights [-]	$R$	Specific Gas Constant [287.05 J/(kgK)]
$U$	Voltage [V]		
$v$	Airspeed [m/s]		

---

# Summary

The following report builds on the Midterm Report, with the aim of further elaborating the final concept and explaining the design process. The final concept is a fully autonomous multirotor aircraft that is electrically powered through a hydrogen fuel cell and capable of vertical take-off and landing (VTOL). This design has been named the *HyDrone*, which is a portmanteau of the words "Hydrogen" and "Drone".

One of the more unique aspects of the HyDrone is its lifting body, which allows for a reduced thrust output during cruise flight, thus saving power. Four coaxial rotor systems have been implemented, which allow for a greater thrust output than four isolated rotors of the same size. Each coaxial system is shrouded in order to reduce blade tip losses and decrease the noise produced by the rotors. Each rotor blade can be rotated along its longitudinal axis such that the pitch angle can be altered for different flight stages.

The safety of the HyDrone was also an important factor during the design process, given that it is meant to fly autonomously whilst carrying a passenger. Redundancy measures have been applied in order to ensure the safety of the passenger during flight, such as reinforcing the passenger compartment or shrouding the coaxial rotors. Carbon fibre has been one of the more favoured materials for this design, mainly due to its high strength-to-weight ratio. Two carbon fibre beams, which carry a shrouded rotor system on both ends, have been placed under the passenger compartment in an 'X' configuration.

The individual subsystems were subsequently integrated in order to form a final product. The idea of fully-autonomous zero-emission flight is still a novel concept that has many in doubt. The long term aim of this report is to boost interest in this endeavour and advance the current trend.



# Contents

<b>1</b>	<b>Introduction</b>	<b>11</b>	<b>8</b>	<b>Structures &amp; Materials</b>	<b>63</b>
<b>2</b>	<b>Executive Overview</b>	<b>13</b>	8.1	Materials	63
2.1	Baseline	13	8.1.1	Weight	63
2.2	Midterm	13	8.1.2	Cost	63
2.2.1	Power Trade-Off	14	8.1.3	Maintenance	63
2.2.2	Concept Trade-Off	14	8.1.4	Ecological Footprint	65
2.2.3	Results	15	8.1.5	Results	65
2.3	Detailed Design	15	8.2	Load Carrying Structure	66
2.3.1	Aerodynamics	15	8.2.1	Shape	66
2.3.2	Structures & Materials	16	8.2.2	Forces	66
2.3.3	Propulsion	16	8.2.3	Stresses	68
2.3.4	Power	17	8.2.4	Results	69
2.3.5	Control & Stability	17	8.3	Shrouds	70
2.3.6	Safety	17	8.3.1	Shape	70
2.4	Final Result	18	8.3.2	Forces	71
<b>3</b>	<b>Conceptual Design</b>	<b>19</b>	8.3.3	Stresses	71
3.1	Mission Statement	19	8.3.4	Impact	72
3.2	User Requirements	19	8.3.5	Results	73
3.3	Flight Profile	20	8.4	Cockpit	73
<b>4</b>	<b>Detailed Approach</b>	<b>21</b>	8.4.1	Shape	74
4.1	Functional Flow Diagram	21	8.4.2	Shell	74
4.2	Functional Breakdown Structure	22	8.4.3	Airframe	75
<b>5</b>	<b>Operations &amp; Logistics</b>	<b>27</b>	8.4.4	Impact	76
<b>6</b>	<b>Regulation &amp; Certification</b>	<b>29</b>	8.4.5	Results	76
6.1	Approach of Literature Study	29	8.5	Landing Gear	77
6.2	Airworthiness	29	8.5.1	Design Loads	77
6.3	Noise	30	8.5.2	Stresses	77
6.4	Autonomous Flight	30	8.5.3	Results	77
<b>7</b>	<b>Aerodynamics</b>	<b>33</b>	8.6	Verification & Validation	78
7.1	Design Options	33	8.7	Sensitivity Analysis	79
7.2	Criteria	33	8.8	Technical Risks	79
7.3	Lifting Body	34	8.9	Recommendations	80
7.3.1	Lifting Body of a Drone	34	<b>9</b>	<b>Propulsion</b>	<b>81</b>
7.3.2	Lifting Body Vehicles	35	9.1	Ducted Coaxial Rotor System	81
7.3.3	Limiting Factors	35	9.2	Blade Element Momentum Theory (BEMT)	81
7.3.4	Trade-Off	36	9.3	Rotor Design	83
7.3.5	Design	37	9.4	Verification & Validation	84
7.3.6	Results	43	9.5	Technical Risks	85
7.4	Shrouds	43	9.6	Recommendations	85
7.4.1	Trade-Off	43	<b>10</b>	<b>Power</b>	<b>87</b>
7.4.2	Design Approach	44	10.1	Required Power & Energy	87
7.4.3	Aerodynamics over the Shroud	45	10.2	Hydrogen Fuel Cell Basics	88
7.4.4	Shroud design	46	10.3	Hydrogen Fuel Cell Components	88
7.4.5	Results	51	10.3.1	Hydrogen Fuel Tank	89
7.5	Landing Gear	51	10.3.2	Balance of Plant	91
7.5.1	Clearance Requirements	51	10.3.3	Fuel Cell Stack	91
7.5.2	Design Options	52	10.3.4	DC-DC Converter and PCU	92
7.5.3	Tradeoff	53	10.3.5	Backup Battery	92
7.5.4	Skid Aerodynamic Design	55	10.3.6	Wiring	92
7.6	Technical Risks	58	10.4	Safety	93
7.7	Recommendations	59	10.5	Technical Risks	93
			10.6	Recommendations	94

<b>11 Control &amp; Stability</b>	<b>95</b>	14.6 ISO Standards . . . . .	133
11.1 Blade Pitch System . . . . .	95	14.7 Recommendations . . . . .	133
11.2 Sensors . . . . .	96	<b>15 Subsystem Interaction</b>	<b>135</b>
11.2.1 Types of Sensors . . . . .	96	15.1 Hardware Block Diagram . . . . .	135
11.2.2 Sensor Distribution & Costs . . . . .	97	15.2 Software Block Diagram . . . . .	135
11.3 Control Flow Diagrams . . . . .	99	15.3 Communication Flow and Data Block Handling Diagram . . . . .	136
11.4 Controlling and Stabilising the Drone . . . . .	100	<b>16 System Integration</b>	<b>139</b>
11.4.1 Dynamic Model . . . . .	100	16.1 Design Overview . . . . .	139
11.4.2 Controller . . . . .	102	16.1.1 Geometry . . . . .	139
11.4.3 Sensitivity Analysis . . . . .	110	16.1.2 Mass Budget Allocation . . . . .	139
11.4.4 Verification & Validation . . . . .	111	16.1.3 Power Budget Allocation . . . . .	139
11.5 Technical Risks . . . . .	112	16.2 Performance Analysis . . . . .	140
11.6 Recommendations . . . . .	113	16.2.1 Payload-Range Performance . . . . .	141
<b>12 Safety System</b>	<b>115</b>	16.2.2 Climb Performance . . . . .	141
12.1 Autorotation . . . . .	115	16.3 Compliance Matrix . . . . .	141
12.1.1 Autorotation Manoeuvre Principle	115	16.4 Sensitivity Analysis . . . . .	142
12.1.2 Autorotation for the HyDrone . . . . .	116	<b>17 Manufacturing, Assembly &amp; Integration Plan</b>	<b>145</b>
12.2 Navigation and Strobe Lighting . . . . .	116	17.1 Production plan . . . . .	145
12.3 Lightning Strike Protection . . . . .	116	17.2 Sustainable Manufacturing . . . . .	146
12.4 Shrouds . . . . .	117	<b>18 Post DSE</b>	<b>147</b>
12.5 Recommendation . . . . .	117	18.1 Design and Development Logic . . . . .	147
12.6 Reliability, Availability, Maintainabil- ity, and Safety (RAMS) . . . . .	119	18.2 Timeline . . . . .	147
<b>13 Noise</b>	<b>121</b>	<b>19 Business Plan</b>	<b>151</b>
13.1 Requirements . . . . .	121	19.1 Cost Estimations . . . . .	151
13.2 Noise Model . . . . .	121	19.1.1 Unit Cost . . . . .	151
13.3 Results . . . . .	125	19.1.2 Development Costs . . . . .	153
13.4 Verification & Validation . . . . .	125	19.1.3 Operational Costs . . . . .	156
13.5 Discussion . . . . .	126	19.2 Market Analysis . . . . .	157
13.6 Recommendations . . . . .	127	19.2.1 Target Audience . . . . .	157
<b>14 Sustainability</b>	<b>129</b>	19.2.2 Market Volume . . . . .	158
14.1 Midterm Review . . . . .	129	19.2.3 Market Share . . . . .	158
14.2 Materials . . . . .	129	19.2.4 Return on Investment . . . . .	159
14.2.1 CFRP Recycling . . . . .	130	<b>20 Conclusion</b>	<b>160</b>
14.2.2 Manufacturing and Mechanical Properties . . . . .	130	<b>21 Recommendations</b>	<b>162</b>
14.2.3 Results . . . . .	131	<b>A Logbook</b>	<b>167</b>
14.3 End-of-Life Plan . . . . .	132		
14.4 Air Pollution & Climate Change . . . . .	132		
14.5 Operational Cost, Comfort and Infras- tructure . . . . .	132		

---

# Chapter 1: Introduction

Urban populations have been growing rapidly throughout the past decades and with this pattern comes a new set of challenges, particularly when it comes to transportation. In many cities, the current state of public transport and road networks is not sufficient to keep up with rising demands for sustainable transportation. As a consequence, traffic congestion is becoming a greater problem within urban environments. Losing time in traffic is a source of great frustration and affects productivity. The primary cause is that conventional transportation networks are constrained to a limited number of roads and motorways. Traffic congestion can readily be alleviated either by digging tunnels or taking to the skies. Today, most personal flight options are limited to helicopter transportation, which is far from ideal, due to the cost and environmental impact.

With the above mentioned background information in mind, Design Synthesis Exercise (DSE) Group 19 has been tasked by the TU Delft to develop an alternative solution in partial fulfilment of the requirements for the degree of Bachelor of Science in Aerospace Engineering. The final design is a fully autonomous multirotor aircraft, electrically powered through a hydrogen fuel cell and capable of vertical take-off and landing (VTOL).

The purpose of this report is to present a detailed design, based on the final choice from the Midterm Report. Each individual subsystem has been elaborated upon to the fullest extent and subsequently integrated in order to form a final product.

The structure of the report is as follows. Chapter 2 presents a summary of the entire design project with a short descriptions of all subsystems that are part of the HyDrone. The mission statement and requirements have been stated in chapter 3. The functional flow diagram and functional breakdown structure can be found in chapter 4. Chapter 5 presents the operations & logistics diagram, accompanied by a detailed description. The relevant regulations & certifications with regard to airworthiness, noise and autonomous flight have been researched and subsequently described in chapter 6.

The individual subsystem designs have been elaborated upon from chapter 7 to chapter 11 in the following order: Aerodynamics, Structures & Materials, Propulsion, Power and Control & Stability.

Chapter 12 provides a description of each individual safety system and how they have been integrated with the relevant subsystems. A thorough analysis of the noise and sustainability of the final product can be found in chapter 13 and chapter 14 respectively. The interactions between each subsystem have been illustrated in chapter 15, whereas chapter 16 presents an overview of the system integration. The manufacturing and maintenance processes have been explored in chapter 17. Potential post DSE activities have been considered in chapter 18, which presents a time-line for the development process from publication of this report to market launch. A business plan has been established in chapter 19, which consists of a cost and market analysis. Section 15.3 illustrates the data handling and communication flow during flight operations. The conclusions of the report can be found in chapter 20, whereas chapter 21 lists recommendations for further improvement of the final design.



---

# Chapter 2: Executive Overview

Urban populations have been growing rapidly throughout the past decades and with this pattern comes a new set of challenges, particularly when it comes to transportation. The current state of public transport and road networks is not sufficient to keep up with the rising demands for sustainable transportation. As a consequence, traffic congestion is becoming a greater problem within urban environments.

The goal of this project is to provide a fully sustainable solution for traffic congestion in the form of personal transport. The aim is to design a personal air-vehicle which is able to take off and land vertically. Furthermore the design should fly autonomous and have zero emissions.

## 2.1 Baseline

Prior to the design process, the requirements for the project had to be established. The first step in identifying the requirements was to analyse the functionality of the system. The second step was to perform a stakeholder analysis. From the former, the system requirements were established whereas the latter resulted in the stakeholder requirements.

Subsequently the requirements were assessed and, if applicable, categorised as either killer, key or driving requirements. The following stakeholder requirements were labeled as driving. These requirements are considered to be the most important since they come from the client.

- **STK-CLI-PERF1** The final design shall carry a single passenger
- **STK-CLI-PERF2** The final design shall have a minimum endurance of 2 hours
- **STK-CLI-PERF4** The final design shall have a minimum cruising speed of  $60\text{km}/\text{h}$ .
- **STK-CLI-PERF5** The final design shall be capable of vertical take-off and landing.
- **STK-CLI-PERF6** The final design shall have a maximum payload (including passenger) of  $100\text{kg}$ .
- **STK-CLI-PERF7** The final design shall be fully autonomous (no user control).
- **STK-CLI-PERF9** The final design shall fit in a box of  $5\text{m}\times 5\text{m}\times 5\text{m}$ .
- **STK-CLI-SUS1** The final design shall be capable of fully zero-emission flight.

Given all the requirements, various options were explored to fulfil these requirements. This was done by dividing and characterising the following subsystems

- Vertical Take-Off
- Propulsion
- Propulsion Mounting Location
- Power
- Safety
- Stability
- Aerodynamics
- Control
- Landing

All options for each subsystem were assessed on feasibility. The options labelled as non-feasible were then removed and with the remaining options a total of 10 concepts were developed. To reduce the number of concepts a trade-off was performed. Each concept was carefully given a score on the following criteria. The importance of each of the criteria is given between square brackets. The weights are relative on a scale from 1 to 5.

- Stability [1]
- Control [3]
- Endurance [3]
- Noise/Disturbance [5]
- Sustainability [5]
- TRL [5]
- Size [3]
- Cruise Speed [2]
- Payload Capacity [3]
- Unit Cost [4]
- User Friendliness [2]
- VTO [2]
- VTL [2]
- Aesthetics [2]
- Maintenance [2]
- Redundancy [5]

The result included three concepts: Multiple rotating propellers on wing and tail/canard, multiple fixed propellers above body, and multiple fixed propellers in/below body. Artist impressions are provided in fig. 2.1, fig. 2.2, and fig. 2.3

## 2.2 Midterm

To end up with one concept to start the detailed design a trade-off had to be performed between the three remaining concepts.

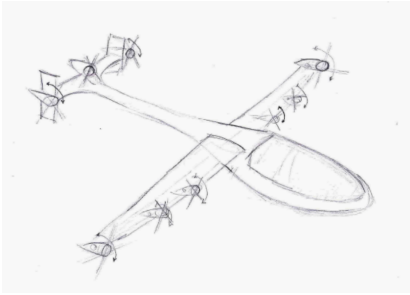


Figure 2.1: Side View Render

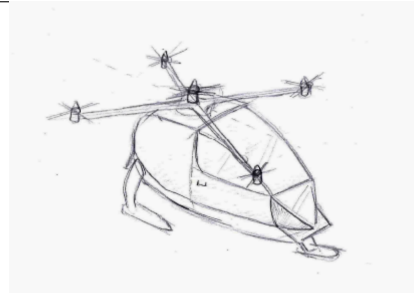


Figure 2.2: Top View Render

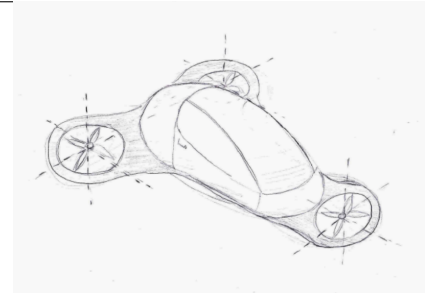


Figure 2.3: Front View Render

## 2.2.1 Power Trade-Off

Since the power subsystem was independent of the concept, a trade-off was performed for the power subsystem itself. The result of the trade-off was implemented in the final concept.

The power subsystems which were considered were replaceable batteries and a hydrogen fuel cell possibly in combination with solar cells. Each of the options were subjected to the following criteria. The weights are given in square brackets and on a scale of 1 to 4. The trade-off is presented in table 2.1

- Specific Energy 120 min flight [4]
- Specific Power 120 min flight [1]
- Safety [4]
- Cost [2]
- Development of Technology [1]
- Development of Infrastructure [1]
- Accessibility [3]
- Degradation (10 % drop) [2]

Table 2.1: Power Trade-Off Table

Criteria	Weight	HFC	HFC (nor.)	Battery	Battery (nor.)
Spec. Energy 120 min flight	4	0.842 $kWh/kg$	1	0.129 $kWh/kg$	0.153
Spec. Power 120 min flight	1	0.421 $kW/kg$	0.763	0.552 $kW/kg$	1
Safety	4	Safe	0.8	Very Safe	1
Cost	2	\$10993	1	\$20900	0.53
Devel. of Technology	1	6.7%	1	5%	0.746
Devel. of Infrastructure	1	62.2%	0.951	65.4%	1
Accessibility	3	Scarcely	0.25	Widely	1
Degradation (10% drop)	2	4000 cycles	1	2000 cycles	0.5
Total Score			14.66		12.42

Based on this trade-off it was chosen to go with a hydrogen fuel cell as the power subsystem. The choice was made not to use solar cells as they can not provide a significant part of the power required which makes them inefficient for this design.

## 2.2.2 Concept Trade-Off

The criteria for the concept trade-off are given below. The weight of each criteria is given in square brackets, expressed in %. The total weight sums up to 100 %.

- Mass [7.5]
- Energy Consumed per Cycle [20]
- Rotor Noise [20]
- Horizontal Distance To Full Stop [7.5]
- Sideways Manoeuvrability [7.5]
- Unit Cost [15]
- Complexity [22.5]

Prior to the trade-off it was realised that fig. 2.2 and fig. 2.3 have very much similarities. The only difference is the location of the rotors, which has effect on the manoeuvrability. Therefore the manoeuvrability of both concepts was assessed and it was found that concept with the rotors located in/below the body was better. Therefore, the final trade-off was performed only between the winged concept (fig. 2.1 and the in/below body multicopter concept (fig. 2.3). Both concepts were further developed and design choices such as the amount, size and configuration of the rotors were made.

Now that all the criteria were determined, they had to be estimated for each of the concepts. It was aimed to do this in a quantitative manner where possible. If not, a qualitative analysis was performed. The result of the analysis are presented in table 2.2 and the relative scores with respect to each other in table 2.3

Table 2.2: Summary Table

Criteria	Multicopter Concept	Winged Concept
Mass	486 kg	396 kg
Energy Consumed per Cycle	63.9 MJ	20.0 MJ
Rotor Noise	Very Good	Satisfactory
Horizontal Distance to Full Stop	116 m	182 m
Sideways Manoeuvrability	135 m	167 m
Unit Cost	101,390 USD	91,206 USD
Complexity	Very Good	Satisfactory

Table 2.3: Trade-Off Table

Criteria	Weights (%)	Multicopter Concept	Winged Concept
Mass	7.5	3.26	4
Energy Consumed per Cycle	20	1.25	4
Rotor Noise	20	4	2
Horizontal Distance to Full Stop	7.5	4	2.53
Sideways Manoeuvrability	7.5	4	3.23
Unit Cost	15	3.60	4
Complexity	22.5	4	2
<b>Sum of (Weight × Score)</b>		<b>3.33</b>	<b>2.98</b>

### 2.2.3 Results

From the trade-off it was chosen that the multicopter is designed in detail. As a starting point, which was the result of the preliminary designing in the midterm phase, the multicopter has the following characteristics.

- In-body rotors
- Hydrogen fuel-cell
- 4 pairs of coaxial rotors

## 2.3 Detailed Design

The various subsystems and components of the chosen concepts were developed further in the detailed design phase. In the following sections an overview of the different subsystems is given.

### 2.3.1 Aerodynamics

The main goal of the aerodynamics team was to design the drone in such a way that it complies the most with all the requirements. The aerodynamics were divided into three components: The body, shrouds around the propellers and the landing gear.

**Body** The body was designed to have a positive lift contribution. In this way the drone uses less power. It also resulted in a lower RPM for the rotors which has a positive effect on noise. The body characteristics are presented in table 2.4 and the final body design can be seen in fig. 2.5, fig. 2.4 and fig. 2.6

Table 2.4: Characteristics Lifting-Body

Angle of Attack[°]	Lift Coefficient	Drag Coefficient	Moment Coefficient	Aspect Ratio	Surface Area [m <sup>2</sup> ]	L/D Body	L/D Drone
-1.0	0.15	0.047	-0.099	0.25	4.0	3.2	0.36

**Shrouds** It was chosen to have shrouds around the propellers. Primarily in order to mitigate safety risks and increase the probability of achieving the acceptable noise level. Besides, shrouds seemed to have a positive influence on the rotor performance.

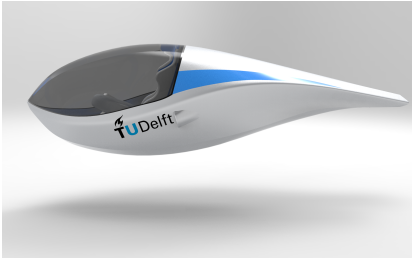


Figure 2.4: Side View Render

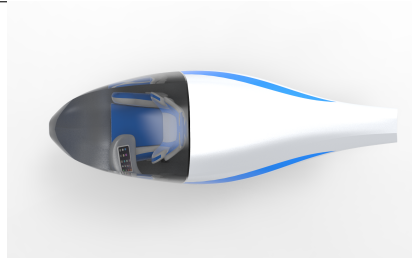


Figure 2.5: Top View Render

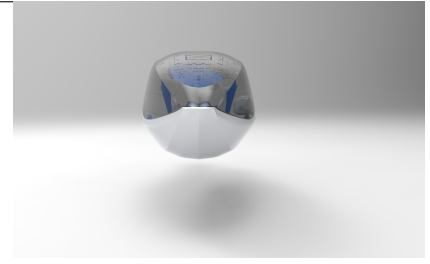


Figure 2.6: Front View Render

The shroud was designed primarily based on a qualitative breakdown of its components and functions. Its main geometric parameters are given in table 2.5 with the variables illustrated and explained in fig. 7.16a and section 7.4.2.

Table 2.5: Main geometric parameters of the shroud

Tip clearance	$\delta$	0.4	cm	Shroud width	$w_s$	15	cm
Vertical wall length	$h_s$	15	cm	Inner shroud radius	$R_i$	95.4	cm
Inlet radius	$r_i$	10.83	cm	Outer shroud radius	$R_o$	110.4	cm
Diffuser angle	$r_d$	11.89	$^\circ$	Margin for outer shell (top)	-	4.17	cm
Diffuser height	$h_d$	4.17	cm	Margin for outer shell (bottom)	-	14.12	cm

**Landing Gear** Four different landing gear concepts were considered: Bumper, running legs, wheels and a skid. The latter was opted to be the best fit for the HyDrone. Mainly because of the others being too heavy, aerodynamically inefficient or having a low TLR.

### 2.3.2 Structures & Materials

After carefully investigating the requirements and loads on the material, the following result was obtained. The cockpit, shrouds and load carrying structure will be fabricated of quasi isotropic carbon fibre in an epoxy prepreg. Mainly because of the high mechanical properties and low weight. When the HyDrone goes out of use, all carbon fibre will be recycled using a fluidised bed process.

The landing gear will be made of 7075-T6 Aluminium. Mainly because up to now, little research has been performed on how composites would function as a landing gear. All aluminium used will be remelted and recycled.

At last, the material that functions as a reinforcement for the shrouds against impact was chosen. The material that is going to be used is a unidirectional aramid fibre in an epoxy prepreg. This guarantees a safe flight, although at the cost of a high price. The windshield will be made of poly methyl methacrylate (PMMA). This material is cheap and transparent with a relative high impact strength.

### 2.3.3 Propulsion

It was chosen to have four coaxial contra-rotating rotor systems. The main advantage is that the output of the thrusts is larger than for a single rotor at the same power level. Furthermore, it presents a feasible redundancy strategy. The total thrust delivered was calculated using the Blade Element Momentum Theory (BEMT). The final characteristics of the propulsion subsystem are presented in table 2.6 and table 2.7.

Table 2.6: Rotor Characteristics(1/2)

Blade Chord Length $c$ [m]	Lift Curve Slope $C_{l_\alpha}$ [1/rad]	Number of Blades $N_b$ [-]	Minimum Radius $R_{Min}$ [m]	Maximum Radius $R_{Max}$ [m]	Upper Blade Tip Pitch $\theta_{u,Tip}$ [°]
0.15	5.73	2	0.05	0.95	4

Table 2.7: Rotor Characteristics(2/2)

Flight Condition	Inlet Velocity $V_{\infty}$ [m/s]	Revolutions per Minute [RPM]	Critical Flight Altitude [m]	Air Density $\rho$ [kg/m <sup>3</sup> ]	Lower Blade Tip Pitch $\theta_{l,Tip}$ [°]
Accelerating	5.909	2568	0 (sea level)	1.225	3.46
Climb	11.818	2022	650	1.150	2.72
Cruise	11.818	1790	650	1.150	3.12
Hover	0	2816	650	1.150	3.47

### 2.3.4 Power

As presented earlier, the power system was chosen to be a hydrogen fuel cell. It was decided that the best suited components for the HyDrone should be bought off-the-shelve. Two Toyota 700 bar fuel tanks weighing 40.5 kg each will be implemented in the HyDrone. For the fuel cell stack, the PowerCell S3-455c was chosen. This stack provides 125 kW and has a mass of 41.6 kg. This combination of fuel tanks and fuel cell stack provide more than enough energy and power for the HyDrone, as is presented in table 2.8. A small battery was added as an alternative power source and multiple design features were added to account for a reliable and safe power subsystem.

Table 2.8: Power &amp; Energy Budgets

	Maximum Power[kW]	Energy [kWh]
Consumption	104.5	173.8
Available	125.0	193.3
Contingency	19.6%	11.2%

### 2.3.5 Control & Stability

**Blade Pitch System** The requirements for the pitch systems are that it is low in maintenance and less complicated than the existing pitch systems of helicopters. Furthermore it should be protected by impacts of the environment. Since no pitch system which satisfies these requirements is commercially available at this moment, it was chosen to design a new blade pitch system.

The electric engine of the pitch system is the Rotereo BLE2. It has a maximum of 4000 RPM, mass of 1.6kg and a maximum power of 200W. In total 8 of these engines are required which sums up to a total mass of 12.8 kg for the pitch system.

**Sensors** The following sensors are used for the HyDrone to fly autonomously.

- 2 CORS GPS: to determine the position of the HyDrone
- 5 LIDAR: to detect and identify the surroundings
- 7 Radar: to detect objects
- 20 Ultrasonic sensors: 3d mapping of nearby objects
- 2 Gyroscope: to determine attitude
- 2 Accelerometer : to determine acceleration

Furthermore, 2 NVIDIA Drive PX2 Processors are installed. To communicate with the ground station 2 4G network dongles are installed.

**Controllers** In order to keep the HyDrone stable in all flight conditions controllers were designed. This system guarantees autonomous, safe and comfortable flight for the passenger.

### 2.3.6 Safety

Various design choices were made to enlarge the safety of the passenger. These systems either reduce the probability of failure or mitigate the impact of emergency's of HyDrone. The main safety systems are listed below

- Autorotation
- Navigation and Strobe Lightning
- Lightning Strike Protection
- Shrouds

Furthermore, all subsystems were designed whilst keeping safety in the back of head. This results in a lot of redundancy built into the HyDrone.

## 2.4 Final Result

All the above mentioned subsystems were combined and utilised in the HyDrone's final design. The HyDrone is presented in fig. 2.7. The performance characteristics are summarised in table 2.9 and the mass budget is presented in table 2.10.



Figure 2.7: Final Design Impression

Table 2.9: Performance Summary Table

Performance Parameter	Value	Performance Parameter	Value
Vertical Acceleration [ $m/s^2$ ]	1.18	Maximum Power Consumption [ $kW$ ]	104.5
Climb Velocity [ $m/s$ ]	11.8	Total Fuel Consumption [ $kgH_2$ ]	4.41
Cruise Velocity [ $m/s$ ]	40	Energy Efficiency [%]	0.44
Cruise Drag Coefficient [-]	0.3	Maximum Noise Level [ $dB(A)$ ]	113
Cruise L/D [-]	0.36	Maximum Range (100 $kg$ Payload) [ $km$ ]	144
Take-off Thrust [ $kN$ ]	6.38	Maximum Manoeuvre Load [ $g$ ]	0.73

Table 2.10: Mass Budget

Component	Mass [ $kg$ ]	Component	Mass [ $kg$ ]	Component	Mass [ $kg$ ]
<b>Structural</b>	149.0	<b>Power</b>	141.2	<b>Other</b>	49.0
Cockpit	58.3	Tanks (+H <sub>2</sub> )	86.0	Electronics	26.0
Skids	21.5	Stack	41.6	Climate System	10.0
Shrouds	62.4	Backup Battery	5.6	Furnishing	13.0
Beams	6.8	BoP + PCU	8.0	<b>Payload</b>	100.0
<b>Propulsion</b>	86.8	<b>Control</b>	20.0	<b>Contingency</b>	22.3
Propellers	54.8	Pitching System	12.8	<b>Total</b>	<b>568.3</b>
Motors	32.0	Sensors	7.2		

---

# Chapter 3: Conceptual Design

In this chapter the mission statement will be presented. The user requirements will be elaborated as well. Finally the flight profile is given.

## 3.1 Mission Statement

The aim of this project is to provide a personal, autonomous, zero-emission aerial mode of transport as an alternative to conventional transport in highly congested urban environments.

## 3.2 User Requirements

To be able to start the design process requirements were set up during the conceptual design phase. While these requirements have been left mostly unchanged some minor adjustment have been made. Some overlapping requirements have been combined and some were added. The updated list of requirements are stated below, where new requirements have been denoted with '\*'. For a more detailed description of the requirement discovery process the reader is referred to the baseline and midterm reports.

**SYS-TECH-POW1** The specific power of the fuel cell of the HyDrone power subsystem shall not degrade more than 10 % over its operational life.

**SYS-TECH-POW2** The refuelling time of the HyDrone shall be less than 10 minutes. [driving]

**SYS-TECH-POW3** At least 20% of the HyDrone power subsystem shall be recyclable. [driving]

**SYS-TECH-POW4** The HyDrone power subsystem shall have an operational life of at least 4000 cycles.

**SYS-TECH-POW5** Failure of the power subsystem shall not damage other subsystems.

**SYS-TECH-SFT1** Primary systems shall be equipped with a fail-safe feature. [driving]

**SYS-TECH-SFT2** The HyDrone shall be more reliable than helicopters of similar size.

**SYS-TECH-SFT3** A visual and/or audible warning system shall be implemented in order to alert the surrounding area of any emergency.

**SYS-TECH-SFT4** Lightning strikes shall not cause primary system failure.

**SYS-TECH-SFT5** The passenger shall not experience a load factor outside the range of  $-1g$  to  $1g$  in horizontal flight.

**SYS-TECH-SFT6** The passenger shall not experience a load factor outside the range of  $0g$  to  $2g$  in vertical flight.

**SYS-TECH-SFT7** The passenger shall not experience a jerking motion in excess of  $0.5 g/s$  under normal operating conditions<sup>[1]</sup>.

**SYS-TECH-SFT8** The vehicle shall have a limit manoeuvring load factor which exceeds a range of  $-1$  and  $3.5$ .<sup>1</sup>

**SYS-TECH-SUS1** The HyDrone shall be a zero-emission vehicle.

**SYS-TECH-SUS2** Of the material used to construct the HyDrone, at least 20% shall be recyclable.

**\*SYS-TECH-SUS3** The noise produced shall not exceed the stage 3 noise limits. (section 6.3)

**SYS-TECH-SOFT1** The HyDrone shall share vehicle sensory information with the manufacturer.

**SYS-TECH-SOFT2** The HyDrone shall allow for fully autonomous flight under all operating conditions.

**SYS-TECH-SOFT3** The HyDrone shall not allow access to its software by unauthorised parties. [driving]

**SYS-TECH-SOFT4** The HyDrone shall be capable of Over-The-Air ("OTA") software updates.

**SYS-TECH-MS1** The HyDrone shall not be permanently damaged by environmental and weather factors present in target markets.

**SYS-TECH-MS2** The structure shall not yield during nominal operations.

**SYS-TECH-MS3** The structure shall not fail under 1.5 times the ultimate load. [driving]

**SYS-TECH-MS4** The structure shall not exceed a  $5m \times 5m \times 5m$  cubical space in storage.

**SYS-TECH-MS5** The HyDrone shall allow for a cargo volume of at least  $0.05 m^3$ . [driving]

**SYS-TECH-MS6** The cargo shall be accessible by the passenger.

**\*SYS-TECH-AERO1** The total absolute pitching moment  $C_{m_{max}}$  shall not exceed the 0.88 (section 7.4)

**SYS-TECH-CONT1** The HyDrone shall be able to detect objects at a distance at which it can avoid collision.

---

<sup>1</sup>[http://rgl.faa.gov/Regulatory\\_and\\_Guidance\\_Library/rgFAR.nsf/0/aead1a7505ef922f852565f6006c1678!OpenDocument#\\_Section2](http://rgl.faa.gov/Regulatory_and_Guidance_Library/rgFAR.nsf/0/aead1a7505ef922f852565f6006c1678!OpenDocument#_Section2)

**SYS-TECH-CONT2** In the event of engine failure, the HyDrone shall be able to perform a controlled landing.

**SYS-TECH-COM1** The HyDrone shall be able to receive information under all operating conditions.

**SYS-TECH-COM2** The HyDrone shall be able to send information under all operating conditions.

**SYS-TECH-COM3** The HyDrone shall be able to communicate with other aerial vehicles.

**SYS-TECH-COM4** The communication system shall allow for direct communication with the authorities.

**SYS-TECH-PERF1** The HyDrone shall have a minimum cruise speed of  $60 \text{ km/h}$ . [driving]

**SYS-TECH-PERF2** The HyDrone shall have a minimum flight range of at least  $120 \text{ km}$ , including take-off and landing, without recharging.

**SYS-TECH-PERF3** The HyDrone shall provide enough engine power to lift-off with with an acceleration of at least  $1.09 \text{ m/s}^2$ .

**SYS-TECH-PERF4** The HyDrone shall provide enough engine power to maintain the specified cruise velocity.

**SYS-TECH-PERF5** The HyDrone shall have a maximum payload of at least  $100 \text{ kg}$ , including the passenger. [driving]

**SYS-TECH-PERF6** The HyDrone shall have a minimum cruise altitude of  $650 \text{ m}$ .

**SYS-TECH-PERF7** The HyDrone shall be able to perform vertical take-off and landing (VTOL). [driving]

**SYS-COST1** The unit cost of the HyDrone shall not exceed  $\text{€}100\,000$ . [killer]

**SYS-COST2** The development costs shall not exceed a total of  $\text{€}10\text{m}$ . [killer]

**SYS-TIME1** The HyDrone's time-to-market shall be less than 10 years.

### 3.3 Flight Profile

As described in the midterm report the mission flight profile has been based on a combination of the range requirement of  $120\text{km}$  and the expected trip range of  $30\text{km}$ . This trip range has been based on the diameter of the target cities Los Angeles, San Francisco and San Jose. The nominal flight profile, which consists of four equal flight cycles, is shown in fig. 3.1.

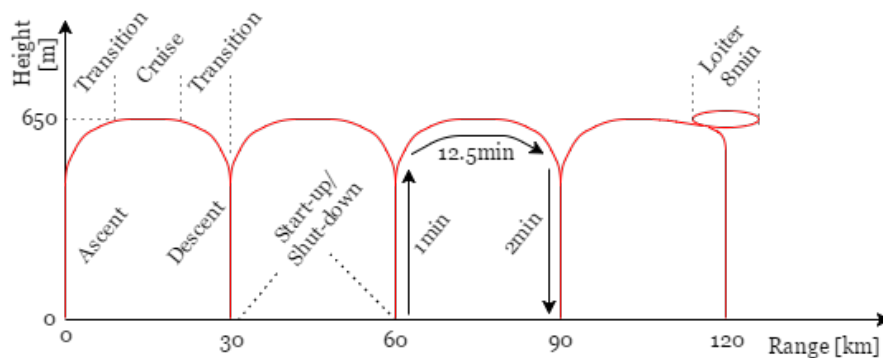


Figure 3.1: The nominal flight profile diagram of the HyDrone

Each flight cycle begins with the pre-flight start-up process after which it ascends to cruise altitude for 1 minute, cruises for 12.5 minutes and descends and lands for 2 minutes. This descent phase includes a 1 minute loiter time. To ensure an efficient flight the transition between ascent, cruise and descent occurs gradually. Using its reserve fuel, the drone is able to loiter for 8 minutes at the end of its final cycle in case the landing pad is occupied. During loiter it is able to signal the landing pad to request priority landing. The cruise altitude is set to  $650\text{m}$ , based on the Code of Federal Regulations [2], which dictates an operating altitude of at least  $1000 \text{ ft}$  above the highest obstacle<sup>2</sup>.

<sup>2</sup><http://www.laalmanac.com/structure/st01.php>, [cited 13-06-2017]

# Chapter 4: Detailed Approach

In order to get a clear overview of all the functions that need to be executed by the system an update of the functional flow in section 4.1 and breakdown structure in section 4.2 was made. The main differences can be found in the parts that were left open in terms of the choice of power source and the winged or multicopter design.

## 4.1 Functional Flow Diagram

The top level functional flow diagram is shown in fig. 4.1. The top level functions are broken down in more detail in fig. 4.2 through fig. 4.5. The update of the functional flow diagrams can mainly be found in the fact that the functions were added to get a more detailed overview. Furthermore due to design choices certain functions were deleted. For example the replacing of a tank as way of refuelling was deleted. Finally extra functions were added which are related to safety as a specific safety system will be designed for the final design.

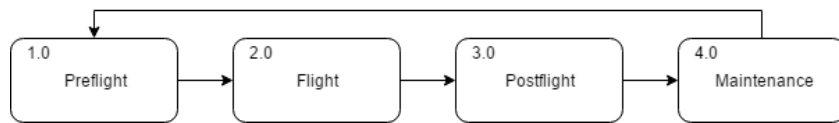


Figure 4.1: Top Level Functional Flow Diagram

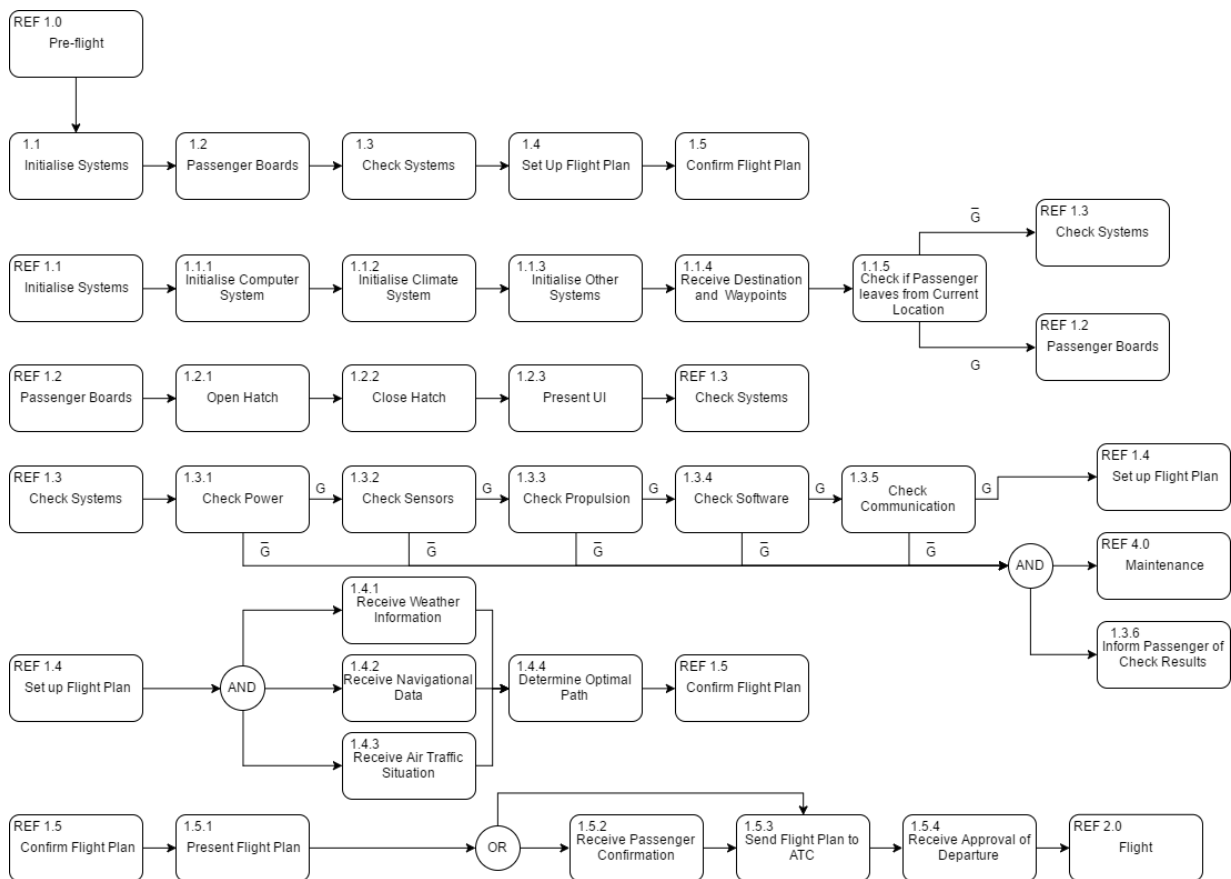


Figure 4.2: Functional Flow Pre-Flight

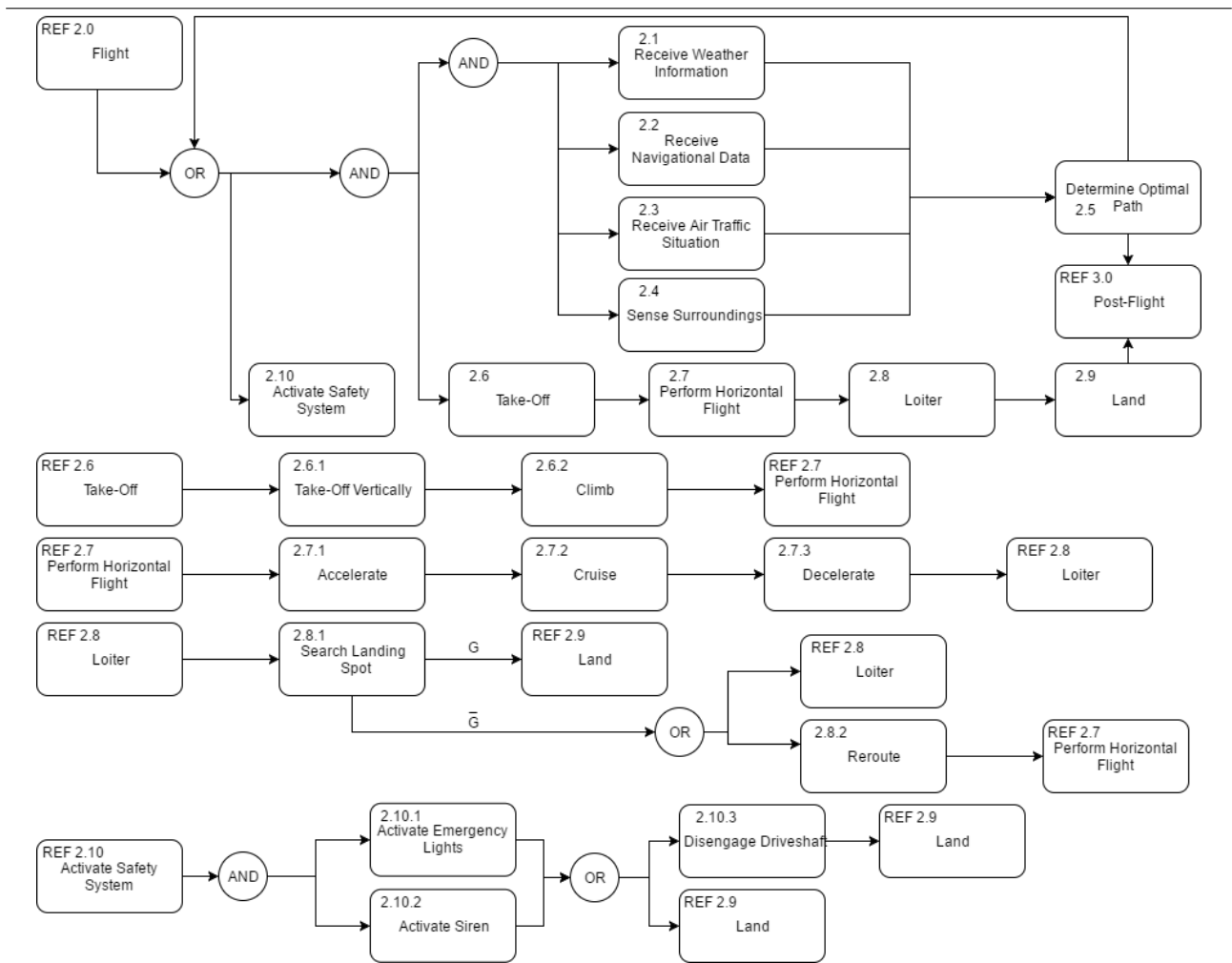


Figure 4.3: Functional Flow Flight

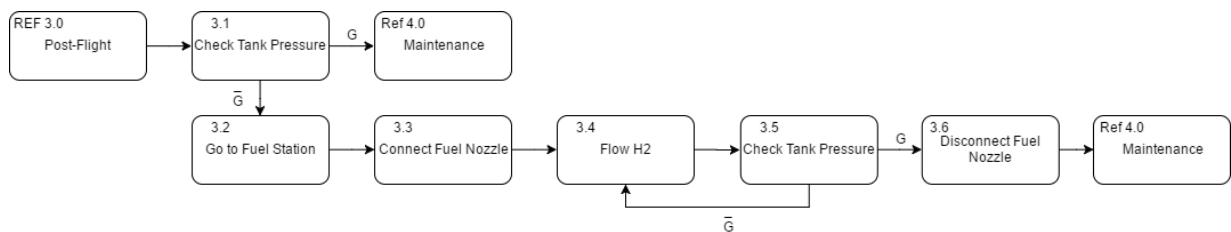


Figure 4.4: Functional Flow Post-Flight

## 4.2 Functional Breakdown Structure

For the functional breakdown structure the update was based on the same design choices that were made at the Midterm Review. Functions were defined more specifically to the configuration of the design. Furthermore, the guidance, navigation and control (GNC) part was updated to get a more elaborate view of the functions that are performed for this aspect. The 'Control' function for instance was broken down in the specific rotors that have to execute a certain change in thrust level to rotate in a required direction. Finally, a safety aspect was added to ensure that the functions involved in this are applied to the design. The Top level functions are presented in fig. 4.6. All lower level functions are broken down in fig. 4.7 through fig. 4.14.



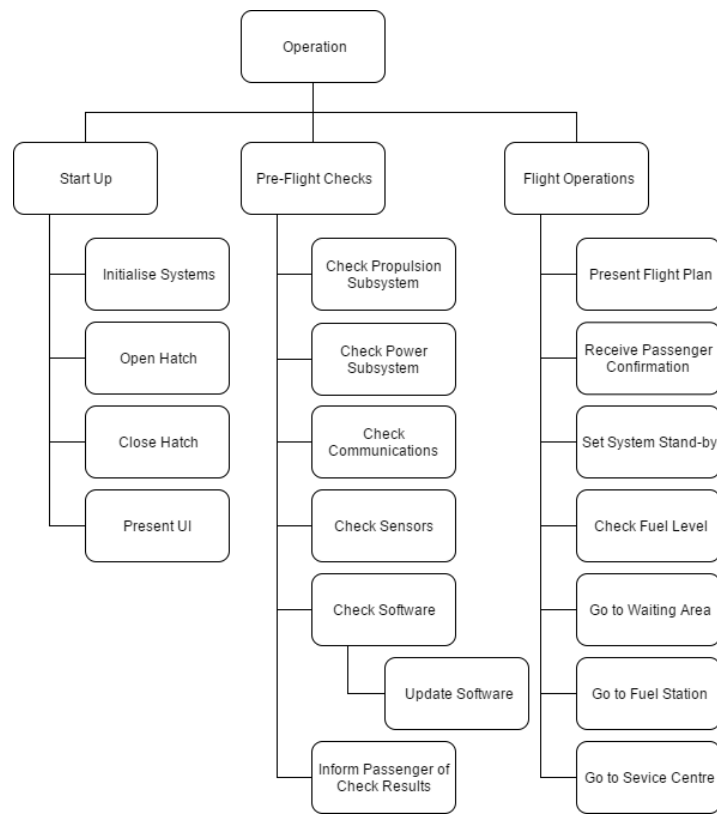


Figure 4.8: Functional Breakdown Structure Operation

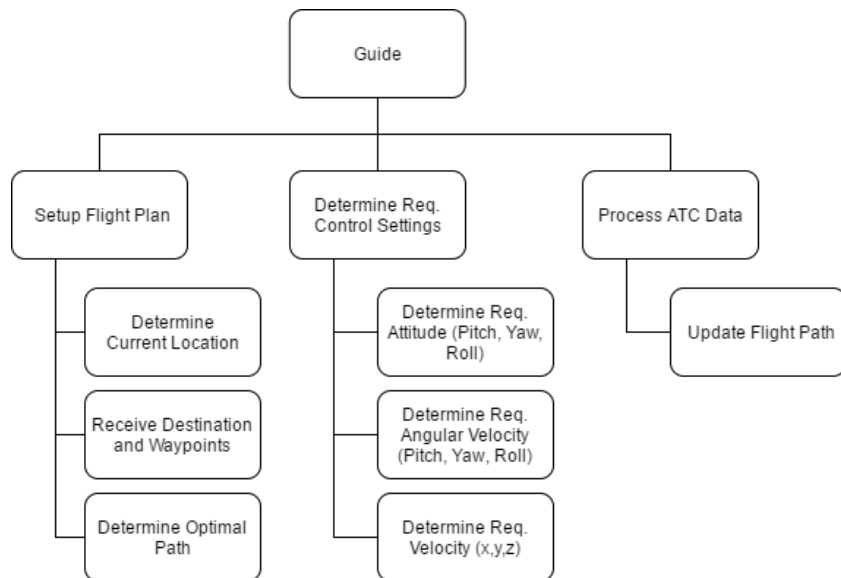


Figure 4.9: Functional Breakdown Structure Guide

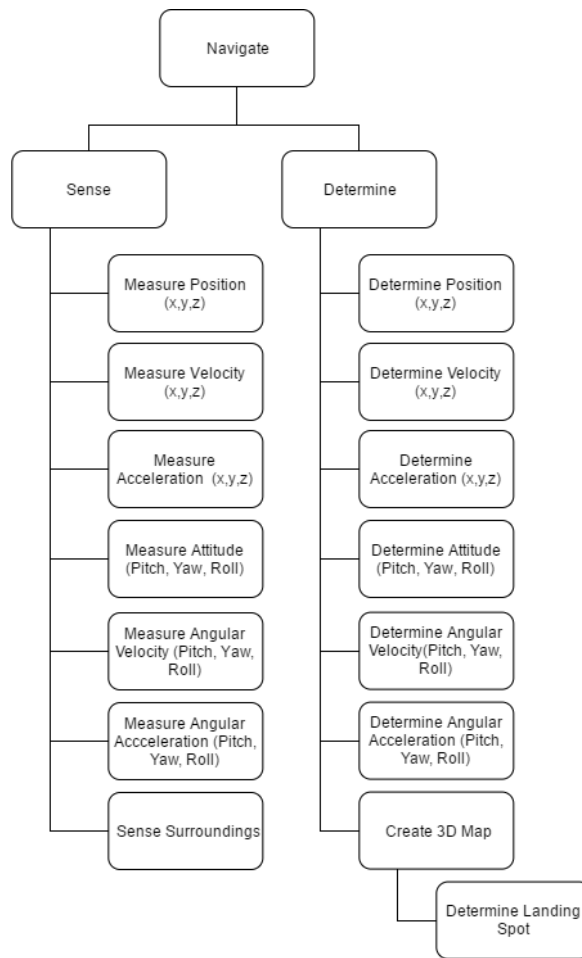


Figure 4.10: Functional Breakdown Structure Navigate

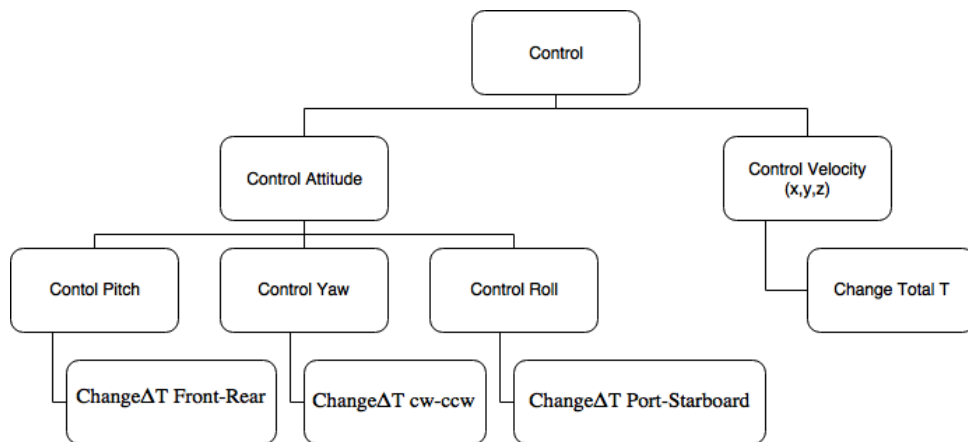


Figure 4.11: Functional Breakdown Structure Control

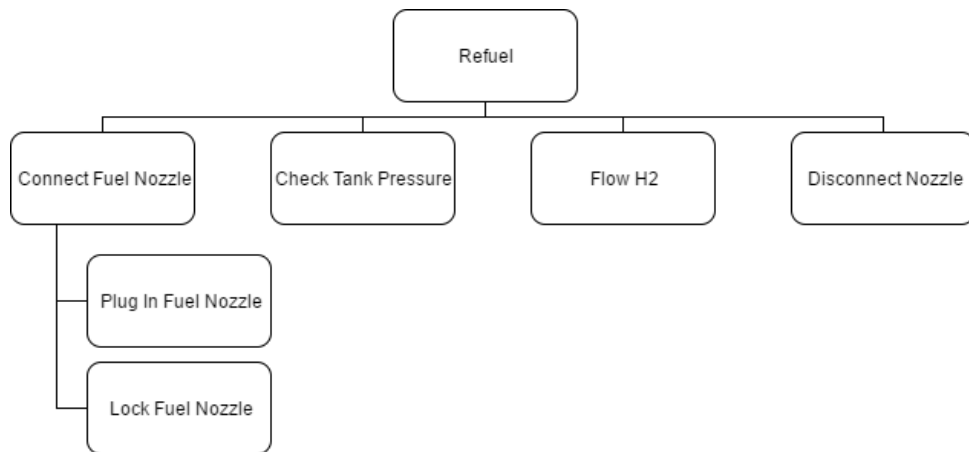


Figure 4.12: Functional Breakdown Structure Refuel

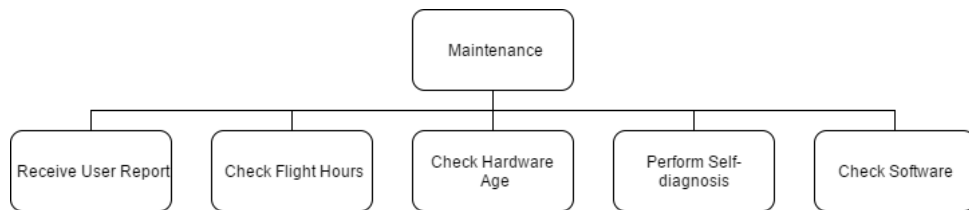


Figure 4.13: Functional Breakdown Structure Maintenance

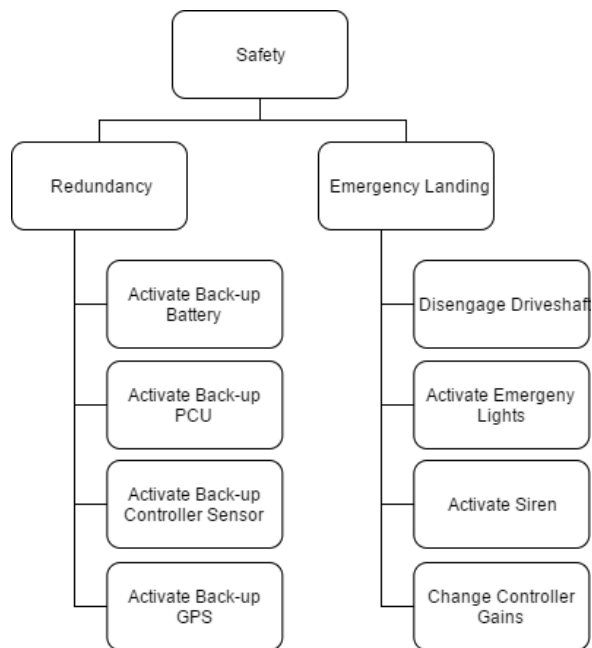


Figure 4.14: Functional Breakdown Structure Safety

---

# Chapter 5: Operations & Logistics

In order to identify all the departments of the logistics & activities, a block diagram has been generated. This diagram can be seen in fig. 5.1. Blocks with the same colour belong to the same logistic department. The lines between the blocks represent the direction of the information or route. The triangle blocks represent a decision or choice. The block diagram shows the concept of how the drone will operate when it is launched in the market.

In this project only the production, assembly and the autonomous operating are elaborated. The remaining divisions as booking, storage, passenger complaints and data server are behind the scope of this project and are only here to represent how in the future the HyDrone operation will be supported.

## Production

The production of the drone starting from the raw materials up to the customer is presented at the top of fig. 5.1. The supplier fabricates the required materials and subsystems. These products will be delivered at the factory where the materials will be further tooled and the final product can be assembled. This will further be elaborated in chapter 17

## Maintenance

The service centre continuously monitors, by means of the 4G network, in which state the drone operates in terms of maintenance. Internal maintenance procedures decide whether the drone can be repaired on the landing spot with limited down time or whether the drone should be transported back to the service centre. How the transportation back to the service centre is performed depends on where the drone is located. In case the drone is on the ground the transportation can easily be performed by truck but if the drone is on top of a building there should be a heavy duty helicopter present for moving the drone away. If the drone can be repaired on the landing spot, a serviceman is sent to the landing spot with appropriate equipment. Additionally, the drone flies to the service centre autonomously for a periodic check up.

## Autonomous refuelling

For refuelling the drone autonomously flies to a fuelling station, which are already present as will be described in section 19.2.1. It will be refuelled automatically. The hydrogen will be produced by factories that meet our standards for sustainability (see chapter 14) such that customers can be sure that they truly fly with zero harmful emissions. Renewable energy is used to produce the hydrogen for the drone at the fuelling stations. Refuelling the HyDrone will take approximately five minutes [3], which is half the time of the requirement.

## Booking platform

Passengers can book a drone online via an mobile app. After booking they can use Near Field Communication (NFC) on their phone which provides them entrance to the drone landing spot and the drone. In case the drone is privately owned the same procedure is followed to guarantee that only you can use your drone. Via the online platform it is also possible to lend privately owned drones to others.

## Storage

In situations when the drone is not used and it cannot stay on a landing spot for a long time because somebody else wants to use it for landing, it has the following procedure: first it checks whether there is a landing spot closer by than the drone depot. In case there is a nearby landing spot the drone will move there, else it will fly to the drone depot. The drone depot is a landing spot in or close to the city where drones are stored when they are not operating. The drone depot should be in the city or very near the city otherwise the drone spends too much energy flying to and from the drone depot. The costs for using existing landing spots is elaborated in section 19.1.3.

**Passenger complaints** During flight the passenger can send a signal on the app to the service centre for maintenance if they detect something unusual. In case of an unhappy passenger they can go to a complaints committee that handles the complaints and problems they have.

**Data server** The central server monitors the flight routes of the drones and prevents that the drone collides with other air traffic.

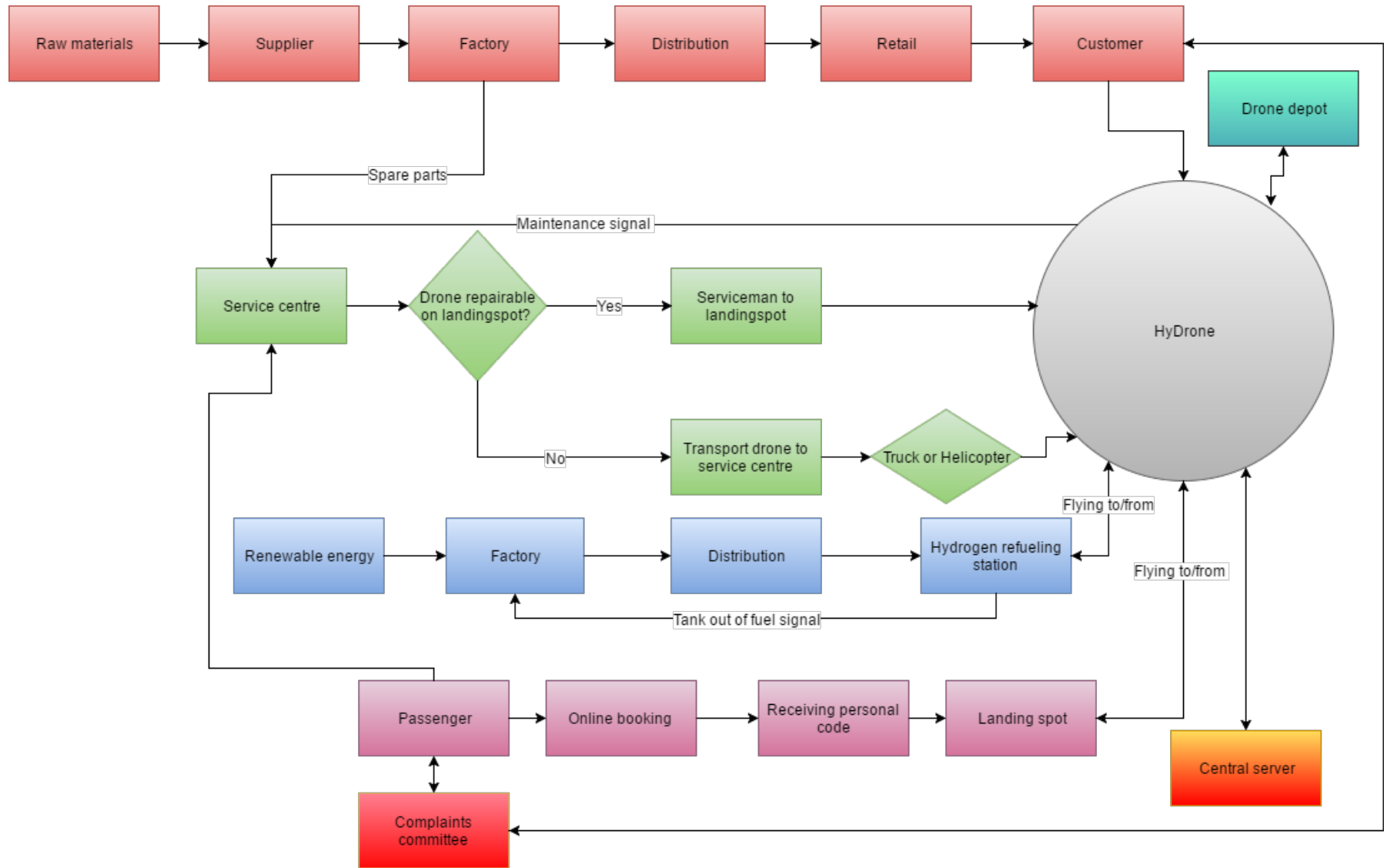


Figure 5.1: Logistics & Operations

---

# Chapter 6: Regulation & Certification

To design a whole new type of vehicle is a challenge in itself, but to truly launch it within a city environment is even harder. Due to many strict regulations and certifications one can not simply design only with the mission profile in mind, one must also ensure that the final design meets all legal requirements. This chapter will set out to identify all the regulations and certifications that must be taken into consideration for the final design.

## 6.1 Approach of Literature Study

Since there is no manned autonomous multicopter already operating present day, there are very little rules which directly apply to such a vehicle. Therefore it was chosen to retrieve regulations and certifications which are meant for helicopters, as this is the most comparable type of vehicle. Also, as the vehicle is to be launched first in San Francisco, USA, the decision was made to obtain all the information regarding regulation and certification from the Federal Aviation Administration (FAA). It was found that not all other countries of interest have such strictly defined regulations. Instead, special permissions have to be acquired. A successful launch in the USA could greatly help expanding this concept to these other countries, as the success will prove that this new mode of transport is in fact viable and functioning within urban environments.

The FAA provides a huge database of regulations regarding aerial vehicles. Not all these regulations directly apply to helicopters, but many do. Stating every single regulation would be bad practice as the reader will no longer see the wood for the trees, instead the most relevant and decisive regulations are presented in this section. For a complete list of all rules the reader is advised to read the Code of Federal Regulations Title 14 [2].

Do note that the final design must conform to every rule imposed by the FAA, listing every rule is, however, beyond the scope of this report. To keep it precise, the emphasis is put on the subjects which define the concept of the HyDrone and make the design unique. The study on legislation has therefore mainly been performed on three aspects which are considered of main importance: Airworthiness, noise and autonomous flight.

The legislation on airworthiness is studied since the vehicle should be certified to operate. Airworthiness consist mainly of safety regulations which ensures the vehicle does not become a hazard to the passenger and people within the operated area. The vehicle will operate in the congested city of San Francisco. The large inhabited cities demand from the design that it shall not be a nuisance to the residents in terms of noise. Because the HyDrone is operated autonomously a study on the legislation of autonomous vehicles has been performed.

## 6.2 Airworthiness

Airworthiness is not simply defined by a single parameter, instead it is a quality characterised by the system as a whole. Many strict regulations apply on every subsystem so that the entire aircraft is deemed safe to fly. The FAA splits airworthiness requirements of a rotorcraft into seven separate subparts:

- General
- Flight
- Strength Requirements
- Design and Construction
- Powerplant
- Equipment
- Operating Limitations and Information

Many of the items within these subparts are quite straightforward. For example, regulation §27.251[2] Vibration simply states: "Each part of the rotorcraft must be free from excessive vibration under each appropriate speed and power condition." This shows that many regulations are not necessarily composed of strict numerical values. This is because the rules set by the FAA are to be met by any aerial vehicle, and these aerial vehicles have great differences. Effectively airworthiness simply states that the seven subparts listed above perform in such a manner that the vehicle does not fail and does not cause any harm to its surroundings.

Regulations on subsystem level regarding airworthiness are taken into account during the designing of these subsystems, e.g.: the structure must be able to carry load factors ranging from +3.5 to -1 (§27.337 Limit manoeuvring load factor [2]) or: the fuel tank must be able to withstand a fall from 50 ft (§27.952 Fuel system crash resistance [2]).

---

## 6.3 Noise

The regulation for noise according to section §36.805 'Noise limits' of the FAA [2] states that any helicopter which applied to be certified after May 2014 must have a noise level no greater than than the 'Stage 3' noise limits. Stage 3 noise limits are defined as follows:

- For Take off - The noise limit is  $106\text{ dB}(EPNL)$ . which decreases linearly with the logarithm of the helicopter weight at a rate of  $3.0\text{ dB}(EPNL)$  per halving of the weight down to  $86\text{ dB}(EPNL)$ , after which the limit remains constant. The reference flight path is defined as a straight line segment inclined from the starting point (500 meters from the centre microphone location and 20 meters above ground level) at a constant climb angle defined by the certificated best rate of climb and at the velocity for minimum engine performance.
- For Flyover - The noise limit is  $104\text{ dB}(EPNL)$  which decreases linearly with the logarithm of the helicopter weight at a rate of  $3.0\text{ dB}(EPNL)$  per halving of the weight down to  $84\text{ dB}(EPNL)$ , after which the limit remains constant. The flight path should be performed at an altitude of 150 meter above ground level at 0.9 the never exceed airspeed.
- For Landing - The noise limit is  $109\text{ dB}(EPNL)$  which decreases linearly with the logarithm of the helicopter weight at a rate of  $3.0\text{ dB}(EPNL)$  per halving of the weight down to  $89\text{ dB}(EPNL)$ , after which the limit remains constant. The Landing manoeuvre is measured at 120 meters above the noise measuring equipment and at an approach angle of  $6^\circ$ .

These regulations apply to helicopter with a weight of no more than  $80,000\text{ kg}$ . The HyDrone design will be in the order of  $500\text{ kg}$  which results in that all the lower limits are used for the limit noise level. The noise limit is given in  $\text{dB}(EPNL)$  which is a abbreviation for the effective perceived noise in decibels. It is a measure of the relative loudness of an individual by passing aircraft.

In order to check whether or not the aerial vehicle truly meets the regulatory noise limits test measurements should be performed. The FAA states that the measurements must be performed at an ambient temperature of 25 degrees Celsius, at sea level pressure, with a humidity of 70% and no wind.

The value of the sound exposure (SEL) denoted as  $L_{AE}$  can be calculated with equation 6.1 (taken from appendix J36.109 [2] ) and is denoted in decibels. It is defined as the time interval squared A-weighted sound pressure over a given time period with respect to the square of the standard reference sound pressure ( $P_0$ ) of 20 micropascals and a reference duration of one second. A-weighting is applied to instrument-measured sound levels in an effort to account for the perceived loudness by the human ear.  $T_O$  is the time interval of the event ( $t_2 - t_1$ ).

$$L_{AE} = 10\text{Log}_{10} \frac{1}{T_0} \int_{t_1}^{t_2} \left( \frac{P_A(t)}{P_0} \right)^2 dt \quad (6.1)$$

At the current stage no actual measurements will be performed, but the Stage 3 noise limits imposed by the FAA are used in the noise level estimations (see chapter 13).

Other than noise limits there are also altitude regulations. These are of importance as they affect the mission profile. According to FAA code of federal regulations section §91.119[2] for low flying aircraft, a minimum height of  $1000\text{ ft}$  ( $305\text{ m}$ ) above the highest object within a  $2000\text{ ft}$  ( $610\text{ m}$ ) radius should be achieved for operation in normal flight conditions (this excludes take-off and landing). Helicopters however can operate at lower altitudes than these prescribed minimums if operation is conducted without hazard to persons or property on the surface. This is because of its ability for precise landing during engine failure and the improved utility of helicopters in law enforcement and health care.

## 6.4 Autonomous Flight

The HyDrone will operate autonomously which demands research in the legislation of autonomous vehicles. Autonomous vehicles are up-and-coming and therefore there is not much regulation since the concept is still in its infant stage. Most of the legislation applies to unmanned aircraft (drones) of small size. Because of this also research on the legislation of autonomous cars have been performed since the concept of cars is further developed.

According to section §135.93[2] on the minimum altitude for the use of autopilot in the FAA the use of autopilot is prohibited during take off, initial climb or a missed approach. For ordinary flight manoeuvres aircraft may not operate below a height of  $500\text{ ft}$  ( $152.4\text{ m}$ ). For approach autopilot may not be used at an altitude of  $50\text{ ft}$  ( $15.2\text{ m}$ ) below the minimum descent altitude. Landing may be performed on autopilot when an approved automatic landing system is present. The certificate holder of the aircraft needs to show to the Federal Aviation Administrator that the autopilot system can be conducted in a safe manner. However, as mentioned earlier the concept of completely autonomous personal aerial vehicles is relative new. It is predicted

---

that legislation concerning the operation of autonomous aircraft will be updated as the designs for autonomous aerial vehicles are improved and that cities are adapted for their use. Take for example the recently passed bill of part 23 of the FFA [2] which is updated to make it easier for autonomous vehicles to be certified to give the autonomous industry an impulse.

The automotive industry is also undergoing a switch to autonomous vehicles. The development is already in a further stage than the aviation industry which makes it a great reference to gain insight in legislation changes. Looking specifically at the state of California, bill SB1298 has been passed in 2012 which permits autonomous vehicles to be operated and tested on the public roads within the state. Later in 2016 bill AB1592 was passed. It authorises the Contra Costa Transportation Authority to conduct a pilot project for the testing of autonomous vehicles that are not equipped with a steering wheel, a brake pedal, an accelerator, or an operator inside the vehicle, provided the testing is conducted only at specified locations and the autonomous vehicle operates at specified speeds <sup>1</sup>. It is believed that in a similar manner the FAA will be updated during the development of fully autonomous aerial vehicles. Therefore the the legislation concerning approved flight manoeuvres which currently apply do not pose a constraint on the autonomous design of the HyDrone.

---

<sup>1</sup><http://www.ncsl.org/research/transportation/autonomous-vehicles-self-driving-vehicles-enacted-legislation.aspx> [cited 26-06-2017]



---

# Chapter 7: Aerodynamics

In this chapter, the remaining elements for the overall system shape are compared and designed from the design perspective of aerodynamics. Firstly, the design options will be presented. Secondly, the trade-off criteria are explained. The remaining of the chapter explains the design process of the body (see section 7.3.2), shrouds (see section 8.3 and landing gear (see section 7.5) in detail. Then the risks and recommendations are presented in section 7.6 and section 7.7.

## 7.1 Design Options

In principal, the system can be classified into three abstract parts

1. The body, defined as the cockpit residing in the middle of the system.
2. The attachments between the body and the propeller.
3. The landing gear.

Before aerodynamic design could start, the focus was on these three trade-offs:

1. To design the body lift positive or not (see section 7.3.4;
2. To include shrouds around the propellers or not (see section 7.4.1);
3. Which landing gear system to choose (see section 7.3.4);

As can be seen from trade-off no. 1, the other structural components are not designed (or assumed) to be lift-positive. Several other options were briefly considered. For instance, one could try to incorporate the above-mentioned separate part into a lift-positive blended body. Next, while retaining the separation between the parts, either both the body and the struts or only the latter can be designed lift-positive. While the struts could theoretically be made to generate positive lift (i.e. 'lifting struts'), it would unnecessarily increase the design complexity by having to function within a propeller wake. This issue of design complexity - the ability to produce a feasible design within the scope of this project - was the key consideration in this decision. A brief literature study yielded the consensus that the most feasible path forward is to focus on a lifting body and determining whether that is desirable.

## 7.2 Criteria

The different options with respect to the aerodynamic design will be examined and judged based on the following criteria. The criteria are chosen such that they comply with the requirements for this project and are elaborated in this section.

### **Complexity**

The complexity of the options reflects the feasibility in real world and give an indication of the development costs. Since two of the key requirements set a limit on the development cost, the complexity has to be examined. The complexity encompasses both the technology readiness level (TRL) as well as the developments costs, which are related to each other.

### **Safety**

Since the drone is going to transport human passengers, it is of uttermost importance to guarantee safety. If this cannot be guaranteed, the system is considered to have failed since it will not be allowed to fly. Therefore, the safety of the considered aerodynamic options will be examined and possibly is the key reason to decide whether or not to actually implement the option.

### **Noise**

The drone has been designed to operate in highly congested areas and will inherently make noise. The key is to keep this noise as low as possible by all means. If the drone produces too much noise, the drone will not meet the noise regulations and is not allowed to fly because of that. Therefore, the given aerodynamic options should have at least a neutral effect, and preferably a positive effect on noise.

### **Sustainability**

Sustainability is an important aspect of the drone, hence the sustainability of each option has been examined. Within the scope of the trade-off regarding the aerodynamic options, the sustainability encompasses the effect on the fuel usage and the materials used. The fuel usage, as well as the use of sustainable materials, depict the degree of sustainability of the option.

## 7.3 Lifting Body

The scope of the project is to come up with a design that is as sustainable as possible. From the conceptual analysis in the midterm report, it was noted that the drone will consume most of the available energy in the cruise phase. In order to reduce the used energy as much as possible, solutions were searched for and found through literature studies. One of these solutions is having the body generate lift itself, or at least not produce negative lift. Obviously, a possible result is that the rotors have to deliver less power since the lifting body takes on a part of the required lift. A detailed study regarding lifting bodies has been presented in this section.

### 7.3.1 Lifting Body of a Drone

In order to provide forward thrust, the drone will be tilted forward. In other words, the pitch of the body will be negative. Therefore, the performance of the body in terms of lift and drag are of great interest since this can possibly have a major influence on the energy usage of the drone.

In fig. 7.1, the lift curves of several commercial drones are depicted. The lift curve belongs solely to the body of the drone. This means that during testing, the engines were shut off. The drones that were tested are the 3D Robotics SOLO<sup>1</sup>, DJI Phantom 3 Advanced<sup>2</sup>, 3D Robotics Iris+<sup>3</sup>, Drone America DAX-8<sup>4</sup> and the Straight Up Imaging Endurance<sup>5</sup>. None of the drone bodies produces lift when the pitch is negative, as can be seen.

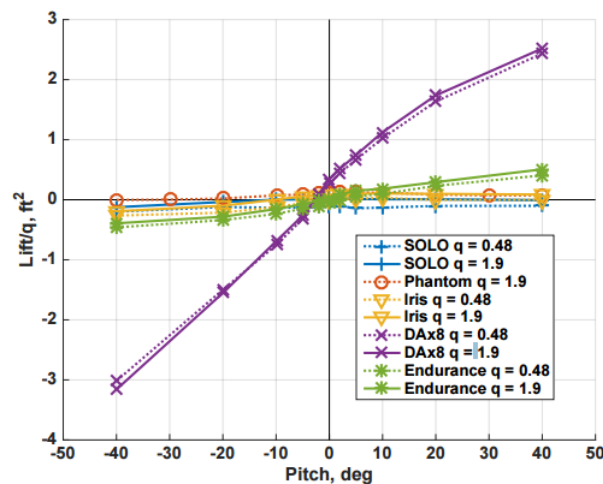


Figure 7.1: Lift vs Pitch Angle [4]

However, wind tunnel studies show that when a properly designed canopy is used, a positive lift contribution from the body can be achieved. An example is the Shrediquette GEMiNI<sup>6</sup>. The wind tunnel test data of this drone is presented in fig. 7.2. It can be seen that a canopy has a positive effect in terms of lift. A similar set of wind tunnel test results are presented in Willard's [5].

<sup>1</sup><https://3dr.com/solo-drone/>

<sup>2</sup><https://www.dji.com/phantom-3-adv>, [cited on 13-06-2017]

<sup>3</sup><https://www.drones.nl/drones/3d-robotics-iris-plus>, [cited on 13-06-2017]

<sup>4</sup><http://www.droneamerica.com/systems/dax8>, [cited on 13-06-2017]

<sup>5</sup><http://www.straightupimaging.com/products/>, [cited on 13-06-2017]

<sup>6</sup><http://shrediquette.blogspot.nl/p/shrediquette-gemini.html>

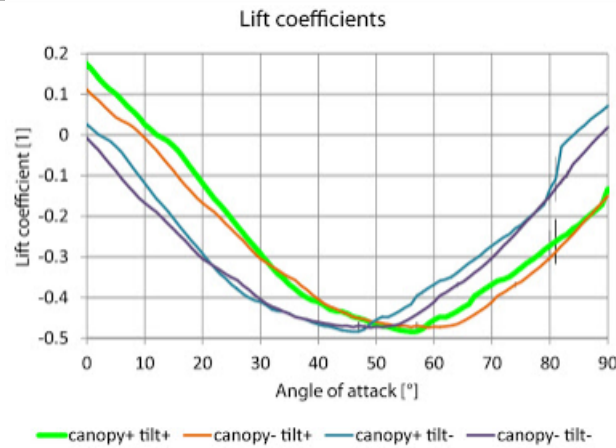


Figure 7.2: Lift vs Pitch Angle of the GEMiNi

The results show that it is indeed possible to have a body which has a positive contribution to the lift. However, it should be investigated if this can be exploited with larger vehicles. The next subsection will present larger vehicles which make use of this principle.

### 7.3.2 Lifting Body Vehicles

In order to make use of the principle of a lifting body, the feasibility of this concept was investigated through a literature study. The reference vehicles and their most important characteristics are presented in table 7.1

Table 7.1: Lifting Body Reference Vehicles [6]

Vehicle	Mach Number	$C_{D_{min}}$	$(L/D)_{max}$	Nominal Weight [kg]
M2-F1	0.15	0.0618	3.44	567
M2-F2	0.45	0.0650	3.13	2720
HL-10	0.6	0.0496	3.6	2720
X24-A	0.5	0.04	4.25	2885
X24-B	0.5	0.0252	4.5	3855

Judging from table 7.1, the concept of a lifting body is indeed feasible. This is not only deduced from the fact that lifting bodies are an existing concept, but that the M2-F1 has a comparable weight and flies at a comparable mach number as the HyDrone. It should be noted that the reference vehicles are meant to fly at a positive angle of attack, whereas the HyDrone operates at negative angles of attack.

From section 7.3.1 and section 7.3.2, it is certainly clear that a lifting body is indeed possible. This section proceeds with identifying the limiting factors of a lifting body for the HyDrone.

### 7.3.3 Limiting Factors

#### Angle of Attack

As is evident from fig. 7.3, the required angle of attack can be determined with eq. (7.1).

$$\alpha = \tan^{-1}\left(\frac{T'}{L}\right) \quad (7.1)$$

The lifting body has been designed such that it can provide a certain amount of lift, thus implying that the total thrust  $T$  can be reduced. But the airspeed must not change, because the selected airspeed is optimal in terms of energy consumption. Therefore, the angle of attack would have to increase. But at large negative angles of attack, it is difficult to come up with a design that produces a sufficient amount of lift. Or at least does not produce negative lift. This demands for unconventional positioning of the body with respect to the propellers and affects the overall complexity of the HyDrone.

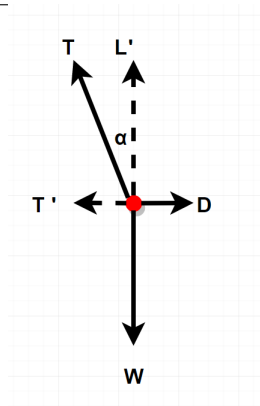


Figure 7.3: Free Body Diagram of the drone

### Size of the Body

Because the rotor size and location are set, the width and length of the body itself are limited in order to still comply with the size requirement. This limits the available surface area which is related to the lift generated by the body. Besides, the following must fit inside the body;

- Passenger
- Fuel Tanks
- Fuel Stack
- Control Panel
- On-Board Computer
- Cooling
- Electronics
- Load Carrying Beam

This requires a relatively large body and will most certainly influence the amount of available options.

### Drag

A possible limiting factor is the lift induced drag. The power saved due to the lift generated shall not be lower than the power required to overcome the extra drag. In section 7.3.5, it is examined whether or not it is favourable to have a lifting body.

### 7.3.4 Trade-Off

A trade-off has been carried out in order to judge whether or not a lifting body is beneficial for the HyDrone.

#### Complexity

The complexity of a lifting body arises from the fact that the angle of attack of the body is limited. A lifting body has a zero-lift angle of attack which shall not be exceeded. If the required angle of the rotor thrust has to be larger than the zero-lift angle of attack of the body, there will be an offset in the rotor's positioning with respect to the body. This is inevitable since the design concept explicitly stated fixed rotors. The required offset will affect the load carrying structure since either the rotors are tilted or the body is. This is depicted in fig. 7.4.

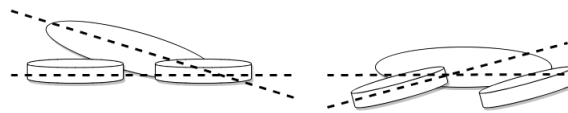


Figure 7.4: Impressions of Configurations if Angles Differ

The left option in fig. 7.4 has a tilted body, which makes it difficult for the passenger to enter the vehicle. This adds to the overall practical complexity of the HyDrone.

The right option will require corners in the load carrying beams and will make the take-off and landing procedures more complex, since the forward rotors must turn the vehicle such that the rotors are in the horizontal plane. This will enhance extra stresses on the back of the landing gear during take-off and landing.

### Noise

Noise is an important aspect of the HyDrone design. Therefore, it has to be investigated whether or not a lifting body has an effect on noise with respect to a non-lifting body.

The HyDrone has 8 large rotors with a diameter of 1.90m each. These rotors are used to provide the forward thrust, as well as the thrust required for hovering flight. The HyDrone should also be capable of vertical take-off and landing, which is exactly what a helicopter does and therefore the HyDrone will be treated as a helicopter in the scope of noise. The main noise sources of a helicopter are listed below [7].

- 
- Rotor Vortex Noise
  - Rotational Noise
  - Blade Slap

The previously made assumption regarding noise is quite critical. That is, the noise sources of a winged aircraft differ quite significantly from those of a helicopter. With regard to helicopters, the main noise source is the rotor, whereas the noise produced by a winged aircraft arises from the aerodynamic characteristics of the airframe [8] [9]. The result of treating the HyDrone as a helicopter is that the noise due to the shape of the body is insignificant with respect to the overall noise level. So as far as the noise is concerned, there is no difference between a non-lifting body and a lifting one.

### Safety

A lifting body will be a so-called passive safety system. If one or multiple rotors fail during cruise, the remaining rotors can position the body such that maximum lift is generated. This way, the decrease in lift due to engine loss is minimised. It also allows the remaining rotors to be utilised for control purposes and guarantee a safe landing. Of course, the lifting body will be of no use when the HyDrone does not have a forward speed, so the added safety will only be present during cruise. Nevertheless, having added safety just by carefully designing the body such that it generates lift is a huge asset.

### Sustainability

A lifting body has the potential to be a positive contribution to sustainability. A reduced thrust output is possible with the lifting body, thus implying that the propulsion system requires less power. If the extra power due to the lift induced drag is less than the power savings due to the lift, the overall power required will be lower if considered for the same flight conditions. This means that less energy is used during a cycle, allowing one to fly more cycles for the same amount of fuel. Investigating a lifting body perfectly fits the project because the goal is to produce a sustainable VTOL air vehicle.

### Result

Although the complexity will increase in terms of structures and materials, it is still a feasible goal. The field of structural analysis is widely developed and more difficult structures have been developed in the past. Besides, it does not require any technology which has not been developed yet. So the Technology Readiness Level remains the same.

As previously assumed, the noise levels will not be affected by the lifting-body. In addition to that, a lifting-body will have a positive effect on safety and sustainability. The advantages in terms of safety and sustainability are more significant than the minor disadvantage due to complexity. Therefore, on the condition that the lifting body is beneficial in terms of power, the HyDrone will have a lifting-body. In the next section, the design of the body is further elaborated.

## 7.3.5 Design

The design process of the lifting body is presented in this section. This encompasses the size, shape, lift and drag characteristics, power savings and shape optimisation.

### Size

As stated in the previous subsection, the size of the body depends on multiple aspects. Initially, in the preliminary design phase, the radius of the rotors including shrouds was determined to be  $1m$ . This means that the total width of two rotors placed next to each other is  $4m$ . Therefore, the maximum width of the body is  $1m$  (see fig. 7.5).

According to Macey[10], a comfortable width for a passenger in a car is  $0.8m$ . Since the passenger will sit in the HyDrone just as it does in a car, a minimum width of  $0.8m$  is assumed. In addition to this, every subsystem will have to fit within the limits and therefore the width of the body is chosen to be  $1m$  in order to have some room for movement. One more factor which contributed to this decision is that the surface area of the lifting body increases as a result, which generally results in more lift<sup>7</sup>.

The next dimension which had to be determined was the height of the body. The minimum (comfortable) height in cars is  $0.95 m$  [10]. To guarantee a comfortable flight, a maximum height of  $1.2 m$  has been chosen. In order to check whether or not this would be high enough, sports cars were examined. For example, a Ferrari F-50 has a height of  $1.12m$ <sup>8</sup>, which includes the ground clearance. Therefore, a body height of  $1.2m$  is assumed to be sufficient. One requirement which follows is that the seat configuration has to be similar to that of a sports car. Finally, the maximum lateral length was determined to be  $5m$ , which simply follows from the size requirement. A top view is provided in fig. 7.5 for clearness.

---

<sup>7</sup>[https://www.grc.nasa.gov/www/k-12/WindTunnel/Activities/lift\\_formula.html](https://www.grc.nasa.gov/www/k-12/WindTunnel/Activities/lift_formula.html), [cited on 15-06-2017]

<sup>8</sup><http://media.caranddriver.com/files/ferrari-f50.pdf>, [cited on 15-06-2017]

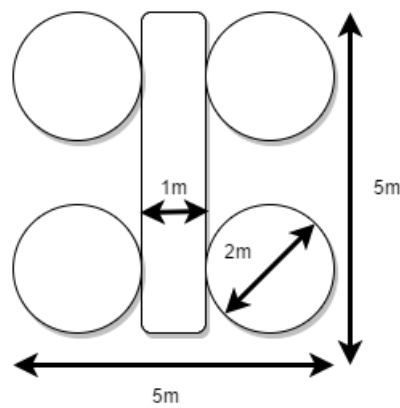


Figure 7.5: Top View of Maximum Dimensions of the HyDrone

### Body Shape

As a result of section 7.3.4, the design of the body will generate lift. Custom designing the body shape would require rigorous computational analysis and not feasible within the given time. Therefore, it was decided to shape the body in the form of an already existing aerofoil, since the dimensions and aerodynamic characteristics are already known.

Since the rotors inevitably have a negative angle of attack, it is preferred to have a body that generates lift at low (even negative) angles of attack. This way, the angle between the body and the rotors is kept to a minimum, which reduces complexity (section 7.3.4 further describes the complexity). Another requirement of the shape of the body is that it is relatively thick. Since the lateral size has been restricted to be 5000mm or less, the aerofoil has to be thick in order to have a height of 1200mm, which was derived previously.

From the two requirements (angle of attack and thickness), the following suitable aerofoil was found: Althaus 94-W-301. The maximum thickness of this aerofoil is 30.1% located at 30.9% of the chord length. In order to have a sufficient height, a chord length of 4m was chosen, which leads to a height equals  $0.301 \cdot 4000\text{mm} = 1204\text{mm}$

The cross section is depicted in fig. 7.6<sup>9</sup>. This aerofoil is the thickest, commercially used aerofoil available in the database of [www.airfoiltools.com](http://www.airfoiltools.com) and it generates lift at small negative angles of attack.

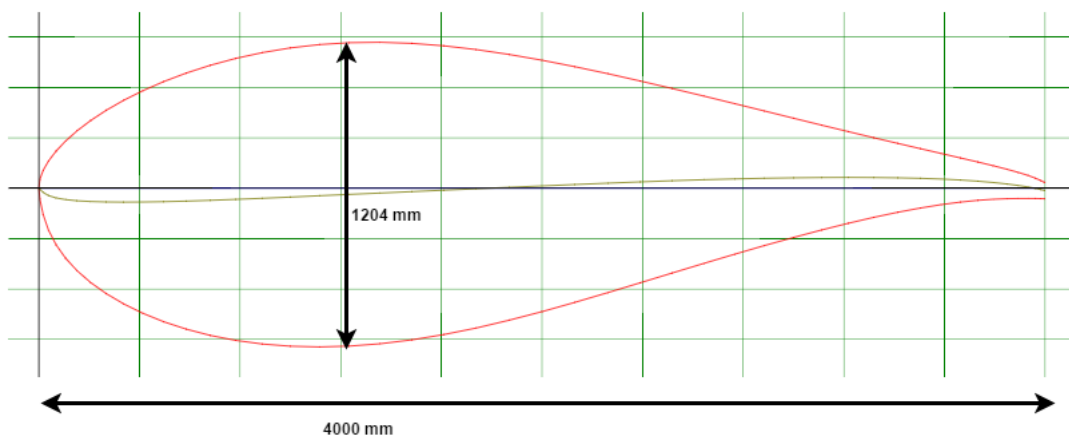


Figure 7.6: Body's Cross Section

### Lift, Drag and Moment of the Body

For a given size, the lift and drag coefficient are a function of the angle of attack, Reynolds number and the free stream mach number [11]. The Reynolds number was calculated as follows.

$$Re = \frac{\rho V c_{body}}{\mu} = \frac{1.15 \cdot 40 \cdot 4}{1.5377 \cdot 10^{-5}} \approx 10.4\text{million} \quad (7.2)$$

Such a high Reynolds number inevitably leads to turbulent flow. A consequence of turbulent flow is that the skin friction drag increases, along with the shear stress of the structure[12].

The calculated Reynolds number was used in XFLR5 to generate the following  $C_l - \alpha$  and  $C_d - \alpha$  curves. One should note that XFLR5 rounds 10.4 million down to 10 million. This introduces a small error in the calculated 2-dimensional lift and drag coefficients.

<sup>9</sup><http://airfoiltools.com/airfoil/details?airfoil=ah94w301-il>, [cited on 20-6-2017]

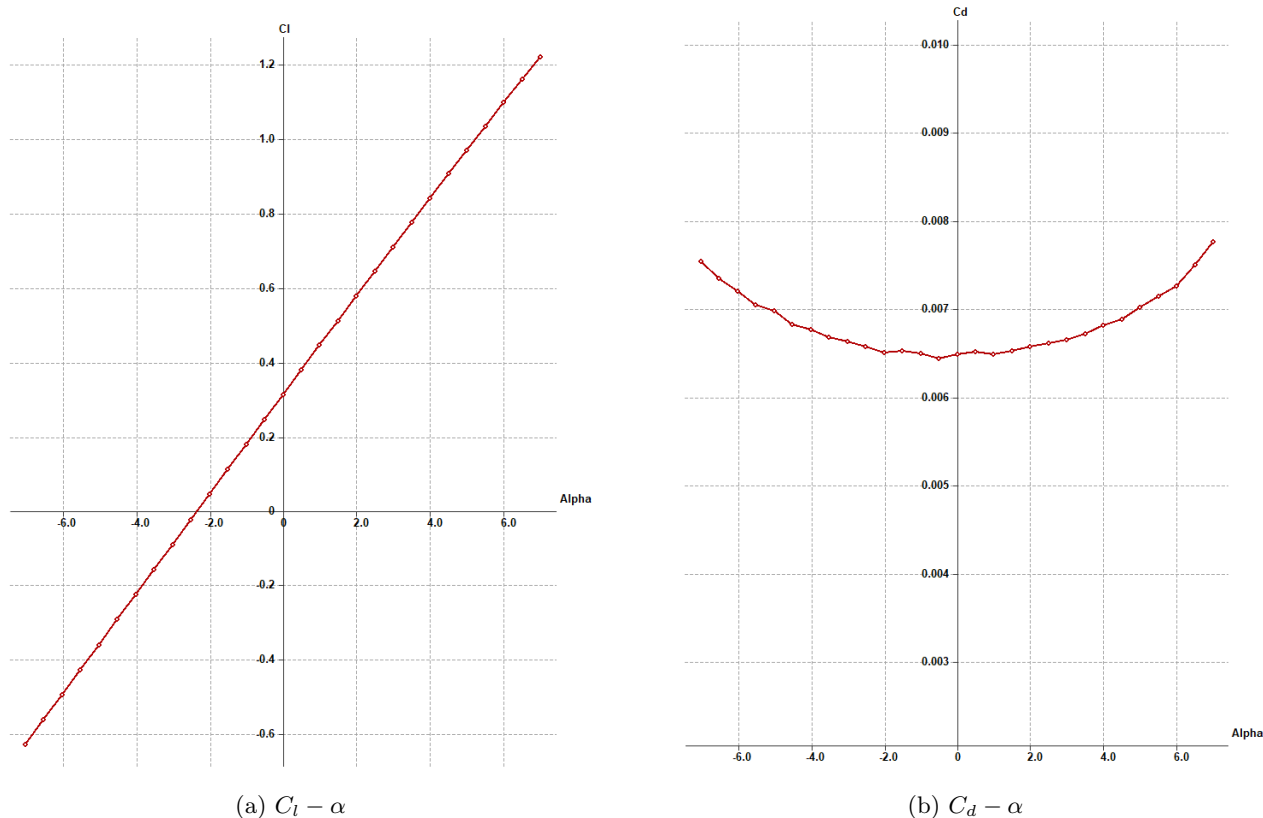


Figure 7.7:  $C_l - \alpha$  and  $C_d - \alpha$  curves at  $Re=10,000,000$

To estimate the lift and drag of the lifting-body, the lift and drag coefficients of the infinitely long wing have to be converted to the finitely long wing case. These differ significantly since a wing with a finite length is affected by wing-tip vortices, whereas an infinitely long wing is not [11].

From [13] the following relation for  $C_{L\alpha} - C_{l\alpha}$  was found

$$C_{L\alpha} = \frac{C_{l\alpha}}{\sqrt{1 + \left(\frac{C_{l\alpha}}{\pi AR}\right)^2 + \frac{C_{l\alpha}}{\pi AR}}} \quad (7.3)$$

eq. (7.3) is valid for low aspect ratio ( $AR \leq 4$ ), straight wings at incompressible flow.

The HyDrone's cruise velocity is  $40m/s$  at an altitude of  $650m$ , which results in a Mach number of 0.12.

$$M = \frac{V}{a} = \frac{V}{\sqrt{\gamma RT}} = \frac{40}{1.4 \cdot 287.06 \cdot 283.92} \approx 0.12 \quad (7.4)$$

This is below Mach 0.3, which implies that incompressible flow can be assumed [11]. Furthermore, the aspect ratio has been determined as follows.

$$AR = b/c = 1/4 = 0.25 \quad (7.5)$$

Equation (7.3) is proven to be accurate for an aspect ratio of 0.5 [11]. It is assumed that the relation will be reliable for an aspect ratio of 0.25 as well.

The finite drag coefficient of the wing has been calculated as follows.

$$C_D = C_{d_0} + C_{D_i} = C_{d_0} + \frac{C_L^2}{\pi e AR} \quad (7.6)$$

The shape of the body is rectangular, leading to an assumed span efficiency factor  $e$  of  $0.7$ <sup>10</sup>. As a sanity check, a closer look was taken at the M2-F2 vehicle. This lifting-body vehicle has an  $e$  of 0.772 [6] and therefore 0.7 seems to be a reasonable value for the HyDrone's lifting body.

From fig. 7.7a the 2-dimensional lift curve slope,  $C_{l\alpha}$ , is determined to be 0.133. Filling in eq. (7.3) gives

$$C_{L\alpha} = \frac{0.133}{\sqrt{1 + \left(\frac{0.133}{\pi \cdot 0.25}\right)^2 + \frac{0.133}{\pi \cdot 0.25}}} \approx 0.112 \quad (7.7)$$

For any aerofoil,  $\alpha_{C_l=0}$  equals  $\alpha_{C_L=0}$  [11]. From fig. 7.7a,  $\alpha_{C_l=0}$  was determined to be  $-2.341^\circ$ . Using this point, eq. (7.8) the line defining  $C_L$  as a function of  $\alpha$ .

$$C_L = 0.112\alpha + 0.263 \quad (7.8)$$

As an initial goal, the body will be designed such that the amount of lift generated is roughly 10% of the weight. As said, this is initial and it will be investigated if and how much power is saved by the lifting body.

<sup>10</sup><https://www.grc.nasa.gov/www/k-12/airplane/induced.html>, [cited on 23-06-2017]

This results in the criteria that the lifting-body should generate 552 N based on an initial mass of 563 kg. Using eq. (11.8) a necessary lift coefficient of 0.15 was found.

$$C_L = \frac{L}{0.5\rho V^2 S} = \frac{552}{0.5 \cdot 1.15 \cdot 40^2 \cdot 4} \approx 0.15 \quad (7.9)$$

Filling in the required lift coefficient in eq. (7.8) and solving for  $\alpha$  yields an angle of attack of  $\approx -1^\circ$ . This angle of attack is the angle of the *lifting-body* with respect to the free stream velocity and differs from the angle of attack of the rotors.

The drag coefficient at this flight condition is calculated using eq. (11.7)

$$C_D = 0.0065 + \frac{0.15^2}{\pi \cdot 0.7 \cdot 0.25} = 0.0474 \quad (7.10)$$

The zero-lift drag coefficient was determined using fig. 7.7b and equals approximately 0.0065. At the cruise speed the body itself will have a total drag of

$$D = 0.5\rho V^2 S C_D = 0.5 \cdot 1.15 \cdot 40^2 \cdot 4 \cdot 0.0474 \approx 175N \quad (7.11)$$

The extra drag generated by the lifting-body in comparison to non-lifting is found by filling in  $C_{d_0}$  in eq. (7.11) as  $C_D$ . It is found that due to the lift, an extra drag of approximately 151 N is induced. Note that the area for calculating the drag of the total drone is  $5m^2$ , whereas the area to calculate the lift and the induced drag equals  $4m^2$ . This is done because it is assumed that (aerodynamic) lift is solely generated by the body which has an area of  $4m^2$

Lastly the pitching moment of the body was examined. It is important to estimate this moment as much as possible since it requires extra thrust to counter this moment. Using XFLR5 the 2-dimensional pitching moment coefficient,  $C_m$ , was found to be -0.099 at an  $\alpha$  of  $-1^\circ$ . In the contrary to lift- and drag coefficients, the moment coefficient does not need an correction for a finite wing<sup>11</sup>. The total moment generated by the body equals

$$M = 0.5C_M\rho V^2 S c = 0.5 \cdot -0.099 \cdot 1.15 \cdot 40^2 \cdot 4 \cdot 4 \approx 1460Nm \quad (7.12)$$

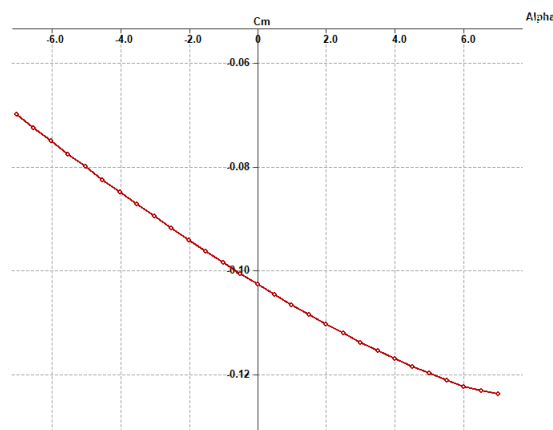


Figure 7.8:  $C_M - \alpha$  Curve for the Body

As evident from fig. 7.8  $\frac{\delta C_M}{\delta \alpha}$  is negative. This means that the body possesses longitudinal stability and will have the natural tendency to go back to the an equilibrium after a disturbance. Of course is the control system going to take care of disturbances and therefore having longitudinal stability is not that important.

### Power Savings due to Lifting Body

First of all the total drag of the HyDrone without a lifting body in order to calculate the initial power needed during cruise. The drag coefficient of the HyDrone is assumed to be 0.3. This value is based on fig. 7.9 at an initial angle of attack of  $-17^\circ$  following 'the canopy+tilt+' line. This is assumed to be conservative since the HyDrone's body is not going to operate at an  $\alpha$  of  $-17^\circ$  since it does not generate lift at that angle.

<sup>11</sup><http://people.clarkson.edu/~pmarzocc/AE429/AE-429-4.pdf>, [cited on 20-6-2017]

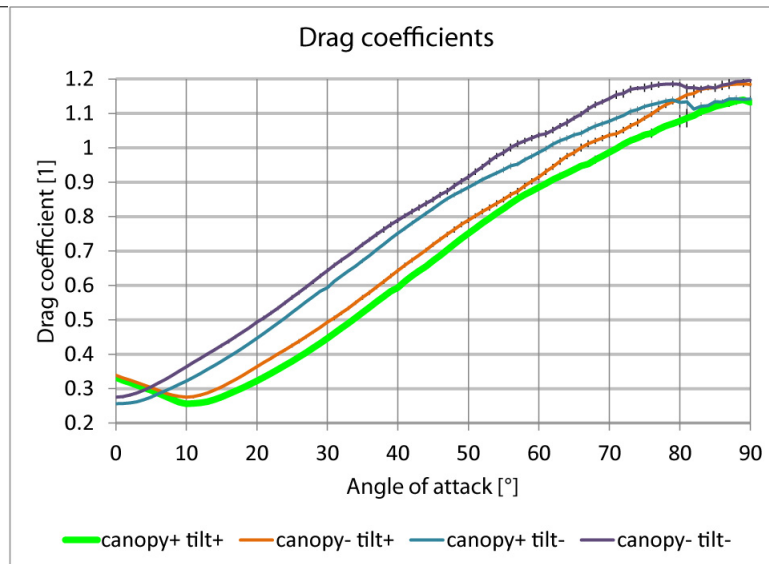


Figure 7.9:  $C_D - \alpha$  curve for the Shrediquette GEMiNi

It is realised that this test was performed at a much lower Reynolds number (lower speed, smaller reference length, different configuration) and therefore not utterly represent the HyDrone. However there is very little data available about drone drag coefficients and there is no data of drones with the same configuration as the HyDrone. Besides, doing an CFD analysis of the HyDrone will simply cost too much time and moreover is out of the scope of this project. Because the drag coefficient is most probably not correct the HyDrone will be designed conservatively.

That being said, the total drag of the HyDrone with a non-lifting body is calculated to be

$$D = 0.5\rho V^2 S C_D = 0.5 \cdot 1.15 \cdot 40^2 \cdot 5 \cdot 0.3 = 1380 N \quad (7.13)$$

The non-lifting body is assumed to have the same shape as the lifting-body but then the angle of attack of the body is chosen such that no lift is generated. The wetted area  $S$  is conservatively estimated to be  $5 m^2$ . This value is found by calculating the top view area as seen in fig. 7.5 and realising that the body's length (chord) is now  $4m$ . This area is multiplied by the sinus of  $17^\circ$  to end up with the wetted area. The calculation is showed below

$$S = (4(\pi \cdot 1^2) + 4 \cdot 1) \cdot \sin(17) = 4.84 m^2 \approx 5 m^2 \quad (7.14)$$

It is assumed that  $1380 N$  is the total drag of the HyDrone when it does not generate lift. This means that total drag of the HyDrone when it does generate lift equals  $1380 N + 151 N = 1531 N$ . In fig. 7.10 the effect of the lifting body is depicted.

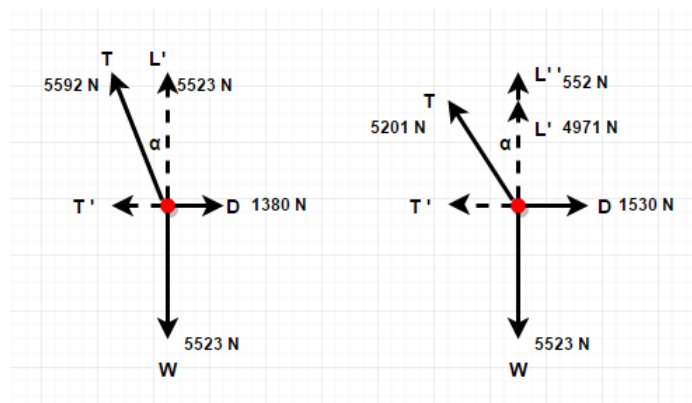


Figure 7.10: Free Body Diagram to Show Effect of Lifting Body

As evident from fig. 7.10 the total thrust required is less when using a lifting-body, however the angle of attack is bigger. The values of the angle of attack influence the incidence angle which is important in the power calculations in section 9.2 and section 9.3. The method presented in these sections is followed for both the non-lifting body as the lifting body. The results are presented in table 7.2.

Table 7.2: Characteristics Lifting-Body and Non-Lifting Body during Cruise

	Rotor Angle of Attack[°]	Body Angle of Attack[°]	Thrust Required[N]	RPM	Air Density [kg/m <sup>3</sup> ]	Power Required [kW]
Lifting Body	-17.2	-1	5201	1792	1.15	71.1
Non-Lifting Body	-14.6	-2.3	5592	2159	1.15	80.3

From table 7.2 it can be deduced that a lifting body uses less power at the same flight conditions than a non-lifting body. Furthermore, it can be seen that the RPM is lower, hence a lower tip speed which results in less noise [7]. Therefore it is indeed beneficial to have a lifting body.

### Induced Drag Reduciton by Shape Optimisation

The body of the HyDrone is considered to be a low-aspect ratio wing. For these kind of wings, the lateral edged play an important role in lift and drag. That is, it affects the tip vortices. As soon as there is a pressure gradient between the upper and lower side of the wing, a flow from the lower to the upper side is developed. This flow tends to join the flow and roll up the upper side. Therefore the effective span is smaller than the geometric span and the induced drag will be larger [14]. This phenomena is best visualised in fig. 7.22

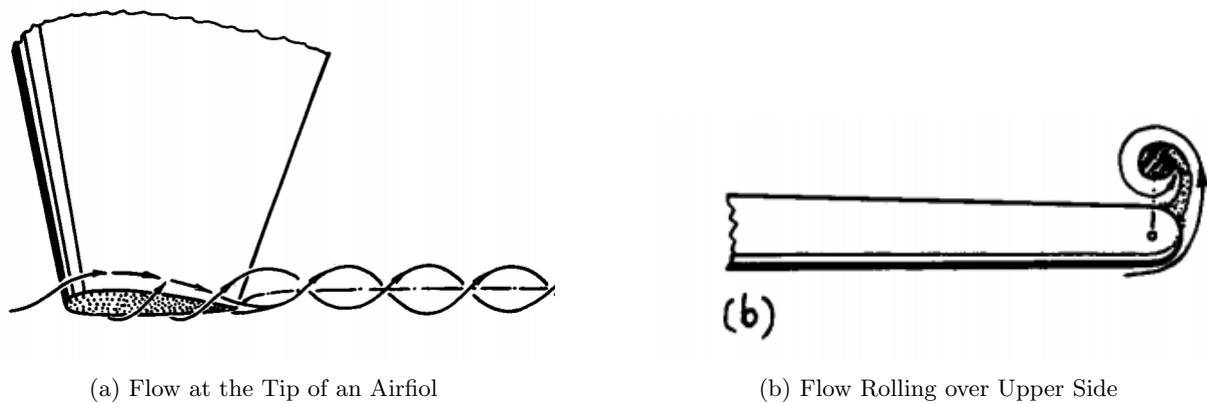


Figure 7.11: Phenomena at the Wing Tip due to Pressure Gradient[14]

One other parameter of influence on the effective span is the plan form shape. These can be rectangular, slightly tapered or elliptical. Studies were performed on what the best combination is of the wing tip and plan form shape [15]. The tested combinations are depicted in fig. 7.12

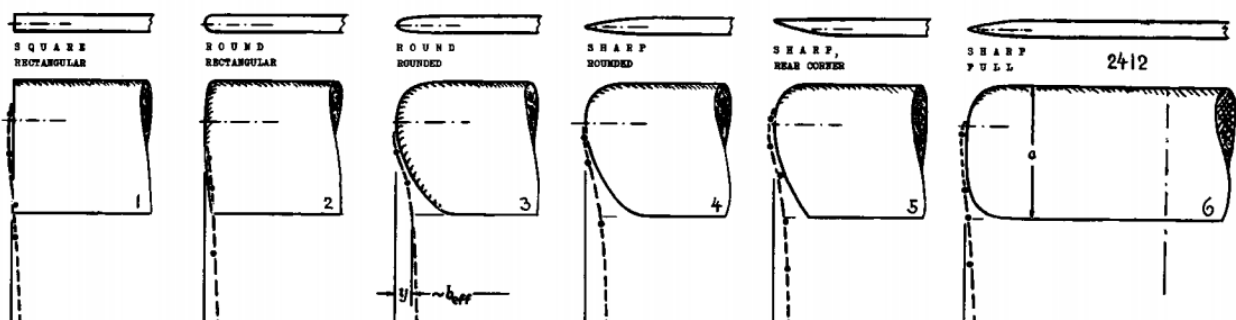


Figure 7.12: Different Combination Tested [15]

The combination which has the least induced drag is number 5 in fig. 7.12. It is the most effective in keeping the induced drag as low as possible. Therefore it is aimed to design the body in such a way that it approaches this particular shape as much as possible.

## 7.3.6 Results

The final design of the HyDrone's body is shown in fig. 7.13, fig. 7.14 and fig. 7.15. In fig. 7.13 it can be seen that the body has indeed the shape of the chosen aerofoil. In section 7.3.5 the induced drag was covered. Studies showed that there is a shape combination such that the induced drag is kept as low as possible. This shape was aimed to implement as much as possible. fig. 7.14 and fig. 7.13 show the implementation.



Figure 7.13: Side View Render

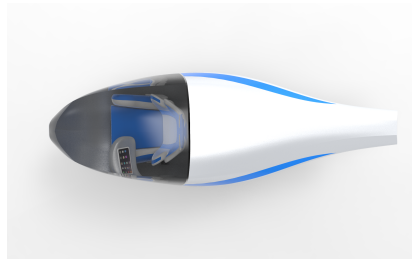


Figure 7.14: Top View Render

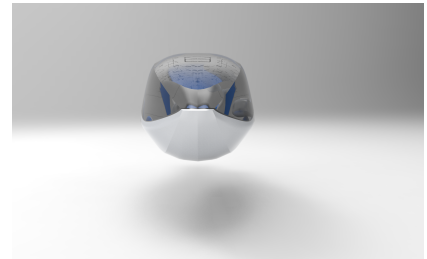


Figure 7.15: Front View Render

The final characteristics of the body are given in table 7.3. The L/D ratio for the body was calculated using the lift and drag of the body only. The L/D ratio for the total drone was determined using again the same lift together with the drag of the total drone. Please note that these L/D ratios *exclude* the lift contribution of the rotors. The L/D ratios are purely determined by the aerodynamic characteristics.

Table 7.3: Characteristics Lifting-Body

Angle of Attack[°]	Lift Coefficient	Drag Coefficient	Moment Coefficient	Aspect Ratio	Surface Area [m <sup>2</sup> ]	L/D Body	L/D Drone
-1.0	0.15	0.047	-0.099	0.25	4.0	3.2	0.36

## 7.4 Shrouds

In the previous phase of this Design Synthesis Exercise it was decided to implement a low-rotor multicopter design as this would be the best concept for the HyDrone. This left the choice open to incorporate shrouds.

In this section the decision will be made and design of the shrouds will be worked out. First of all, the pros and cons of shrouds are explored and the decision to implement shrouds is justified in section 7.4.1. Then, the approach to shroud design is laid out. This is explained in section 7.4.2. After that, several underlying aerodynamic principles and flight conditions are highlighted in section 7.4.3. Next, the design choices for individual elements of the shroud is considered in section 7.4.4. Finally, a brief overview of the resulting shroud geometry is presented in section 7.4.5.

### 7.4.1 Trade-Off

Since the choice was made for a low-rotor multicopter design (as presented in chapter 3) the idea has come up to include protective shrouds around the propellers. It is not a clear-cut choice whether to include shrouds or not. Below the pros and cons are discussed and the decision is made.

The arguments in favour of having shrouds pertain to noise, safety and increase in propeller efficiency. The arguments against are additional mass, added complexity of the design and controllability (due to positive induced pitching moment as explained in section 7.4.3) and increased maintenance. The arguments are ordered according to the criteria defined in section 7.2.

#### Noise

The most important argument is noise-related. While it is difficult to predict noise levels, qualitatively shrouds reduce noise significantly as is explained in chapter 13. Shrouded propellers can allow for significant reductions in noise propagation by incorporating a combination of shielding, absorbing lines, and transformation of lower frequency noise into higher frequency noise that dissipates more quickly in the atmosphere.[16]

Important to note is that the viability of the HyDrone is critically dependent upon regulatory approval. And there are no regulations yet specifically applicable for a class of vehicle that frequently operates within densely populated urban environments or with this configuration and mass. Consequently, it is uncertain exactly which noise levels have to be adhered to. Therefore, it is important to aim as much noise reduction as possible.

Modelling of noise production without taking into account the beneficial effect of shrouds, does not meet all the requirements adapted from helicopters (see section 13.1). And as section 6.3 explains, the only urban

---

operations helicopters are rated for emergency landings, so updated regulations are likely to have stricter noise level requirements.

### Safety

In three ways safety is increased by shrouds: firstly, the ground operations are safer as the shroud functions as a physical barrier to the propellers. It effectively reduces the threat the HyDrone poses to bystanders or leftover items on the landing pad. Secondly, they serve as physical barrier to a propeller path of propagation if it becomes detached or part of it breaks off during ground operations or in flight. This is not unprecedented and with a total of 16 propeller blades, the risk is not negligible. Finally, they protect the propeller blades against bird strikes.

### Sustainability

Sustainability is approached from the perspective of reduction in total fuel consumption over the nominal flight trajectory. The benefit of shrouds is the increase in propeller efficiency. The principles behind this are further explained in section 7.4.3. It generally also contributes to the thrust coefficient in hover. The downside of shrouds is the increase in frontal area during cruise which increases the total drag.

### Complexity

The most important argument against is that the complexity increases. Section 7.4.2 alludes to the complexities associated with the use of shrouds in the variety of flight conditions, especially for fixed-rotor aircraft. The associated risk is mentioned in section 7.6.

Another argument against is the mass penalty. Its circumference is already sizeable. Generally, the shroud would sustain aerodynamic loading, its own weight and impact damage, determining the thickness of the shrouds. This is even more the case if it were designed to carry the propeller thrust and weight. While it is true that incorporating shrouds increases the MTOW of the vehicle (defined as the 'total mass'). At first, the total allowable mass for the shrouds was budgeted to 20% of the total mass.

Then, after the design effort in section 7.4.4 and chapter 8, a conservative estimation yielded a shroud mass 62.4 kg, being 10.98% of total mass. To explore the benefits of excluding the shrouds, a sensitivity analysis (see section 16.4) yielded increased maximum range, power and energy margins and slightly reduced noise. Interestingly, while significant, the effect is not excessive nor surprising.

### Results

It is chosen to include shrouds primarily in order to mitigate this risk and increase the probability of achieving acceptable noise levels. Also, benefits in safety and propeller efficiency can be cited and the modest increase in mass. These outweigh the perceived downsides.

## 7.4.2 Design Approach

The design approach starts with decoupling the problem into several smaller problems. Associated with the decoupling is the implicit assumption that the resulting solution would be valid. Whether this is the case, can only be determined by either proving by reason or by experiment. Also, 'valid' is interpreted as a 'best-effort design'. The requirements on this system are less strict than on others.

This design freedom is much welcomed as the complexity is sizeable, while tools meant for managing complexity are scarce or out of reach.

The shroud is to operate in all flight conditions: hover, takeoff and cruise. For each condition the associated flowfield around the duct is distinct. Furthermore, each flight conditions optimisation takes on alternate meanings. Also, the entire inner, outer, top and bottom surfaces could be changed in any way. Correlating differing flow patterns with differing (design) objectives together with a multitude of variables to modify, is a challenge.

The constraints that are as follows. The design should

1. Be larger than the propellers.
2. Not weigh more than the budgeted 20% of total mass.
3. Not produce more drag than is equivalent to a  $C_D$  of 0.3 minus the lifting body drag and interference drag during cruise.
4. Not produce a moment coefficient of more than  $C_m = 0.979$ <sup>12</sup>
5. Not have a shroud width larger than  $w_s = 0.15$  m and a height larger than  $h = 0.3$  m.<sup>13</sup>

---

<sup>12</sup>The aerofoil chosen previously for the lifting body has  $C_m = -0.099$ . The moment coefficient of the entire system,  $C_{m_{max}}$ , is limited by the maximum capability of the rotors aft and rear in producing a counter moment while providing sufficient thrust for both lift and drag in cruise. This is set by the maximum thrust production of the rear rotors, which, in turn, is limited by the rear rotors' maximum engine rpm: 3500. And the engines' limit is reached at  $C_{m_{max}} = 0.88$ .

<sup>13</sup>This originates from the requirement that the entire subsystem must fit in hypothetical cube of  $5m \times 5m \times 5m$ . Then, a two-way coupling with propulsion and structures yielded a decision to constrain the maximum outward dimension. To accommodate a design with larger shroud width  $w_s$ , either the rotor radius or the body geometry would have to be reduced. If the rotor radius

The design objectives are strongly related to geometric variables. The single-sided cross-section is decoupled into the following variables: inlet radius, diffuser angle, diffuser exit radius, vertical wall length, tip clearance and outer shell curvature. These variables and their design are elaborated on in section 7.4.4.

Other geometrical parameters that are relevant to the shrouds are: inner shroud radius  $r_i$ , outer shroud radius  $r_o$  and shroud width  $w_s$ . The inner shroud radius is defined as the perpendicular distance from the vertical wall of the shroud to the propeller axis. The outer shroud radius is defined as the largest distance between the propeller axis and the outer shell curvature. Then, the shroud width is the difference between the inner and outer shroud radii. Figure 7.16a and fig. 7.16b illustrate these variables.

Note that the design only considers the outer contours of the shroud. Its internal dimensions are not of influence in the aerodynamic design and are therefore discussed in chapter 8.

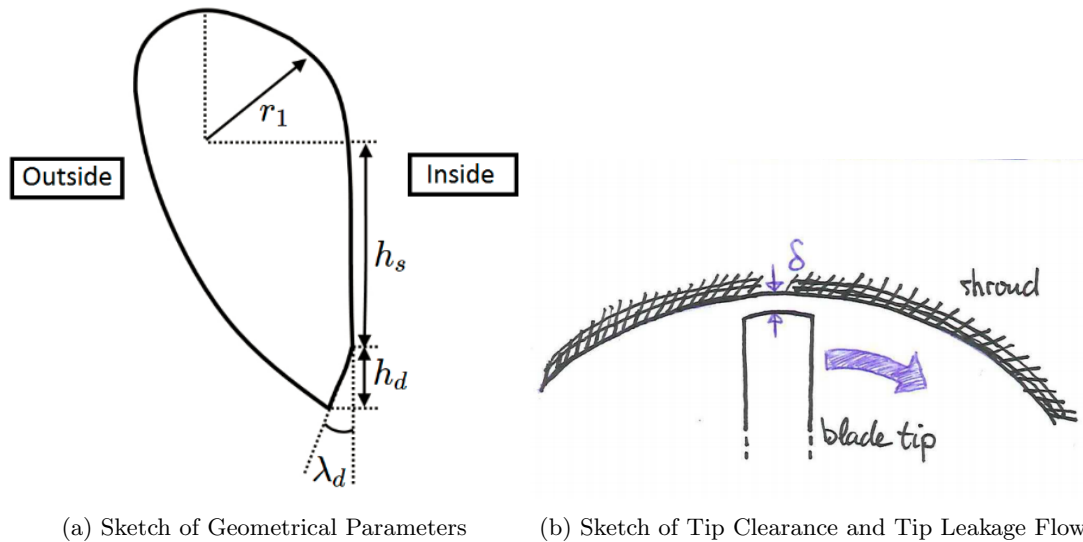


Figure 7.16: Sketches of Geometrical Parameters

### 7.4.3 Aerodynamics over the Shroud

#### Flight phases:

Figure 7.17b illustrates the flow field for a duct in cruise conditions. Then, fig. 7.17a illustrates it for hover conditions. Finally, fig. 7.18 illustrates the flow over the shroud and a body.

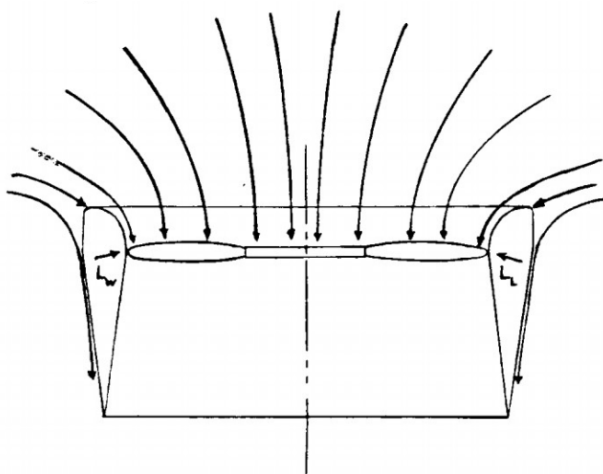
At the LE the free-stream velocity  $V_\infty$  is aligned with the flow direction induced by the low pressure region above the propellers, increasing the airflow speed over the top surface. Then at the TE they effectively work against each other, reducing the airflow over the surface. This asymmetry in flow over the LE and TE results in a lower static pressure on top of the LE. Assuming for simplification that the pressure on the bottom is equal, then effectively more lift is generated at the LE than at the TE. This results in a moment in the direction that is opposite to the pitch angle. In effect, it has the tendency to self-stabilise to a condition where the propeller axes are oriented vertically. In short, it wants to return to the hover condition.

This tendency to self-stabilise has proven detrimental to designs that are built around the coander effect, such as the Hiller flying platform, the VZ-1 Pawnee. Fortunately, this can be countered by producing a moment in the opposite direction by imposing a thrust differential between the front and rear propellers.

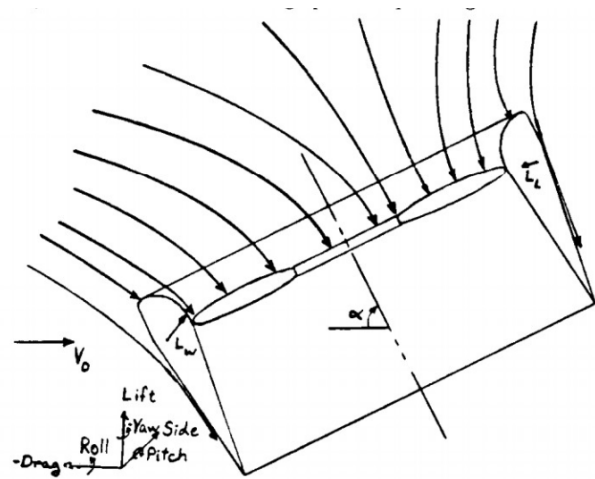
Please note that the downflow through shroud bends the flowfield to some extent. This downwash may certainly affect the aerodynamics of the rear rotors. It is, however, assumed that the effect on rotor performance is not affected. Next to that, the effect on the shrouds is not looked at.

The inflow in takeoff and hover are uniaxial and approximate that of a ducted fan design. As a sidenote, in takeoff the stagnation point is thought to be closer to the inlet than in hover as the inlet velocity is larger. As there is literature available on uniaxial duct performance, this flight condition is chosen to size the inlet and diffuser in section 7.4.4. What remains is the outer shell curvature which - is assumed - does not contribute much to the propeller performance inside the duct. Therefore, it makes sense to size it to cruise conditions.

were to be reduced, a higher propeller rpm would be required to produce sufficient thrust. This increases the blade tip speed and thereby the noise. Furthermore, the body is already narrow and reducing the width would hinder the placing of other system components. Also, an increased shroud width comes at a mass penalty.



(a) Flow Representation of Shroud-Propeller in Vertical Flight[17]



(b) Flow Representation of Shroud-Propeller in Horizontal Flight[17]

Figure 7.17: Flow Representation of Shroud-Propeller Configuration in Vertical and Horizontal Flight

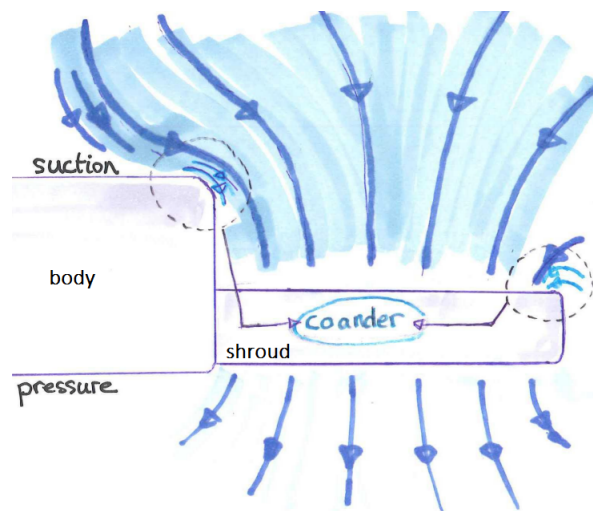


Figure 7.18: Flow Representation of Body-Shroud-Propeller in Vertical Flight

#### 7.4.4 Shroud design

A series of design choices are made relating to the shroud as a whole and for each geometric variable defined in section 7.4.2.

##### Pre-design decisions

The decoupling of the shroud geometric variables was preceded by several design decisions: For instance, it is decided to not incorporate an standard NACA aerofoil shape - neither on the inside or the outside. Even though it appears to be a common practice nowadays in (tilt- and fixed-rotor) axial-flow duct design. Literature indicates that negative camber (i.e. concave with respect to the propeller) aerofoils affects propeller efficiency positively.[18] In particular, the contribution to the thrust coefficient by the duct is positive and about a fifth of the propeller thrust coefficient at low advance ratios. At higher advance ratios, however, it can become negative.[18] This relationship between advance ratio and duct thrust coefficient is dependent on duct geometry and propeller characteristics, neither of which have been established at this point. It is, for that reason, assumed that the inner duct's net contribution to the thrust is zero in any and all flight conditions. Note that also the outer curvature may more reliably contribute to the thrust. However, it turns out that it cannot feasibly be estimated - within this time frame, that is. Therefore, also this contribution is assumed zero in all flight phases. While this may be conservative for hover (and perhaps take-off), it may underestimate the down force during cruise as the shrouds are at a significantly negative angle of attack of  $-17.2^\circ$ .

Remembering the constraint no. 1 (see above), introducing camber on the inner wall requires either dissimilar propeller sizes or tip clearances. The alternative is to awkwardly have to place the propellers at two locations

along the cord for which identical propeller sizes and tip clearances are possible. Then, however, the propeller pitch is constrained. It is therefore decided to make the wall along the pitch space straight and introducing outward (again: concave) 'moving' extensions: the inlet and diffuser lips - still leveraging the above-mentioned benefits of 'negative camber'.

So far, the inner geometry has been classified. Unfortunately, conventional shrouds with pure aerofoil designs on the outside do not hold up well in anything but axial flow, while the HyDrone is to operate under angles of attack around  $75^\circ$  during cruise flight. This causes whole sorts of problems if one were to use any thin (aerofoil) shape, some of which are due to sharp inlet angle causing flow separation. In addition, flat plates generally tend not to be preferred head-first into the wind due to form drag.

In terms of design conditions, the inlet and diffuser are sized for hover conditions, as is explained later in this subsection. The effects of other flight phases are out of scope in this design effort due to lacking experimental data and non uni-axial inflow. There are no numerical models, short of CFD, that can accurately represent these conditions as more elaborately mentioned above in section 7.4.2. Furthermore, the outer shell curvature is designed for cruise.

For the current design, it is decided that the design will be axisymmetric and only cross-section of the leading edge is considered. This will simplify design and manufacturing and a lot of complexities are ignored.

It is important to note that for fig. 7.18, one could expect the inflow of air to reduce the static pressure at the top of the body, helping it generate lift. While certain configurations seem to achieve this [19], it is assumed zero as it is difficult to analyse.

**Shroud Inlet Radius  $r_i$ .** The inlet has the design of a quadrant, which - in hover<sup>14</sup> - runs from parallel to the rotor disks to all the way parallel to the propeller axes (i.e. horizontal to vertical). Other inlet shapes could be used, but to limit the design variability a quadrant is used. A potent second reason is that the experimental data used, tested this specific shape. And that research will be used as a primary guide to size the inlet.

Smooth and rounded inlets will allow air to enter the duct with minimal separation (see fig. 7.20). A sharp inlet curvature can cause the air to separate, resulting in a smaller effective propeller area with the blade tips generating less lift. An extreme example of this is visualised in fig. 7.19. Sharp inlet curvature can also create turbulent airflow as the flow enters the rotor disk. Both are ideally minimised, calling for a larger inlet lip radius. On the other hand, excessively large inlet radii increase skin friction drag and reduce the part of width budget of  $w_s = 15\text{ cm}$  for the upper part of the outer shell curvature. However, as will be explained later in this subsection, the inlet radius takes precedence over the upper part of the outer shell curvature. To be frank, the bottom part of the curvature is what matters more in the outer shell curvature. Also, while the shroud is not explicitly sized for climb performance in terms of drag, it is useful to note that from the flat plate perspective a smaller radius is preferred. Therefore, there must be an optimum middle way.

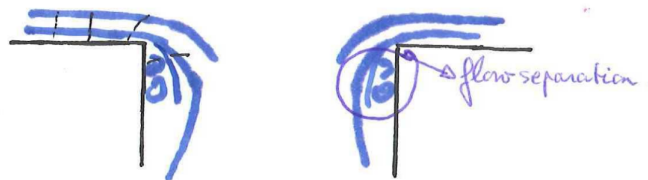


Figure 7.19: Sketch of Shroud Inflow with Sharp Inlet Lip ( $r_i \approx 0$ )

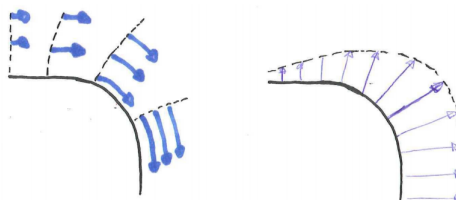


Figure 7.20: Figure Illustrating Coander Effect

The approach to determining this optimum is by first looking at what curvature radii achieve the best experimental performance. Then, the sizing constraints are taken into account to choose a design point.

<sup>14</sup>Sizing for other flight conditions is out of the scope of this design project: the complexities introduced with non uni-axial inflow, as is the case for cruise, and the distinct void in experimental test results for both non-uniaxial inflow or accelerating axial inflow ducts (especially those that can be used for design), are striking.

To determine the inlet radius, it is assumed that the ratio of inlet radius to inner shroud diameter (i.e. inlet ratios) is relatively good predictor for larger inner shroud diameters. It is also assumed that propeller shape and engine settings do not affect inlet design significantly. This is a key assumption as the experimental testing data upon which this is based used an inner shroud diameter of 29 cm[20], while the HyDrone's is 6.7 times larger.

[20] evaluates the performance of a duct with three different inlet ratios in hover while also varying propeller pitch and engine rpm. The performance is measured in terms of the thrust coefficient, the power coefficient and the ratio power to thrust  $\frac{C_p}{C_T}$ . The purpose of evaluating these performance parameters is not to obtain performance characteristics for use in propeller sizing as for that the experiment is assumed to be too dissimilar to the HyDrone's shrouds. Rather, reduced performance is indicative of the degree of flow separation at the inlet and the inlet ratios that perform best, may be appropriate for the HyDrone as well.

The inlet ratios are given names that refer to their relative sizes (small, med and large) to simplify presenting and discussing results. This experimental testing revealed for inlet ratios as defined in table 7.4 summarised results as presented in table 7.5. The inlet radii corresponding with the inlet ratios are obtained by simply multiplying the inlet ratios with the inlet diameter of 1.90 m. Larger values of the thrust coefficient are favourable as are lower values of power coefficient and the power to thrust ratio  $\frac{C_p}{C_T}$ . The tests were performed at a range of speeds, from 1200 RPM to 3600 RPM.

Table 7.4: Nomenclature for the Inlet and Diffuser Ratios[20] and corresponding Inlet Lip Radii and Diffuser Angles for the HyDrone

Inlet			Diffuser	
label	inlet ratio [-]	shroud $r_i$ [m]	label	diffuser angle $\lambda_d$ [°]
small	0.014	0.0266	small	1.03
med	0.057	0.1083	med	1.40
large	0.114	0.2166	large	1.82

Table 7.5: Summarised Results from [20] of Duct Hover Performance with Varying Inlet Lip Radii and Diffusion Angles. Note: **Bold** = favourable; ' ? ' = dependent on RPM; '~' = approximately equal

	inlet			diffuser		
Thrust	<b>large</b>	>med	>small	<b>small</b>	>med	>large
Power	small	>large	> <b>med</b>	small ?	large	> <b>med</b>
$\frac{C_p}{C_T}$	small	> <b>med</b>	~ <b>large</b>	small ?	large	> <b>med</b>

The consensus is that med to large inlet ratio achieves best performance. This corresponds to an inlet radius of 0.1083 and 0.2166 m. Therefore, based on performance the inlet radius becomes: 10.83 cm  $< r_i < 21.66$  cm. However, including the size budget, it becomes: 10.83  $< r_i < 15$  cm - margin for outer shell. At the end of this subsection, a value for  $r_i$  will be picked.

Ducted Fan Design Code <sup>15</sup> was also explored to evaluate the inner duct designs by simulating the pressure distribution for reference propellers. Conversations with experts from the Aerospace Engineering department of the TU Delft yielded the view that this analysis is unfeasible within the given time constraints. Outside coaching would also only be possible past internal deadlines.

**Diffuser angle and exit radius ( $\lambda_d$  and  $R_e$  in resp. ° and m).** It is important to not make the diffuser angle or the length too large as this introduces aerodynamic losses of several kinds. The main loss sources are, according to [20]: diffuser flow separation, reverse flow, blade wake turbulence and skin friction drag. Note that the diffuser angle is not the same as the actual *diffusion angle* of the flow. If the diffuser angle is too large, boundary layer thickening due to transition and flow separation can cause the actual exit wake area to be less than exit area<sup>16</sup>. On the other hand, a diffuser angle too small does not effectively reduce the exit velocity, which generally is a diffuser's main purpose as it tends to improve thrust efficiency. Another argument against a large diffuser angle and radius is the sizing of the outer shell curvature. It is in the shell's best interest to have more of the total width budget,  $w_s$ , to be able to round off the curvature at the bottom. This is treated later in this subsection at the outer shell sizing. The design point must be somewhere in-between.

The diffuser angle sizing is based on the same source as the inlet radii, operating under the key assumption that the diffusion angle is indicative for the performance of the HyDrone's larger shroud. Also similar to the inlet ratios, diffusion angles are labeled (small, med and large). The coefficients and their labels are noted

<sup>15</sup><http://web.mit.edu/drela/Public/web/dfdc/>

<sup>16</sup>Which is  $\pi \cdot R_e^2$ .

in table 7.4 along with the corresponding diffuser exit radius. and the experimental results as summarised in table 7.5.

The consensus is that the med diffusion angle achieves the best performance. This corresponds to a diffuser angle of  $11.89^\circ$ . Instead of the exit radius,  $R_e$ , the height of the diffuser,  $h_d$ , is considered more critical as the shroud height budget of  $h = 30 \text{ cm}$  on the inner part of the shroud has to fit the inlet radius, vertical wall height and this diffuser height. In equation form:  $h = 30 > r_i + h_s + h_d$ . At the end of this subsection a value for  $h_d$  will be picked.

**Vertical wall length ( $h_s$  in m).** The minimum value is set by the minimal propeller pitch (i.e. distance between propellers) of 10% of propeller radius ( $= 0.095 \text{ m}$ ) as defined for helicopters by [7]. The maximum value is set by the size budget and at a mass penalty. It also does a number on the drag as the front area increases proportionally with  $h_s$ . Increasing the propeller pitch can effectively reduce noise by the co-axial rotation propellers.[21][7] This requires a larger vertical wall length. Increasing the vertical wall length achieves a similar purpose: reduction of noise. It accomplishes an effectively lower velocity intake which results in a higher propulsive efficiency, lower internal drag (as long there is no separation) and more uniform inflow (which lead to lower noise) according to [16].

Now, consider the lower limit set by the minimal propeller pitch and the upper limit is set by the size budget, as the noise benefits perhaps outweigh the mass penalty. The resulting design space for the vertical wall length is:

$$9.5 \text{ cm} < h_s < 30 \text{ cm} - r_i - h_d$$

At the end of this subsection, a value for  $h_s$  will be picked.

**Tip clearance ( $\delta$  in m).** It is usually defined as a percentage of the total rotor diameter. The parameter is often-used in gas turbine design. Due to effects described in section 7.4.3 the pressure 'leakage' is minimised for minimal tip clearance (preventing tip vortices like in fig. 7.21), thereby maximising propeller efficiency and blade loading near the tip. In fact, for uni-axial turbines efficiency decreased linearly with tip clearance.[22] A lower limit is set by (conceivably) manufacturing tolerances and thermal expansion (of shroud and propellers). Since establishing the lower limit requires in-depth analyses and it is not important to further design, the value is assumed to be 4 mm.

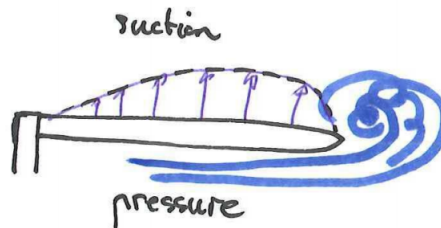


Figure 7.21: Figure illustrating Tip Vorticity

**Outer shell curvature.** This is where design gets more fuzzy. The outer shell can be separated into two sections: (1) Above the stagnation point in cruise, and (2) below the stagnation point. As no flow simulations could be performed within the budgeted time, a point is assumed based on engineering gut-feeling. Also, the precise point is not important, because the ideas behind this doubly-curved surface are set the stage for future design iterations. Therefore, the exact curvature will not be determined, but the result does include an impressionistic sketch and a discussion of (the principles behind) its main features.

Two objectives are set: (i) Minimising the pitching moment effect to satisfy constraint no. 4 in cruise.<sup>17</sup> And (ii): Minimising the drag polar in cruise.<sup>18</sup>

The chosen way to go about achieving these objectives is by borrowing from the conventional aerodynamics playbook: Incorporating an aerofoil-like shape into the design. The way this works for objective (i) is that the local static pressure is lower when the airflow is accelerated more. And a low static pressure in section (2) of the outer shell curvature is key to reducing the pressure differential between sections (1) and (2), so that the resultant lift vector can be reduced (if at all upward - this is unknown) to reduce the difference between the LE and TE shroud lift. How this works in aerofoils is by introducing camber so that over the top of the aerofoil the flow is accelerated more than over the bottom, so there is pressure difference to have lift. Instead of generating

<sup>17</sup>See section 7.4.3 for an explanation why this is desirable and why this is important during cruise.

<sup>18</sup>This is deemed more critical than vertical flight as most energy is expended in cruise, effectively sizing the power subsystem. Also, the body shape is likely to generate much more pressure drag than the shrouds. While a quick calculation reveals that the both have a similar top-down area, shrouds are less of a bluff body shape. For the body:  $5 \cdot 1 = 5 \text{ m}^2$ . For four shrouds, taking a radius of 1.05 m to be conservative and a constant shroud width of 15 cm:  $4 \cdot 2\pi \cdot 1.05 \cdot 0.15 = 3.96 \text{ m}^2$

more upward lift by introducing a larger positive curvature (i.e. positive camber) on the top, what is desired to achieve the opposite effect is the opposite shape: increased curvature on the bottom, or 'section (2)'.

As mentioned up in this subsection, the curvature of section (1) is largely at the whim of the inlet lip radius. Certainly, the section (2), as is decided, is more important. Attempts could be made to additionally increase the static pressure along section (1) but section (2) is easier to analyse. Nevertheless, somewhat of a curvature is desirable if only for the same reason the inlet radius should be decreased: better drag performance in vertical flight. However, again, this is critical and therefore not explicitly sized for.

However, there are also constraints that pose limits on the design of the outer shell curvature: the sizing constraint (no. 5) and mass constraint (no. 2). As alluded to before in the diffuser design, it is in the shell's best interest to have as much of the total width budget,  $w_s$ , as possible to be able to round off the curvature more at the bottom. What that means is that it is considered best for bottom of the outer shell curvature if (a) the curvature is not too steep so that it causes flow separation or early transition, which negatively impacts the ability to achieve either objective<sup>19</sup>, and if (b) the angle at the end with the diffuser is not too small so that significant pressure drag is generated behind the LE shroud. Unfortunately, due to time constraints there has not been the opportunity to feedback aerodynamic analysis - if XFOIL were to work as well - to the diffuser sizing.

In terms of mass, the effects of slightly larger curvatures are small. This can readily be shown by comparing the circumference if section (2) of the outer shell curvature were a straight line - or: circle with infinite radius - or a slightly curved line, that fits between two points that are a width  $w_s$  and a height of just more than  $h_s$  apart. This is not likely to make or break constraint no. 2.

In theory, one could attempt to adjust the shape of the outer shell as to accelerate the airflow below the stagnation point, thereby reducing the pressure difference and the resultant lift vector generated by the leading edge compared to the trailing edge. The curvature in fig. 7.16a is believed to achieve that due to its large radius. Of course, this is based on the assumption that the flow would remain attached and accelerates over this body.

Note that achieving objectives (i) and (ii) (or better said: validation that the proposed 'inverse aerofoil'-shape achieves the desired effect) is contingent on the aerodynamic analysis of the (leading edge of the) shroud under cruise flow. If there were any, windtunnel test results for, for example, a variety of non axi-symmetric blunt nosecones - at preferably similar Reynold's numbers - could be used to validate this idea. However, a literature review to dig up validation material turned up nothing useful.

Another attempted approach entailed simulating the entire shroud curvature using XFOIL, a solver using panel methods that incorporates most aerodynamic effects[23]. This has the potential side-benefit of providing an actual estimate for the 2D drag, lift and moment polars which would probably be reasonably accurate if the author of XFOIL is to be believed[23]. As for the input 'aerofoil' shape, a shape similar to fig. 7.16a, with all variables ( $r_i$ ,  $\lambda_d$ ,  $R_e$ ,  $h_s$ , etc.) in Excel to create an input coordinate file. This manual procedure was necessary as the shape as-is cannot be entirely defined by the traditional aerofoil parameters (e.g. camber, thickness-over-chord ratio, etc.). As a result, simply modifying an existing aerofoil in the "Geometry Manipulator"[23] would not be enough. For the angle of attack, an initial range was chosen between  $-15^\circ$  and  $-20^\circ$ , being not entirely sure how much of a down- or upwash the duct inflow would generate in front of the LE. This is rather difficult to judge without fluid flow simulations. Neither was it worth to find papers to validate as it would be more relevant if the analysis actually came through. Since the shape is blunt relative to a normal aerofoil, there may be strong separation bubbles present. The original paper describing XFOIL[23] mentions that in the presence of such bubbles an increased number of panels may be required to converge to a solution. Unfortunately, this effort turned out to be futile as XFOIL's numerical model would not converge to a result, irrespective of the number of panels or the angles of attack.

### Big picture

To conclude, a best-effort design of the outer shell curvature is made, which is down-cambered with a modest angle to the diffuser at the bottom and smoothly transitioning into the quadrant-shaped inlet.

Remember that for the inlet radius the result is:  $10.83 < r_i < 15$  cm - margin for outer shell. To leave margin for the outer shell, the lower end of the spectrum is chosen:  $r_i = 10.83$  cm. Then, remember that for the vertical wall length the result is:  $9.5$  cm  $< h_s < 30$  cm -  $r_i - h_d$ . As the noise reduction of a longer vertical wall probably outweighs the benefits of the increase in thrust efficiency due to a longer diffuser but to still retain 'a' diffuser, a value is chosen of, say:  $h_s = 15$  cm. Now, the remaining parameter, the diffuser height can be calculated by maximising the budget:  $h_d = 4.17$  cm. The resulting height budget is condensed in table 7.6.

The remaining parameters can then be deduced: the exit radius is

$$R_e = r_i + \delta + h_d \cdot \tan(\lambda_d) = 95 + 0.4 + 4.17 \cdot \tan(11.89^\circ) = 96.28 \text{ cm}$$

The margin for the outer shell on the top side is

$$w_s - r_i = 15 - 10.83 = 4.17 \text{ cm}$$

<sup>19</sup>For both objectives: i. Increased static pressure that contributes to the pitching moment; ii. Increased form drag or friction drag.

Next, the margin for the outer shell on the bottom side is

$$w_s - h_d \cdot \tan(\lambda_d) = 15 - 4.17 \cdot \tan(11.89^\circ) = 14.12 \text{ cm}$$

Table 7.6: Height Budget

<b>Budgeted height</b>	<b>30.0</b>	<b>cm</b>
$r_i$	10.83	cm
$h_s$	15	cm
$h_d$	4.17	cm
<b>Sum total</b>	<b>30.0</b>	<b>cm</b>
Difference	0	cm

## 7.4.5 Results

At this stage, a best-effort shroud design has been achieved. Design main particulars are presented in table 7.7 with variables defined earlier in fig. 7.16a. Renderings are in section 16.1.

To recap on the constraints that were originally set in section 7.4.2: Constraint 1 has been adhered to with the inner shroud starting 4 mm away from both propellers due to the vertical wall and tip clearance. Constraint 2 has been reached as well. Unfortunately, constraints 3 and 4 could not be evaluated but the design decisions were made with these criteria in mind as well. Then finally, the sizing budgets (constraint no. 5), as previously shown in table 7.6 and section 7.4.4, have not been surpassed.

Table 7.7: Main geometric parameters of the shroud

Tip clearance	$\delta$	0.4	cm	Shroud width	$w_s$	15	cm
Vertical wall length	$h_s$	15	cm	Inner shroud radius	$R_i$	95.4	cm
Inlet radius	$r_i$	10.83	cm	Outer shroud radius	$R_o$	110.4	cm
Diffuser angle	$r_d$	11.89	°	Margin for outer shell (top)	-	4.17	cm
Diffuser height	$h_d$	4.17	cm	Margin for outer shell (bottom)	-	14.12	cm

## 7.5 Landing Gear

The preliminary design of the landing gear is performed in this section. In order to design the landing gear, balance and clearance requirements are to be defined: section 7.5.1 analyses the required clearance the landing are to provide. Subsequently, a landing gear concept is chosen from four conceptual options in section 7.5.3. Finally, the aerodynamic performance of the landing gear is analysed more in section 7.5.4 and a design modification is suggested.

After the choice for landing gear, the system's structural analysis and design work was performed in section 8.5.

### 7.5.1 Clearance Requirements

In order to come up with the required dimensions of the landing gear firstly their position had to be determined. The further the landing gear is position outwards (away from the cg) the more stable the vehicle will be during landing. However, positioning the landing gears at the very end of the arms would mean that they have to be attached to the shrouds (they could not simply be attached to the load carrying beams, since the landing gears would cross the rotating plane of the propellers). Attaching the landing gears to the shrouds greatly increases the load the shrouds must carry, making them far heavier. Another down side of putting the landing gears at the very ends of the arms is that it would impose a large bending moment on the centre of the vehicle. Thus design decision was made to attach the landing gears as aft as possible, without having to reinforce the shrouds: right in between the shroud and the body.

In order to start designing the landing gear initial dimensions have to be determined. Not only is the landing gear designed to withstand all loads during landing, but it is also designed to prevent the body from tipping over and/or hitting the ground. The aircraft tipping over is referred to as 'Rollover'. This can happen in two modes: Dynamic Rollover, and Static Rollover. Dynamic Rollover occurs during landing/take-off when the propellers are still spinning and generating thrust. Due to the thrust and possibly also side-wind and a sloped landing ground, the rotor craft is flipped onto its side. Static Rollover is when no external forces cause the vehicle to tip, but due to a high bank angle the cg has moved beyond the pivot point(the point about which the aircraft tips, i.e. the point where the landing gear touches the ground). Static Rollover typically occurs at a larger bank

angle than Dynamic Rollover. It should be noted that the actual Dynamic Rollover angle is not determined as it is too complex to estimate at this stage, but the landing gear will be designed such that it prevents the vehicle from getting damaged when landing at extreme angles such as the Dynamic Rollover angle.

Typical angles at which Dynamic Rollover occurs are between  $5 - 8^\circ$  [24]. As safety margin the maximum defined angle times a safety factor (1.5) was used as the critical angle at which the landing gear should provide safe landing. Thus a bank angle of  $8^\circ \times 1.5 = 12^\circ$  during landing was used as design constraint. A rear view of the vehicle in the described situation can be seen in fig. 7.22a, in this figure  $h_{lg}$  is the minimum required height of the landing gear to prevent the shrouds from being damaged. Do note that this configuration assumes landing gears which are completely orthogonal to the body, this does not provide the best Static- and Dynamic Rollover stability, as the pivot point is relatively close to the centre of gravity.

A more favourable configuration is displayed in fig. 7.22b here the landing gear is set at a slight angle, so that the pivot point is moved further away from the centre of gravity. This also makes the landing gear less rigid during landing, having a completely orthogonal landing gear results in a very little stroking distance during landing, which results in great load factors imposed on the body.

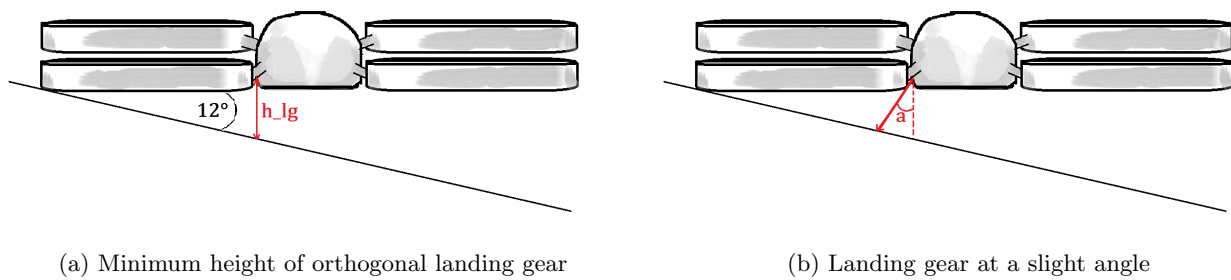


Figure 7.22: Rear view sketch of HyDrone with landing gear

Thus far the clearance is only discussed for bank angle, but the skids should also prevent the HyDrone from getting damaged when it lands at a certain pitch angle. A helicopter should be able to land at a pitch angle range of  $+15^\circ$  to  $-5^\circ$  [25]. Due to the symmetric aspect of the HyDrone quad-copter configuration the decision was made to design the skids such that the vehicle can land at a pitch range  $+15^\circ$  to  $-15^\circ$  without damaging the structure. The sketch displayed in fig. 7.23 illustrates what dimension of the landing gear needs such that a landing at  $\pm 15^\circ$  can be accomplished.

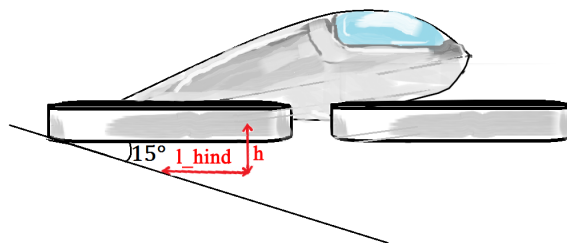


Figure 7.23: Landing under extreme pitch angle of  $15^\circ$

As can be seen in the figure for a given  $h$  a  $l_{hind}$  has to be set to protect the vehicle from getting damaged. Similar to the bank angle analysis performed before the value for  $l_{hind}$  is found only through simple geometry.

Since at this stage no decision has been established for the type of landing gear, no exact final dimensions which comply with the clearance requirements can be provided. Instead the final dimensions of the landing gear are presented in section 8.5 in table table 8.5.

## 7.5.2 Design Options

This subsection introduces the four different landing gear design options, of which the first two are often-used in helicopter design: skids, wheels, running legs and bumpers. The latter two are unconventional options that may be interesting from respectively a safety and a mass point of view. In this work, 'running legs' refers to

running-specific prostheses as in [26]. Figure 7.24 provides simple sketches of the four landing gear options considered.

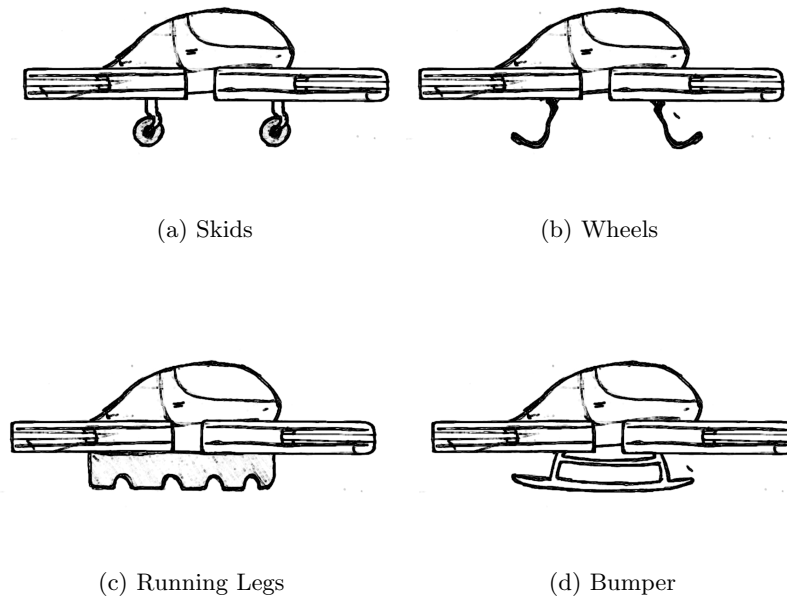


Figure 7.24: Landing gear concepts

### 7.5.3 Tradeoff

This section proposes a set of relevant criteria along with a short description of relative importance, works out criteria for the design options and presents a tradeoff table akin to SEAD Space.

#### Criteria:

For the consideration of the four different landing gear types, a set of criteria was established to judge relative suitability to the HyDrone. These criteria include a relative assessment of their adverse effect on aerodynamics, most notably their effect on drag of the whole system as well as on the design of other components (defined as **cruise aerodynamics**). Obviously, a first-order mass estimate of the landing gear is also included as the HyDrone is mass-constrained (defined as **mass**), which is thought to be sufficiently illustrative without explicitly incorporating weight impact of structurally redesigning to other components. Also, the maturity of the type of landing gear with respect to aerospace usage is qualitatively assessed (defined as **complexity**) wherein a high maturity is desired to minimise development risk and resource requirements. Arguably, resources are better focused on components with higher risk and mission criticality such as the propulsion subsystem. As a fourth criterion, a first-order unit cost estimate is included (defined as **cost**). The final criterion pertains to the susceptibility to maintenance (defined as **maintainability**).

Note that manufacturability and sustainability are left out as explicit criteria. In principle, all four components can be made manufacturable with appropriate production processes and is strongly coupled with detailed design choices. Furthermore, maintainability can be framed as an element of sustainability - wear and tear and frequent replacement of landing gear components increases material use - as can mass. However, as most of the pollution is tied to material choice and production processes, a detailed sustainability analysis is left for a later design phase (see chapter 18).

Each design option has positive and negative aspects. The major points are highlighted below. Note that a multitude of assumptions are made to estimate key parameters due to time constraints. Regardless, it should be sufficient for their purpose in a side-by-side tradeoff.

#### Wheels:

For conventional helicopters, wheels have an advantage over skids, bumper and running legs which is the ability to taxi without flying. That is to say, to move laterally on the ground without hovering. The other options are forced to air taxi, potentially having to conform to more stringent regulatory inter-aircraft clearance requirements for the simple reason that hovering induced downwash affects the controllability of aircraft in the vicinity. As such it is dependent on the positional scatter of drones on the landing pad, which may be a legitimate concern for destinations where multiple HyDrones converge (like fueling stations). Nonetheless, this could be resolved by increasing the landing area and the need for taxiing is limited regardless. Additionally,

please note that dependent on regulatory necessity, skids could be fitted wheels as well at a pricepoint of 500 to 1000 2017USD per side (according to a personal price quote for the Robinson R44 and R66) depending on wheel type.

A significant downside is increased design complexity and maintainability as wheeled landing gear incorporate more rotating parts, which also increase the risk of failure and wear and tear. Also, if the wheels are not solid, they have to be pressurised to 50-75 psi.<sup>20</sup>

To estimate the mass of the wheeled landing gear no reference systems have been found to provide sufficient clearance for the HyDrone. Therefore, an exact mass estimation is difficult. Comparatively, however, it is deemed likely that such system would not be lighter than skids as the loads are more concentrated and more components are required *three or four* wheels and auxiliary systems for the set clearance requirements.

### Running legs:

For simplicity sake, the running leg mass was estimated by upscaling commercially available prosthetic running legs, assuming a linear coupling between maximum load and component mass (defined as specific load). It is also assumed that the maximum load requirement on the landing gear can be approximated as two times the total system weight on a singular landing gear to account for asymmetric landing and residual downward velocity upon touchdown. So with a specific load  $\sigma_s$  of  $\frac{2.3 \text{ kg}}{75 \text{ kg}}$  [26] and total system mass  $m_{total}$  of about 580kg, eq. (7.15) gives a running leg mass  $m_{runninglegmass}$  of 17.8 kg - quite low.

$$m_{runningblade_{mass}} = 580 \cdot \frac{2.3}{75} = 17.8 \text{ kg} \quad (7.15)$$

Running legs' major downside is the complexity: it has been rarely used outside the prosthetic industry, let alone as primary structural component in the aerospace industry.

Another downside is the maintainability. As the running legs would routinely be exposed to friction induced by residual horizontal velocity at landing and current prosthetics are made of carbon fibre by hand layup, they would be susceptible to damage degrading performance (such as fibre kinking and interlaminar separation). To mitigate this and other design and analysis problems, a significant R&D effort would have to be undertaken with extensive validation testing for certification.

In terms of cruise aerodynamics, running blades are susceptible to flutter and in terms of overall drag contribution smaller than wheels and the bumper. The overall drag contribution is difficult to estimate. As the blades are flat and pointing towards the propeller axes, in cruise they would be angled into the wind. If they can thus be seen as flat plates under an angle of attack, the frontal area is an effective indicator for drag and the influence of flutter is not too large, then it appears that the drag would be smaller than the wheeled and bumper options but larger than the skids.

### Bumper:

An advantage of a bumper is its potential to cushion landing through elastic deformation or deflation mechanics, providing airbag-like capability for crash landings. This would increase survivability and reduce probability of permanent damage for low-altitude drops and multiple-engine out scenarios. This capability comes, however, at a mass penalty and decreased maintainability characteristics.

A significant downside is the large mass. To illustrate this, an estimation was performed with assumptions to (likely) underestimate the mass. The assumptions are related to the geometry (thickness, circumference and lateral clearance requirements) and material used.

The padding would have to be thick for elastic dissipation of energy and transfer loads effectively. Assuming that the square circumference between the attachment point on the struts is lined with thick (soft) rubber pads of  $\rho_{rubber} = 1.1 \cdot 10^3 \frac{\text{kg}}{\text{m}^3}$ <sup>21</sup>, a thickness of just  $t_{bumper} = 0.1 \text{ m}$  and the clearance of 0.43 m, the bumper mass would be  $m_{bumper} = 234 \text{ kg}$ . Here the lateral clearance to satisfy banking and pitch angle requirements are neglected.

Another downside is its aerodynamic effects. Padding as undercarriage lining the body reduces its effective camber and therefore the body produces less lift. In addition, the overall drag would increase. For example, as the frontal area would be significantly increased as the bumper acts as a 'wall' into the wind. Also, the increased surface gradient at the bottom of the trailing and leading edges are increased if the bumper's corners are not sufficiently rounded with flow separation and transition as a result.

Note that an inflatory/deflatory system was deemed infeasible due to component complexity and lack of historical precedence.

### Skids:

From table 7.8 it is apparent that the skids consist of the skidtube, crosstube and other components. It is assumed that the Bell Helicopter OH-58C is sufficient as reference. The commercial listing price for the landing gear kit of the Bell Helicopter OH-58C is about 18,225 2017USD weighing 42.18 kg. As there are few

<sup>20</sup>[helitowcart.com/accessories/wheels/single/](http://helitowcart.com/accessories/wheels/single/)

<sup>21</sup>[http://www.engineeringtoolbox.com/density-solids-d\\_1265.html](http://www.engineeringtoolbox.com/density-solids-d_1265.html)

commercially available skids for aircraft of smaller size and this helicopter has a MTOW of 1451.5 *kg* - almost three times as much as the HyDrone -, it is assumed that with a cheaper design the price and mass can half to 9,113 2017 USD and 21.09 *kg*.

Table 7.8: Information on Reference Skid (Bell Helicopter OH-58C) for Price and Mass <sup>22</sup>

Component	Mass [kg]	Material	List Price [2017USD]	Units sold total	Notes
Skidtube	10.1	6061-T6	4,990	5000	incl. wear plates
Crosstube	5.35		3,395		
Landing gear kit	42.18		18,225		

The main advantage of skids is low complexity. They appear to be the landing gear of choice for light helicopters and have no moving parts. Therefore, the development risk is low.

### Results:

To summarize, skids appear to be the more suitable choice for the HyDrone. The dealbreaker for bumper was the additional mass and adverse effect on aerodynamics, and for running legs the dealbreaker was the high complexity due to its low TRL. Then, the wheels offer no significant benefit for HyDrone’s mission compared to skids, while increasing the cost and maintainance. If the mission changes in the future or new regulations require ground taxiing capability, wheels can be added to the skids at a fraction of the total cost.

## 7.5.4 Skid Aerodynamic Design

This subsection considers skid design in more detail from an aerodynamic point of view. At first, the broad aerodynamic characteristics of conventional skids are surveyed. Upon identification of a point of improvement, a design solution is suggested. Due to complexities relating to the skids’ structural analysis in section 8.5, this solution serves as a measure for future work.

### Skid Aerodynamic Characteristics

At first aerodynamic polars of skid landing gears are evaluated to identify better design solutions. Note that the skids are at a negative angle to the free stream velocity that is uncommonly large for helicopter designs. Also consider that these polars were found for conventional helicopter types. Thus, the following assertions are surrounded with some uncertainty concerning their applicability to the HyDrone.

#### Pitching Moment and Lift Coefficients

The pitching moment coefficient is important for longitudinal stability. From fig. 7.25a it can be deduced by observing the differences between the baseline configuration and the configuration without skid landing gear, that the skid landing gear contribute negatively to the pitching moment coefficient  $C_m$ . Rough extrapolation from the figure until  $\alpha = -17^\circ$  suggests contribution to the pitching moment of just  $-0.1$ . Compared to the budget discussed in section 7.4.2 this is small and therefore manageable.

Furthermore, from fig. 7.25b it is apparent that the landing gear contribute little to the lift coefficient. Interestingly, the effect of the landing is positive with a value of 0.04 at an angle of attack of about  $-10^\circ$ . From this source, there is no reason to assume this would become significant for even more negative angles of attack.

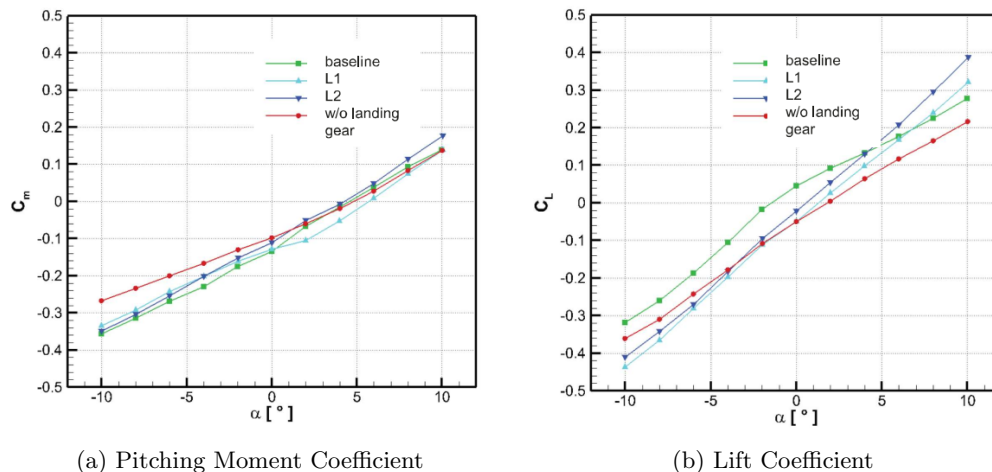


Figure 7.25: TEL Utility Helicopter with Conventional Skid Landing Gear (baseline) and without,  $Re_\infty = 1 \cdot 10^6$  [27]

## Drag coefficient

From fig. 7.26 it may, with caution, be deduced that for increasingly negative  $\alpha$  the total helicopter drag increases. However, the contribution due to landing gear, while considerable, remains approximately constant for negative  $\alpha$ .

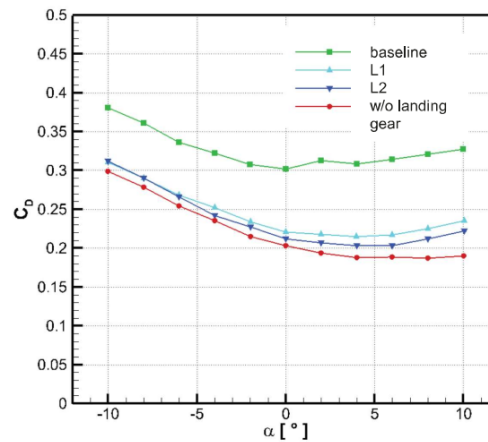


Figure 7.26: Drag coefficient vs  $\alpha$  of TEL utility helicopter with conventional skid landing gear (baseline) and without,  $Re_\infty = 1 \cdot 10^6$  [27]

The total drag breakdown of a conventional helicopter is presented in fig. 7.27. It shows a contribution from the skid landing gear of 21%. This is a significant portion of the total drag. By optimising the conventional skid design one could achieve potentially large performance gains.

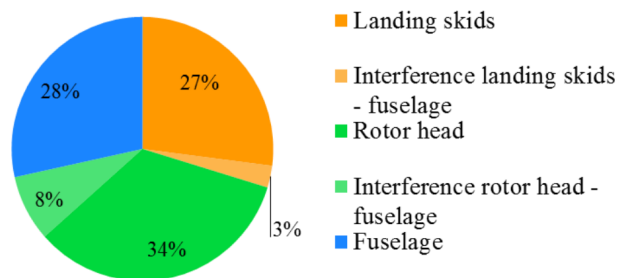


Figure 7.27: Drag Breakdown of TEL Utility Helicopter with Conventional Skid Landing Gear [28]

## Wake

It appears that skids have a negligible effect on the pressure distribution in the symmetry plane[29]. However, they do in the cross sectional plane[29]: the skids alter the wake structure significantly as can be seen from the total pressure loss contours in fig. 7.28. While these are for a somewhat different Reynolds number and a positive  $\alpha$ , they are still indicative of wake interaction. These large areas of total pressure loss were generated behind the cross beams of the skids and are transported downstream. [29] These effects are not surprising considering that the conventional skid landing gear design incorporates cross tubes with a circular cross section. Compare a cylindrical shape and an aerofoil in a wind tunnel test. For the cylindrical shape, there will be massive flow separation after the severe surface curvature. This could potentially disturb the flow around the aft section of the shrouds and fuselage.

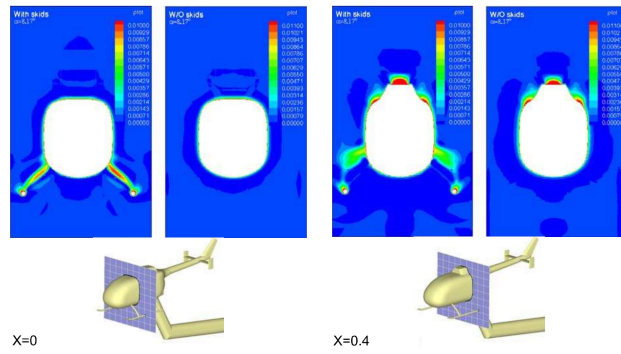


Figure 7.28: Total Pressure Loss in the Fuselage Wake at Selection Cross Sections at Distance X for a Model based on the EuroCopter BO-105 Helicopter,  $Re_{\infty} = 8.51 \cdot 10^6$ ,  $\alpha = 8.17^{\circ}$ . [29]

### Design modifications

The baseline skid landing gear shape can be modified to improve its performance.

An obvious and effective design modification is fairing the circular cross beams to reduce form and interference drag. This can be achieved by enclosing the cross beams with streamlined panels. The aerofoil used for this purpose should have a relatively high thickness-over-chord ratio to accommodate the cross beam diameter and not extrude too far back and front. Note that the inner circular cross beams are still the main load carrying component.

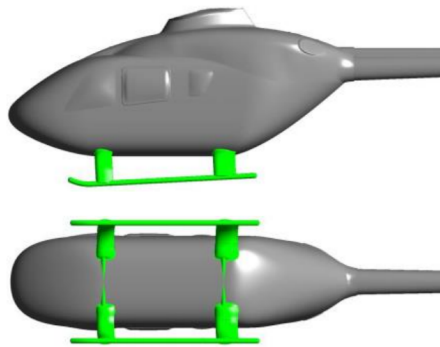


Figure 7.29: Illustration of a Faired Landing Gear [30]

An appropriate aerofoil geometry to illustrate the fitting of the circular cross beams is the DU-06-W200. Its maximum thickness is 19.8% chord and occurs at 31.1% chord. It has 0.5% maximum camber. In section 8.5 the cross beams have a circular diameter of 4.6 cm. To encompass the tube, the maximum thickness is to be slightly larger, say 4.8 cm. Therefore, the aerofoil is to have a chord length equal to 24.2 cm. The setup is illustrated in fig. 7.30.

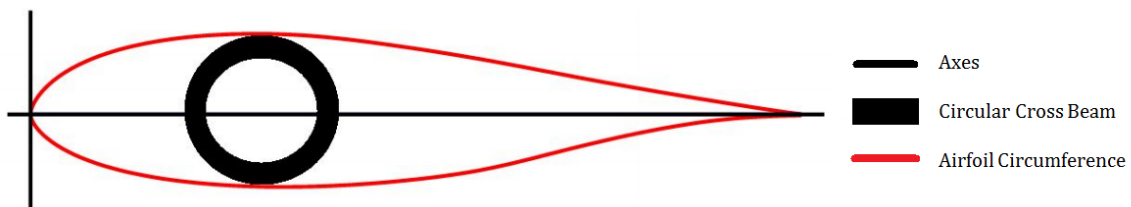


Figure 7.30: Illustration of the DU-06-W200 Airfoil and Cross Beam

Applying these changes can result in a potential total drag reduction of 26.8% by just fairing the cross-beams. Then the contribution of the skids to the helicopters total drag drops from 21% in fig. 7.27 to 7% in fig. 7.31. In fact, the overall drag coefficient of helicopters with faired cross beams approaches those obtained from helicopters without any landing gear, even at negative angles of attack (see data series L1 in fig. 7.26).

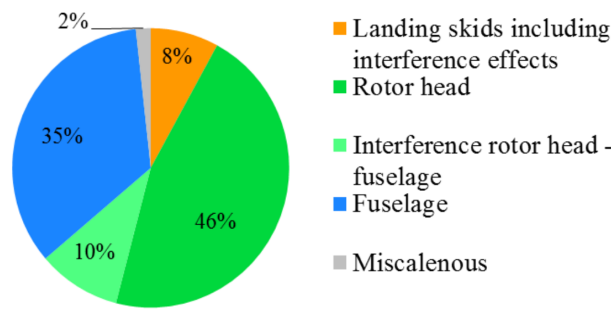


Figure 7.31: Drag Breakdown of TEL Utility Helicopter with Faired Skid Landing Gear,  $Re_\infty = 1 \cdot 10^6$  [28]

This becomes clear in fig. 7.32 which indicates the mean axial velocity distribution for a baseline configuration with conventional circular cross beams (top) and a version outfitted with fairings around the cross tubes which are similar to those proposed above (bottom left). The rest of the helicopter remained unchanged. From the figure, it is apparent that for the conventional version the axial velocity is reduced at the location of the cross beams. This would be due to the high form and interference drag.[27] Clearly, this effect is severely reduced for the version outfitted with fairings.

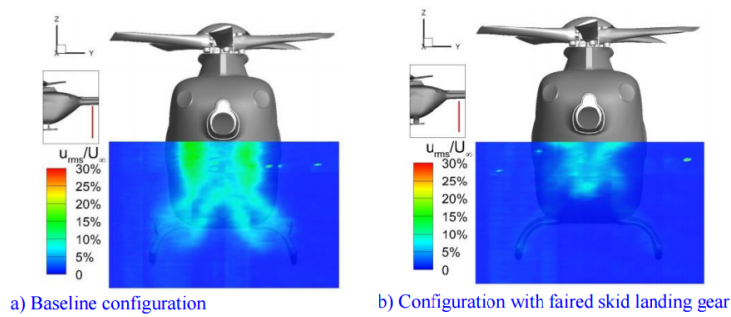


Figure 7.32: Mean Axial Velocity Distribution for the (a) Baseline Configuration, and (b) the Configuration with Faired Cross Beams, based on Stereo PIV;  $Re_\infty = 1 \cdot 10^6$ ,  $Ma_\infty = 0.116$ ,  $\alpha = 0^\circ$ . [27]

Note that the mass and cost penalty have not been analysed in any detail. However, using glass fibre with a hand lay-up process it should neither cost or weigh much. Furthermore, technology readiness level for the modification high, and therefore the development costs and the risk low.[27]

Therefore, encompassing the circular crossbeams with a streamlined fairing in the form of an aerofoil is recommended as future modification to the skid landing gear.

## 7.6 Technical Risks

Evaluating the technical risks of the aerodynamic design is an important tool to ensure the quality and safety of the design. A technical risk map was made to graphically represent this. The following risks were assessed and risk mitigation measures were proposed. In table 7.9, the risks before mitigation are denoted, and in table 7.10, the risks after mitigation.

1. Lifting-Body
2. Shrouds
3. Landing Gear

Table 7.9: Technical Risk Map: Aerodynamic Subsystem

Feasible in Theory			1, 2	
Working Laboratory Model				
Based on Existing Non-Flight Engineering				
Extrapolated from Existing Flight Design				
Proven Flight Design		3		
	Negligible	Marginal	Critical	Catastrophic

---

## Lifting-Body

The general principle of a lifting-body is a proven flight design as showed in section 7.3. However, in this particular configuration with this particular shape has not yet been used in any type of vehicle. Therefore it is assumed that it is feasible in Theory. The risks associated with the lifting-body is that it generates less than the calculated lift, or even worse, no lift. This can be possible since a lot of assumptions were made. A lot of unforeseen aerodynamic effects which affect the total lift generated can be present as well. The only way to mitigate this risk is to design the power and propulsion subsystem on the case that no lift is generated, as is illustrated in table 7.10. In this way the HyDrone will be able to fly regardless the presence of a lifting-body.

## Shrouds

The shrouds are classified as a relatively high-risk design component. While there are working laboratory models for rotor ducts with nearly axial air inflow (vertical flight mode), none could be found that were designed to operate at extreme angles of attack for extended duration (horizontal flight mode). Due to the complexity of the problem, design is performed for a limited set of conditions, using significant assumptions and without validation. Considering the potential effects on most notably the drag polar during horizontal flight, noise production due to unsteady flows, interaction with the propeller on the inside, potential positive net lift contribution during vertical flight, future development of the shrouds may prove to have a critical effect on the HyDrone's design.

To mitigate this risk, actions were proposed in section 7.7. Incorporating these measures can decrease the risk substantially, as is illustrated in table 7.10.

## Landing Gear

From an aerodynamics perspective the landing gear are low-risk: flight proven and likely not very large contributor to the total drag polar (as mentioned in section 7.5.4) and almost insignificant other aerodynamic characteristics.

As such, it can be stated that for the subsequent design iterations of the skid, the effects on the rest of the design are marginal. That is, even if the  $C_D$  values are higher due to the fact that the current design has larger skid tubes or that the cited wind tunnel and simulation data was based as different Reynolds numbers, angles of attack and fuselage shape (affecting fuselage-landing gear interference) compared to the HyDrone. Table 7.10 shows that the risk changes subtly.

Table 7.10: Technical Risk Map: Aerodynamic Subsystem after Mitigation

Feasible in Theory	1	2		
Working Laboratory Model				
Based on Existing Non-Flight Engineering				
Extrapolated from Existing Flight Design				
Proven Flight Design	3			
	Negligible	Marginal	Critical	Catastrophic

## 7.7 Recommendations

In this section recommendations for each aerodynamic component is given: body, shrouds and landing gear.

### Body:

- In section 7.3.5 it was stated that the initial lift generated by the body would be 10% of the total weight. This was used as a starting point and the current lift- and drag coefficient are a result of this initial statement. Using these values it was investigated whether or not it was beneficial to have a lifting body in terms of power needed. This was indeed the case and 9.2 kW is saved during cruise. From that point it was decided not to iterate it any further. It would simply cost too much time to iterate since it had to be done manually. That is, the input values used (RPM, blade pitch) in the code had to be adjusted by hand until convergence of the power. This is left to be done in a further study of the HyDrone.
- Another point of improvement is the estimation of the overall drag coefficient of the HyDrone. As explained in section 7.3.5, the drag coefficient is the closest estimation which could be supported by literature. It is advised to do studies on drones with the same configuration at the same Reynolds number. It is also recommended to carefully model a drone to perform a CFD analysis.
- The HyDrone's body is based upon an existing aerofoil design. However, aerofoils are not built to fit somebody inside. Therefore one might think that there are more optimal shapes which generate lift and can fit a person. This might be a major point of improvement of the HyDrone.
- The body is really thick for an aerofoil. It has to be investigated how this affects the flow around the body, after all the side area is as large as the wing area. This possibly introduces a lot of (big) vortices which are not taken into account in the current drag estimations since these only hold for normal wings.

- The minimum 'sharpness' of the wingtip should be investigated. As explained in section 7.3.5 having a 'sharp' wingtip reduces the induced drag in comparison to a straight wingtip (fig. 7.12, number 1 vs number 5). Currently it is not known if the shape is 'sharp' enough and similar to the desired shape to actually have a positive effect.
- It is disputable if the body could actually be treated as a wing. All the relations used were indeed for low-aspect ratio wings, but an aspect ratio of 0.25 has not been investigated yet. This should therefore be investigated further.
- Finally research should be performed regarding the noise level of the body. In section 7.3.4 it is assumed that the HyDrone's airframe noise will be insignificant in comparison to the rotor's noise. But the extraordinary shape of the HyDrone might actually contribute to the noise level. Therefore it is strongly recommended to investigate the contribution.

### Shrouds:

As mentioned in section 7.4.2 a large number of factors are involved in the design of an effective shroud. Below follows a list of specific recommendations to improve the shroud design.

- The current design is contingent on the assumption that a shroud can be decomposed into relatively independent geometric parameters to reduce the complexity of the design. Then the shape of the outer shell was only roughly defined, and the other parameters ( $r_i$ ,  $h_s$ ,  $h_d$  and  $\lambda_d$ ) were determined by setting upper or lower limits, then qualitatively assessing the cost-benefit of changing their sizes and their impact on one another. Finally, using sizing budgets some sort of compromise was reached. Due to this approach, the design point is probably far from optimised.  
To actually achieve a more optimised design point, much more information is required about actual the operating conditions and interactions.
- Dependent on flow analysis (see also section 13.4), it may be considered to increase the total shroud height to increase the vertical shroud length. This accomplishes an effectively lower velocity intake which results in a higher propulsive efficiency and lower internal drag (as long there is no separation) and more uniform inflow (which lead to lower noise) at a mass and cruise drag penalty.[16] Lengthening the duct also allows for a larger propeller pitch which decreases the noise production.[7][21] This is also mentioned in section 13.6.
- Consider all flight phases: accelerating climb, climb at constant velocity, cruise and hover. Now specific geometric parameters are sized for just a single flight condition.
- Consider both the leading and trailing edge of the shroud.
- Consider non-axisymmetric design, as the trailing edge operates in a different flowfield and affiliates with different design objectives that are not considered here. In section 7.4.4 was axisymmetry was assumed to simplify design.
- Revisit the tip clearance. As mentioned in section 7.4.4, determining which specific value of the tip clearance is feasible and desirable requires more indepth analysis of, e.g., thermal expansion and aero-elasticity on the one hand and propulsive efficiency on the other. It would be unfortunate if the propellers were to damage the shrouds under certain loading conditions.
- Investigate the exact balance between shroud dimensions and the ability to effectively rely on autorotation as safety mechanism.
- investigate the effects of the duct's contribution to the thrust coefficient in different flight conditions.
- Investigate to what extent the pitching moment is a driving requirement and how much the shrouds affects it. It was assumed that it may be, and sizing was therefore taken as a design objective for the outer shell curvature. And while there is historical precedence for excessive pitching moment adversely affecting the operation of previous aircraft such as the Hiller flying platform, the VZ-1 Pawnee.
- Consider 3D effects from interference with the body. It is not unlikely, especially for the rear shrouds and inboard parts, that the inflow may be disturbed and the effects on shroud and body are coupled.
- Revisit the outer shell curvature, as it is merely roughly defined at this stage and the reasoning behind it has to be verified.
- The design of the inlet and diffuser depended heavily on the assumption that the experimental results from [20] scales to the HyDrone. However, a better approach might be to solve the
- Evaluate airflow around the front and rear shrouds at leading edge and trailing edge under all flight conditions.
- Re-evaluate tilt-rotor design, which may simplify design as there is a substantial body of research on the topic and the flow conditions are less diverse.
- Investigate flow separation at inlet lip at leading edge and outer curvature at trailing edge during cruise.
- Determine the aerodynamic loads. Even though three out of five constraints were aerodynamic characteristics, it was out of the scope to obtain the aerodynamic loads. For any modestly accurate prediction the physical dynamics have to be modelled.
- Investigate internal pressure distribution.

- 
- while at odds with a rounded diffuser shape, consider a sharper bottom to facilitate flow reattachment.
  - Consider blending the shroud into the body to reduce interference drag effects.

**Landing gear:**

The recommendations for the landing are:

- To investigate the mass and cost penalty of fairing the cross tubes.
- To investigate the aerodynamic characteristics of this skid shape in combination with the body under the relevant angles of attack. The data from wind tunnel testing and CFD simulations is only suggestive of the skid's characteristics due to all these differences.
- Implement the fairings in the next design iteration if the resulting analysis is favourable.



---

# Chapter 8: Structures & Materials

This chapter describes the process and methods used in the design of the structural subsystem. It starts with an overview and selection of materials to be used in section 8.1. Using this information the load carrying structure, shrouds, cockpit and landing gear design methods are described in section 8.2, section 8.3, section 8.4 and section 8.5 respectively. Thereafter the verification and validation procedure, sensitivity analysis and technical risk assessment are detailed in section 8.6, section 8.7 and section 8.8. Finally, recommendations for the post-DSE project phase are given in section 8.9.

## 8.1 Materials

A critical factor in the structural design is the selected material. When designed properly the material has large influence on the weight, cost, maintenance and ecological footprint of the HyDrone. Ideally all those four aspect should be reduced to a minimum. However most materials do perform better at one of those aspects and worse on another, compared to its competitors. In order to select the right materials a balance should be found, to select the material which fits the best to the HyDrone. Structural materials of the HyDrone are selected for the design of the cockpit, shrouds, load carrying beams, landing gear and reinforcements against impact. In table 8.1 an overview of some typical aerospace structural materials and their most influential properties on the 4 aspects described before are given. From those table, materials are chosen best performing for some specific requirements as described below on the basis of the four aspects. In addition Polymethylmethacrylaat (PMMA) has been added, a common used material for production of windshields.

### 8.1.1 Weight

Weight has great influence on the design of the HyDrone. Increase in weight causes an decrease of flight performance, decrease in efficiency and an increase in noise. All of those are of major importance to the HyDrone, therefore weight is set as most important aspect of the material selection. The weight is dependent on the density of the material used and the amount of material used. Naturally a combination of high mechanical properties like Yield Strength, Youngs Modulus, Shear Modulus and Impact Strength will reduce the amount of material needed. Therefore a material with a low density and high mechanical properties suited would be most suitable to assure a low weight.

It should be noted that due to the fibre orientation of composites the material properties cause the mechanical properties to differ over the orientation of the composite, strength necessary in multiple directions may come with a weight penalty. This becomes perfectly clear when looking at the unidirectional (UD) layup of carbon fibre (CF). It shows very high mechanical properties in the  $0^\circ$  plane, however in the  $90^\circ$  plane the mechanical properties are modest. The CF with Quasi Isotropic (QI) orientation the mechanical properties are in between. Those properties are obtained in all fibre directions. Similar behaviour can be seen for Aramid Fibre (AF) and S-Glass Fibre (SGF). Metals do not have this kind of behaviour, no influence of fibres is present, so mechanical properties are apply in all directions for Aluminium (Al) and Titanium (Ti). Last it should be noted that no values are available for the impact strength of metals. Metals are often better resistant to impact due to higher ductility.

### 8.1.2 Cost

When it comes to selecting a material the production and manufacturing price of the material should be taken into consideration. In table 8.1 the price in 2016 €/kg is given for high volume purchase from a primary producer, which might be reasonable for the primary materials used in the structure. No specific value has been given to the manufacturing of materials since this is highly dependent on the shape an the manufacturing process used to create a part. However it should be noted that the manufacturing of composite parts are more expensive then the manufacturing of metal parts [31]. During the structural design it should be taken into consideration that the unit cost of 100.000 Euro as stated in section 3.2 will not be exceeded. Therefore the material cost is the second most important aspect when selecting the material. After all, the weight determines whether the HyDrone is able to fly or not and how well it will perform.

### 8.1.3 Maintenance

The maintenance of the HyDrone should be minimised in time and cost. Less time spend on maintenance is cheaper and more convenient, furthermore in general reparation of a part is cheaper then its replacements. The maintainability of metal is known to be more when components age, due to corrosion and fatigue damage. On

Table 8.1: Typical Materials Used in the Aerospace Industry and their Properties [31]

Material /Fibre	Treatment /Lay-up, %Fiber, prepreg	Cost [€/kg]	Density [kg/m <sup>3</sup> ]	Yield Strength [Mpa]	Youngs Modulus [Gpa]	Shear Modulus [Gpa]	Impact Strength [kJ/m <sup>2</sup> ]
CF	QI, 65-70, UD Prepreg	34.3-38.1	1550-1580	603-738	49.7-60.1	19.0-23.0	40.0-63.0
CF	UD 0°, 65-70, UD Prepreg	34.3-38.1	1550-1580	1740-2170	129-154	129-154	154-188
CF	UD 90°, 65-70, UD Prepreg	34.3-38.1	1550-1580	46.8-56.7	8.5	8.5	2.0-4.0
AF	QI, 45-50, UD Prepreg	43.9-72.1	1380	355-392	23.5-30.9	8.85-11.5	16.0-19.0
AF	UD 0°, 45-50, UD Prepreg	43.9-72.1	1380	1100-1390	60.0-80.0	2.1	146-179
AF	UD 90°, 45-50, UD Prepreg	43.9-72.1	1380	27.0-35.0	5.5-8.0	2.1	2.0-4.0
SGF	QI, 65-70, UD Prepreg	17.9-28.5	1840-1970	457-504	19.0-21.0	9.16-9.23	7.0-10.0
SGF	UD 0°, 65-70, UD Prepreg	17.9-28.5	1840-1970	1700-1760	47.6-47.8	4.70-4.75	187-228
SGF	UD 90°, 65-70, UD Prepreg	17.9-28.5	1840-1970	62.0-62.1	12.7-13.3	4.70-4.75	2.0-4.0
Al	7075-T6	4.08-4.60	2770-2830	359-530	69.0-76.0	26.0-28.0	N/A
Al	2024-T861	2.22-2.51	2750-2780	400-462	12.0-75.7	28.0-29.4	N/A
Ti	alpha-beta alloy	19.4-20.4	4460-4550	1070-1260	113-124	44.9-47.2	N/A
PMMA	Impact Modified	3.40-3.95	1110-1180	37.9-58.4	1.6-3.3	0.493-1.23	29.7-78.8

Table 8.2: Energy Needed for the Production of Material and Parts [31]

Material /Fibre	Embodied Energy Primary Production [MJ/kg]	Autoclave Moulding Energy [MJ/kg]	Compression Moulding Energy [MJ/kg]	Rough Rolling, Forging Energy [MJ/kg]	Extrusion, Foil Rolling Energy [MJ/kg]
CF	263-290	20,9-23	3,33-3,68	-	-
AF	221-243	20,9-23	3,33-3,68	-	-
SGF	96,4-106	20,9-23	3,33-3,68	-	-
Al 7075-T6	184-203	-	-	10,6-11,7	20,9-23,1
Al 2024-T861	185-204	-	-	10,4-11,5	20,4-22,6
Ti	611-674	-	-	12,5-13,8	24,7-27,3
PMMA	96.4-106	20.9-23	3.33-3.68	-	-

the other hand, repair of composites parts are hard, often large parts need to be replaced, those parts are often more expensive and repair cost more time. Metal material often can be repaired [32].

### 8.1.4 Ecological Footprint

All materials used have an influence on the environment, one more than an other. In table 8.2. the embodied energy, which is the energy used to produce a 1 kg of the material and the energy needed for typical production processes of both composites and metals. The production energy does not differ for the different fibre lay-ups for a composite, which are shown in table 8.1

Just as with the cost, the ecological footprint, in terms of energy usage, is strongly dependent on the weight of the structure. Besides the direct energy needed for production of the materials and the structure, energy is used during the operational life of the HyDrone. Although the use of hydrogen results into a very small ecological footprint chapter 10, the use of it should be minimised by efficient flight, lower weight will result in a more efficient flight.

The last stadium of the HyDrone and the ecologic footprint is the after operations life. When the HyDrone will not be used anymore an after life solution should be found. Concerning the materials a way to process them should be found. For metals widely known and used recycling methods are used. The recycling of polymers is less known and widely spread, however due to the increase of demand more efficient processes are developed [33]. It is assumed that the recycling of composites will be clearly feasible when the end of life of the HyDrone has come.

### 8.1.5 Results

After carefully considering the four aspects as described above, materials have been selected for the design of the cockpit, shrouds, load carrying beams, landing gear and reinforcements against impact.

**Cockpit, Shrouds and Load Carrying Structure** For the cockpit, shrouds and load carrying structure, quasi isotropic carbon fibre is selected. The high mechanical properties and the low density will result in the lowest weight and the best flight performance. The quasi isotropic orientation of the material is selected because the HyDrone is able to flight in all directions, due to which the direction of forces and the location of stress can differ a lot, quasi isotropic orientation is most suited for composites to deal with those different load cases. It should be noted that the cost are moderate high. It is therefore expected that it will stay within reasonable proportions. Furthermore the embodied energy of carbon fibre is high as well, however less material weight will be used in comparison with other materials, which reduces the differences. Although those disadvantages, it is believed that carbon fibre is the best suited material. Main reason is that minimising the weight is of such large importance, first for the flight performance and second because it has influence on all other parameters.

**Landing Gear** The landing gear material is based on the conventional usage of 7075-T6 Aluminium. Although composites seem to have suitable mechanical properties, only little research has been done on how composites would exactly perform as landing gear. Since a proper landing is of major importance to have a safe landing, without any damage, 7075-T6 Aluminium has been selected as the material for the landing gear.

**Impact Reinforcement** Unidirectional AF is selected to be used as reinforcement material against impact. This material has the best highest impact strength for its weight, making it most suited. The penalty in terms of high cost, maintenance intensity and moderate high energy consumption during production, is taken to guarantee a safe flight, also in case of impact. For the windshield PMMA is used, a cheap and transparent material with relative high impact strength, low density and low required production energy.

## 8.2 Load Carrying Structure

In this section the method used to design the load carrying structure and the results that follow from it will be discussed. The purpose of this structure is to transport the thrust force from the rotors to all other components. It also serves as a mounting point for many elements of the vehicle such as the landing skids and the cockpit.

### 8.2.1 Shape

The size and shape of the load carrying structure is primarily based on the limit loads it needs to endure during flight. Additionally, some constraints are present.

The first constraint follows from the design of the coaxial rotors, for which it is desirable to be placed at a distance of  $20\text{cm}$  from each other, as described in section 9.3. Including a margin of  $5\text{cm}$  this constrains the beam height within the shroud to  $15\text{cm}$ . A second constraint pertains the cabling connecting the power and control subsystems with the electric motors and sensors. These cables must be shielded from the environment. This requires either a closed hollow structure or additional shielding. A final constraint is based on the filament winding process for carbon fibre reinforced composites. This construction method is the least costly and most efficient CFRP construction process but benefits from a closed section shape without sharp edges[34].

Additionally, to simplify the analysis of the structure a generalised expression for the beam shape was set. Several shapes were considered based on their excellent resistance to bending. This includes an I, C and ellipse shaped beam. Based on the mentioned constraints the shape was chosen to be an ellipse as shown in fig. 8.1. In this figure it can be seen that the beam is chosen to have a constant shape with a linearly varying size, where the ellipse at the centre of the drone is a factor  $p$  times the size of the beam at the rotor. Beam length is  $l_{arm} = 1.98\text{m}$  based on the distance from the centre of the drone to the rotor and thickness is kept constant along the beam for simplicity. As concluded in section 8.2.4, the optimal beam will have a width  $2a_1 = 8\text{cm}$ , height  $2b_1 = 12\text{cm}$ , skin thickness  $t = 14\text{mm}$  and growth factor  $p = 1.5$

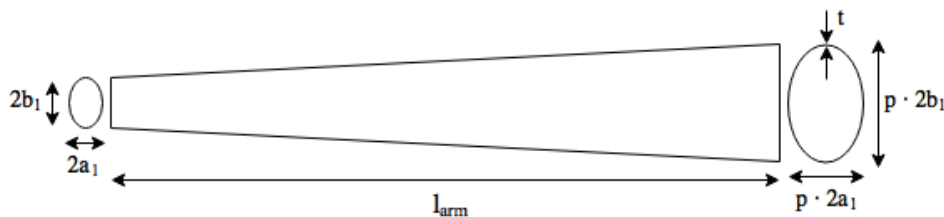


Figure 8.1: Shape Parameters of the Beam

### 8.2.2 Forces

The load carrying structure is modelled as a beam upon which several forces act, which is shown in fig. 8.2. In this figure the distributed loads are shown in green and the point loads are shown in red. The load  $W_{cockpit}$  shows the force of the cockpit weight on the beam, including all its content and payload. The load  $D$  denotes the drag due to the airflow over the beam inside the shroud and  $W_{beam}$  indicates the weight of the beam itself. The thrust, which is placed under installation angle  $i$ , is indicated by  $T$  and the force of the landing skid, which is mounted on the load carrying beam, is indicated by  $F_{gear}$ . The force  $W_{end}$  includes the weight of the electric motors, the propellers and the weight of the shroud, which is transferred to this point by its attachment struts. The reaction torques of the rotors are not taken into account in this analysis since the counter rotation of the top rotor eliminates the torques induced by the bottom rotor. A similar argument is made for the gyroscopic procession effects.

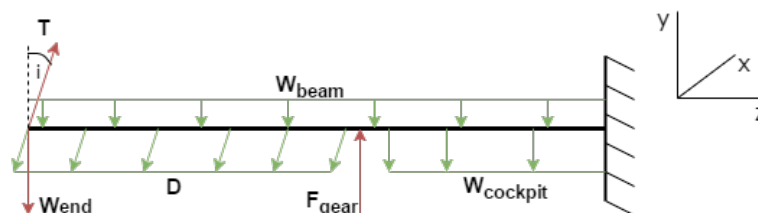


Figure 8.2: Free Body Diagram of the Load Carrying Beam

To determine the internal forces and moments the beam has been split up into elements of size  $\delta z$ , as shown in fig. 8.3 given by Megson[35].

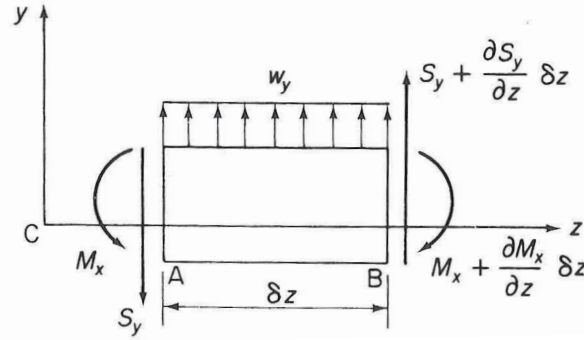


Figure 8.3: Element of the Load Carrying Beam

The shear forces and moments acting on each element  $j$  are found using equations eq. (8.1) and eq. (8.2), where the summation process starts from the left hand side of fig. 8.2 since both the moment and shear forces are zero at  $j = 1$ .

$$\vec{S}_{j+1} = \begin{bmatrix} S_x \\ S_y \\ S_z \end{bmatrix}_{j+1} = \vec{S}_j + \vec{F}_j \quad (8.1)$$

$$\vec{M}_{j+1} = \begin{bmatrix} M_x \\ M_y \\ M_z \end{bmatrix}_{j+1} = \vec{M}_j + \begin{bmatrix} S_y \delta z \\ S_x \delta z \\ Q_z \end{bmatrix}_j \quad (8.2)$$

In these equations  $Q_z$  is the torque acting upon element  $i$ . The forces given in vector  $F_j$  are using the beam reference frame.

So far the problem has been described as a static case. However, in reality this is a dynamic system. While the analysis of most dynamic effects is outside the scope of this report the acceleration due to the load factor needs to be taken into account. Using D'Alembert's principle this dynamic problem is converted to a static problem by multiplying the weights by the load factor[36].

The beam weight acting on an element is determined using equation eq. (8.3), where  $A_c$  is the cross-sectional area of an ellipse as described by eq. (8.4). The cockpit weight is assumed to act as a constant distributed loading.

$$W_{beam_j} = nA_j \rho g \delta z \quad (8.3)$$

$$A_c = \pi a_j b_j - \pi(a_j - t)(b_j - t) \quad (8.4)$$

Since the beam is to be designed based on the limit case where the load factor  $n = 3.5$  the thrust is set such that this is achieved. The distributed drag load on the beam is found using eq. (8.5). This drag is caused by the airflow in the shroud, which is created by the rotors.

$$D_j = C_D * \frac{1}{2} \rho_{air} V_{beam}^2 2a_j \delta z \quad (8.5)$$

In this equation  $V_{beam} = V_\infty + v_u = 35m/s$  is the airflow velocity at the beam, which was determined using the methods described in section 9.2.  $\rho_{air}$  is the air density and  $2a_j \delta z$  is the frontal area of the element. The drag coefficient  $C_D$  of the beam is determined using fig. 8.4[37] and found to be 0.75, where a Reynolds number of  $Re = 10^5$  was used. The Reynolds number at the beam, determined using eq. (7.2), was found to be  $Re \approx 3.5 \cdot 10^5$  using  $l = 12cm$ . This difference in Reynolds number was assumed to be negligible.

To determine  $F_{gear}$  again a load factor of 3.5 was assumed, with the thrust set to 2/3 of the weight. This results in a ground load factor of 2.83 acting through the landing gear[38]. During flight logically  $F_{gear} = 0$

The direction of some of these forces are dependent on the state of the system and may only be known in a different reference frame. In order to determine the forces in the beam frame several transformation matrices are used. As an illustration the transformation of  $W_{end}$  from the earth frame to the beam frame is shown in eq. (8.6)[39]. In this example the weight in the earth frame is negative due to its downward direction. This force is transformed through the pitch angle  $\theta$ , bank angle  $\phi$  and beam angle  $\chi$ , which denotes the angle between the longitudinal direction and the load carrying beam. A similar transformation is performed for the thrust and drag, which act with the installation angle  $i$ .

$$\vec{F}_j^B = \begin{bmatrix} \cos(\chi) & 0 & \sin(\chi) \\ 0 & 1 & 0 \\ -\sin(\chi) & 0 & \cos(\chi) \end{bmatrix} \begin{bmatrix} \cos(\phi) & \sin(\phi) & 0 \\ -\sin(\phi) & \cos(\phi) & 0 \\ 0 & 0 & 1 \end{bmatrix} \begin{bmatrix} 1 & 0 & 0 \\ 0 & \cos(\theta) & \sin(\theta) \\ 0 & -\sin(\theta) & \cos(\theta) \end{bmatrix} \begin{bmatrix} 0 \\ -W_{end} \\ 0 \end{bmatrix}_j^E \quad (8.6)$$

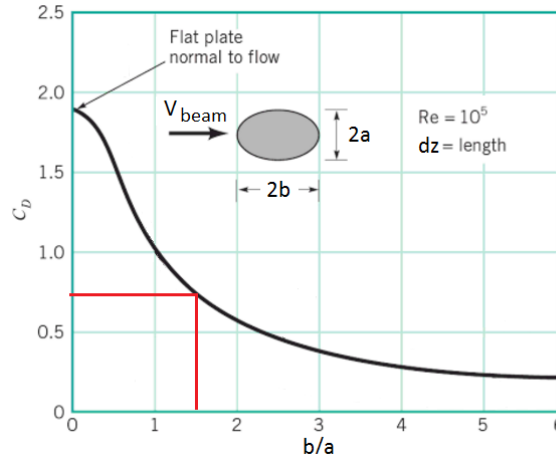


Figure 8.4: Drag Coefficient of an Ellipse

### 8.2.3 Stresses

To analyse whether the structure is able to cope with the forces as described in section 8.2.2 the stresses at each location of the beam need to be found. In order to perform this analysis in MatLab the continuous ellipse is discretised. To ensure an efficient analysis it is desirable to have the discretised points placed approximately equidistant from each other. This is done by placing point  $i = 1$  at a set point on the ellipse and finding the tangent to the curve, as is shown in fig. 8.5. Moving a set distance  $ds$  along the tangent, finding position  $x_{i+1}$  and using eq. (8.7) to find  $y_{i+1}$  the new point  $i + 1$  is found. This is repeated up to point  $m$ , at which the entire ellipse is discretised. Using this method for small values of  $ds$  will give  $\delta s \approx ds$ . This process is only performed for element  $j = 1$ . The location  $x_{j=n}$  and  $y_{j=n}$  of the points on element  $n$  are found by multiplying  $x_{j=1}$  and  $y_{j=1}$  by factor  $p = \frac{a_{j=n}}{a_{j=1}}$ .

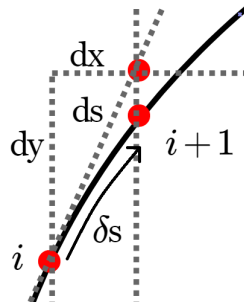


Figure 8.5: Determination of the Location of Point  $i$

$$y_{1,i+1} = \sqrt{b_1^2 \left(1 - \frac{x_{1,i+1}^2}{a_1^2}\right)} \quad (8.7)$$

To find the normal stress  $\sigma_z$  at each point  $i, j$  equation eq. (8.8) is used, where  $I_{xx}$  is given by eq. (8.9),  $I_{yy}$  is given by eq. (8.10) and  $I_{xy} = 0$  due to symmetry.

$$\sigma_{z_j,i} = \frac{S_{z_j}}{A_j} + M_{x_j} \frac{I_{yy_j} y_{j,i} - I_{xy_j} x_{j,i}}{I_{xx_j} I_{yy_j} - I_{xy_j}^2} + M_{y_j} \frac{I_{xx_j} x_{j,i} - I_{xy_j} y_{j,i}}{I_{xx_j} I_{yy_j} - I_{xy_j}^2} \quad (8.8)$$

$$I_{xx_j} = \frac{\pi}{4} a_j b_j^3 - \frac{\pi}{4} (a_j - t)(b_j - t)^3 \quad (8.9)$$

$$I_{yy_j} = \frac{\pi}{4} b_j a_j^3 - \frac{\pi}{4} (b_j - t)(a_j - t)^3 \quad (8.10)$$

In order to determine the shear stresses the beam is first idealised using the method described by Megson[35] in chapter 20, where it is assumed that the structure is thin walled. This method approximates each element  $j$  as direct stress carrying booms placed at all points  $i$ , connected by skin of zero thickness carrying shear stress only. The area of these booms is calculated using eq. (8.11), after which new approximate moments of inertia are calculated using eq. (8.12), eq. (8.13) and eq. (8.14).

$$B_{j,i} = \frac{t\sqrt{(x_{j,i+1} - x_{j,i})^2 + (y_{j,i+1} - y_{j,i})^2}}{6} \left(2 + \frac{\sigma_{j,i+1}}{\sigma_{j,i}}\right) + \frac{t\sqrt{(x_{j,i-1} - x_{j,i})^2 + (y_{j,i-1} - y_{j,i})^2}}{6} \left(2 + \frac{\sigma_{j,i-1}}{\sigma_{j,i}}\right) \quad (8.11)$$

$$I_{xx_j} = \sum_{i=1}^{i=m} B_{j,i} y_{j,i}^2 \quad (8.12)$$

$$I_{yy_j} = \sum_{i=1}^{i=m} B_{j,i} x_{j,i}^2 \quad (8.13)$$

$$I_{xy_j} = \sum_{i=1}^{i=m} B_{j,i} x_{j,i} y_{j,i} \quad (8.14)$$

The shear flow in the beam element can then be found using eq. (8.15), where  $q_{b_{j,i}}$  is evaluated using eq. (8.15) and  $q_{s,0}$  is determined using eq. (8.17). Here  $A_{e_j}$  is the cross sectional area of the ellipse and the equation is a simplified form of the one stated by Megson. This simplification was based on the symmetry of the ellipse, causing the shear centre to be placed at  $x = y = 0$ .

$$q_{s_{j,i}} = q_{b_{j,i}} + q_{s,0_j} \quad (8.15)$$

$$q_{b_{j,i}} = -\frac{S_{x_j} I_{xx_j} - S_{y_j} I_{xy_j}}{I_{xx_j} I_{yy_j} - I_{xy_j}^2} \sum_1^i B_{j,i} x_{j,i} - \frac{S_{y_j} I_{yy_j} - S_{x_j} I_{xy_j}}{I_{xx_j} I_{yy_j} - I_{xy_j}^2} \sum_1^i B_{j,i} y_{j,i} \quad (8.16)$$

$$q_{s,0_j} = \frac{1}{2A_{e_j}} \sum_{i=1}^{i=m} q_{b_{j,i}} [(x_{j,i} - x_{j,i+1})y_{j,i+1} + (y_{j,i+1} - y_{j,i})x_{j,i+1}] \quad (8.17)$$

$$A_{e_j} = \pi a_j b_j \quad (8.18)$$

The shear stress  $\tau_{sz_{j,i}}$  is then found using eq. (8.19).

$$\tau_{sz_{j,i}} = \frac{q_{s_{j,i}}}{t} \quad (8.19)$$

The normal and shear stresses have been found in the  $z$  direction and the beam wall direction respectively. However, the used material might experience a higher stress in a different plane. Therefore the principle stresses, as well as the maximum and minimum shear stresses are determined using eq. (8.20) and eq. (8.21) respectively. Since a CFRP material is used, these stresses have been multiplied with 2.35 in accordance with ISO 11439[40].

$$\sigma_{max,min} = \frac{\sigma_z}{2} \pm \frac{1}{2} \sqrt{\sigma_z^2 + 4\tau_{sz}^2} \quad (8.20)$$

$$\tau_{max,min} = \pm \frac{1}{2} \sqrt{\sigma_z^2 + 4\tau_{sz}^2} \quad (8.21)$$

## 8.2.4 Results

To determine the beam parameters  $a_1$ ,  $b_1$ ,  $t$  and  $p$  using the software described above an iterative process was used. These parameters could be altered with the design goal of determining the lowest beam mass for which the structure is able to cope with all forces. This was done while taking the constraints given in section 8.2.1 into account.

The beam was evaluated for flight with a load factor  $n = 3.5$  at various pitch and bank angles as well as landing impact. The optimal beam parameters that were found are given in table 8.3a and the resulting maximum stresses are shown in table 8.3b, where the mass includes the mass of both beams. As can be seen  $\sigma_{max} < \sigma_{yield}$  from the chosen material. Both the principle normal stresses and maximum shear were found to occur during flight with  $n = 3.5$ ,  $\theta = \phi = 0$ . The internal shear  $S_y$  and moment  $M_x$  in this load case is shown in fig. 8.6a and fig. 8.6b respectively, while  $S_x \approx S_z \approx M_y \approx M_z \approx 0$  and therefore not shown. The principle stresses and shear are visualised in fig. 8.7a and fig. 8.7b respectively, where it should be noted that the scales of the axes do not match causing the beam to be shown warped.

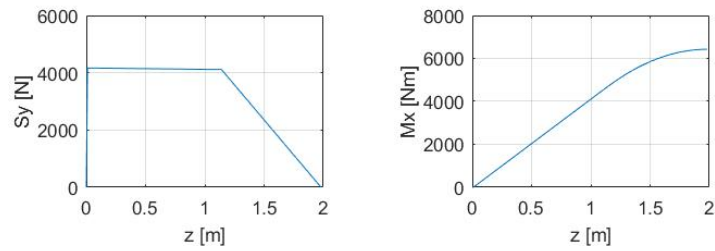
Table 8.3: Beam Parameters and Accompanying Mass and Stresses

Parameter	Value
width ( $2a_1$ )	8cm
height ( $2b_1$ )	12cm
t	1.4mm
P	1.5

(a) Parameters

Result	Value
$\sigma_{max}$	640MPa
$\tau_{max}$	321MPa
Mass	6.8kg

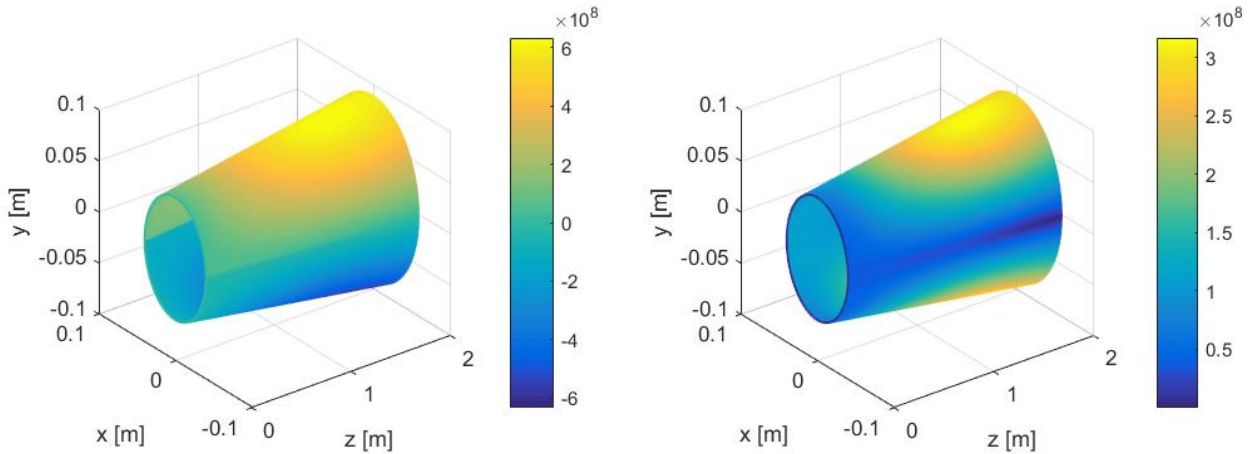
(b) Results



(a) Internal Shear Force  $S_y$

(b) Internal Moment  $M_x$

Figure 8.6: Loading During Horizontal Flight with  $n = 3.5$



(a) Maximum Absolute Principle Stresses  $\sigma_{max,min}$  [MPa]

(b) Maximum Shear Stresses  $\tau_{max}$  [MPa]

Figure 8.7: Loading During Horizontal Flight with  $n = 3.5$ ,  $\theta = \phi = 0^\circ$

## 8.3 Shrouds

The shroud is mainly designed to have optimal aerodynamic performances. Based on this shape, two analysis are done to determine the cross-sectional thickness. First the limit loading case during a manoeuvre with a load factor of 3.5 is analysed, based on the distributed force on the shroud. Second the situation of an external impact is analysed, based on the energy absorbed by the material.

### 8.3.1 Shape

The shrouds will have an inner radius ( $R_i$ ), just larger than the propellers, of  $0.954m$ , an outer radius ( $R_o$ ) of  $1.104 m$  section 7.4.5 and a height ( $h$ ) of  $0.3m$ . For the stress calculation it is assumed that the cross-section of a shroud is a perfect rectangular, with a width of  $0.15m$  and a constant cross section. The shroud will be supported by the load carrying beam as described in section 8.2 and two extra supporting beams. The three beams are placed with an even space between them, so with a 120 degree angle between all beams. A sketch of the configuration is shown in fig. 8.8. Using this configuration the beams will never encounter the full aerodynamic force encountered by the propeller blades at the same time, which decreases the total force due to a pressure increase of the propellers on the shroud structure.

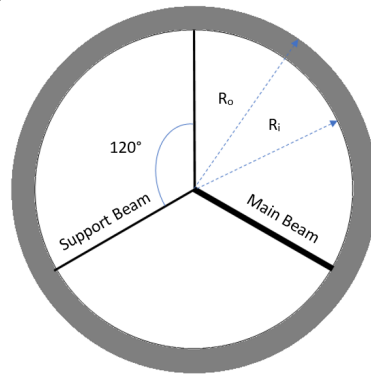


Figure 8.8: Top View of the Shroud Configuration

### 8.3.2 Forces

Considering that the shroud is not designed to carry any other structural forces than its own, the forces acting on the shroud are due to gravity and aerodynamics. The maximum loading case occurs when the loading factor of 3.5 is met, in case of no impact. Since the force is mainly produced by the weight of the shroud, it is assumed that the force is distributed evenly with its weight over the whole shroud and goes through the centre of gravity of its cross-section. So any offset due to aerodynamic forces is neglected. In this simplification, the total resulting force distributed over the shroud is assumed to be  $3.5W_{Shroud}$ . The loading case is analysed for different flight angles, to be complete it is analysed from a zero degree angle relative to the x-axis of cross-section up until a 90 degree angle equal to the y-axial direction. Due to the simulated symmetry in the cross-section and the shroud being circular all possible loading directions are taken into account in this way. The front shrouds contains a reinforced part, this will cause a increased distributed weight and therefore the forces on the part of the reinforcement. The reinforcement will be further elaborated in section 8.3.4. The forces caused by aerodynamic disturbances and pressure difference on the inside of the shroud due to the propeller rotation are expected to be small, therefore neglected. Due to the relative small height of the shroud end the large open up and down side, pressure increase is assumed to be small. Assumed is that no torque would occur on the shroud, therefore the distributed forces are assumed to cancel each other.

The beams inside the shroud are assumed to be exposed to the same loading case as the shroud, so the forces are simulated distributed over the beams through its cross-sectional centre of gravity and the total force being  $3.5W_{Shroud_{Beam}}$ . Forces on the two support beams due caused by the propellers is determined in the same way as for the main beam section 8.2.2. Assumed is that no torque would occur on the beam, the distributed forces over the shroud are assumed to cancel each other.

### 8.3.3 Stresses

The stresses in the shroud and the supporting beams during the described loading case will be a combination of shear stress, directly caused by the forces on the shroud and beams and normal stresses caused by bending of the structure. The shroud is modelled as if it was a thin-walled beam. Furthermore a safety factor of 2.35 is used, as explained in section 8.2.3. It should be noted that the assumed cross-section differs slightly from the real cross-section in terms of shape, circumference and the moment of inertia. Due to a higher moment of inertia, the stresses in the structure might be lower and the required thickness is lower accordingly, decreasing the required weight. On the other hand the circumference assumed is larger, which causes a little increase in area and weight. The assumed forces in the stress calculation are taken very conservative, this should take care of this offset.

The normal stresses in the shroud were determined by assuming that the shroud should carry all bending stresses by itself around one point, without help of the beams within the shroud. The normal stresses were determined using eq. (8.8), the same assumptions as mentioned in section 8.2.3 regarding the normal stresses are assumed valid for the normal stress calculations of the shrouds as well.

In reality, the beams would take some of the stress as well. Therefore the determined stress might be higher than the stress which will actually occur in the structure. However due to the very rough estimation of the forces it might be good to take some extra safety in consideration with those calculations. Furthermore it makes the design more redundant.

The normal stresses caused by bending in the supporting beams was determined in the same way. However instead of being able to carry the whole bending moment, the beams are designed to carry the stresses caused by a third of the shroud. Again this was a very strong and conservative assumption, with the same reasoning as in the design of the shroud.

The shear stress in both the shroud and its beams was determined using eq. (8.22), eq. (8.23) and eq. (8.24) [35]. Where  $S_x$  and  $S_y$  are the shear stresses in x and y direction,  $I_{xx}$ ,  $I_{yy}$  and  $I_{xy}$  are the moments of inertia in x, y and z direction,  $t$  is the thickness,  $x$  and  $y$  are the distances in x and y direction and  $s$  is the distance over which the shear flow  $q$  goes. Furthermore it was assumed that, during any displacement, the shape of the beam cross-section is maintained. Furthermore the assumption of closely spaced rigid diaphragms is made. Stating that during displacement, the shape of the beam cross-section is maintain by a system of closely spaced diaphragms.

$$q_s = -\frac{S_x I_{xx} - S_y I_{xy}}{I_{xx} I_{yy} - I_{xy}^2} \int_0^s tx \, ds - \frac{S_y I_{yy} - S_x I_{xy}}{I_{xx} I_{yy} - I_{xy}^2} \int_0^s ty \, ds + q(s, 0) \quad (8.22)$$

$$q_{s,0} = -\frac{\oint q_b ds}{\oint ds} \quad (8.23)$$

$$\tau = \frac{q_s}{t} \quad (8.24)$$

Last the principal stresses are found using eq. (8.20) and eq. (8.21).

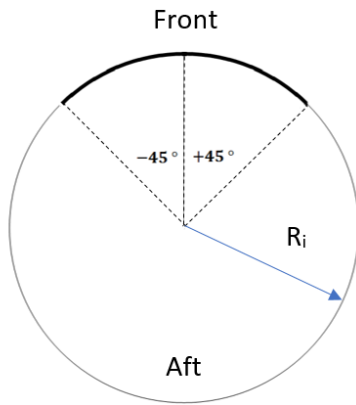
### 8.3.4 Impact

In the urban environment where the HyDrone will fly, an impact with an external object is likely to happen during flight. Although the possibility of avoiding an impact is already increased by autonomous flight, during the design of the shrouds the possibilities of external impact was taken into consideration, with as guideline section 29.631 of chapter 14 in the Code of Federal Regulation [2]. Which state "The rotorcraft must be designed to ensure capability of continued safe flight and landing (for Category A) or safe landing (for Category B) after impact with a 2.2-lb (1.0 kg) bird when the velocity of the rotorcraft (relative to the bird along the flight path of the rotorcraft) is equal to  $V_{NE}$  or  $V_H$  (whichever is the lesser) at altitudes up to 8,000 feet." Where  $V_H$  means maximum speed in level flight with maximum continuous power and  $V_{NE}$  means never-exceed speed. The HyDrone was designed in such a redundant way that after a bird strike, with as result an engine loss, safe flight and landing could be continued. However such an impact could cause a lot of damage to the shrouds, propellers and engines, which is at least very inconvenient.

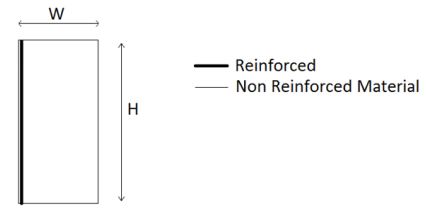
The shrouds of the HyDrone were designed in such a way that the shrouds will not fail in case of a frontal impact with a bird of 1.0 kg with a relative velocity equal to the HyDrone his cruise velocity of 40m/s. The actual relative velocity might be higher due to the velocity of the bird, however it is assumed that the possibility that the flight path of the bird is in line with the HyDrone is small, moreover if that would be the case it is highly likely that the bird or the HyDrone would try to avoid the collision by making a manoeuvre, which would decrease the relative velocity in case of collision. In advance the round shape of the shroud might cause a reduction in impact energy. That is, not all kinetic energy of the bird will be absorbed by the impact, but also a part of the energy will remain kinetic as the bird will touch a part of the shroud which will deflect the flight path of the bird. So the possibility of an destructive impact is largest at areas perpendicular to the free stream.

In case of the shrouds, the front is exactly perpendicular to the flight path in cruise flight, when moving left or right over the shroud the area becomes less perpendicular up until the point where the shroud is parallel to the body, after which the the area becomes again more perpendicular to the flight path up until the most aft part where it is exactly perpendicular again. However in this latter part, the shroud will not protect the propeller and engine against a frontal impact. Sideways impact may occur however the probability is lower since the flight paths only cross for a short moment, the energy during this impact will be lower due to lower relative velocity. Furthermore it is assumed that the shroud will deflect a bird enough to avoid damage to the propeller and the motor when the impact occurs more then 45 deg left or right from the shroud, seen from the impact direction. Additionally assumed is that the possibility of an impact which will damage the aft propeller and engine is small, since those are partly protected by both the front and the aft shroud, moreover the possibility that a bird strike occurs at the aft shroud is considered small due to deflection of the flight path of a bird due to the air flow caused by the front propellers.

Taking this reasoning and made assumptions into consideration, it was decided that only a 90 deg angle of the front shafts will be reinforced against external impact fig. 8.9a and fig. 8.9b, since this part is considered most likely to take an impact which may result in critical impact to the engine and shrouds.



(a) Top View of the Shroud with the Reinforcement Marked



(b) Cross-Sectional View of the Shroud with the Reinforcement Marked

Figure 8.9: Geometry and Placement of the Reinforcement in the Shrouds

This part of the shroud was designed in such a way that it can absorb all kinetic energy of the bird. This energy is determined using equation 8.25, where  $m_{bird}$  is the mass of the bird,  $1kg$  and the  $V_{ref}$  is the relative velocity,  $40m/s$ . This results in a total kinetic energy of  $E_k = 800J$ .

$$E_k = \frac{1}{2}m_{bird}V_{ref}^2 \quad (8.25)$$

The maximum absorbed energy of the material was determined by multiplying the impact strength of the material by the cross-sectional area. Where the cross-sectional area is set as the smallest cross-section in which the material can fail. In the case of shroud, this is the height combined with the thickness, since the shroud will be hollow with an extra reinforcement in total three plates will protect the rotors, of which the first two should be sufficient to absorb the impact, such that the HyDrone can continue its flight without to much structural damage.

This is quite a conservative way of determining the required thickness of the reinforced part of the shrouds. As said, the possibility of a frontal impact is small due to the round shape of the shroud. Furthermore, this round shape will absorb some energy as well, it is not the material only which should absorb all the energy. Last the cross-sectional area is taken the smallest, due to the shape of the shroud and to the area of the impact object, the energy will probably be dissipated over a larger area. However this shape also results in a larger frontal area of the shroud, then just its height, due to which not the full frontal area is protected. Placing the reinforcement on the top of the shroud will result in protection of the most area with the lowest slope and therefore biggest possibility of a frontal impact. Also the lower part of the shroud does not protect the propellers from frontal impact, due to the flight angle and the cross-sectional area of the shroud an impact at the lowest part from a flight path in line with that part of the shroud will be lower then the propeller.

During landing and take-off the drone will follow a vertical flight path. Assumed is that the possibility of an impact is very small, due to the low speed and the normal flight direction of birds. Furthermore if an impact would occur the impact energy would be low, resulting in little damage. Furthermore shrouds would not protect the propellers due to the flight path.

### 8.3.5 Results

To determine the thickness of the shroud, the reinforcement for the front shrouds and the beam dimensions an iterative process has taken place, with as goal to find the lowest mass. The aft two shrouds will have a cross-section with a constant thickness set to  $1.0\text{ mm}$  this is slightly higher then required, however decreasing this thickness even further would give difficulties during manufacturing [31]. The two front shrouds have in addition to this constant cross-section a reinforcement of  $15\text{ mm}$ . The beams are designed have a radius of  $15\text{ mm}$  and a thickness of  $5.5\text{ mm}$ , for manufacturing ease the beams for the front and aft shrouds are set to be equal, only minor weight savings would be possible. The weight, including the two supporting beams, of each front, impact reinforced shrouds is  $19.7\text{ kg}$ . The weight of each aft shroud is  $9.0\text{ kg}$ . The total weight of all four shrouds including reinforcements and beams is  $62.4\text{ kg}$ .

## 8.4 Cockpit

The following section will set out to describe the loading analysis performed on the cockpit so that a design could be established, starting from a aerodynamic shape and ending in a complete reinforced cockpit structure.

### 8.4.1 Shape

The shape of the cockpit was mainly determined by the decision of having a lift generating body: as an entirety the cockpit has to have an aerofoil shape. Another aspects which determines the sizing of the cockpit is the design size requirement set of  $5 \times 5m^2$ , as the shrouds have a required outer radius of  $2.2m$  the cockpit will have to sink at the very front and back so that the entire aircraft does not exceed the  $5m$  width constraint. fig. 8.10a displays a sketch of what the final structure will look like (shrouds and propellers excluded).

To give a simplistic overview of which parts the cockpit consists, an exploded view of the assembly sketch is shown in fig. 8.10b. Note that the load carrying beams are included in this drawing for the sake of completeness, but their calculations have been performed in section 8.2.



(a) Simple Sketch of Structure Assembled

(b) Exploded View Sketch of Cockpit

Figure 8.10: All Indicated Dimensions of Landing Skid

### 8.4.2 Shell

Firstly the shell of the cockpit was analysed. In principle only the load carrying beams are to carry the loads, so then the shell would only have to be able to carry its own weight. However since the design choice was made to have a lift generating body, the extra imposed forces due to the aerodynamic shape also had to be analysed. To simplify the lifting body analysis, it was treated as an aerofoil. This is a conservative assumption as the curved shapes of the body will be stronger than the simple flat plate assumption of the simplified aerofoil analysis. In fig. 8.11 a free body diagram is shown indicating the simplification of the problem.

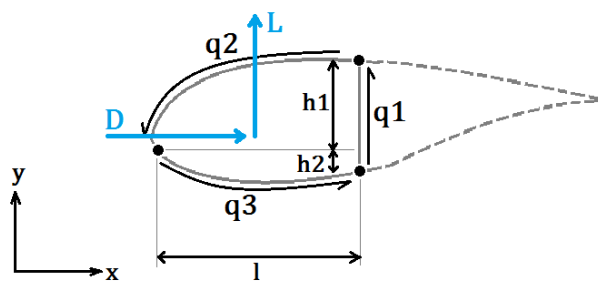


Figure 8.11: Idealised Cross Section of Body

As can be seen in the presented figure the body has been turned into an idealised aerofoil cross section (through methods described in [35]). This idealised section consists of three booms carrying the direct stresses, connected by shear stress only carrying skin panels. The skin panel through which  $q_2$  acts is the front window, the skin panel related to  $q_3$  is the bottom of the body and the skin panel carrying  $q_1$  is a reinforcing plate behind the passenger. The aft part of the aerofoil (indicated with the dotted outline) is assumed to only prevent flow separation and by itself does not carry any forces, a separate analysis is performed on this part later in this subsection. The lift,  $L$ , and drag,  $D$ , are assumed to act through the shear centre.  $q_1$ ,  $q_2$  and  $q_3$  are the shearflows induced by the applied loads. Next the following set of equations was established from the FBD (eq. (8.26)).

$$\begin{aligned}
S_x &= -q_2 \cdot l + q_3 \cdot l \\
S_y &= -q_2 \cdot h_1 - q_3 \cdot h_2 + q_1 \cdot (h_1 + h_2) \\
S_x \cdot d_x + S_y \cdot d_y &= -2 \cdot (l \cdot h_1) \cdot q_2 - 2 \cdot (l \cdot h_2) \cdot q_3
\end{aligned} \tag{8.26}$$

The first two equations follow from taking the sum of forces in x and y direction, the third equation follows from taking the sum of moments positive in clockwise direction around the bottom right boom. Here  $d_x$  and  $d_y$  are the horizontal and vertical distance from the bottom right boom to the point at which  $S_y$  and  $S_x$  act, respectively. Taking  $S_x = D$  and  $S_y = L$  and plugging in the known dimensions, the system of equations can be solved. From this follow solutions of  $q_1$ ,  $q_2$  and  $q_3$  as functions of  $L$  and  $D$ . The related shear stresses are simply found by dividing the shearflows by the thickness  $t$  of the skin through which they act. Now an iteration process can be set in motion, testing multiple values for  $t$  and seeing if the related skin shall not exceed maximum allowable shear stress of that skin.

Simply calculating the shear stresses under cruise conditions will not suffice, as the body will experience more extreme conditions than cruise. Therefore a maximum combination of  $L$  and  $D$  was plugged into the system. This combination was found by trying maximum flight velocities combined with maximum  $C_L$  and  $C_D$  values, 1.7 and 5.26 respectively (this  $C_D$  value is so high because of the induced drag, due to the extremely low aspect ratio,  $A$ , the induced drag increases drastically with increasing  $C_L$ ). It was noticed that changing the  $L/D$  ratio could impose more critical cases than having both maximum lift and drag at the same time. This is because if for example the lift is far higher than the drag, the shearflow distribution changes and will act more in a vertical plates rather than be distributed evenly over the skins. Therefore any combination of  $L$  and  $D$  was considered within their maximum values. Again the limit load case described was multiplied by a safety factor of 2.35 to find the ultimate loading.

Now that the front part of the cockpit shell has been designed, the rear part has to be analysed. As mentioned before, the aft part of the shell is assumed to not carry any of the aerodynamic loads and only has to carry its own weight. To simplify the calculations, the complicated shape of the rear part of the shell was assumed to be a clamped cone. fig. 8.12 shows the free body diagram used for the stress analysis, here  $W$  is the distributed weight and  $n$  is the load factor equal to 3.5 (note that there is a decreasing distributed weight, as the cone gets thinner and therefore weighs less as it narrows down). Fortunately this analysis could be performed by using the code produced in section 8.2.2. Only some small adjustments had to be made, but generally the problem was far more simplistic than the complex beam analysis.

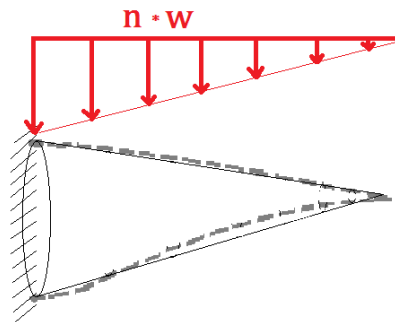


Figure 8.12: Aft Part of Shell Simplified into Polygon

### 8.4.3 Airframe

Now that the body shell was designed such that it can withstand the aerodynamic forces acting on it and the rear part does not yield under its own loading, a frame has to be designed which can carry the shell. The frame is made such that it rests on the load supporting beams, but is able to carry the entire weight of the shell in a limit load case. It is positioned just aft of the passenger, at the same longitudinal location as the reinforcing panel separating the passenger from the fuel tanks and stack. In order to perform calculations on the frame it has been simplified into a clamped arch shape with constant radius  $r$ , on which a point load acts generated by the weight of the entire shell times a load factor  $n$  (shown in fig. 8.13a).

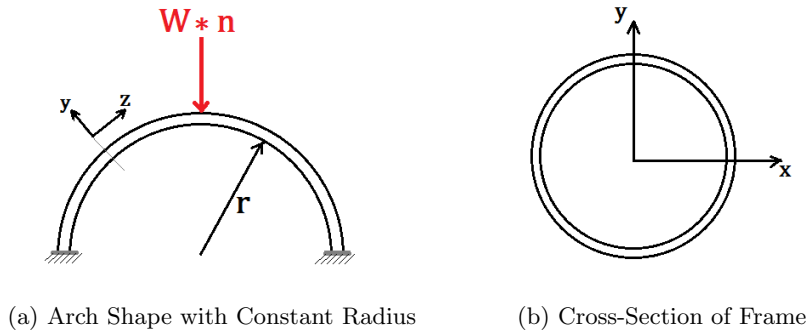


Figure 8.13: Simplified Airframe of Cockpit

This statically indeterminate system was solved through using Castigliano's theorem as described in [35] using eq. (8.27) till eq. (8.29).

$$c_i = \frac{1}{2} \int_0^l \frac{M^2}{EI} dz \quad (8.27)$$

$$c_e = - \sum F_i \cdot \Delta_i \quad (8.28)$$

$$\frac{\delta c}{\delta R} = 0 \quad (8.29)$$

Here  $c_i$  and  $c_e$  are the internal and external complementary energy, respectively.  $F \cdot \Delta$  is a force times its caused deflection, this assumed to be zero. Now taking  $\delta c = (c_e + c_i) = 0$ , the derivative of  $c$  with respect to a reaction force,  $R$ , can be taken to be zero. This allows for the system of equations to be solved.

From this method equations for the shear force, normal force and moment were found. Next the frame was analysed as having a closed thin-walled circular cross-section with variable radius and thickness (as displayed in fig. 8.13b). From this cross-section the normal stress and shear stress could be determined through eq. (8.8) and eq. (8.22) (dividing the shearflow by the thickness) respectively. Again eq. (8.20) and eq. (8.21) with a safety factor of 2.35 were used to find the ultimate stresses.

In eq. (8.8)  $M_x$  is the internal moment about  $x$ , positive when causing tension in the positive  $y$  direction.  $N$  is the normal force and  $A$  is the cross-sectional area. eq. (8.22) could be greatly simplified:  $I_{xy}$  equals 0 due to symmetry, and  $S_x$  is also 0 in the imposed analysis. The ultimate stresses were found by calculating the normal stress and shear stress for every combination of  $x$ ,  $y$  and  $z$  and taking the maximum encountered values.

Iterating the values of both the radius and thickness of the cross-section resulted in a minimum weight solution strong enough to withstand the applied loads. The decision was made to have a constant cross-section throughout the frame to reduce manufacturing complexities and thus production costs.

#### 8.4.4 Impact

For the impact reinforcement of the body the exact same methodology described in section 8.3.4 was used. The decision was made to design the entire window such that it could withstand impacts (impact strength of PMMA taken from [31]), moreover there will also be a Kevlar reinforced skin section on the nose of the body shell to ensure the safety of the passenger. In the same analogy of the shrouds reinforcement, only that part of the nose where one would expect hard impact is reinforced.

As will be evident from section 8.4.5 the impact design constraint for the window is more critical than the shear stress constraint. Thus the window thickness is determined by impact resistance rather than the shear analysis performed in section 8.4.2.

#### 8.4.5 Results

In this subsection all the results produced with the analysing methods described throughout this section are summarised. The analysis from section 8.4.2 produced the following optimised results (all mentioned thicknesses are indicated in fig. 8.14):  $t_1 = 1.4mm$ ,  $t_2 = 1.6mm$ ,  $t_3 = 2.0mm$ ,  $t_4 = 1.0mm$ .

The optimisation process of section 8.4.3 resulted in the following radius and thickness for the cross-section of the arch shaped frame:  $r = 1.4cm$ ,  $t = 1mm$ .

Lastly the analysis from section 8.4.4 to withstand bird strike impact found minimum required thicknesses of:  $t_2 = 5.5mm$ ,  $t_5 = 9mm$ . Note that the thickness of the window determined through the section 8.4.2 is overruled by the result of section 8.4.4. A summary of the mentioned results and the mass of the entire cockpit are presented in table 8.4.

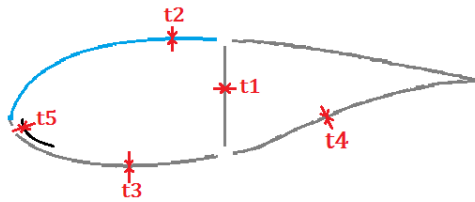


Figure 8.14: Overview of Designed Thicknesses

Table 8.4: Cockpit Analysis Results

	Parameter	Value
<b>Shell</b>	t1	1.4 mm
	t2	5.5 mm
	t3	2.0 mm
	t4	1.0 mm
	t5	9.0 mm
<b>Frame</b>	r	1.4 cm
	t	1.0 mm
<b>Assembly</b>	mass	58.3 kg

## 8.5 Landing Gear

This section will proceed where section 7.5 left off. With the required clearance and type of landing gear determined, a stress analysis could be performed in order to determine the required thickness and radius of the cross-section of the landing gear elements.

### 8.5.1 Design Loads

The FAA provides extensive conditions to which a landing gear must comply in order to be certified. [2] § 27.501 'Ground loading conditions: landing gear with skids' gives multiple different load cases under which the landing gear should not yield. One can not simply say that one of the load cases is the most critical, since they all impose different types of loads so critical values for shear stress may be found under a different load case than critical values for compressive/tensile stress. Therefore a stress analysis was performed on the skids for all of the load cases defined by the FAA, next the most critical found values throughout all the cases were used to decide the thickness and radius of the beams of the skid. The following five loading cases were deduced from [2] § 27.501:

- A: Vertical reaction loads in level attitude induced by dropping the aircraft from a height of  $0.5m$ , measured from the lowest point of the landing gear to the ground.
- B: Vertical loads plus horizontal drag loads in level attitude, taking the drag to be 50% of the load described in A. The total resultant load must equal the magnitude of vertical load in A.
- C: Vertical loads combined with horizontal side loads in level attitude. The sideloads must be considered both acting inwards and outwards and equal 25% of the load in A. The vertical load equals the load in A.
- D: One skid landing in level attitude, taking the vertical load imposed on the skid to be equal to the load described in A.
- E: Special condition: a load of 1.33 times the maximum take-off weight acting up and aft at an angle of  $45^\circ$  along the longitudinal axis of the aircraft. The load is applied only at the forward end of the skid tube.

The drop from the specified height was translated into a load by calculating the gained velocity when falling  $0.5m$  and then assuming a constant deceleration over a stroking distance of  $0.2m$  [38]. All the other described load cases are self-explanatory and follow from the first one. Only load case E differs significantly from the rest, but the description of E is also self-evident.

The imposed reaction loads were translated into internal loads through use of simple static equilibrium equations e.g. making a cut somewhere along the skid tube, imposing an internal load, and equalling the sum of forces (or moments) to be 0.

### 8.5.2 Stresses

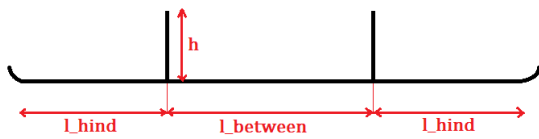
In order to transform the imposed internal loads into stresses the exact same methodology was used as in the previous section, namely: eq. (8.8), eq. (8.22)(dividing the shearflow by the thickness), eq. (8.20) and eq. (8.21) all with a safety factor of 2.35. In this analysis both the tube of the skids as well as the struts connecting the tubes to the vehicle are assumed to have a circular hollow cross-section.

### 8.5.3 Results

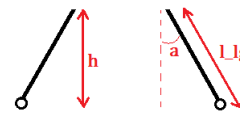
Through iteration an optimum weight saving ultimate load carrying cross-section was found for both the tubes and the struts. table 8.5 presents the complete mass of the landing gear and all the dimensions found to be optimum from the performed analysis, fig. 8.15 gives an overview of what dimensions the table refers to.  $r$  and  $t$  are the radius and thickness of the cross-section, respectively.

Table 8.5: Landing Gear Dimensions

	Parameter	Value
<b>Tube</b>	l.hind	0.53 m
	l.between	1.24 m
	r	2.3 cm
	t	1.0 cm
<b>Struts</b>	h	0.43 m
	l.lg	0.49 m
	a	30°
	r	2.1 cm
	t	1.5 cm
<b>Assembly</b>	mass	21.5 kg



(a) Side View of Landing Skid



(b) Rear View of Landing Skid

Figure 8.15: All Indicated Dimensions of Landing Skid

## 8.6 Verification & Validation

In order to verify the structural analysis software first unit tests was performed. The development of the software was already performed by programming different units which were linked together. These units provide conveniently sized blocks for the unit tests and consist of **(1)** the determination of internal forces, **(2)** the discretisation of the ellipse, for the load carrying structure only, **(3)** the calculation of the normal stresses, **(4)** the calculation of shear stresses and **(5)** the determination of the the maximum principle and shear stresses. After the unit tests some system tests were performed to ensure that the units were correctly integrated.

**Unit Tests:** **(1)** The calculation of the internal forces was verified by setting different load cases and recalculating the internal forces for different positions along the  $z$ -axis by hand using statics. This was also done for the combined transformations along several axes. **(2)** The discretisation of the ellipse was checked by evaluating the position of multiple pairs of points  $i$  and  $i + 1$ . It was checked by hand whether both these points were correctly placed on the ellipse and whether the spacing  $\delta s \approx ds$ . Additionally, it was verified that their position scales correctly with  $P$  for different positions  $z$ . **(3)** As with (1) the normal stresses were calculated by hand for given moments at several positions. **(4)** The shear flow calculation was verified by setting the same inputs as a sample problem from Megson[35] and comparing their results. **(5)** The final unit was comparing the results with hand calculations.

**System Tests:** The first system test that was performed was the zero test. By setting variables to zero one by one the change in their influence was observed. As expected setting some variables, such as  $a_j$  and  $b_j$ , to zero caused the code not to run. This was seen as acceptable since this does not occur in practice. All other variables behaved as expected. Next, variables were doubled or halved to evaluate whether the results would scale as expected. For most variables this turned out to be true. E.g. doubling forces doubled shear, moments and stresses, doubling  $V_{beam}$  quadrupled beam drag and doubling thickness approximately doubled the weight. Doubling thickness however also approximately halved the shear flow. This was unexpected, since for a constant thickness cross section the shear flow is independent of thickness. After the code was scrutinised it was found that during integration the area used in eq. (8.17) was the area  $A_j$  instead of the much larger cross-sectional area  $A_{e_j}$ , of which the latter is independent of thickness. After adjusting this, the system behaved as expected. The third system test was to test the convergence of results with decreasing the beams mesh size. It was found that decreasing mesh size beyond  $ds = 0.01$  and  $\delta z = 0.001$  would not result in a significant change in results showing only a 0.3% difference. Finally, the code was verified by calculating stresses analytically for a simplified load case.

A lack of established data of structural design in similar applications caused a need for new test data. However, due to time and resource constraints the required tests to obtain this data could not be performed. Therefore the desired validation procedure will be described. This procedure consists of two parts; the software validation and the design validation.

As a software validation several tests could be performed. The first test setup would consist of a load test of structural parts in bending, fitted with strain gauges. From the stress strain relation  $E = \sigma/\epsilon$  the stress could be determined and compared to the software results for an equal structural part. A similar test could be performed in a wind tunnel, such that the modelled drag effects are validated. The model evaluation described above does not assess whether the forces used in the model are comparable to what the HyDrone would endure during operation. This information would follow from more advanced analyses performed in cooperation with the other engineering divisions. This would include tests of scaled down models, and eventually full scale tests.

## 8.7 Sensitivity Analysis

Most the assumptions made throughout the performed analyses have purposely been conservative, to account for unexpected factors which could render the design non-feasible. Nevertheless so, it is still important to see how strongly results will deviate when input parameters are changed. Throughout this chapter quite a substantial amount of code has been produced, this section will perform an analysis on that code to investigate its sensitivity. The results of the sensitivity analysis are summarised in table 8.6. For this analysis the characteristics for which the structure was designed are tested by increasing them one by one by 10%, next the influence this has on the weight of a structural sub-system is measured. The decision was made to merely display the change in output weight (instead of e.g. shear flow and thicknesses), because this is what, in the end, matters most and plays the largest role in system integration. Note that in this analysis the sub-systems are treated as stand-alone components, e.g. the snowball effect of increasing the weight of one system on another system is not taken into account. If a certain sub-system structure analysis is not based on one of the altered input variables an 'x' is placed in the cell.

Table 8.6: Sensitivity Analysis on Structure Design

Input	Output			
	Wbeams	Wshrouds	Wcockpit	Wlanding gear
Thrust +10%	+8.24%	x	x	x
Wtot +10%	+15.36%	+1.15%	+0.88%	+8.33%
Drag +10%	+4.67%	x	+2.21%	x
Lift +10%	x	x	+0.53%	x
Impact energy +10%	x	+1.89%	+6.37%	x

Overall the weight of structural components is quite sensitive to change in input characteristics. In particular an increase in total weight has a large influence on the weight of the sub-systems, this is because for a large part the load factor of 3.5 times the weight was the critical design factor. What is interesting to deduce from this sensitivity analysis is that the weight of the load carrying beams is most sensitive to change of input parameters, this happens because the beam consists only of one part, whereas the shrouds, cockpit and landing gear are assemblies of multiple parts, so if one part increases in weight it may not have as much as an influence on the weight of the sub-system assembly.

## 8.8 Technical Risks

The evaluation of the materials and structures of the HyDrone in terms of technical risk is of major importance to ensure the safety. All subsystems listed below are evaluated and graphically represented in the technical risk map shown in table 8.7.

- |                        |                   |
|------------------------|-------------------|
| 1. Load Carrying Beams | 4. Body           |
| 2. Landing Gear        | 5. Shrouds        |
| 3. Windshield          | 6. Reinforcements |

Table 8.7: Technical Risk Map: Materials & Structures

Feasible in Theory				
Working Laboratory Model				
Based on Existing Non-Flight Engineering				
Extrapolated from Existing Flight Design			4, 5	1
Proven Flight Design		6	2, 3	
	Negligible	Marginal	Critical	Catastrophic

---

**Load Carrying Beams** The CFRP load carrying beams are of major importance for flight. In case of failure one or more coaxial rotor systems can become uncontrollable or even completely lost, which will result in a crash landing. Failure of the load carrying beams would be catastrophic. The four rotor system configuration is not common used in passenger carrying aerospace, however often present in smaller drones. Although The use of CFRP in aerospace industry is relative new, it is shown that the use of composites in load carrying structures work well by among others the Boeing 787 [41]. When the load carrying structure fail landing should start immediately

**Landing Gear** Aluminium skids are widely used in the helicopter industry. Failure of the skids during landing may result in severe damage to the body, shrouds, electric motors and propellers. Also the possibility of injury to the passenger is present in case of a heavy landing. When the landing gear is failed, extra controlled and soft landing should be performed to minimise damage.

**Windshield** PMMA windshields are widely used in the aviation industry [42]. Failure of the windshield would result in reduced flight performance and reduced passenger protection against external objects. In case of failed windshield flight velocity should be lowered and landing should be started as soon as possible to reduce the possibility of impact and its effects.

**Body** The composite body, just like the windshield, protects against external object and assures an efficient flight. In case of failure performance reduce and passenger may be less protected, landing should be started as soon as possible. Although little passenger rotorcopters have a composite fuselage, the KC 518 [43]has proven flight possibilities.

**Shrouds** The shrouds protect the electric motors and propellers against external impact and improve aerodynamic performances. Failure would decrease performance and protection. In case of deformation the shroud may damage the propellers, decreasing the performance further and enforce landing. Shrouded engines are not very common in the aerospace industry. Some composite shrouded propellers are existing, for example the Airbus E-fan, multiple helicopter tail rotors, although the configuration is different. Furthermore smaller drones sometimes have shrouds.

**Reinforcements** The aramid reinforcement protect the HyDrone against external impact. In case of failure, the passenger or a propeller can be less protected. Flight velocity should be lowered and landing should be started as soon as possible. Aramid fibre reinforcement is used in among other the Boeing 787 Dreamliner and the Airbus A350XWB

## 8.9 Recommendations

To improve the design material and structural design of the HyDrone all materials and structures should be analysed more in depth, below a overview of the proposed analysis.

- Strong simplifications are made during the structural analysis, especially at the shrouds and cockpit. For a more accurate analysis a finite element analysis should be performed.
- Dynamic loading cases should be analysed in more detail.
- The deflection of structural parts should be analysed. Special focus on the load carrying structure. Large deflection can cause failure, smaller deflection may cause deflected thrust directions.
- A detailed vibrations analysis should be done, in order to make sure the electric motors and propellers do not rotate with a frequency equal to an eigenfrequency of a structural component.
- A fatigue analysis should be performed. An investigation of the degradation of the material over time should be done in order to produce a proper maintenance plan.
- A more elaborate analysis on the reinforced impact structure should be performed. Taking into account the geometry of the structure.
- Protection against released propeller blades should be investigated.
- The assembly of the structural parts should be investigated as well as its influence. This includes assemble of the shrouds, propellers, electric motors, floor and body to the load carrying beams.
- Interior design should be further analysed. Support and placing of the floor and of various interior parts.
- More thorough investigation in materials should be done. More materials should be compared to optimise cost and weight.
- The manufacturability of materials should be further investigated. Materials may or may not be suited for production of the part for which they are selected. This may influence weight and cost.
- The influence of both everyday and extreme weather conditions on the material should be investigated in more dept.

# Chapter 9: Propulsion

The design process of the HyDrone’s propulsion system has been described in this chapter, where Section 9.1 presents a general overview of shrouded and coaxial rotors. The theory used to calculate the thrust and induced power of a single coaxial rotor system has been explained in section 9.2. The rotors were designed based on the given theory, where the results have been scrutinised in section 9.3. The verification and validation strategy has been presented in section 9.4. The technical risk map and subsequent analysis can be found in section 9.5. Recommendations for further improvements have been described in section 9.6.

## 9.1 Ducted Coaxial Rotor System

The propulsion system of the final design consists of four coaxial contra-rotating rotor systems, leading to a total of eight rotors. A major benefit is that the total thrust produced by a coaxial rotor system is greater than the output of a single rotor of the same diameter and for the same power. Another benefit is that this configuration presents a feasible redundancy strategy, where the drone is still capable of flying in the event of rotor failure. Each rotor has two blades and the same diameter, where each coaxial system is shrouded in a vertical duct, which increases the thrust, reduces noise and can be perceived as an added safety measure. Shrouding the coaxial systems does add to the weight and can impede the aerodynamic efficiency of the final product when in cruise flight. The benefits are mostly observed during climbing and hovering flight. [44]

## 9.2 Blade Element Momentum Theory (BEMT)

The Blade Element Momentum Theory (BEMT) incorporates the fundamental principles of Blade Element Theory and Momentum Theory, thus allowing for a preliminary analysis of the aerodynamic performance of a rotor. This requires a numerical approach, whereby the rotor is divided into a finite number of annuli, after which the individual thrust and induced power contributions from each annulus are determined and added up to obtain the total thrust and induced power. It is assumed that successive annuli have no mutual effects on each other, thus implying that the rotor blades are modelled as two dimensional aerofoils which generate aerodynamic forces. One can see this as a form of lifting-line theory, but applied to rotating wings. [7] [45]

This method can also be applied to a coaxial rotor configuration, along with some further assumptions. Namely, one must take into account how the slipstream caused by the upper rotor affects the flow into the lower rotor. The more realistic scenario would be to assume that the lower rotor operates partly in the fully developed slipstream of the upper rotor, as depicted in fig. 9.1. The ideal case is when the contracted wake area  $A_{con}$  is half the total area  $A$  of the rotor, which is due to the assumption that the flow at the upper rotor is not affected by the lower rotor. In practice, the contracted area would be smaller, given that this is an ideal assumption. [45]

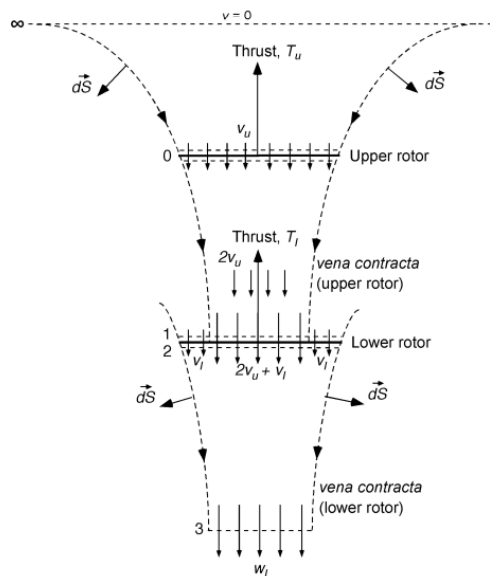


Figure 9.1: Flow Model of Coaxial Rotor System [45]

The following derivations have been extracted from *Leishman & Ananthan* [45]. When considering the upper rotor, the incremental mass flow rate through an annulus is given as follows.

$$dm = \rho(V_\infty + v_u)dA = 2\pi\rho(V_\infty + v_u)ydy \quad (9.1)$$

Equation (9.1) can then be used to establish an equation for the incremental thrust, which is a product of the mass flow rate and the slipstream velocity from the upper rotor, which in this case is twice the induced velocity ( $2v_u$ ).

$$dT_u = \rho(V_\infty + v_u)dA \cdot (2v_u) = 4\pi\rho(V_\infty + v_u)v_u ydy \quad (9.2)$$

Equation (9.2) can then be expressed in non-dimensional terms, as given below.

$$dC_{T_u} = \frac{1}{\rho(\pi r_R^2)(\Omega r_R)^2} dT_u = \frac{2\rho(V_\infty + v_u)v_u}{\rho(\pi r_R^2)(\Omega r_R)^2} dA = \frac{2\rho(V_\infty + v_u)v_u}{\rho(\pi r_R^2)(\Omega r_R)^2} (2\pi ydy) \quad (9.3)$$

Given that  $\lambda_\infty = \frac{V_\infty}{\Omega r_R}$ ,  $\lambda_u = \frac{v_u}{\Omega r_R}$ ,  $\lambda = \lambda_\infty + \lambda_u$  and  $rdr = \frac{1}{r}ydy$ , eq. (9.3) can be expressed as follows.

$$dC_{T_u} = 4\lambda\lambda_u r dr = 4\lambda(\lambda - \lambda_\infty)r dr \quad (9.4)$$

A correction factor, known as the Prandtl tip-loss function, can be applied to eq. (9.4) in order to account for blade tip losses. However, given that the coaxial rotor systems will be shrouded, the tip losses are considered to be negligible. Therefore, this correction factor has not been implemented.

According to blade element theory, the incremental thrust can be expressed as given in eq. (9.5), where  $\sigma = \frac{N_b c}{\pi r_R}$ . The chord length has been kept constant throughout the length of each rotor blade, given that the shroud around each coaxial system reduces the tip losses, thus allowing the blade tips to generate more thrust.

The ideal pitch distribution has been applied to the upper rotors (as well as the lower rotors), which is expressed as  $\theta_u = \frac{\theta_{u,tip}}{r}$ . This assumption leads to a uniform inflow over the rotor, which is an ideal condition.

$$dC_{T_u} = \frac{1}{2}\sigma C_{l_\alpha} r^2 dr = \frac{\sigma C_{l_\alpha}}{2}(\theta_u r^2 - \lambda r) dr \quad (9.5)$$

Given that equations 9.4 and 9.5 are equivalent (momentum theory and blade element theory respectively), an expression for  $\lambda$  can be derived.

$$\lambda(r, \lambda_\infty) = \sqrt{\left(\frac{\sigma C_{l_\alpha}}{16} - \frac{\lambda_\infty}{2}\right)^2 + \frac{\sigma C_{l_\alpha}}{8}\theta_u r} - \left(\frac{\sigma C_{l_\alpha}}{16} - \frac{\lambda_\infty}{2}\right) \quad (9.6)$$

Having established an expression for  $\lambda$ , one can numerically integrate eq. (9.4) over a finite number of sections in order to find the thrust coefficient. The induced power coefficient can also be determined, as is evident below.

$$C_{T_u} = \int_{r=0}^{r=1} dC_{T_u} = 4 \int_0^1 \lambda\lambda_u r dr = 4 \int_0^1 \lambda(\lambda - \lambda_\infty)r dr \quad (9.7)$$

$$C_{P_u} = \int_{r=0}^{r=1} \lambda_u dC_{T_u} = 4 \int_0^1 \lambda\lambda_u^2 r dr = 4 \int_0^1 \lambda(\lambda - \lambda_\infty)^2 r dr \quad (9.8)$$

Using equations 9.7 and 9.8, one can determine the total thrust delivered by the upper rotor and the total induced power.

$$T_u = C_{T_u} \rho A \Omega^2 r_R^2 \quad (9.9) \quad P_u = C_{P_u} \rho A \Omega^3 r_R^3 \quad (9.10)$$

A similar analogy as presented above is applicable to the lower rotor. However, one has to consider the the inflow distribution within the slipstream and outside the slipstream separately. The blade pitch distribution of the lower rotor is also ideal, hence  $\theta_l = \frac{\theta_{l,tip}}{r}$ . The lower rotors have the same solidity  $\sigma$  as the above rotors, given that the blades have the same constant chord lengths.

Therefore, for  $r < r_c$ , the inflow distribution is given as follows.

$$\lambda(r, \lambda_\infty) = \sqrt{\left(\frac{\sigma C_{l_\alpha}}{16} - \frac{\lambda_\infty + (A/A_{con})\lambda_u}{2}\right)^2 + \frac{\sigma C_{l_\alpha}}{8}\theta_l r} - \left(\frac{\sigma C_{l_\alpha}}{16} - \frac{\lambda_\infty + (A/A_{con})\lambda_u}{2}\right) \quad (9.11)$$

For  $r > r_c$ , the inflow distribution is given by eq. (9.12).

$$\lambda(r, \lambda_\infty) = \sqrt{\left(\frac{\sigma C_{l_\alpha}}{16} - \frac{\lambda_\infty}{2}\right)^2 + \frac{\sigma C_{l_\alpha}}{8}\theta_l r} - \left(\frac{\sigma C_{l_\alpha}}{16} - \frac{\lambda_\infty}{2}\right) \quad (9.12)$$

Equations 9.11 and 9.12 can then be used to determine the thrust delivered by the lower rotor, along with the induced power. Finally, the total thrust and induced power of a single coaxial rotor system can be determined by adding up the individual thrust and induced power values of the individual rotors.

## 9.3 Rotor Design

Four critical flight conditions have been considered when applying BEMT, namely climbing flight, hover, cruise and take-off. These four conditions have been examined in order to determine the necessary load and power requirements that allow the drone to successfully fulfil its flight tasks. There would almost certainly be discrepancies between theoretical and hypothetical experimental results, given that a significant number of assumptions have been made when applying the theory given in section 9.2. It should be noted that only an individual coaxial rotor system is examined when applying BEMT, which has led to the assumption that each coaxial system operates at exactly the same thrust and induced power. The results from applying BEMT have been presented in table 9.1, giving the total thrust output and the induced power required to generate the necessary thrust for each flight condition.

Table 9.1: Total Thrust and Power

Flight Condition	Total Thrust [ $N$ ]	Total Power [ $kW$ ]
Accelerating	6376	91.432
Climb	6056	87.296
Cruise	5256	71.128
Hover	5576	76.768

The more realistic operational condition of a coaxial rotor system is when there is a torque balance between the upper and lower rotors, which implies that the rotors are operated at the same induced power ( $P_u = P_l$ ). The required thrusts for each flight condition were initially determined in order to calculate the induced power, based on the fact that each coaxial system is torque balanced.

The hover condition simply requires that the total thrust delivered is equal to the weight of the vehicle, whereas climbing and accelerating flight require a greater thrust output, due to the added influence from the vertical drag. Given that the body of the HyDrone generates lift itself, less thrust is required for level cruise flight. However, in case the aerodynamic efficiency of the lifting body is hindered, the necessary thrust required to compensate for this loss can be delivered, given that the total required power is below the available power of  $111.2kW$  (which is the maximum available power multiplied by the controller and engine efficiency, see section 10.3.3).

It should also be noted that three coaxial systems are capable of producing enough thrust to keep the HyDrone in either cruise or hovering flight. In the event one of the coaxial rotor systems fails during cruise flight, the remaining systems will each require an induced power of  $27.1kW$  to generate enough thrust ( $1752N$ ), whereas an induced power of  $30kW$  per rotor system would be required in order to maintain enough thrust for hovering flight ( $1859N$ ). Multiplying the above power values by three subsequently gives the total induced power required for the given flight conditions, which are both below the threshold of  $111.2kW$ .

The BEMT input parameters that have been kept constant for both rotors (aside from the blade tip pitch angle) are given in table 9.2. The two dimensional lift curve slope  $C_{l_\alpha}$  has been based on the *ARA – D 10%* propeller aerofoil<sup>1</sup>. It is assumed that the rotors do not generate thrust below the minimum radius, due to the presence of the rotor hub. The main limiting factor when determining the number of blades  $N_b$  and the chord length  $c$  was the mass, given that this had to be kept to a minimum whilst implementing sufficient thrust generating capabilities. Given that the selected *ARA – D 10%* propeller aerofoil has a thickness to chord ratio of 10%, the maximum thickness of each blade is then  $0.015m$ , knowing that each blade has a chord length of  $0.15m$ . A single rotor blade has a mass of about  $3.20kg$ , given that its maximum dimensions are  $0.15m \times 0.015m \times 0.9m$  and that each blade is made of carbon fibre, which has a density of approximately  $1580kg/m^3$  (see table 8.1). There are 16 rotor blades in total, adding up to and overall mass of around  $51.20kg$ . It should be noted that this is a conservative estimate, given that the maximum thickness of the aerofoil was used to determine the volume.

Table 9.2: BEMT Constant Inputs (Single Coaxial System)

Blade Chord Length $c$ [ $m$ ]	Lift Curve Slope $C_{l_\alpha}$ [ $1/rad$ ]	Number of Blades $N_b$ [ $-$ ]	Minimum Radius $R_{Min}$ [ $m$ ]	Maximum Radius $R_{Max}$ [ $m$ ]	Upper Blade Tip Pitch $\theta_{u,Tip}$ [ $^\circ$ ]
0.15	5.73	2	0.05	0.95	4

The inputs that vary per flight condition can be found in table 9.3. The blade pitch distribution has been established according to the ideal pitch distribution, namely  $\theta = \frac{\theta_{tip}}{r}$ . In practice, this type of distribution is

<sup>1</sup><http://airfoiltools.com/airfoil/details?airfoil=arad10-il> [cited 22-06-2017]

not feasible, given that the blade pitch reaches absurdly high angles closer to the root. For this reason, a tip pitch threshold of  $4^\circ$  has been established in order to mitigate this phenomenon. The upper blade tip pitch angle  $\theta_{u,Tip}$  was kept constant at  $4^\circ$  for each flight condition, given that this significantly increases the available thrust. A variable pitch system has been designed in section 11.1, thus giving the option to change the blade pitch in order to satisfy the thrust and power requirements of the critical flight conditions. It should be noted that the pitching system is not compatible with the ideal pitch distribution, given that only a constant change in the pitch angle along the length of a blade is possible. If one were to follow something more in line with the ideal pitch distribution, each blade would have to be divided into a finite number of sections and have an individual pitching system, such that each section of a blade can have a different change in pitch angle. This would be a very complex solution and has therefore been ruled out.

Table 9.3: BEMT Variable Inputs (Single Coaxial System)

Flight Condition	Inlet Velocity $V_\infty$ [m/s]	Revolutions per Minute [RPM]	Critical Flight Altitude [m]	Air Density $\rho$ [kg/m <sup>3</sup> ]	Lower Blade Tip Pitch $\theta_{l,Tip}$ [°]
Accelerating	5.909	2568	0 (sea level)	1.225	3.46
Climb	11.818	2022	650	1.150	2.72
Cruise	11.818	1790	650	1.150	3.12
Hover	0	2816	650	1.150	3.47

Take-off is assumed to occur at sea level, which is why accelerating flight is initiated at an air density of  $1.225\text{kg/m}^3$ . The other three flight conditions have all been examined for an altitude of  $650\text{m}$ , which is slightly above the required minimum cruise flight altitude according to the flight regulations presented in section 6.3. The inlet velocity required for accelerating flight was assumed to be half of the inlet velocity for non-accelerating climbing flight, given that the velocity changes over time. When observing the RPM values given in table 9.3, it is evident that the cruise condition requires a much lower rate than the other conditions, given that less thrust is required due to the lifting body. The maximum available RPM of 3500 is limited by the motor, a *Joby JM2*<sup>2</sup>. However, the maximum allowable RPM is limited by the relevant aircraft noise regulations, given that the tip velocity of the rotor is the most significant contributor to the overall noise produced by a rotorcraft [7].

The main limitation of BEMT is that the three dimensional aerodynamic characteristics of the blades and rotors are not taken into account. One can assume that the blades are two dimensional aerofoils, which is less accurate but also requires less rigorous analysis. The vertical distance between the upper and lower rotors is also not factored into BEMT, only the contracted slipstream wake area on the lower rotor. According to *Florent* [46], the distance between the upper and lower rotor is typically somewhere between 10% and 20% of the rotor radius. Increasing the distance between the rotors reduces the contracted wake area, thus decreasing the interference power loss [7]. For this reason, a vertical distance of  $20\text{cm}$  between the lower and upper rotors has been selected. This is also the safest option when adhering to the given range, due to the possibility of a blade coming loose and affecting the other working rotor.

## 9.4 Verification & Validation

Verifying the Matlab code used to estimate the thrust and induced power was simply a matter of checking whether the rotor analysis method had been implemented correctly. BEMT is an iterative process when applying the Prandtl tip-loss function, which accounts for the blade tip losses [45]. In this case, the correction factor was neglected due to the presence of the shrouds, which nearly eliminates the tip losses. Therefore, the total thrust and induced power of each critical flight condition were solved numerically without having to iterate the process for the correction factor. The process was iterative in the sense that the inputs were altered until the desired results were obtained.

Validating the results from table 9.1 is complicated, given that no rotor analysis software exists that allows one to model rotors in a coaxial configuration. Certain interactive programmes such as *X-Rotor* can be used to examine the performance of rotors and rotary wings, but are not compatible with coaxial rotor systems. Examining the upper and lower rotors individually would not be practical, given that the lower rotors operate partly in the fully developed slipstream of the upper rotors. Therefore, with regard to the lower rotors, the areas within and outside the contracted wake area would have to be analysed separately. *X-Rotor* allows one to use the required thrust as input for a single rotor, but when considering a pair of rotors in a coaxial configuration, one is primarily concerned with the combined output.

<sup>2</sup><http://www.jobymotors.com/public/views/pages/products.php> [cited 22-06-2017]

The results from table 9.1 could also be validated against experimental data, which would require carbon fibre rotor blades, with the same specifications as given in table 9.2 and table 9.3, that have been tested in a controlled environment. The calculations have been made without having considered the body of the HyDrone, which is why testing a single coaxial rotor system with the necessary physical characteristics would be sufficient to validate the results presented in section 9.3.

## 9.5 Technical Risks

The list given below presents the relevant components of the propulsion subsystem, which have been placed in a risk map according to how the flight performance of the HyDrone could be affected in case of failure. As is evident in table 9.4, none of the components appear in the red section of the map, given that a rigorous risk mitigation strategy has been implemented.

1. Coaxial Rotor System.
2. Shroud.
3. Carbon Fibre Blade.
4. *Joby JM2* Motor.

Table 9.4: Technical Risk Map: Propulsion

Feasible in Theory				
Working Laboratory Model		4		
Based on Existing Non-Flight Engineering				
Extrapolated from Existing Flight Design		2		
Proven Flight Design		3	1	
	Negligible	Marginal	Critical	Catastrophic

Coaxial rotor systems are a proven flight concept and have been implemented in aircraft such as the *Kamov Ka-50* and the *Ehang 184*. In the event that one of the four coaxial systems fails during flight, the remaining three rotor systems will still be able to generate enough thrust that allows the HyDrone to land safely. Such a situation is considered to be a critical event, given that landing procedures would have to be taken into effect as soon as possible, which may not be possible due to a lack of available space on the ground.

Certain contemporary small sized quadcopters are equipped with shrouds, but applying them to a passenger drone has not been done before. Therefore, this concept has been extrapolated from existing flight designs, given that the HyDrone requires significantly larger shrouds than the available drones on the market. The shrouds are meant to increase the overall propulsive efficiency, reduce the noise and are also an added safety measure.

Composite materials such as carbon fibre are commonly used to construct rotary wings, which is why this is considered to be a proven flight design. In the event that a rotor blade comes loose during flight, the damage suffered by the coaxial rotor system and the duct will likely be less than if it were an aluminium or titanium blade of the same size, given that the carbon fibre blades would be much lighter.

The *Joby JM2* motor is specifically designed for electric aircraft, but has not been tested in flight, hence why it is a working laboratory model<sup>3</sup>. Each rotor is driven by an individual motor (eight motors in total) in order to ensure that no more than one rotor is affected in the event a single motor fails. Given that the HyDrone is capable of landing safely when only three of the coaxial rotor systems are in operation, two of the eight motors can fail without significantly endangering the passenger.

## 9.6 Recommendations

More advanced rotor analysis models exist, given that many simplifying assumptions have to be made in order to apply BEMT. One such model is the Finite Volume Method (FVM), which requires more computational power and could be used to validate the BEMT results.

The coaxial rotors and shrouds were examined separately and not as an integrated system. It should be noted that the blade tip losses were assumed to be negligible when applying the BEMT, due to the presence of the shrouds. However, the slipstream was assumed to be unaffected by the shroud, when in practice this is not the case. The effects the shrouds have on the propulsion system's performance were only examined qualitatively.

<sup>3</sup><http://www.jobyaviation.com/S2/> [cited 22-06-2017]



---

# Chapter 10: Power

In this chapter the power subsystem of the HyDrone will be worked out. In the previous phase of this Design Synthesis Exercise it was decided to implement a hydrogen fuel cell (HFC) in the design as this would be the best power subsystem suited for the HyDrone. A relatively long endurance can be achieved with a HFC without emitting any harmful substances.

First of all, it must be defined what the power subsystem must achieve. This is explained in section 10.1. Next, the basics of how a hydrogen fuel cell works, are described in section 10.2. Then, all different components of the power subsystem were analysed and a specific type was chosen in section 10.3. After that, in section 10.4 the various safety measures in the power subsystem are highlighted and the overall safety of this subsystem is justified. Furthermore, the technical risks concerning the power subsystem are laid out in section 10.5 and finally the recommendations to improve the design of the power subsystem are presented in section 10.6.

## 10.1 Required Power & Energy

In section 9.3 the method to calculate the required power for propulsion in each flight phase was explained. This is by far the largest subsystem regarding power consumption, but some other systems have to be powered as well: the climate control/air conditioning, the control subsystem, the user interface and the PCU for instance. The air conditioning is responsible for a large portion of the power not needed for propulsion. It is infamous for using up to 5 kW compared to 500 W for other subsystems[47]. A local air conditioning unit in direct contact with the passenger could reduce this power consumption for the HyDrone to below 700 W<sup>1</sup>. Many different types of sensors and actuators continuously have to be operated. Referring to section 11.2, It was assumed that in the worst case scenario 5 RADARs, 5 LIDARs and 1 GPS are operated at the same time. This comes down to a total continuous power consumption of 220 W. Another 80 W is required to operate the PCU (see section 10.3.4. Furthermore, the blade pitch system was assumed to operate nominally at 400 W in total. When changing the blade pitch, it consumes a maximum of 1600 W, bringing the total nominally required power and total maximum required power for all subsystems besides propulsion to 1.4 kW and 2.6 kW respectively. The first is the nominal accessory power which is multiplied by the mission time to find the total required energy to operate the systems besides propulsion later in this section. The second is the maximum accessory power and is used to find the best suited stack (see section 10.3.3). For a clear overview of the power of all subsystems, please refer to table 16.2.

The maximum power is relevant to determine the optimum fuel tank. However, this does not dictate the required size of the hydrogen fuel tank. To determine this, the required energy was needed. The energy of each flight phase could simply be found using eq. (10.1).

$$E_{phase} = P_{phase} \cdot t_{phase} \quad (10.1)$$

The required energies for each phase are given in table 10.1. The given values are for a single cycle.

Table 10.1: Required Power & Energy

Phase	Power [kW]	time [s]	Energy[kWh]
Acceleration	91.4	10	0.25
Climb	87.3	50	1.21
Cruise	71.1	750	14.82
Descent	76.8	120	2.56
Other	1.43	930	0.37
Total			19.21

The nominal mission profile contains four cycles. So multiplying the total energy by four gives the energy required for the total nominal mission profile, 76.9 kWh. However, this value assumes 100% efficiency of the power subsystem, which is obviously not true. When all components were selected the total power subsystem efficiency was found to be 44.2%. This is a multiplication of the individual component's efficiencies as presented in eq. (10.2).

$$\eta_{total} = \eta_{BoP} \cdot \eta_{stack} \cdot \eta_{PCU} \cdot \eta_{motors} \quad (10.2)$$

These efficiencies will be explained in the section 10.3. Dividing the previously mentioned nominal mission profile power by the total efficiency gives a total required energy of 173.8 kWh. This is the amount of chemical

---

<sup>1</sup><http://www.electric-vehiclenews.com/2009/06/how-to-power-heating-and-ac-in-electric.html>, [cited 12-06-2017]

energy that must be stored in the hydrogen. Hydrogen has a specific energy of  $39.443 \text{ kWh/kg}^2$ . Dividing these values yields a total required hydrogen mass of  $4.41 \text{ kg}$ . The next section will explain how this hydrogen is used to generate power and produce water.

## 10.2 Hydrogen Fuel Cell Basics

A hydrogen fuel cell generates power through the reverse electrolysis of water. This means that hydrogen and oxygen chemically react with each other to form water and electricity. A proton exchange membrane (PEM) fuel cell has the highest efficiency of up to 60%<sup>[48]</sup>. A setup of a PEM fuel cell is illustrated in fig. 10.1<sup>3</sup>. As PEM fuel cells have the highest efficiency they are best suited for the HyDrone.

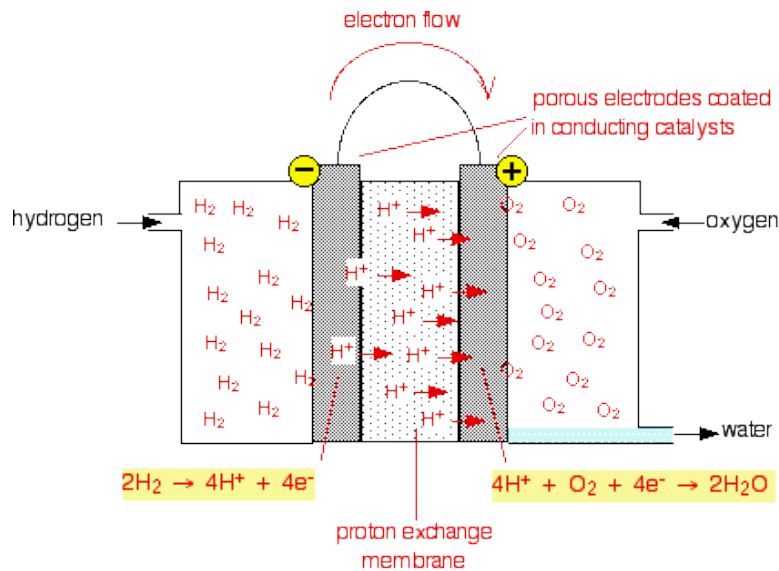


Figure 10.1: Proton Exchange Membrane Fuel Cell

Combining the anode (oxidation) and cathode (reduction) reactions results in the following net redox reaction:



This means that two moles of dihydrogen react with a single mole of dioxygen to form two moles of water. So for every mole of dihydrogen a mole of water is produced. One mole of dihydrogen weighs  $2.016 \text{ g}$  and one mole of water weighs  $18.016 \text{ g}$ . In other words, for every  $2.016 \text{ g}$  of used hydrogen  $18.016 \text{ g}$  of water is produced. The total mass of the produced water was then calculated with eq. (10.4).

$$m_{\text{H}_2\text{O}} = m_{\text{H}_2} \frac{18.016}{2.016} \quad (10.4)$$

In section 10.1 it was determined that  $4.41 \text{ kg}$  of hydrogen was needed to generate enough electric energy to successfully fly the nominal mission profile. Filling this value into eq. (10.4) yields  $39.4 \text{ kg}$  of produced water.

## 10.3 Hydrogen Fuel Cell Components

There are many components required to have a fully operational hydrogen power subsystem. A schematic sketch of the whole subsystem is given in fig. 10.2.

On the far left side of the schematic are the only two non-electrical components. The hydrogen from the fuel tank and oxygen from the air flow in a gaseous state through the balance of plant (BoP) and into the stack. Many small fuel cells are stacked very close to each other here to maximise the membrane surface area while keeping the volume as low as possible. The gasses react as explained in section 10.2 to form electricity. If necessary, the electric voltage is cranked up to the voltage that the electric motors run on. This high voltage electricity is controlled and distributed by the power control unit (PCU). A small portion of the power is needed by other systems such as the climate system and the sensors form the control subsystem. By far the largest part of the power is used by the electric motors in the propulsion subsystem. In case of a HFC failure (anywhere left

<sup>2</sup><http://www.h2data.de>, [cited 13-06-2017]

<sup>3</sup><http://www.chemguideforcie.co.uk/2016section6/learning6p4a.html>, [cited 09-06-2017]

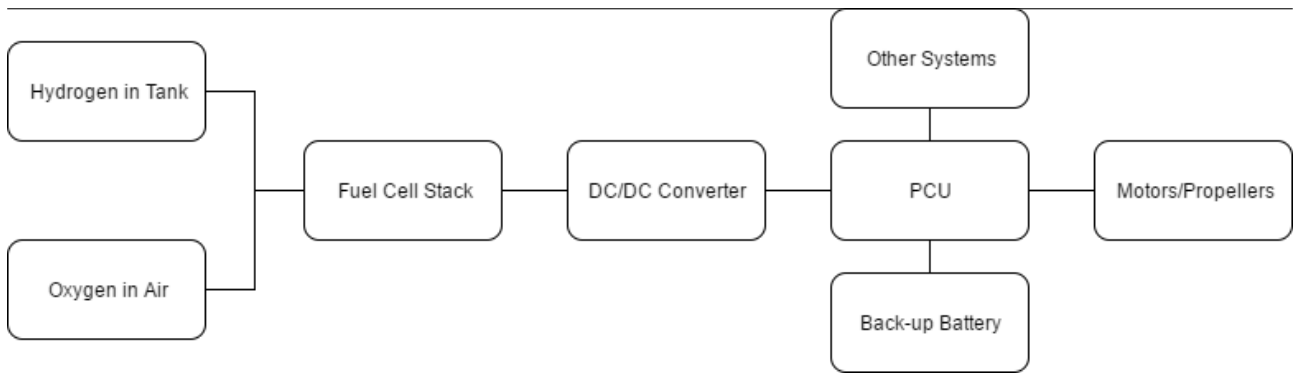


Figure 10.2: Electric Block Diagram

of the PCU in fig. 10.2), the backup battery comes in as an alternative power source, which can be used to safely land the HyDrone. All of these components will be elaborated on in more detail in the following subsections.

### 10.3.1 Hydrogen Fuel Tank

The first HFC was demonstrated as early as 1839<sup>4</sup>, but it was not implemented in a vehicle until 2015 in the Toyota Mirai. This is mainly because the vehicles requires a lot of power and energy relatively while there is not much space available and weight must be minimised. Only recently the gravimetric- and volumetric density of hydrogen storage cylinders have increased. It is now possible to safely store hydrogen at 700 bars and achieve a gravimetric density of 5.7%[49]. A rather simple stress analysis was performed to investigate if a theoretical pressure vessel design could possibly outperform an existing design. If this were to be the case, the hydrogen fuel tank could be designed by the design team itself. A 700 bar cylindrical fuel tank with spherical end caps produced by Hexagon Composites has an empty mass of 43 kg, a length of 845 mm and an inner radius,  $r_i$ , of 210 mm. The stresses in a theoretical design of the same dimensions were investigated, starting of with the hoop stress at the inside of the cylindrical part, which is the critical stress in the critical location of this design. This was done using eq. (10.5)<sup>5</sup>.

$$\sigma_{hoop} = \frac{P_{tank} (r_i^2 - r_o^2)}{r_o^2 - r_i^2} \quad (10.5)$$

It was assumed that the tank is made of carbon fibre reinforced polymer (CFRP) and that the fibres are placed unidirectional (UD) in the circumferential direction. The ultimate tensile stress of UD carbon fibre is 1500 MPa<sup>6</sup>. CFRP type 4 pressure vessels are designed with a minimum burst ratio of 2.35 according to ISO 11439. This means that the tank has to be designed for a pressure,  $P_{tank}$ , of at least 1645 bar in stead of 700 bar. Rewriting the equation for the outside radius,  $r_o$ , and filling in this pressure results in an outside radius of 0.2344 m. This yield a thickness of 0.0244 m. The mass of the cylindrical structure looking purely at hoop stress was then calculated with eq. (10.6), assuming a CFRP density of 1600 kg/m<sup>3</sup>.

$$m_{cylindrical} = \rho_{CF} \frac{r_i + r_o}{2} 2\pi t_{tank} (l_{tank} - 2r_o) \quad (10.6)$$

This results in a mass of 20.5 kg The second mass component to be analysed is the unidirectional carbon fibres that carry the axial stress. This stress is calculated with eq. (10.7).

$$\sigma_{axial} = P_{tank} \frac{r_i^2}{r_o^2 - r_i^2} \quad (10.7)$$

This equation was rewritten to find the required outside radius, which was determined to be 0.2212 m, corresponding to a thickness of 11.5 mm. The mass of the CFRP was found using eq. (10.6) again. This resulted in a mass of 9.4 kg. The stresses in the radial direction are assumed to be taken up by the resin of the CFRP and is therefore not further worked out. Additionally the thicknesses of the circumferential and axial are assumed not to influence each other. The masses of these two layers are simply added up to find the total mass of the cylindrical part, which then is 29.9 kg.

The stresses in the spherical end caps are the final stresses to be analysed. In reality, the stresses in the end caps do occur in every direction, but for simplicity the CFRP is assumed to be uniform or equally strong in every direction. The thin walled assumption is also assumed. The stress can then be calculated with eq. (10.8)[50].

<sup>4</sup><http://www.sae.org/fuelcells/fuelcells-history.htm>, [cited 09-06-2017]

<sup>5</sup><http://www.mydatabook.org/solid-mechanics/stress-for-thick-walled-cylinders-and-spheres-using-lames-equations/>, [cited 07-06-2017]

<sup>6</sup>[http://www.performance-composites.com/carbonfibre/mechanicalproperties\\_2.asp](http://www.performance-composites.com/carbonfibre/mechanicalproperties_2.asp), [cited 07-06-2017]

$$\sigma_{sphere} = \frac{P_{tank} r}{2t_{tank}} \quad (10.8)$$

Rewriting this for the thickness yields virtually the same thickness as for the axial stress in the cylindrical section, 11.5 mm. This is concordance with the thin walled assumption.  $\nu_t = 18.2$  so the thin walled assumption is valid. The mass of the end caps with this thickness of 11.5 mm can be calculated with eq. (10.9)

$$m_{endcaps} = \rho (r_o + r_i)^2 \pi t_{tank} \quad (10.9)$$

This yields a mass of 10.8 kg and thus a total tank mass of 40.7 kg. In reality the mass of the end caps will be larger as there must be multiple layers of fibre in different directions. Usually these kind of pressure vessels are manufactured with filament winding. It is remarkable that Hexagon Composites has been able to manufacture a carbon fibre type 4 pressure vessel of 43 kg, which includes a reinforced valve. This is just slightly higher than the ambitious theoretically calculated value of 40.7 kg. Because of this and the fact that companies sell certified pressure vessels it was determined that a hydrogen fuel tank could best be bought of the shelves of specialised companies.

Next, a literature study was performed to find the hydrogen fuel tank that will be installed in the HyDrone. An overview of several different 700 bar hydrogen cylinders on the market is given below in table 10.2.

Table 10.2: Hydrogen Fuel Tanks on the Market

Tank	Company	Empty Mass (kg)	Volume (L)	H2 Capacity (kg)	%wt
A	Hexagon Composites[49]	43	64	2.6	5.7
B	MAHYTEC[51]	17	20	0.81	4.5
C	MAHYTEC/Holthausen <sup>7</sup>	38	37	1.5	3.8
D	Holthausen <sup>8</sup>	31	26	1	3.1
E	Holthausenn <sup>9</sup>	53.6	52	2	3.6
F	Toyota (Mirai Front) <sup>10</sup>	40.5	60	2.45	5.7
G	Toyota (Mirai Rear) <sup>11</sup>	42.2	62.4	2.55	5.7

The gravimetric density, in table 10.2 given as 'wt%', is extremely important for the HyDrone. Like all aerospace projects, mass should be kept as low as possible. Immediately the fuel tanks from Hexagon Composites and Toyota stand out because they share the highest gravimetric density. Another important thing to note is that none of the tanks have enough capacity to store all required hydrogen in a single tank. Therefore combinations of fuel tanks were investigated to find the optimal solution. It was decided that it was only relevant to investigate the combinations with fuel tanks of a gravimetric density over 4%. These combinations are presented in table 10.3

Table 10.3: Hydrogen Fuel Tank Combinations

Option	Combination	Empty Mass (kg)	Volume (L)	H2 Capacity (kg)	%wt	margin (%)
1	2xA	86	128	5.2	5.7	17.9
2	6xB	102	120	4.86	4.5	10.2
3	2xF	81.1	120	4.9	5.7	11.1
4	2xG	84.4	124.8	5.1	5.7	15.7
5	1xA+1xE	96.6	116	4.6	4.5	4.3
6	1xA+1xF	83.5	124	5.05	5.7	14.5
7	1xA+1xG	85.2	126.4	5.15	5.7	16.8
8	1xF+1xG	82.7	122.4	5.0	5.7	13.4

Many more options were possible, but were all ruled to be impractical as they were either heavier or a combination of more than two different fuel tanks. Options 1 through 4 are options for which only 1 type of fuel tank is used. The final column, 'margin', shows the percentage-wise margin the fuel tank capacity has on the required energy of 173.9 kWh. So if the required energy were to be higher due to unforeseen circumstances, but remains within the margin, this would not be a problem. A higher margin therefore, will yield a more robust design. However, if the margin is too high this means that the total design will be over-designed and therefore heavier. It was decided that this margin must be at least 10%. This safety margin resulted in the elimination

<sup>7</sup>[http://www.mahytec.com/wp-content/uploads/2015/12/H2\\_700bar.pdf](http://www.mahytec.com/wp-content/uploads/2015/12/H2_700bar.pdf), [cited 08-06-2017]

<sup>8</sup><http://www.waterstof-centrum.nl/product/700-bar-waterstof-cylinder-26-1-verkoop>, [cited 08-06-2017]

<sup>9</sup><http://www.waterstof-centrum.nl/product/700-bar-waterstof-cylinder-52-1-verkoop>, [cited 08-06-2017]

<sup>10</sup><http://pressroom.toyota.com/releases/2016+toyota+mirai+fuel+cell+product.download>, [cited 08-06-2017]

<sup>11</sup><http://pressroom.toyota.com/releases/2016+toyota+mirai+fuel+cell+product.download>, [cited 08-06-2017]

of design option 5. Options 2 was eliminated next as its gravimetric density was lower than the other design options. From the six options that were left, option 3 was closest to the 10% margin and had the lowest final mass. Therefore the choice was finally made to use option 3 for the HyDrone as its margin is closest to 10%. So two identical Toyota tanks of 40.5 *kg* each, with a total hydrogen capacity of 4.9 *kg*. This comes down to a total potential energy of 193 *kWh*. Contact was established with Toyota in San Francisco about the cost of the fuel tanks, but unfortunately they could not give this information. Therefore the cost estimation of the hydrogen fuel tanks was based on production cost figures published by Strategic Analysis[52]. In 2011 the production cost for a type 4 hydrogen fuel tank and BoP together was 26.02 \$/*kWh* for a two tank configuration. Multiplying with a factor of two gave the estimated sales price. For the HyDrone this comes down to \$10,059.33 before inflation is taken into account.

### 10.3.2 Balance of Plant

The balance of plant is the component that regulates the flows of hydrogen and oxygen to the next component, the stack. The BoP contains, among others, a temperature regulator, humidifier and pressure regulator to make sure the two gasses flow into the stack in the optimum state. The balance of plant is 90% efficient[53], so 10% of the energy contained in the fuel tank is used to power the BoP. The other 90%, or 155.5 *kWh*, of the chemical energy is converted to electricity in the fuel cell stack.

### 10.3.3 Fuel Cell Stack

Another reason why hydrogen fuel cells are starting to gain in popularity after so many years is that the specific power of the HFC stacks has increased by a significant amount over the last years. A number of the most recent fuel cell stacks suited for the automotive industry available on the market today are compared in table 10.4.

Table 10.4: Hydrogen Fuel Cell Stacks

Company	Stack	Nominal Power (kW)	Mass (kg)	Volume (L)	GPD (kW/kg)	VPD (kW/L)	margin (%)
PowerCell	S3-335c <sup>12</sup>	98.2	33.1	29.1	2.97	3.37	-6.0
PowerCell	S3-455c <sup>13</sup>	125	41.6	37.0	3.00	3.38	19.6
Toyota	Mirai <sup>14</sup>	114	57	36.8	2.00	3.10	9.1
Honda	Clarity <sup>15</sup>	103	51.7	33.0	1.99	3.12	-1.4
Nuvera	Andromeda 2[54]	80	140	78.0	0.57	1.03	-23.4
PureMotion	Model 120[55]	120	900	1806	0.13	0.07	14.9
Ballard	HD100[56]	100	285	528	0.35	0.19	-4.3

From table 10.4 can quickly be deduced that there is one company well ahead of all others. PowerCell produces two different HFC stacks that have a gravimetric power density (GPD) of about 3.0 *kW/kg* compared to 2.0 *kW/kg* from the next 'best' company, Toyota. The final column again indicates the margin in the same way as in table 10.3, only this time for required power instead of energy. The maximum required power calculated in chapter 9 is 91.4 *kW*. Taking into account a maximum accessory power (see section 10.3.4) of 2.6 *kW* and a 90% controller- and motor efficiency[57], the maximum power required from the stack is 104.5 *kW*. For the selection of the desired HFC stack the same minimum 10% margin over this power was desired. This left only two stacks of which the S3-455c is the lightest. This was therefore determined to be the best suited stack for the HyDrone, even though it is notably over-designed. However, as the required power contains some uncertainty this conservative option was considered an excellent choice. A simple exhaust tube was added to the design, which releases the produced water to the outside air.

The stack's energy efficiency is 54.6% so of the 156.5 *kWh* coming into the stack through the BoP 85.5 *kWh* is converted to electricity. The mass of the fuel cell stack is 41.6 *kg*. Contact was established with the Swedish company PowerCell to enquire about the cost of their fuel cell. Unfortunately they would not give this information without signing an NDA, which was not an option. Therefore the cost estimation was based on production costs published by the US Department of Energy[58]. They reported that a hydrogen fuel cell stack is produced for 154 \$/*kW*. This value was multiplied by two to find a realistic sales price of \$38,500 before inflation is taken into account.

<sup>12</sup><http://www.powercell.se/wp-content/uploads/2017/05/S3-Fuel-Cell-Data-Sheet.pdf>, [cited 08-06-2017]

<sup>13</sup><http://www.powercell.se/wp-content/uploads/2017/05/S3-Fuel-Cell-Data-Sheet.pdf>, [cited 08-06-2017]

<sup>14</sup><http://pressroom.toyota.com/releases/2016+toyota+mirai+fuel+cell+product.download>, [cited 08-06-2017]

<sup>15</sup><http://news.honda.com/newsandviews/article.aspx?id=9432-en>, [cited 08-06-2017]

---

### 10.3.4 DC-DC Converter and PCU

This subsection deals with how the generated power is converted and distributed. The PowerCell S3-455c generates a maximum of 125 kW at 420 A. The output voltage can simply be calculated using eq. (10.10)

$$U = \frac{P}{I} \quad (10.10)$$

This results in an output direct current (DC) of 298 V. The electric motors require a voltage of 300 V. This means the power only has to be converted by a insignificant ratio to be used by the motors. DC-DC converters for PEM fuel cells generally have a 95% efficiency when converting the stack output voltage by a factor of approximately 2[59]. As the voltage ratio is notably closer to 1 for the HyDrone, namely 0.993, it was considered valid to assume that a DC-DC converter is not imperative between the fuel cell and the motors. Therefore a 100% efficiency and zero mass was assumed for this component. As the electric motors can also be configured for a higher voltage a DC-DC converter may very well be necessary after all. This is because a higher voltage, and thus a lower current, corresponds to a lower power loss.

The power control unit (PCU) is the component that distributes the power. The largest part of the power will be distributed to the eight individual electric motors. It will also control the smaller currents required by the other subsystems as described in section 10.1. Two PCUs are included in the design to account for redundancy. Only one of the two PCUs will be active at the time. As the HyDrone is fully autonomous, this PCU has to be managed by an AI supercomputer. The NVIDIA Drive PX 2 is the computer used by Tesla and is also suited for the HyDrone. This processor uses 80 W<sup>16</sup> and will cost about \$2500 per unit. This will further be explained in section 11.2. More research is required in the electronics branch to design or select a specific PCU. The processor is assumed to dictate the PCU's power consumption and to be representative for the total PCU cost.

### 10.3.5 Backup Battery

In chapter 9 the scenario where two engines would fail was discussed. For the electric motor selection it was taken into account that six units must be able to provide enough power to hover. But the scenario in which the whole HFC would fail, could still be catastrophic. To prevent this from happening, an alternative power source had to be taken into account. A backup/emergency battery was the most logical design option. The capacity of this battery was defined as enough to maintain hover for one minute. This one minute was determined to be safe enough to find a suitable landing spot, descent and land. Descent can happen at a higher velocity than during a nominal cycle, thus requiring less energy. A relatively short burst of power would then be given from the batteries to decelerate when at low altitude to comfortably land. Please note, that in cruise conditions, a power subsystem failure could be solved by an autorotation landing, as described in section 12.1. If for any reason a safe landing by autorotation is not guaranteed (e.g. with zero forward velocity) the backup battery can be used to safely land as described above. So if the HFC fails in any condition, a safe landing is always possible. The required capacity of the battery was found by multiplying the required power output with the required time it must maintain this power level. The required power for hovering flight is 76.8 kW. Assuming a 10% power loss from the battery to the propellers, the required energy yields 1.42 kWh. Panasonic 18650 Li-ion Cells have a capacity of 13.6 Wh[60]. A set of 105 of these batteries would provide enough energy. This cells in this set can be connected series and/or parallel in such a way that the output voltage is 300 V which is required for the motors. This set of Li-ion cells will have a total mass of 5.64 kg.

The combined mass of the tanks including hydrogen, stack and backup battery then is 133.2 kg. The mass of all other components in the power subsystem (BoP, PCU and potential DC-DC converter) is estimated to be 6% of this 133.2 kg, making the total power subsystem mass 141.2 kg.

### 10.3.6 Wiring

Conventional vehicles carry a lot of wires with them with a total mass of up to 50 kg<sup>17</sup>. For the HyDrone this would be a real problem as mass should be kept as low as possible. In smaller cars the total wiring harness mass is about 30 kg. This value was originally used to design the drone. Using aluminium alloy wires in stead of conventional copper wires can save 30% on the total harness mass[61]. Weight reduction is of course desirable in the aerospace industry so the aluminium alloy wires were implemented in the HyDrone resulting in a wire harness mass of 21 kg. Another 5 kg were added for the design interface, other dashboard instruments and sensors, bringing the total electronics mass to 26 kg.

---

<sup>16</sup><https://www.gputechconf.jp/assets/files/1062.pdf>, [cited 12-06-2017]

<sup>17</sup><http://blog.caranddriver.com/it-takes-a-lot-of-wiring-to-keep-a-modern-vehicle-moving-witness-this-bentleys-harness/>, [cited 20-06-2017]

## 10.4 Safety

The backup battery is a good example of a safety measure in the power subsystem. It provides an alternative power source in case the primary subsystem fails. However this does not guarantee the safety of the power subsystem, merely its redundancy. Hydrogen fuel cells have to be extremely safe in order to be implemented in the HyDrone, as it will be operated in the airspace of urban environments. Hydrogen itself is a highly flammable gas so it is critical that the hydrogen fuel tank does not rupture or leak under any circumstances. To ensure this safety of the hydrogen storage cylinders manufacturers of these cylinders have to comply with many standards. For 700 bar cylinders implemented in vehicles these are: E.I.H.P. / Rev 12B, ISO 15869 (EU 97/23/EG), FMVSS 304 (modified), Betten 9 (modified)<sup>18</sup>. These standards dictate the following types of tests, none of which may be failed[62][40]:

- Hydrostatic Burst
- Extreme Temp. Pressure Cycle
- Ambient Temp. Pressure Cycle
- Chemical Exposure
- Bonfire
- Gunfire Penetration
- Flaw Tolerance
- Accelerated Stress
- Drop Test
- Permeation
- Hydrogen Cycle
- Softening Temperature
- Tensile Properties
- Resin Shear
- Hydrogen-Compatible Material
- Numerous Internal Tests

In the event of a crash, accelerometers in the tanks' valves instantly shut the valve to avoid releasing hydrogen that could endanger the surroundings. The only exception for leakage of the tank is during a vehicle fire. A pressure relief device (PRD) must then safely release the stored hydrogen. This PRD is activated at an elevated temperature due to a fire below it. The setup was tested with multiple bonfires. Even though hydrogen is highly flammable, it is not dangerous to release the hydrogen with a suited PRD. This is because hydrogen is the lightest element known to the universe. Therefore, when released, it escapes up into the atmosphere rapidly, before a fire below it can ignite it[63]. The passenger and surroundings will therefore never be harmed by the hydrogen.

Other components in the power subsystem are purely electrical and only risk overheating and short circuit. The overheating is simply overcome by a temperature regulating system which ensures the power subsystem stays within safe operating temperatures.

All wires are encased with a waterproof and electrically insulated cover. All other components are also protected from water in case the exhaust might leak inside the drone. The exhaust is very unlikely to leak though, as there are no high pressures acting on it and it is not exposed to substances other than pure  $H_2O$  on the inside and air on the outside.

## 10.5 Technical Risks

Evaluating the technical risk of the power subsystem is an important tool to ensure the quality and safety of the design. A technical risk map was made to graphically represent this. The following risks were assessed:

1. Hydrogen Fuel Tank
2. Balance of Plant
3. Hydrogen Fuel Cell Stack
4. Exhaust
5. Power Control Unit
6. Backup Battery
7. Wiring

This technical risk assessment is focused on the safety of the design and the capability to meet its performance requirements. The probability of failure of a component and the consequence on the safety of the design is plotted in table 10.5.

Table 10.5: Technical Risk Map: Power Subsystem

Feasible in Theory				
Working Laboratory Model				
Based on Existing Non-Flight Engineering		5		
Extrapolated from Existing Flight Design		1	2,3	
Proven Flight Design	6	4		7
	Negligible	Marginal	Critical	Catastrophic

<sup>18</sup><https://energy.gov/eere/fuelcells/high-pressure-hydrogen-tank-testing>, [cited 13-06-2017]

---

**Hydrogen Fuel Tank** If a hydrogen fuel tank were to malfunction in any way it can be shut off by the BoP and there is still one more fuel tank left so the impact of a single tank failure was considered marginal. Boeing demonstrated a HFC powered propeller prototype aircraft[64]. So a hydrogen fuel tank was used before in flight and was therefore placed in the probability 'Extrapolated from Existing Flight Design'.

**Balance of Plant** The HFC reference aircraft was considered again in order to judge the probability of failure of the BoP. The consequence of failure of this component is higher though as there is only one BoP and the HyDrone will be forced to activate its backup battery in order to safely land. The mission will be compromised and the impact was therefore determined to be critical.

**Hydrogen Fuel Cell Stack** The exact same reasoning was applied for the risk of stack failure. It should be noted, though, that the selected stack from PowerCell is still being validated. Its technology has been used on an aircraft before but the particular model has not. As the technology is extrapolated from an existing flight design, the probability of failure of the PowerCell stack was deemed the same.

**Exhaust** The exhaust is a simple rubber tube and is not exposed to damaging circumstances. Even though failure is unlikely, it could be critical for the mission if water were to leak in the HyDrone damaging electronic components. This risk was therefore mitigated by making sure that all electric components are made waterproof. The risk was then considered marginal.

**Power Control Unit** The PCU that will be used in the HyDrone is the same model that is used by autonomously driving Teslas. So the probability is in the 'Based on Existing Non-Flight Design' category. The consequence if the PCU fails could be catastrophic so it was determined that a second PCU must be installed in case the primary experiences some sort of failure. By doing this, the risk was mitigated to a 'marginal' consequence.

**Backup Battery** The backup battery is the secondary power source and will only be activated if the HFC system fails. During nominal flight the HFC works and the mission will not be affected by a battery failure, besides required maintenance before the drone can take-off again. So the consequence was ruled to be negligible. Batteries are commonly used in drones so the probability was determined to be very low.

**Wiring** A wiring failure of some sort could shut down all electronics short-circuit. This would be catastrophic for the mission as autorotation cannot be guaranteed. The electric pitching system must work for this to safely happen. Luckily aluminium wires are implemented in modern aircraft like the Airbus A380. So even though the risk could have catastrophic impact the probability is very low so mitigation was not necessary.

## 10.6 Recommendations

As the power subsystem is quite innovative for the aerospace industry, there are quite a few recommendations to be made for the further development of the DSE.

First of all, the BoP should be investigated in more detail. It consists of many sensors and regulators, which should all be specifically selected or an existing balance of plant must be picked off-the-shelf. If the latter option is chosen it must be made sure that the BoP is suited for both the fuel tanks and stack.

Next, the electric components such as DC-DC converters should be elaborated upon. The stack and electric motors may be able to operate on the same voltage, but all smaller components will most likely be operated at a lower voltage and current. This would require small converters and resistors. These were not investigated in this DSE, but cannot be left out if this DSE were to continue. Following the same logic, the PCU must also be designed in more detail. To obtain the correct and reliable distribution of the power, a very sophisticated Printed Circuit Board is required.

Furthermore, the development of the hydrogen technology should be closely followed. It is more than likely that this technology will encounter multiple breakthroughs in the next years. Lighter fuel tanks will probably appear on the market soon.

Finally, the cost of all power subsystem components should be further researched. For this DSE the cost estimates are purely based on average production costs. Multiple manufacturers were contacted to enquire about their products' cost. Unfortunately, none of them were willing to give this information without signing a non-disclosure agreement.

---

# Chapter 11: Control & Stability

In this section the control and stability aspects of the drone will be discussed. First a suitable system for variable pitch will be looked into. Second the appropriate sensors will be selected and their optimal placement is elaborated upon. Third the control diagrams are worked out, for a complete overview of the system. Finally the flight characteristics of the drone are tested based on a dynamic model and designed controllers.

## 11.1 Blade Pitch System

During the flight profile of the HyDrone the velocity varies significantly between hovering and cruise speed. The blades of a drone are in general designed for the particular purpose of the drone. Drones which are for example used for filming require stable and efficient hovering, the type of blades used for this purpose are lacking efficiency at higher speeds. Worse still, they cannot reach efficient high cruise velocities as they are specifically designed for hovering<sup>1</sup>. In order for the HyDrone to fly efficiently in all flight phases a variable pitch system needs to be designed. Helicopters use this kind of system but this system is quite complicated and vulnerable and therefore needs regular maintenance. For the HyDrone a low maintenance system is required to maximise operational time. Designing a low maintenance blade pitch system requires that it is less complicated than the helicopter pitch system which contains more movable parts especially when more blades are added to the rotors. Furthermore it should be protected to impacts from the environment. As no existing designs meet these standards a new pitch system is designed to specifically meet the needs of the HyDrone. Figure 11.1 shows a sketch of this new pitch system.

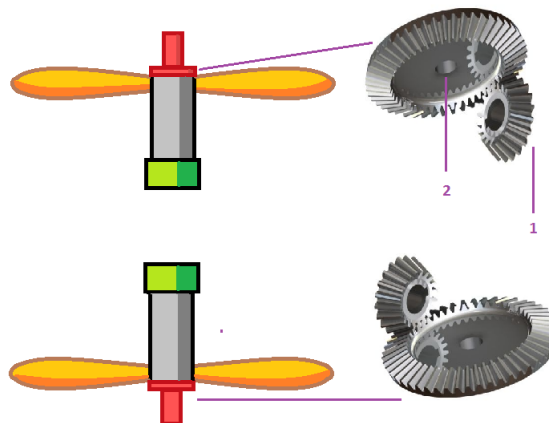


Figure 11.1: Blade Pitch System

Each propeller (orange/yellow) has its own propulsive shaft (grey) with an individual electrical engine (green) in order to operate as coaxial counter-rotating rotor propulsion system with variable rpm. The propellers are attached to the propulsive shaft, they can move  $360^\circ$  around their longitudinal axis. At this attachment the propellers are inserted into bevel gears (number 1 in fig. 11.1) and fixed to them. So part 1 and 2 in fig. 11.1 spin together with the propulsive shaft, only part 2 has an own propulsive shaft (red in fig. 11.1). In order to make the pitch rotation possible a disc gear (number 2 in fig. 11.1) is mounted right above the upper rotors bevel gears (number 1 in fig. 11.1) and right below the lower rotors bevel gears. These disc and bevel gears coincident with each other in a way that moving the disc, rotates the bevel gears which turn the blades of the rotor around their longitudinal axis. The disc is propelled by its own shaft which rotates with the same rpm as the propulsive shaft and the rotor blades, by reducing or slowing the disc shaft rpm a little tiny bit down or up by use of the electrical engine for the pitch (red in fig. 11.1), the disc starts (number 1 in fig. 11.1) to rotate with respect to the rotor propulsive shaft. After the correct pitch angle is achieved by rotating the disc the rpm of the disc is set equal to that of the propulsive shaft and rotor. These tiny disc rpm adjustments are made by an electric engine (red in fig. 11.1) on the top and bottom of the respectively upper and lower rotor.

In case of distress when the propulsive system fails or jams the electric engine of the propulsive shaft (grey in fig. 11.1) can be automatically decoupled from the main shaft to let auto-rotation be possible for the rotors.

---

<sup>1</sup><http://learnrobotix.com/uavs/quadcopter-basics/quadcopters-multirotors-motors-propellers-basics.html>[cited 9-07-2017]

---

The vulnerability in case of distress is that if the electric system fails the disc for the pitch control (number 2 in fig. 11.1) can rotate freely around because the electric engine of the disc shaft (red in fig. 11.1) is not able to hold it on the same rpm as the main shaft (grey in fig. 11.1) which is now in auto-rotation mode. In this case when the electric engine fails of the disc (Red in fig. 11.1) the air around the rotor changes every time the blade pitch. In order to prevent this a lock-up system needs to be added to the design. In case the electric system fails the lock-up system keeps the rpm of the two shaft the same and prevents adjustments in the blade pitch angle. The HyDrone lands in case of distress with the latest blade pitch angle right before failure.

### Costs & Weight

The HyDrone has 4 co-axial counter rotating rotors. Each rotor has it's own blade pitching system which results in 8 pitching systems propelled by 8 electric engines. The engines should have an minimal rpm of 3000 because during flight the HyDrone never surpasses this value. This value can be achieved by increasing the rpm of the electrical engine by gears. Also holding the disk with equal rpm as the propulsive shaft of the blades is crucial. Therefore high torque electrical engines are used. For this purpose the electrical engine Roterio BLE2 ( <sup>2</sup> ) is chosen with the following product specification: Max rpm 4000, mass 1.6 kg, max power 200W, brush less, 230V, max holding torque 518 Nm. Each electrical engine costs 800 \$ so the total amount of costs for 8 electrical engines for the pitch system is 6400 \$ with an max total power of 1600W and a mass of 12.8 kg.

The weights and costs of the disc, shaft and bevel gears is not taken into account because compared to the weight and costs of the electric engine they are negligible. Nevertheless calculating the costs for these parts are so highly dependent of the type and size that a rough estimation is useless compared to the dominating part which are the electrical engines. Due to this uncertainty it is also difficult to select the appropriate engine for the blade pitch and also lot of uncertainties as vibrations and twisting of the blades by turbulence have to be taken into account. Furthermore also has to be investigated if the electrical engines of the blade pitch systems are able to hold the same rpm as the propulsive shaft without deviations that affect the blade pitch angle in a negative way. Furthermore the engine selection for the pitch system is made only on basis of rpm and the largest possible torque combined with a reasonable weight. So in short, calculations and tests on a laboratory model should be performed to investigate if this concept is feasible in reality.

## 11.2 Sensors

The HyDrone should fly autonomously therefore appropriate sensors are required to monitor and control the HyDrone. An overview of the sensors and subsystems is presented in fig. 15.1. All the sensors and subsystems are connected to the autonomous operating software which process all the received data and determines the appropriate action.

### 11.2.1 Types of Sensors

Determining the position and monitoring the surrounding of the HyDrone is a crucial part of the autonomous system. If this system does not function perfectly, safety can not be guaranteed. Still this system can be unnecessary expensive if the wrong sensor types are chosen. Therefore different sensors are explored for determining the position and scanning the surrounding.

#### Positioning

The most common way to determine the position is by using the Global Positioning System (GPS). Unfortunately, with an accuracy of about 5 meters horizontal depending on the weather conditions, this is not sufficient. The accuracy for altitude is far worse with 10 meters <sup>3</sup>. To overcome this accuracy problem a Continuously Operating Reference Station (CORS) GPS is chosen for determining the position of the HyDrone. The CORS GPS has an accuracy of 10 cm <sup>4</sup> which is accurate enough for landing and manoeuvring through narrow spaces. The CORS GPS differs from a standard GPS system in a way that it has a fix based ground station with its exact position known. The exact known position is compared to the standard GPS position. The deviation between these two is the error and at the same time the correction for the HyDrone's standard GPS position. In this way the accuracy of the standard GPS location is enhanced from 5 m to 10 cm. For this purpose a \$235 high precise GPS system of REACH is used designed for drones. Reach RTK GNSS <sup>5</sup> Product specifications : 12 gram, 26 mm x 45 mm Antenna: 20 gram, 30 mm x 30 mm 60\$. For redundancy 2 GPS systems are used making it cost 590\$ and with a total power consumption of 40 W.

#### Surrounding

---

<sup>2</sup><http://www.directindustry.com/prod/oriental-motor/product-15581-1850227.html> [cited 9-07-2017]

<sup>3</sup><http://gpsinformation.net/main/altitude.htm> [12-07-2017]

<sup>4</sup><http://www.icsm.gov.au/mapping/surveying4.html> [cited 7-07-2017]

<sup>5</sup><http://www.directionsmag.com/entry/finally-affordable-high-precision-gps-for-drones/470208> [cited 13-07-2017]

---

The HyDrone has to manoeuvre around obstacles and scan the ground for an appropriate landing spot. Scanning the surrounding is an essential part of this aside of the GPS position. For scanning of the surrounding different types of systems can be used with each their own advantages and disadvantages. A quick overview of the systems is given now.

*Light Detection and Ranging* Light Detection and Ranging (LIDAR) is a surveying system which uses laser beams to measure the distance of the objects in the surrounding by illuminating it. This method can recognise and visualise small details like surface type and can create 3d maps of the environment. Unfortunately the system is expensive and a lot of data is produced by all the reflected laser points which needs to be processed in order to render a 3d map. The price of the system largely depends on the radius that it is able to scan and the angle of view. To reduce costs it is important to identify how much of the surrounding must be scanned in detail. For autonomous flight it is important that the surrounding is scanned in detail right below the HyDrone in case of landing. LIDAR systems have problems mapping the environment during snow and thick fog conditions due to reflection so a system that scans far away in the flight path direction is not a reliable system for all weather conditions. Therefore LIDAR is only used to scan the ground for recognising obstacles during landing and determining if the ground is suitable for landing. LIDAR is at this moment an expensive system starting at \$8000 going to \$70000<sup>6</sup> which Google and Uber use, but prices are drastically dropping in the coming years. The costs for the sensor are estimated to be around \$500 or less<sup>(7)</sup> in a couple of years.

*Radar* system detects objects in the surrounding by radio waves. The resolution is less compared to the LIDAR system but it has many other advantages. Radar can cross a larger distance and is hardly influenced by weather conditions or dust. Scanning the surrounding for obstacles and determining their speed a Radar system is perfect. Especially when there is no need for detailed mapping of the surrounding.

*Ultrasonic sensors* system is a very short distance low resolution surveying system. Due to the slow speed of the sound waves compared to light and radio waves, small deviations of less than 1.0 cm are detectable, so they are excellent for very near 3d mapping of the surrounding. Unfortunately the low resolution prevents it from finding small details like the fuel stations fuel pistol. It is only possible to measure small differences of large objects not small objects. Therefore ultra sonic sensors will be used to detect objects close around the HyDrone for example people or objects.

*Camera image recognition* system uses high resolution cameras to map the environment. The optical-character recognition capability gives them new capabilities that are totally missing in other systems like colour contrast and texture of surfaces. Unfortunately these capabilities and range degrade very fast when light levels dim.

### 11.2.2 Sensor Distribution & Costs

Now the different type of sensors where discussed, the right ones must be selected and be located on the right place on the HyDrone in order to function optimal and reduce the amount of sensors needed which reduces costs.

The LIDAR system is therefore only used for mapping the ground under the drone with a certain radius depending on the altitude. The Innoviz HD-SSL which goes into mass production early 2019<sup>8</sup> is selected for our system with the following specifications: view field 100°x25°, spatial resolution 0.1°x0.1°, range 200m, dept accuracy <2cm, resolution 6M pixels/sec, 25 frames/sec, size 5 x 5 x 5cm, 20 Watt, 600 grams. Start price of 500 dollars but decreases with increased volumes.

For redundancy and optimal view angle 5 LIDAR sensors are mounted on the bottom of the HyDrone. These have to be distributed in a way to have acceptable blind spots of the LIDAR system. Therefore 3 LIDAR system are mounted with their 100° in the longitudinal direction and with the 25° view angle in the lateral direction. One at the front and back and one in the middle all on the longitudinal axis. Two LIDARS are used on the side of the middle lateral axis with their 25° view directed in the longitudinal direction. The blind spots are calculated with trigonometric and the following results follow: 0.84m (Blue arrow in fig. 11.2a). So if the drone lands and the ground clearance is less than 0.84 meter blind spots occur under the drone (red zone in fig. 11.2a). The max coverage on 200m height is 477m X 95m of one LIDAR. Its clear that overlapping of the laser beams occur at a distance larger than 0.84 from the bottom of the HyDrone and at a ground clearance larger than 1.68m the middle LIDAR system can be shut down due to the overlapping. It is only enabled during landing mode or for redundancy when an other LIDAR fails. In the lateral direction the blind spots start at 0.42 m for the 100° (blue arrow fig. 11.2b). The blind spot that occurs if the ground clearance is less than 0.42 m is reduced by the LIDAR system in the middle that has an lateral beam angle of 25°.

The total costs for only the LIDAR sensors is thus 2500\$ with a power consumption of 100W and a mass of 3kg.

---

<sup>6</sup><http://spectrum.ieee.org/tech-talk/semiconductors/optoelectronics/mit-lidar-on-a-chip>[cited 14-06-2017]

<sup>7</sup><http://spectrum.ieee.org/transportation/advanced-cars/cheap-lidar-the-key-to-making-selfdriving-cars-affordable>[14-06-2017]

<sup>8</sup><http://news.techtime.co.il/2017/05/24/innoviz-lidar-sensor/>[cited 14-06-2017]

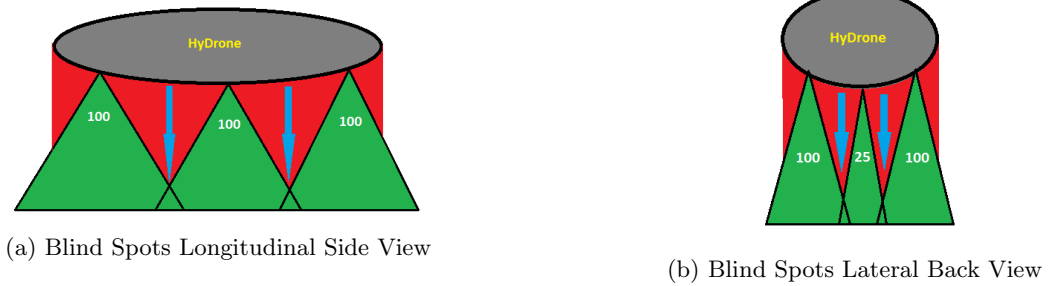


Figure 11.2: Blind Spots of LIDAR System

The radar system for spotting objects around the drones flight direction the system consist out of 6 radars mounted on the HyDrone body sides and one at the top looking upward. Due to the 6 radars on the side with their narrow beam (green) blind spots (red) occur as can be seen in fig. 11.3 which should not be a drawback because the ultrasonic sensors (blue spots in fig. 11.3) take care about the surrounding about a range of 6m around the HyDrone. In case there is something in the surrounding within this range the HyDrone will not take off. For this purpose Devantech SRF08 Ultrasonic Range Finder <sup>9</sup> are used with the following product specifications: range 3cm-6m, 5v, 15mA, 75mW, size 43 x 20 x 17mm, cost 49\$ beam width 20°, 4 gram. The ultrasonic sensors are distributed over the sides of the body. In total 20 ultrasonic sensors (blue spots) are distributed as can be seen in fig. 11.3 in order to get a 360° view around the HyDrone. The total costs are 980\$, power consumption of 1.5W and a mass of 80 grams.

The radar system consist out of a special for drones designed lightweight Echodyne MESA-K-DEV <sup>10</sup> is used which can even detect power lines in the air with the following specifications: view angle azimuth 60° and 40° in elevation, beam switch speed 1 μs, range 750m, size 2.2 x 7.5 x 2.5cm, mass 0.820 kg, Frequency K-band, polarisation horizontal, 20 Watt.

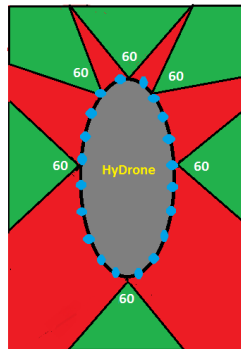


Figure 11.3: Radar Blind Spots Top View

The price of this product has yet to be determined but estimating it conservatively it will cost \$1000 for each radar making it \$7000 for 7 radars with a total weight of 5.74 kg and a power consumption of 140 W. Prices will decrease if the product is more mass produced. The procedure about radar system failure is that when one radar fails the HyDrone will land at the nearest landing spot, even if the failure occurs at the front where redundancy is taken into account by using 3 radars.

For autonomously fuelling the LIDAR system which remotely sense the surrounding in detail finds the exact position of landing at the fuel station so that the fuel opening is directed to the fuel pistol. With the use of CORS GPS it is able to land at 10 cm accuracy at the fuel station. The autonomous fuelling pistol finds the fuel tank opening by the use of camera image recognition. In low level light conditions lighting or infrared light can be used to illuminate the area where the fuel opening is present to let the camera image recognition system do the work properly.

The sensors for attitude and acceleration are compressed into one sensor system which is designed by Microchip MM7150-AB0 - MEMS Module, Tri-Axis Gyroscope, Tri-Axis Accelerometer, Tri-Axis Magnetometer for \$27.26. To include redundance 2 of these sensors are used for the design making it \$54.52. The product specifications are: 13.25 mA, 3.3 V, Power 43.73 mW, dimensions 17 x 17 mm.

<sup>9</sup><http://www.robotshop.com/en/devantech-ultrasonic-range-finder-srf08.html>[cited 27-07-2017]

<sup>10</sup><http://echodyne.com/products/>[cited 15-06-2017]

Communication between the ground station server and other HyDrones occurs through the data transmitter and receiver. Being far away from the ground station server which results in a powerful antenna. To overcome this problem the data transmission goes through the mobile network. The mobile network works always under all acceptable weather condition. If not then the weather conditions are not appropriate for the HyDrone to fly. For this purpose a Huawei E8372h-153 4G LTE dongle is used which costs \$100 <sup>11</sup>.

The autonomous software will be the most expensive part of the autonomous system because it involves a lot of testing and documentation which are expensive and time consuming procedures during the developing process. The costs for designing the autonomous system is elaborated in section 19.1.2. The developing costs for the autonomous system will be for the HyDrone's autonomous system lower compared to space autonomous systems due to less strict documentation and tests compared. This is due to the fact that in space projects a failing autonomous system results in failing the whole project. In case of the HyDrone the risk is spread out over the total number of sold HyDrones. If the autonomous system of one HyDrone fails the whole fleet can be taken down and a software update can be executed on the autonomous system to fix the problem. The damage and impact on the total fleet and the HyDrone project is therefore reduced significantly. Due to this the costs for testing and documentation of the autonomous system decrease.

The autonomous system will operate on an supercomputer which is also used by Tesla which is the drive Drive PX 2 processor and will cost \$15000 per unit, but Tesla is reported to pay approximately \$1500 for the kit<sup>12</sup>. This is due to the fact that for higher production rates the price drops significantly. Two PCUs are needed to account for redundancy. With the expected production rate for the HyDrone the estimated cost of the supercomputer is \$2500 per unit or \$5000 per drone.

A complete overview of the control costs, mass and power consumption when everything is switched on and functions on maximal power is represented in table 11.1.

Table 11.1: Control Budget

Sensor	Number	Cost(dollar)	Power(W)	Mass (gram)
GPS	2	590	40	64
LIDAR	5	2500	100	3000
Radar	7	7000	160	5740
Ultrasonic	20	980	1.5	80
Gyroscope	2	54.52	0.044	-
Processor	2	5000	160	-
4G dongle	2	200	-	-
Total	40	16324.52	461.54	8884
Pitch	8	6400	1600	12800
Total	48	22724.52	2061.54	21684

### 11.3 Control Flow Diagrams

The autonomous system fig. 11.4 ensures that the HyDrone goes from point A to point B. The input for this process is the desired position and the actual position is the output and also the feedback for the controller. The function of the controller is to take the difference between the input and the calculated output and determine an appropriate action for the system to make the difference go to zero. In order to achieve this the controller gives an signal to the power subsystem considering how much trust has to be delivered and the appropriate attitude. This results in an acceleration which is used to calculate the velocity. When the desired velocity is achieved there goes a signal back to the power subsystem to decrease the power for holding the specific achieved velocity. The velocity can also be calculated by the controller from the position change every time in the control loop represented in fig. 11.4.

#### Velocity

During the flight the velocity varies constant. Not only by going from hovering to cruise mode and back to landing but also the perturbations on the velocity caused by wind and other elements. These perturbations must be overcome automatically to hold the velocity constant. The control flow of the velocity is represented in fig. 11.5 with number 1. The velocity is adapted by changing the rotor speed and the blade pitch which varies constant with the velocity of the HyDrone.

#### Acceleration

<sup>11</sup><https://www.4gltmall.com/huawei-e8372-lte-wifi-stick.html>[cited 16-06-2017]

<sup>12</sup><https://www.fool.com/investing/2016/10/27/tesla-motors-inc-is-using-nvidia-corporations-driv.aspx>,[cited 20-06-2017]

The acceleration can be positive at increasing speed but also negative when braking during flight. Also a manoeuvre with or without disturbances deviate the acceleration from the desired acceleration. To keep the acceleration as constant as possible the accelerometer constantly monitors it and gives feedback to the controller. The control flow of the acceleration is represented in fig. 11.5 with number 2.

### Attitude

During flight the attitude of the HyDrone should be kept fixed. It is expected that disturbances that change the attitude in a undesirable way are filtered out by the attitude control system. These disturbances are measured by the lateral and orthogonal axis gyroscope which measure the angular rate, subsequently changed into angle change. The new angle is then compared with the desired angle and if that does not match the rotor system dissolves the difference. The control flow of the attitude is represented in fig. 11.5 with number 3.

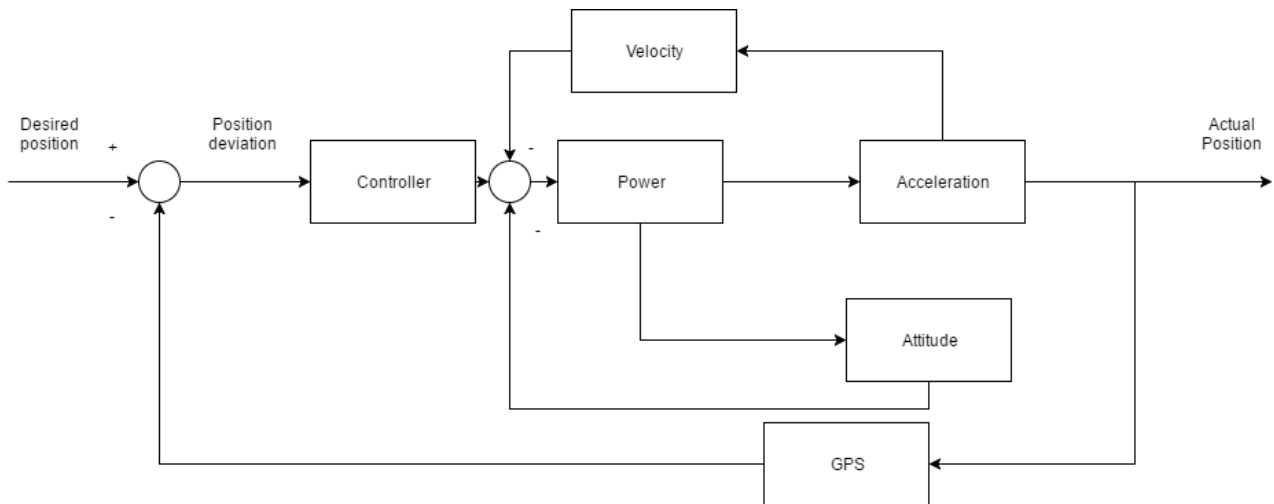


Figure 11.4: Control Flow Diagram Considering Changing Position

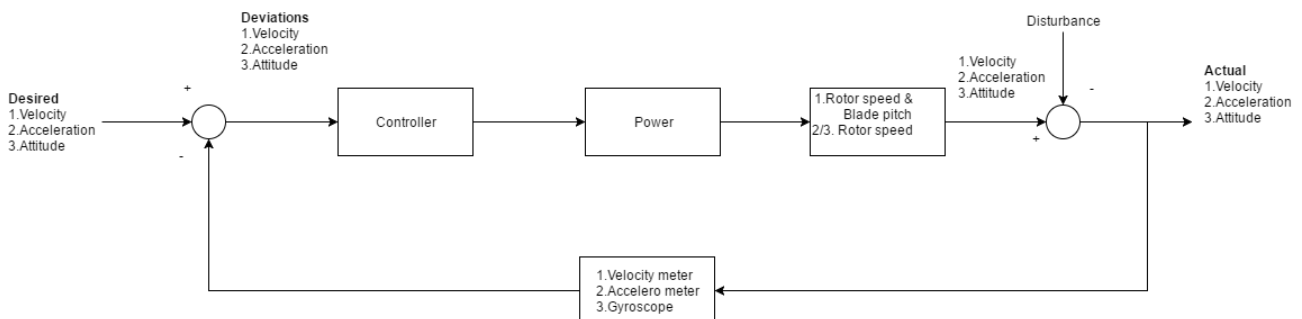


Figure 11.5: Control Flow Diagram: Velocity, Acceleration, Attitude.

## 11.4 Controlling and Stabilising the Drone

Now that the control systems for the HyDrone have been determined a program to control the drone needs to be designed. Firstly a dynamic model which describes the movement of the drone based on the thrust produced by the rotors is formed. Based on this controllers for the different flight phases are constructed. The coaxial configuration is modelled as one rotor to make sure that the amount of equations equals the amount of unknowns.

### 11.4.1 Dynamic Model

The design of the primary base structure is a x-beam which has an inclination. The origin of the x-y-z axis is fixed at the centre of the symmetric x-beam structure with the x-axis pointing forward along the orientation of the beams, the y-axis pointing to the left and the z-axis pointing upwards. An overview of this model is given in fig. 11.6.

As can be seen each rotor produces a thrust in the z direction of the body frame. This is the total thrust produced by the combination of the two coaxial rotors. Furthermore, the rotors opposite to each other rotate

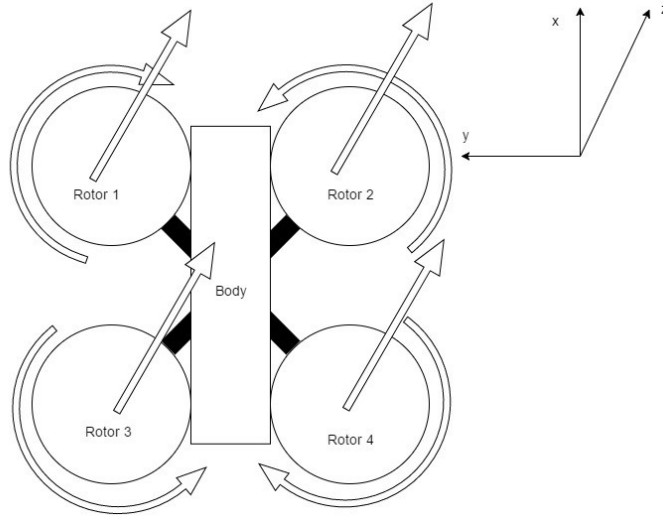


Figure 11.6: Free Body Diagram Control Forces and Torques

in the same direction which is the usual configuration for quadcopter drones. This rotation causes a reaction torque due to the drag of the rotors which is opposite to the direction of rotation. The dynamic model is based on formulas from Gibiansky[65] which were altered for an x-configuration.

### Centre of gravity

Based on weight of the subsystems and their particular place in the design the first step is to determine the centre of gravity (cg) of the HyDrone. The mass distribution is symmetric in the xz-plane, so there is no cg shift in the y direction. The masses of the subsystems and the body are assumed to be point masses. To calculate the cg eq. (11.1) and eq. (11.2) are used.

$$x_{cg} = (m_1x_1 + m_2x_2 + \dots + m_nx_n)/m_{total} \quad (11.1)$$

$$z_{cg} = (m_1z_1 + m_2z_2 + \dots + m_nz_n)/m_{total} \quad (11.2)$$

From this the cg of the HyDrone is determined to be (x;z)=(-8.17;21.93).

### Mass moment of inertia

With the cg of known the mass moment of inertia was determined. The HyDrone was approximated using point masses. At each rotor location there is a point mass  $m_R$  which represents the mass of the rotor, engine, shrouds, pitch system and part of the structure that supports the rotors. The remainder of the mass is represented as a point mass in the middle of the drone. As the drone is symmetrical about the xz plane only a shift of the c.g. of the body in the x and z direction is considered. To calculate the mass moments of inertia eq. (11.3), eq. (11.4) and eq. (11.5) are used.

$$I_{xx} = 4m_R(w_{drone}/2 - r_R)^2 + 4m_Rz_{cg}^2 \quad (11.3)$$

$$I_{yy} = 2m_R(l_{drone}/2 - r_R + x_{cg})^2 + 2m_R(l_{drone}/2 - r_R - x_{cg})^2 + 4m_Rz_{cg}^2 \quad (11.4)$$

$$I_{zz} = 2m_R((l_{drone}/2 - r_R + x_{cg})^2 + (w_{drone}/2 - r_R)^2) + 2m_R((l_{drone}/2 - r_R - x_{cg})^2 + (w_{drone}/2 - r_R)^2) \quad (11.5)$$

The mass moment of inertia of the HyDrone are 369.45, 370.46 and 725.41  $kgm^2$  around the x, y and z axis respectively.

### Body forces

The next step is to identify and calculate all forces that act on the body. As the controller of the drone will control the angular velocity of the rotors a relation between the angular velocity and the thrust produced is needed. This relation is given by eq. (11.6) and acts in the z direction of the body frame.

$$T_b = \left( \frac{K_v K_\tau \sqrt{2\rho A}}{K_t} \omega \right)^2 = k_T \omega^2 = k_T (\omega_1^2 + \omega_2^2 + \omega_3^2 + \omega_4^2) \quad (11.6)$$

In this equation it is assumed that the motor resistance is negligible, the zero torque current is small and momentum theory is used to express the thrust as a function of the air velocity. As the cruise altitude is constant,  $\rho$  is also constant so that a relation between the angular velocity and thrust is found. As the rotor setting and air density is different for all flight phases the  $k$  factor is changed according to the phase the HyDrone

is flying in. The  $k$  factor is based on the provided thrust for a rotational velocity which are given in table 9.1 and table 9.3 in chapter 9. It is assumed that the  $k$  factor stays constant throughout the flight phase.

The drag of the drone is calculated using eq. (11.7). The drags are defined in the body frame in the x, y, and z direction and  $\rho$  is again taken constant for the different flight phases.

$$D_b = C_D \frac{1}{2} \rho v^2 S = k_D v^2 = \begin{bmatrix} k_{Dx} \\ k_{Dy} \\ k_{Dz} \end{bmatrix} \cdot [v_{xb}^2 \quad v_{yb}^2 \quad v_{zb}^2] \quad (11.7)$$

In cruise an extra factor of 150.6  $N$  is added to the drag which represents the lift induced drag.

The lift is calculated using eq. (11.8). The lift acts in the z direction of the body frame and only the velocity in the x and y direction (inertial frame) contribute to the lift.

$$L_b = C_L \frac{1}{2} \rho v^2 S = k_L v_{xy}^2 \quad (11.8)$$

### Acceleration in the inertial frame

Adding these forces and the weight of the HyDrone will give the total forces expressed in the body frame. As the position is expressed in the inertial frame the forces need to be transformed. The inertial frame is a non-moving frame with the z-axis representing the altitude which is perpendicular to the xy-frame with x pointing to the north and y to the west. The transformation matrix is shown in eq. (11.9). Here the body frame is transformed to the inertial frame by undoing the roll, pitch and yaw angle.

$$\begin{bmatrix} \cos(\psi) & \sin(\psi) & 0 \\ -\sin(\psi) & \cos(\psi) & 0 \\ 0 & 0 & 1 \end{bmatrix} \cdot \begin{bmatrix} \cos(\theta) & 0 & -\sin(\theta) \\ 0 & 1 & 0 \\ \sin(\theta) & 0 & \cos(\theta) \end{bmatrix} \cdot \begin{bmatrix} 1 & 0 & 0 \\ 0 & \cos(\phi) & \sin(\phi) \\ 0 & -\sin(\phi) & \cos(\phi) \end{bmatrix} \quad (11.9)$$

All the calculated body forces are multiplied with the  $R$  matrix to get to the inertial frame. Based on these forces the linear accelerations are calculated using eq. (11.10).

$$\begin{bmatrix} a_x \\ a_y \\ a_z \end{bmatrix} = \begin{bmatrix} 0 \\ 0 \\ -g \end{bmatrix} + 1/m \begin{bmatrix} T_x + D_x + L_x \\ T_y + D_y + L_y \\ T_z + D_z + L_z \end{bmatrix} \quad (11.10)$$

**Angular accelerations** After this the angular accelerations were determined. These will be expressed in the body frame as the roll, pitch and yaw angles are also in this frame. The torques are caused by the thrust of the rotors, the drag of the rotors and the moment of the cockpit. The moment of the cockpit is given by eq. (11.11) where again only the velocities in the x and y direction contribute to the moment.

$$M = -C_M \frac{1}{2} \rho v_{xy}^2 S c_{body} \quad (11.11)$$

The torques in the roll, pitch and yaw direction are given in eq. (11.12), eq. (11.13) and eq. (11.14) with their sign determined according to the right hand rule.

$$\tau_\phi = (2.5 - r_R)k(\omega_1^2 - \omega_2^2 + \omega_3^2 - \omega_4^2); \quad (11.12)$$

$$\tau_\theta = (2.5 - r_R - x_{cg})k(-\omega_1^2 - \omega_2^2) + (2.5 - r_R + x_{cg})k(\omega_3^2 + \omega_4^2) + M; \quad (11.13)$$

$$\tau_\psi = b(\omega_1^2 - \omega_2^2 - \omega_3^2 + \omega_4^2); \quad (11.14)$$

Based on these torques the angular accelerations are calculated using eq. (11.15).

$$\begin{bmatrix} \alpha_{phi} \\ \alpha_{theta} \\ \alpha_{psi} \end{bmatrix} = \begin{bmatrix} (I_{yy} - I_{zz})qr/I_{xx} \\ (I_{zz} - I_{xx})pr/I_{yy} \\ (I_{xx} - I_{yy})pq/I_{zz} \end{bmatrix} - I_R \begin{bmatrix} q/I_{xx} \\ -p/I_{yy} \\ 0 \end{bmatrix} (-\omega_1 + \omega_2 + \omega_3 - \omega_4) + \begin{bmatrix} \tau_\phi/I_{xx} \\ \tau_\theta/I_{yy} \\ \tau_\psi/I_{zz} \end{bmatrix} \quad (11.15)$$

With the linear and angular accelerations the position and attitude can be determined. These are acquired by multiplying the accelerations with  $\Delta t$  to obtain the velocities which are then multiplied with  $\Delta t$  to obtain the position and attitude. A  $\Delta t$  of 0.1 s is used as this provide accurate results without requiring too much computational power. For this an iterative program is written in MATLAB in which the initial position, attitude, velocities and accelerations are taken as input. The program is used to investigate the performance of the drone.

## 11.4.2 Controller

In order to stabilise the drone in all flight phases a controller needs to be designed. It was decided to use two types of controllers. The first is able to stabilise the attitude angles of the drone and maintain or change altitude. This will be used to inspect the performance of the drone when deviations as turbulence are applied

to the drone. The second will make sure that the drone can fly to a desired position with a desired cruise velocity. This will be used to assess the nominal performance of the drone and design safety procedures. For both controllers the formulas are based on Luukkonen[66]. These formulas were altered to for an x configuration and suit the specific flight phase.

### First controller

The first controller is a proportional derivative (PD) controller. This controller uses the error and the derivative of the error to calculate the required  $\omega$  of the rotors. A PD controller is used as it provides fast and reliable outputs and it has limited complexity.

For this controller the inputs are the current and desired roll, yaw and pitch angle and angular velocity. Furthermore, the current and desired z position and velocity are specified. From this a desired thrust and torque is calculated which is show in eq. (11.16), eq. (11.17), eq. (11.18) and eq. (11.19). In these equations the proportional and derivative errors are multiplied with their respective gains to calculate the desired thrust and torques. A correction for the lift and moment of the cockpit and a shift in centre of gravity were taken into account.

$$T_d = \left( \frac{-L_z}{m} + g + K_{z,D}(z_d - \dot{z}) + K_{z,P}(z_d - z) \right) \frac{m}{\cos\phi\cos\theta} \quad (11.16)$$

$$\tau_{\phi,d} = \left( K_{\phi,D}(\dot{\phi}_d - \dot{\phi}) + K_{\phi,P}(\phi_d - \phi) \right) I_{xx} \quad (11.17)$$

$$\tau_{\theta,d} = \left( K_{\theta,D}(\dot{\theta}_d - \dot{\theta}) + K_{\theta,P}(\theta_d - \theta) \right) I_{yy} - x_{cg}mg - M \quad (11.18)$$

$$\tau_{\psi,d} = \left( K_{\psi,D}(\dot{\psi}_d - \dot{\psi}) + K_{\psi,P}(\psi_d - \psi) \right) I_{zz} \quad (11.19)$$

The values that come from eq. (11.16) up to and including eq. (11.19) are the required thrust around all body axis to stabilise the drone. These will be achieved by changing the angular velocity of the rotors. In order to calculate the angular velocities eq. (11.20), eq. (11.21), eq. (11.22) and eq. (11.23) are used.

$$\omega_1^2 = \frac{T_d}{4k} + \frac{\tau_{\phi,d}}{4k(2.5 - r_R)} - \frac{\tau_{\theta,d}}{4k(2.5 - r_R - x_{cg})} + \frac{\tau_{\psi,d}}{4b} \quad (11.20)$$

$$\omega_2^2 = \frac{T_d}{4k} - \frac{\tau_{\phi,d}}{4k(2.5 - r_R)} - \frac{\tau_{\theta,d}}{4k(2.5 - r_R - x_{cg})} - \frac{\tau_{\psi,d}}{4b} \quad (11.21)$$

$$\omega_3^2 = \frac{T_d}{4k} + \frac{\tau_{\phi,d}}{4k(2.5 - r_R)} + \frac{\tau_{\theta,d}}{4k(2.5 - r_R + x_{cg})} - \frac{\tau_{\psi,d}}{4b} \quad (11.22)$$

$$\omega_4^2 = \frac{T_d}{4k} - \frac{\tau_{\phi,d}}{4k(2.5 - r_R)} + \frac{\tau_{\theta,d}}{4k(2.5 - r_R + x_{cg})} + \frac{\tau_{\psi,d}}{4b} \quad (11.23)$$

The angular velocities are then put in the dynamic model. Based on this the linear and angular accelerations are calculated which are integrated to obtain the position and attitude.

This controller is tested for several deviating situations including an increase in angular velocity for roll, pitch and yaw and linear velocity in the z direction. The gains used for this controller are presented in table 11.2.

Table 11.2: Gains Controller Deviations

Parameter	Value
$K_{z,D}$	1.0
$K_{z,P}$	0.5
$K_{\phi,D}$	1.75
$K_{\phi,P}$	1
$K_{\theta,D}$	1.75
$K_{\theta,P}$	1
$K_{\psi,D}$	1.75
$K_{\psi,P}$	6

For the attitude changes an initial angular velocity of 60 *deg/s* and for the altitude changes an initial velocity in the z-direction of -5 *m/s* is chosen. The results are presented in fig. 11.7, fig. 11.8, fig. 11.9 and fig. 11.10. In these figures the position, velocity, acceleration, attitude, angular velocity and rotor velocity are plotted. It is important to note that in order for the stabilisation to perform well the deviations should not only damp in a short time. Besides that the rotor velocities should be below their maximum of 366.51 *rad/s* (3500 *RPM*) and the accelerations should feel comfortable which is below 1g.

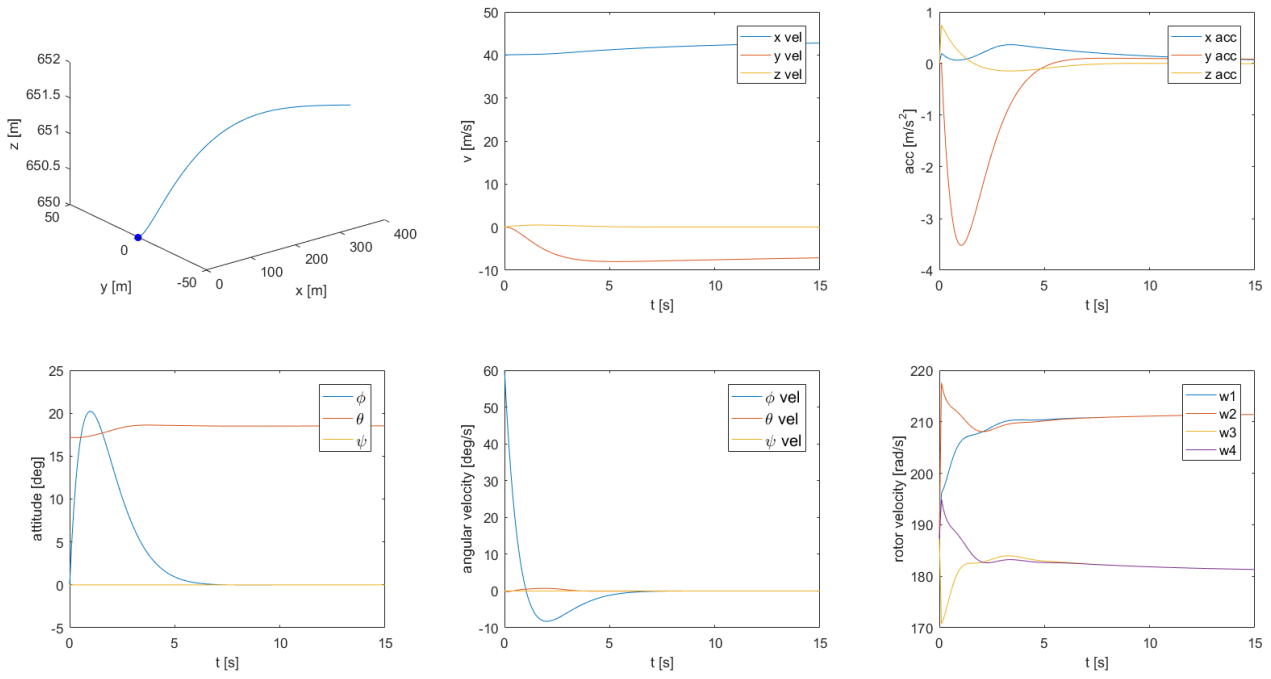


Figure 11.7: Deviation of  $60 \text{ rad/s}$  in  $\phi$  Direction

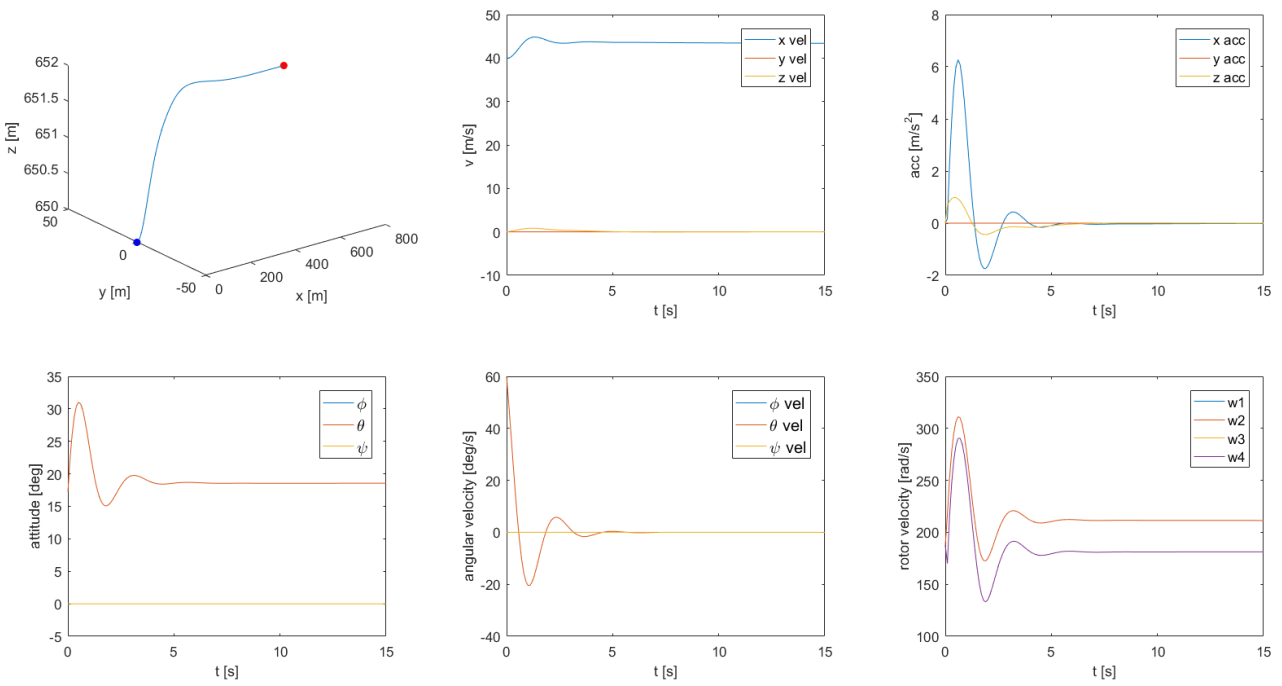


Figure 11.8: Deviation of  $60 \text{ rad/s}$  in  $\theta$  Direction

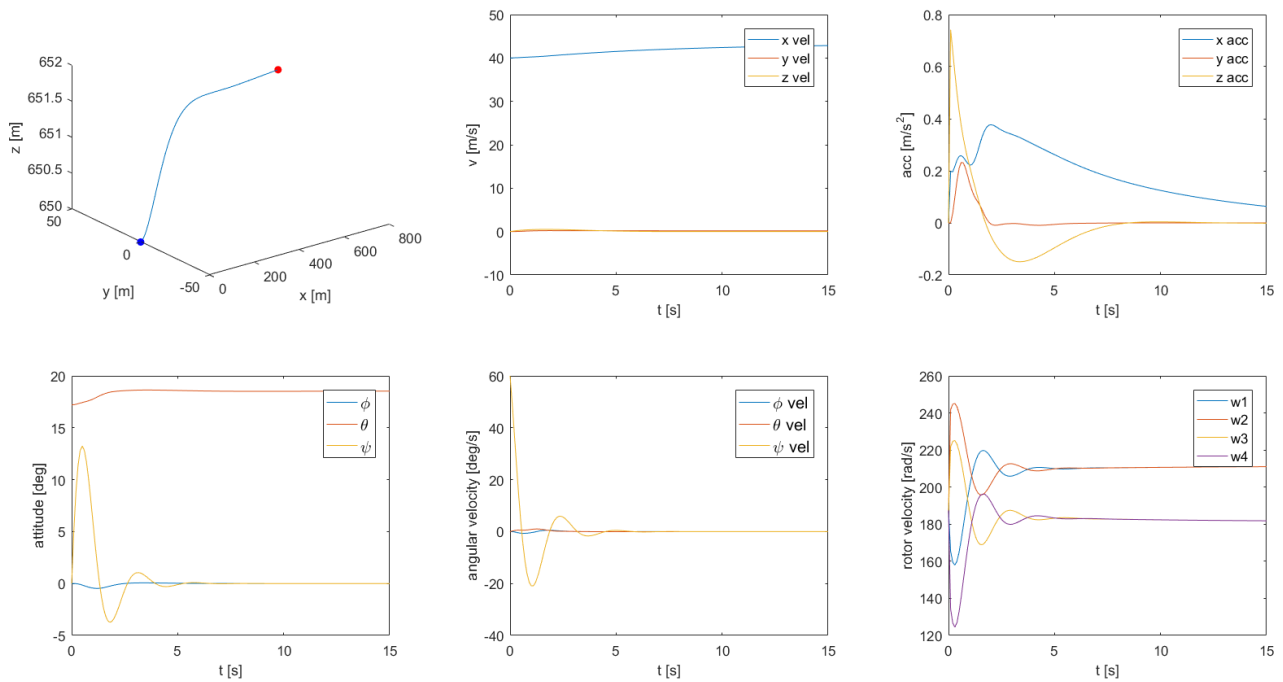


Figure 11.9: Deviation of 60 rad/s in  $\psi$  Direction

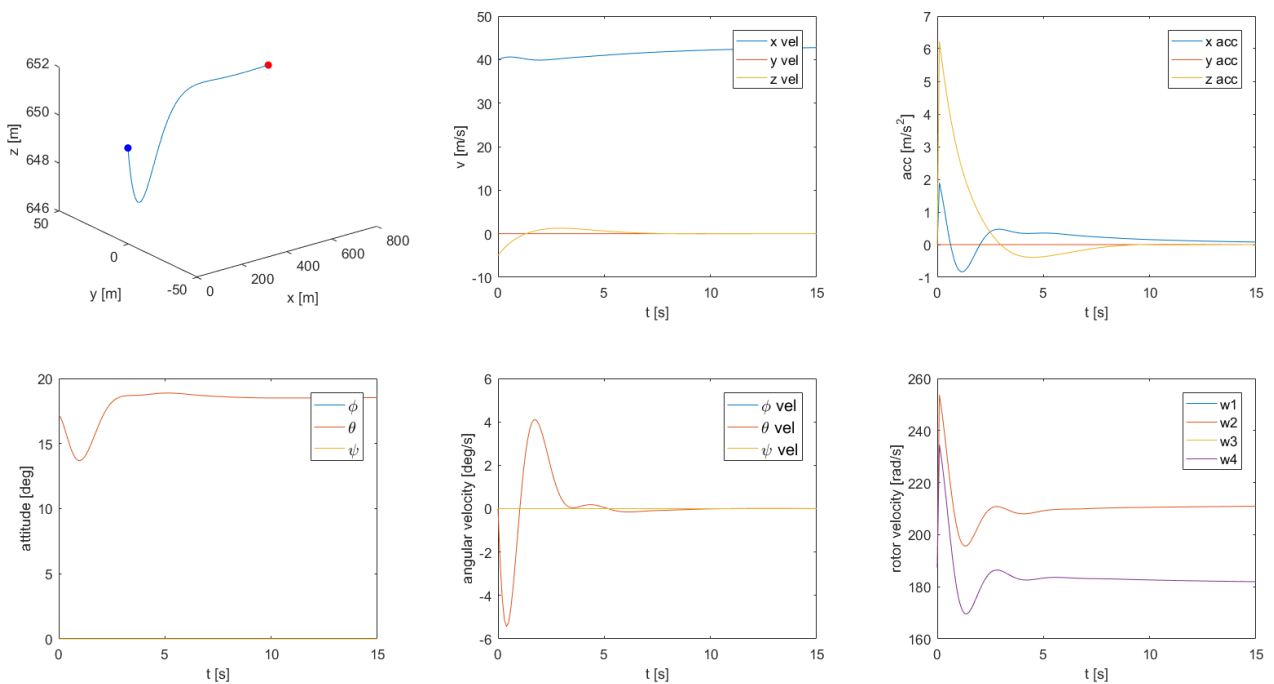


Figure 11.10: Deviation of -5 m/s in Altitude Direction

As can be seen for all situations the HyDrone performs well in terms of stabilising itself. The angles go to zero within approximately five seconds and the z velocity is damped within eight seconds. Furthermore the rotor velocities stay well under their maximum rotational velocity and the accelerations and angular velocities can still be considered comfortable for the passenger.

### Second controller

The second controller enables the HyDrone to automatically fly between waypoints. This will be used to assess the nominal flight performance of the HyDrone and safely land in case of emergency. In this second controller the time of simulation is much larger so that a steady-state-error develops. That is why it was decided to use a proportional-integral-derivative (PID) controller in this case. This controller takes as inputs the current attitude and angular velocities and the current and desired position, velocity and acceleration in all directions.

The first step is to calculate the  $d_x$ ,  $d_y$  and  $d_z$  factors using eq. (11.24), eq. (11.25) and eq. (11.26). These

factors give a relation for how far the HyDrone is from its desired position, velocity and acceleration. In order to minimise the steady-state error the error in the velocities in the x and y direction and the z position are integrated for cruise. As the dynamic model does not use continuous functions but time steps this integration will be the summation of the error multiplied with  $\Delta t$ . Furthermore, for take-off and landing it is not the steady-state-error of the z position that needs to be minimised but rather the z velocity, so that one makes sure that the HyDrone does not land with a velocity that is too high. That is why the controller is changed for this flight phase accordingly.

$$d_x = K_{x,P}(x_d - x) + K_{x,D}(\dot{x}_d - \dot{x}) + K_{x,DD}(\ddot{x}_d - \ddot{x}) + K_{x,I} \int_0^T (\dot{x}_d - \dot{x}) dt \quad (11.24)$$

$$d_y = K_{y,P}(y_d - y) + K_{y,D}(\dot{y}_d - \dot{y}) + K_{y,DD}(\ddot{y}_d - \ddot{y}) + K_{y,I} \int_0^T (\dot{y}_d - \dot{y}) dt \quad (11.25)$$

$$d_z = K_{z,P}(z_d - z) + K_{z,D}(\dot{z}_d - \dot{z}) + K_{z,DD}(\ddot{z}_d - \ddot{z}) + K_{z,I} \int_0^T (\dot{z}_d - \dot{z}) dt \quad (11.26)$$

Based on the above determined factors the desired roll, pitch and yaw angles are determined using eq. (11.27), eq. (11.28) and eq. (11.29). The position of the HyDrone is controlled by changing the roll and pitch angle. The yaw angle follows the angle that is made between the x and y velocity so that the HyDrone is always pointed in the direction of flight which is most comfortable for the passenger. The angular velocities are then obtained by dividing the desired angles by the time it should take to get to this angle. The desired angles and angular velocities are inserted in eq. (11.17), eq. (11.18) and eq. (11.19) to get the desired torques. The desired thrust is calculated using eq. (11.30).

$$\phi_d = \arcsin \left( \frac{d_x \sin(\psi) - d_y \cos(\psi)}{\sqrt{d_x^2 + d_y^2 + (d_z + g)^2}} \right) \quad (11.27)$$

$$\theta_d = \arctan \left( \frac{d_x \cos(\psi) - d_y \sin(\psi)}{d_z + g} \right) \quad (11.28)$$

$$\psi_d = \arctan \left( \frac{\dot{y}}{\dot{x}} \right) \quad (11.29)$$

$$T_d = m \left( (d_z - L_x/m) (\sin(\theta) \cos(\psi) \cos(\phi) + \sin(\psi) \cos(\phi)) + (d_y - L_y/m) \cdot \right. \\ \left. ((\sin(\theta) \sin(\psi) \cos(\phi) - \cos(\psi) \sin(\phi)) + (d_z + g - L_z/m) \cos(\theta) \cos(\phi)) \right) \quad (11.30)$$

Finally the desired torques and thrust are inserted in eq. (11.20), eq. (11.21), eq. (11.22) and eq. (11.23) which are used in the dynamic model to obtain the position and attitude.

This controller was tested for different situations. The first objective was to design a controller which is applicable for all these situations. Still it early became clear that this was not feasible with this type of controller. For example the gains needed in cruise show a large difference with the gains used for landing. Furthermore, as already described the error in the z direction is integrated for cruise while for take-off and landing the velocity in the z direction is integrated. That is why a different controller was designed for the different flight phases. The gains of each controller are presented in tables at the end of this section for a compact overview. Finally for all phases a time that an angle should be achieved is stated. This was tuned the same way as the gains, namely by trial and error.

### Nominal take-off and landing

The first phase that will be investigated are take-off and landing for nominal conditions. According to the mission profile these should both take approximately 60 s excluding loiter time which results in a vertical velocity of 11.818 m/s. The gains used for both take-off and landing are shown in table 11.3. The time for an angle to be achieved is set to 2 s.

The take-off procedure is shown in fig. 11.11a and landing is shown in fig. 11.11b. As can be seen during take-off the HyDrone is accelerated to a velocity close to 11.818 to an altitude of 630 m from here it goes into the cruise phase which is described in the next section. For landing the HyDrone first brakes down to a velocity of 0 m/s from there it performs a vertical landing again with a velocity of approximately 11.818 m/s. The landing procedure takes a little longer as the HyDrone first needs to accelerate downwards and then minimise its velocity when it hits the ground. During landing the maximum rotational velocity is 302 rad/s which produces a thrust of 1459 N. When taking off the maximum rotational velocity is 230 rad/s which produces a thrust of 1788 N. This difference in combination of thrust produced for a certain rotational velocity can be found in the  $k_T$  factor which is significantly smaller for landing than for take-off.

### Cruise

The cruise phase is started from an altitude of 630 m with a velocity in the z direction of 11.818 m/s which is the climb velocity. From here the HyDrone is directed to a forwards velocity of 40 m/s at an altitude of 650 m till it reaches the nominal range of 30 km. The gains used in this phase are presented in table 11.4. As the angular velocities should be minimised the time for an angle to be achieved is set to 10<sup>9</sup> s. This might seem

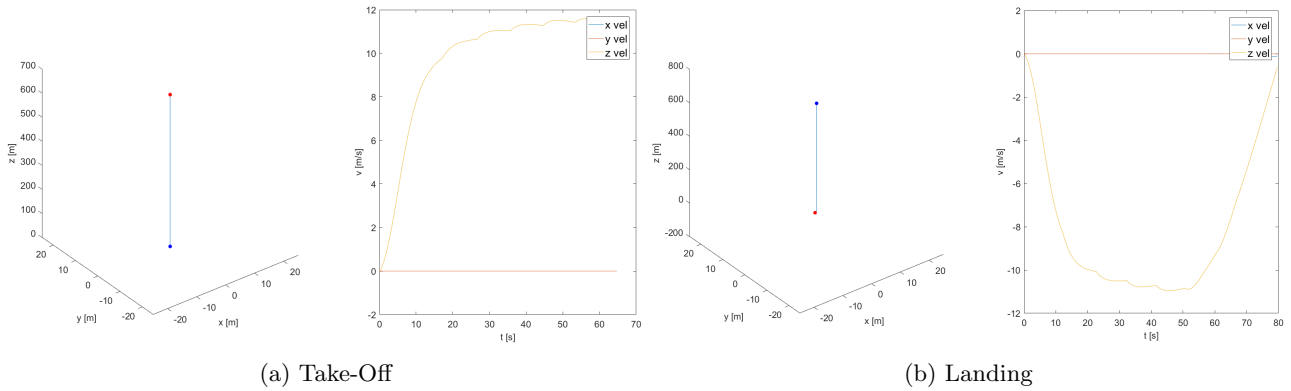


Figure 11.11: Nominal Flight Take-Off and Landing at 11.818  $m/s$

high but it makes sure that the changes in attitude during cruise are negligibly small as the required angular velocity goes to zero.

The plot for cruise is shown in fig. 11.12. As can be seen at the start of the phase there is much angle deflection in the pitch direction. This is in order to get to the stable flying condition at an angle of approximately  $18^\circ$  at a velocity of  $40 m/s$ . Furthermore, it can be noted that the two rotors at the front rotate at a higher velocity than the ones at the back. This is in order to compensate for the moment that is created by the lifting body. Rotating at approximately  $205 rad/s$  the front rotors produce a thrust of  $1572 N$  each while the back rotors which rotate at approximately  $180 rad/s$  produce a thrust of  $1211 N$  in cruise. The maximum rotational velocity to get into cruise is  $226 rad/s$  so that the back rotors produce  $1910 N$  thrust.

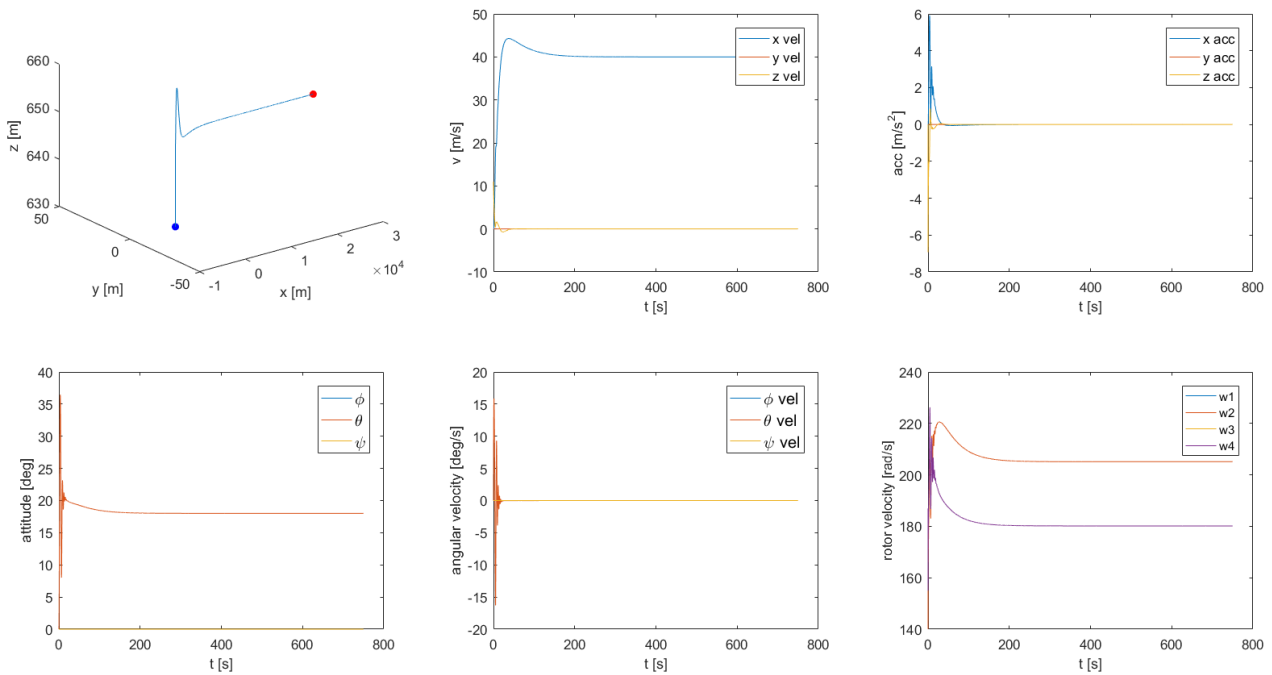


Figure 11.12: Cruise Phase at 650  $m$  Altitude and 40  $m/s$

## Manoeuvre

During cruise it might happen that the HyDrone needs to evade an obstacle. For this a manoeuvring phase is designed. In this manoeuvre the HyDrone roll over so that it moves 100 m in the positive y direction. The gains for this manoeuvre are presented in table 11.5. The time for the angles to be achieved is set to 10 s.

The plot for the manoeuvre is shown in fig. 11.13. As can be seen the HyDrone reaches a roll angle of 40 deg so that it reaches a velocity in the y direction of more than 10 m/s with a acceleration of approximately  $7 \text{ m/s}^2$ . During this manoeuvre the HyDrone increases its altitude with one meter which can be later corrected when it returns back to the cruise phase. Rotor two has the largest rotational velocity of 270  $\text{rad/s}$  which produces a thrust of 2726 N. At the end of the manoeuvre the HyDrone gets back into cruise conditions.

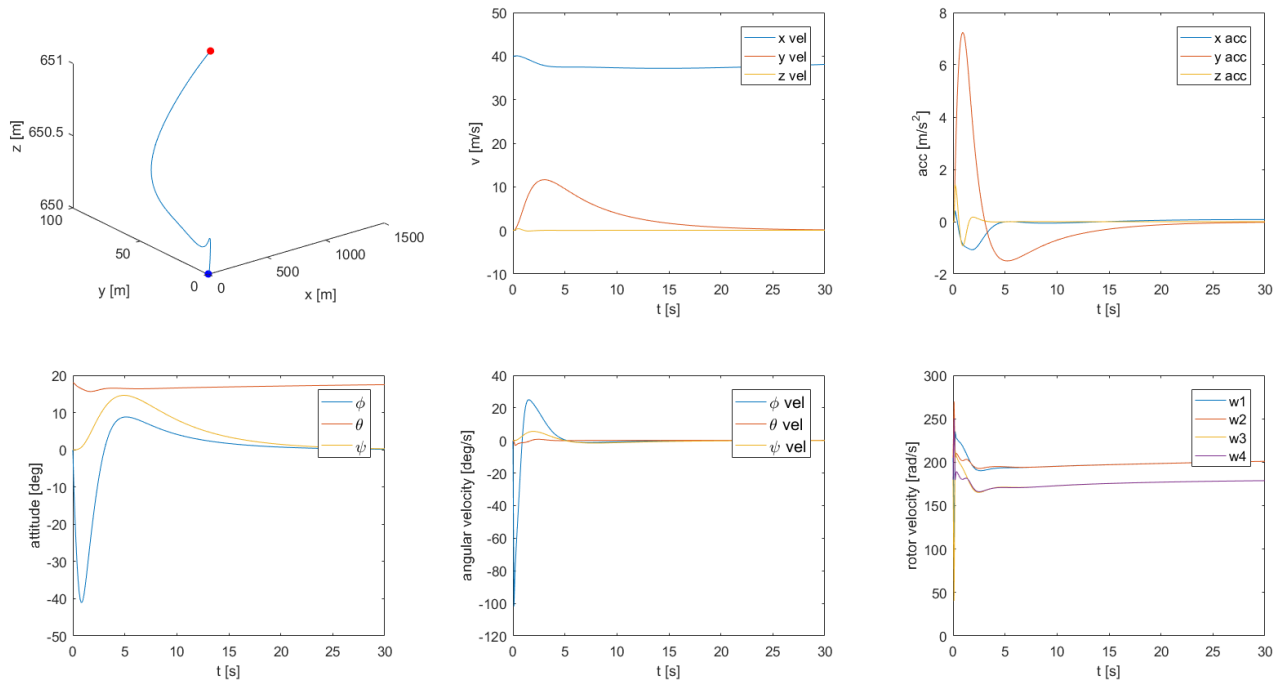


Figure 11.13: Manoeuvre 100 m in the Y-Direction

## Emergency Landing

A nominal landing will involve the HyDrone to slow down and then reduce altitude. As it is of more interest from a control point of view, whether the HyDrone can land anywhere, it was decided to look into the possibilities of landing at the exact x and y location from where the landing is initiated. This would be useful for example when the GPS system fails and the HyDrone needs to land immediately. The gains needed to tune controller are presented in table 11.6. The time for the angles to be achieved is set to 1 s.

The plots for landing are shown in fig. 11.14. As can be seen the HyDrone quickly decelerates by decreasing the pitch angle and thrust. The minimum pitch angle is 16deg. As the body is already at an angle with the rotors the angle perceived by the passenger will be approximately -30deg. This can still be considered reasonable especially when one realises that this type of deceleration is not present in nominal landing. The jumps in the rotational velocities of the rotors are caused by waypoints needed to get the velocity in the z direction to almost zero when landing. It is interesting to note that the thrust is so much decreased that it reaches a negative rotor velocity. In reality this would not be efficient but instead the pitch would be set to a negative angle. As the program does not take this into account this is now represented by a negative rotational velocity which does have the same effect in the model. The minimum rotational velocity during landing is in the back rotors which is 152  $\text{rad/s}$ . This produces a minimal thrust of -864 N. The maximum rotor velocity is 211  $\text{rad/s}$  which produces a thrust of 1665 N by the aft rotors.

## Safety

The final procedure that will be considered is related to safety. A look is taken into whether the drone is still able to safely land when two rotors stop working. It is assumed that these two rotors are not in the same coaxial system. With this assumption taken into account the most critical case is considered. This is when from each front rotor coaxial system one rotor fails. The front rotors are considered most critical as they need to produce most thrust in cruise. In order to model this the  $k$  factor is multiplied with 0.4. This is based on the assumption that when the upper rotor fails only 40% of the total thrust is generated with the same rotational velocity of the rotors. The gains needed to tune are shown in table 11.7. Again the time for the angles to be achieved is set to 1 s.

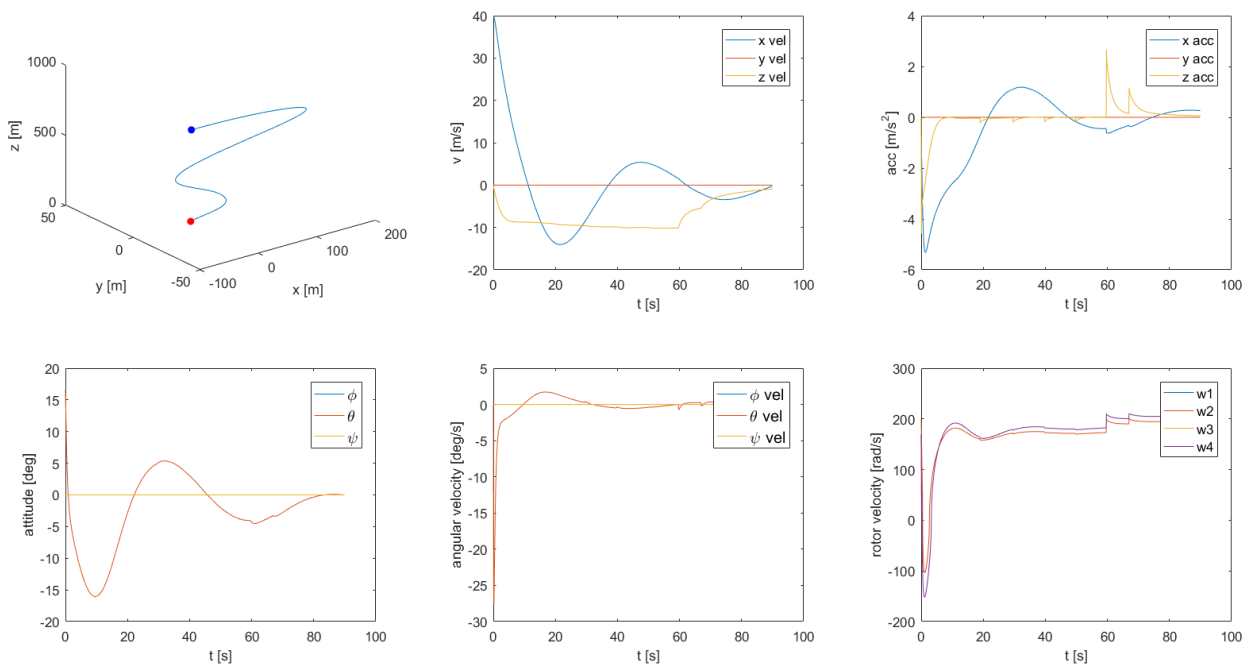


Figure 11.14: Emergency Landing with Braking

The plots for the safety procedure are shown in fig. 11.15. As can be seen the front rotors need to rotate at a much higher velocity in order to compensate for the lost of one rotor. Still the HyDrone is able to stabilise fairly well and land close to the desired location where  $x$  and  $y$  are zero. The maximum pitch angle is quite large at more than  $20^\circ$  especially when considering the angle between the rotors and the body. Still this is an emergency procedure so this should not be a problem. The maximum rotational velocity is  $316 \text{ rad/s}$  which produces a thrust of  $1494 \text{ N}$ . The maximum velocity of the aft rotors is  $214 \text{ rad/s}$  which produces a thrust of  $1713 \text{ N}$ .

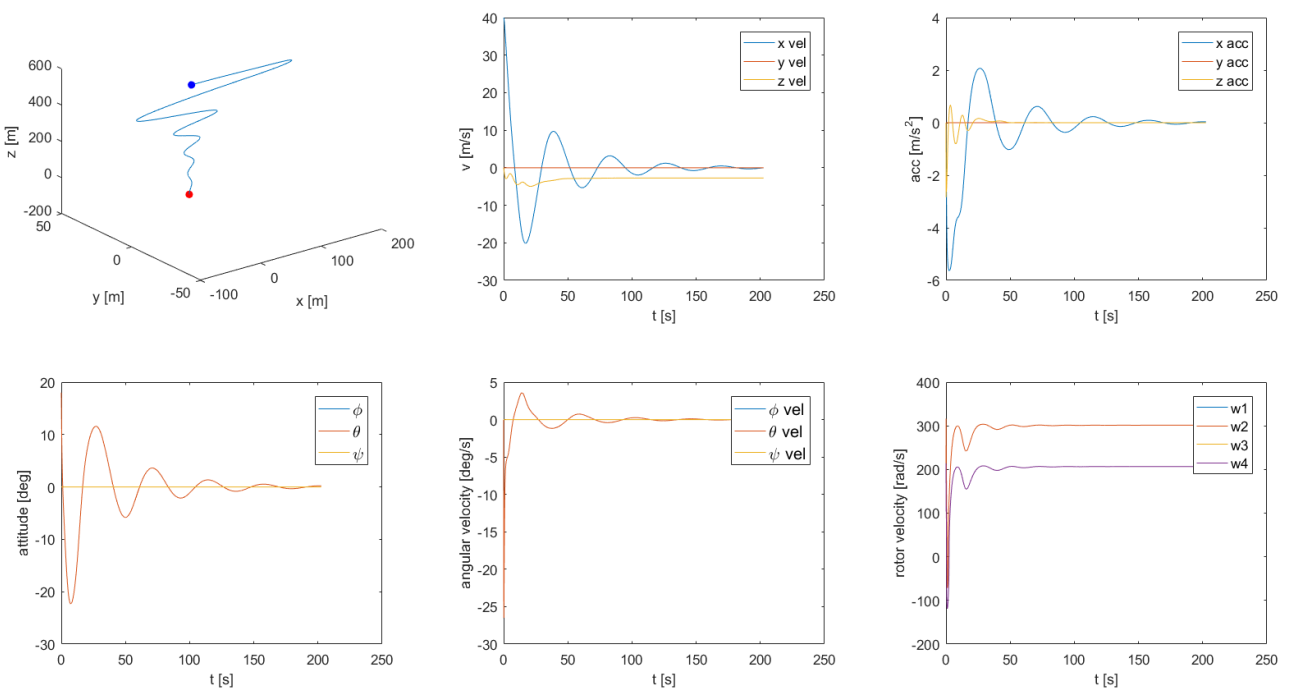


Figure 11.15: Safety Landing with Two Rotors Failing

Table 11.3: Gains Take-Off and Landing

Variable i	Parameter Value			
	$K_{i,P}$	$K_{i,D}$	$k_{i,DD}$	$K_{i,I}$
x	0.285	0.995	$1.00 \cdot 10^{-3}$	0.20
y	$8.55 \cdot 10^{-2}$	$7.5 \cdot 10^{-2}$	0.01	0.20
z	$1.85 \cdot 10^{-3}$	$5.5 \cdot 10^{-3}$	$1.00 \cdot 10^{-5}$	$2 \cdot 10^{-2}$
$\phi$	21.0	10.0		
$\theta$	$5 \cdot 10^{-3}$	0.075		
$\psi$	4.00	7.50		

Table 11.4: Gains Cruise

Variable i	Parameter Value			
	$K_{i,P}$	$K_{i,D}$	$k_{i,DD}$	$K_{i,I}$
x	$1.85 \cdot 10^{-8}$	$1.95 \cdot 10^{-2}$	$1.00 \cdot 10^{-8}$	$2 \cdot 10^{-2}$
y	$8.55 \cdot 10^{-8}$	$5.95 \cdot 10^{-2}$	0.10	0.20
z	0.19	0.75	0.10	$2 \cdot 10^{-2}$
$\phi$	$3.00 \cdot 10^{-2}$	7.50		
$\theta$	0.30	0.75		
$\psi$	$3 \cdot 10^{-2}$	$7.5 \cdot 10^{-3}$		

Table 11.5: Gains Manoeuvre

Variable i	Parameter Value			
	$K_{i,P}$	$K_{i,D}$	$k_{i,DD}$	$K_{i,I}$
x	$1.85 \cdot 10^{-4}$	$5.95 \cdot 10^{-2}$	$1.00 \cdot 10^{-3}$	$2 \cdot 10^{-2}$
y	$8.55 \cdot 10^{-2}$	$7.5 \cdot 10^{-1}$	$1 \cdot 10^{-2}$	$2 \cdot 10^{-2}$
z	$1.85 \cdot 10^{-3}$	5.50	0.10	$2 \cdot 10^{-2}$
$\phi$	21.0	10.0		
$\theta$	$5 \cdot 10^{-3}$	7.50		
$\psi$	4.00	7.50		

Table 11.6: Gains Emergency Landing

Variable i	Parameter Value			
	$K_{i,P}$	$K_{i,D}$	$k_{i,DD}$	$K_{i,I}$
x	$1.85 \cdot 10^{-3}$	$5.95 \cdot 10^{-2}$	$1.00 \cdot 10^{-3}$	$2 \cdot 10^{-2}$
y	$8.55 \cdot 10^{-2}$	$7.5 \cdot 10^{-2}$	$1 \cdot 10^{-2}$	$2 \cdot 10^{-2}$
z	$1.85 \cdot 10^{-3}$	0.35	0.10	$2 \cdot 10^{-2}$
$\phi$	21.0	10.0		
$\theta$	$5 \cdot 10^{-3}$	7.50		
$\psi$	4.00	7.50		

Table 11.7: Gains Safety Landing

Variable i	Parameter Value			
	$K_{i,P}$	$K_{i,D}$	$k_{i,DD}$	$K_{i,I}$
x	$1.85 \cdot 10^{-4}$	$5.95 \cdot 10^{-2}$	$1.00 \cdot 10^{-3}$	$2 \cdot 10^{-2}$
y	$8.55 \cdot 10^{-2}$	$7.5 \cdot 10^{-2}$	$1 \cdot 10^{-2}$	$2 \cdot 10^{-2}$
z	$1.85 \cdot 10^{-3}$	0.25	0.10	$2 \cdot 10^{-2}$
$\phi$	21.0	10.0		
$\theta$	$5 \cdot 10^{-3}$	7.50		
$\psi$	4.00	7.50		

### 11.4.3 Sensitivity Analysis

In order to test the robustness of the program a sensitivity analysis is performed.

**Gains** During the tuning of the gains, it was already found that these are rather sensitive. Especially for procedures which includes much unsteady movement as a manoeuvre or landing. Also for the cruise condition

---

changes in the gains can result in large differences and destabilisation. This is caused by the large time of simulation so that any small disturbance due to incorrect tuning results in a large one. Overall the gains are thus fairly sensitive and can not be changed without affecting the performance in a large way.

**Centre of Gravity** Another interesting aspect that can be investigated in terms of sensitivity is a shift in the centre of gravity. This has two reasons: firstly the calculated centre of gravity might change due to changes in the weights or placement of the different subsystems and secondly the payload that is taken with the the HyDrone can be distributed in different ways which changes the centre of gravity. The shift in the x direction will have the largest influence on the performance of the HyDrone as this large changes the  $\tau_\theta$ . That is why this shift will be considered. Furthermore, only the cruise phase is considered as this shows the nominal performance of the drone. With the same gains the centre of gravity can be moved backward till  $-0.17\text{ m}$  and forwards till  $-0.01\text{ m}$ . This seems a good result as the centre of gravity is not expected to change by much. Furthermore, the current centre of gravity lays between the two boundaries so that there is still a margin in both the positive and negative x direction.

**Lifting body characteristics** The body of the HyDrone generates lift so that less thrust needs to be produced. In creating this lift also drag and a moment around the y-axis is produced. The constants  $C_L$ ,  $C_D$  and  $C_M$  are based on estimations and might vary in the final design. Looking at the critical case a decrease in  $C_L$ , increase in  $C_D$  and increase in  $C_M$  is considered. Again a look is taken into the cruise condition. Decreasing the  $C_L$  with 20% makes the rotors rotate faster in order to compensate for the lost in lift. Still the HyDrone performs well. The same hold for an increase in the  $C_D$  of 20%. If the  $C_M$  is increased by 20% the front rotors rotate at a higher velocity and the aft at a lower. This to compensate for the larger moment while still maintaining the same total thrust to stay at the same altitude. Thus changing the characteristics of the lifting body does influence the way the HyDrone cruises but the same performance can be achieved.

**Rotor Characteristics** Finally a look will be taken into a change in the performance of the rotors. This will be done in the same way for the safety procedure, but now all  $k$  factors of the rotors will be decreased by 20%. This does not change the cruise conditions of the HyDrone much besides the fact that the rotors need to rotate faster in order to produce the same amount of thrust.

In conclusion the program that controls and stabilises the drone can be considered robust except for changes in the gains. These need to be selected carefully in order for the HyDrone to perform optimally.

#### 11.4.4 Verification & Validation

In order to verify the code both a unit and a system test were carried out. The difference units include the transformation matrix, thrust, lift, drag, moment, linear and angular acceleration and the controller. For the transformation matrix it was found that at first it produced results that were opposite to what was expected. For example a roll in the positive direction resulted in a body force in the z direction transformed partly to the positive y direction in the inertial frame. Due to this it was realised that the angles that transform the body frame to the inertial frame are the negative roll, pitch and yaw angles. Furthermore, the drag constant  $k_d$  was multiplied with the velocity squared to obtain the drag. It was realised that using this method the direction of the velocity can not be taken into account. This was solved by multiplying the squared velocity with the sign of the velocity to obtain the correct factor. Finally for the controller at first the moment caused by a shift in the centre of gravity was not taken into account. This way the HyDrone was never able to stabilise itself around the y axis. The shift was later added to the controller. The remainder of the units showed the expected results so that with the changes all units could be verified.

The system test is performed setting parameters to zero and checking whether the results is as expected. Firstly the  $k$  factor which relates the rotational velocity with the thrust is set to zero. It was found that this causes divisions by zero so that that no results could be calculated. That is why the  $k$  was set to  $10^{-9}$ . This causes the rotors to rotate at a very high velocity to try and generate some thrust. Secondly the mass was set to zero but this again caused divisions by zero so that it was set to  $10^{-9}$ . This causes the HyDrone to fly away at a very high velocity which makes sense as only a small thrust produces a large acceleration. Finally the gains of the controller were set to zero. If the starting values were unsteady, for example an angular velocity, this causes unstable flight behaviour for the HyDrone as the motion is not damped. Still if the HyDrone starts in a stable condition it stays stable only correcting for the moment a centre of gravity shift. The motion is not damped but stays the same. As a results are as expected the program could be verified.

A method to validate the program would be to test it on a real drone. This could also be a smaller scale model which would be easier to manufacture result in less losses when it crashes. The data acquired should then be compared with the data from the program. Based on this it can be investigated whether the controller calculates the relevant parameters to control and stabilise the drone. Furthermore, the dynamic model can be

compared with the real data in order to check whether it performs well at estimating the position and attitude of the drone.

## 11.5 Technical Risks

Evaluating the technical risk of the control & stability subsystem is an important tool to ensure the quality and safety of the design. A technical risk map was made to graphically represent this. The following risks were assessed

- |                |                              |
|----------------|------------------------------|
| 1. Blade pitch | 5. Processor                 |
| 2. GPS         | 6. Autonomous software       |
| 3. LIDAR       | 7. Gyroscope & Accelerometer |
| 4. RADAR       | 8. 4G                        |

This technical risk assessment is focused on the safety of the design and the capability to meet its performance requirements. The probability of failure of a component and the consequence on the safety of the design is plotted in table 11.8. For determining the effect on the HyDrone project the amount of redundancy is taken into account and if a save landing can be performed if failure occurs of the particular system.

Table 11.8: Technical Risk Map: Control & Stability Subsystem

Feasible in Theory				1
Working Laboratory Model		6		
Based on Existing Non-Flight Engineering		3,5		
Extrapolated from Existing Flight Design	2,8			
Proven Flight Design		4		7
	Negligible	Marginal	Critical	Catastrophic

### Blade pitch

In table 11.8 it can be seen that only the pitch system contains an unacceptable high risk. The risk should be mitigated in order to make it acceptable for this from scratch designed pitch concept. The mitigation of this risk can only be performed by making a laboratory model which will be subjected to various test. After these test a better view will be given about the feasibility in reality and reliability.

### GPS

The GPS system is a proven flight design and is only used for monitoring and navigating where the drone has to go by the central server. In case of failure there is always a second GPS system and nevertheless the GPS system is neither used for stability nor control, it's just for positioning. The LIDAR and RADAR system can always find a way to a appropriate landing spot.

### LIDAR

The LIDAR system is till now only used for remote sensing mapping by air crafts but not for navigating. In the car industry the LIDAR system is used for navigating by companies as Uber and Google as mentioned in section 11.2. So therefore it is based on non flight engineering. Due to the multiple LIDAR sensors redundancy is taken into account and therefore failure hardly impact the control of the HyDrone.

### RADAR

The radar system is nowadays common on vehicles, aircraft and drones. In the design there is no redundancy taken into account for the particular radars ( Front, back , and top side) because in case one malfunctions the drone will continue the flight in the direction of the remaining working radars. At the front 3 radars are present so the drone can continue the flight in the preferred direction if one fails.

### Processor

The processor processes all the flight data measured by the sensors and calculates the strategy how to act on it. The processor can malfunction due to an electrical power peak, overheating or defaulting components. Therefore always a back up processor is available which can take over the data processing of the defaulted processor.

### Autonomous software

The autonomous system contains the strategy how to act on the measurements the sensors are sending to the processor. This software may contain an unknown bug which for example can not handle certain circumstances or situation to which the HyDrone is exposed at that moment. If the sensors register movements of the drone which are out of the boundaries where in the drone should fly, the emergency autonomous system is activated which sets in the landing procedure. The effect of a bug in the autonomous software on the HyDrone project is strongly reduced by the risk spread out over the total number of operating HyDrones as mentioned and is elaborated before in section 11.2.2.

---

## Gyroscope & Accelerometer

The Gyroscope and accelerometer are used for determining the movements and the attitude of the HyDrone. To account for redundancy 2 accelerometers and gyroscopes are used. If these 2 both fail the HyDrone becomes uncontrollable and can not perform a save landing even not in auto rotation mode. Due to no information about attitude and movements for the safety system for balancing the HyDrone in auto rotation mode. Even if the risk is spread out over the total fleet of HyDrones the result when failure occurs is catastrophic for the HyDrone and especially for the passenger.

### 4G

The 4G data network is used for receiving and sending data. To account for redundancy 2 4G data dongles are used. If the two data dongles fail than the drone can safely land on a appropriate landing spot. The 4G data connection does not influence the control and stability of the HyDrone at all. The only drawback is that there is no communication with the central data server, so it's unable to get information about the position of the HyDrone.

After mitigation in table 11.9 the risk of the blade pitch system should be marginal on the HyDrone otherwise the blade pitch system is not feasible in reality and should be excluded from the design to decrease the risk of failure of the HyDrone. In case of pitch system failure the drone should perform a safe landing due to the lock up system. Due to the 8 pitch systems on the drone one failing pitch system should not have an influence on the safety but only on the efficiency of the flight. The probability of multiple failing blade pitch systems is negligible and if it happens than the probability of occurrence is spread out over the total number of HyDrone resulting in an even lower probability and effect on the HyDrone project.

Due to be able to perform a safe landing and the low probability of occurrence the pitch system is classified into marginal influence on the HyDrone project based on a working laboratory model.

Table 11.9: Technical Risk Map: Control & Stability Subsystem After Mitigation

Feasible in Theory				
Working Laboratory Model		1,6		
Based on Existing Non-Flight Engineering		3,5		
Extrapolated from Existing Flight Design	2,8			
Proven Flight Design		4		7
	Negligible	Marginal	Critical	Catastrophic

## 11.6 Recommendations

The main recommendation from the control and stability section is to take a more in-depth look into tuning the controllers. As followed from the sensitivity analysis they have a large influence on the performance of the HyDrone. Therefore it is crucial that they are tuned in the most optimal way. Until now the controllers have been tuned by hand by running the program until the HyDrone showed stable performance. Still this does not mean that the used gains are the optimal ones. Furthermore, tuning by hand has the consequence that for all the different flight phases different gains are used and makes it impossible to find a set of gains that can be applied in all flight phases. That is why a method which can automatically find the optimal optimal gains for the controllers would be of great use. Research is done into automatic tuning for example by Gaing[67]. Applying such technique would make the whole control design more robust. Besides this a careful look needs to be taken into the pitch system. As this has never been used in flight design at least a laboratory model should be made to test the performance of this system. This also includes taken into account whether the engines can operate accurately to provide the required RPM. Finally extra research should be done in the lock up system so that constant pitch can be assured even in case of engine failure.



---

# Chapter 12: Safety System

Maybe the most important of all for the design of the HyDrone is the safety system. As opposed to conventional drones, the HyDrone will carry a passenger which makes safety all the more significant. Therefore a study has been performed on safety systems so that hazards to the passenger and residents of the city in which the drone shall be operated are avoided.

Figure 12.1 shows the amount of accidents and fatalities of small helicopters, which operate in a similar manner, per year, from which can be concluded that there is a lot of room for improvement on safety measurements for rotorcraft. Designing for safety is an integral process and is accounted for on every subsystem level as has been discussed in the previous chapters.

Safety is approached from multiple perspectives, from redundancy built in critical systems and measures to decrease the probability or impact of risks. This chapter will discuss the latter and focuses on the stand alone safety subsystems which are not directly linked to any specific subsystem.

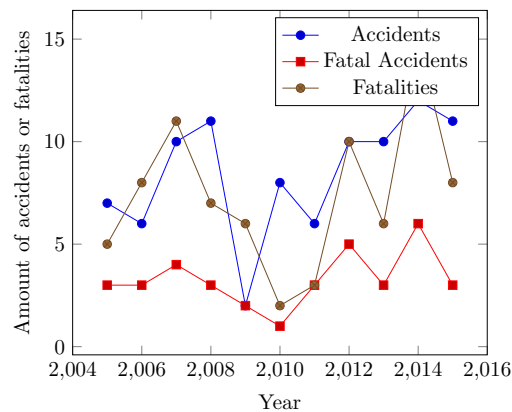


Figure 12.1: Registered Accidents and Fatal Accidents of light (less than 1000kg) helicopters per year

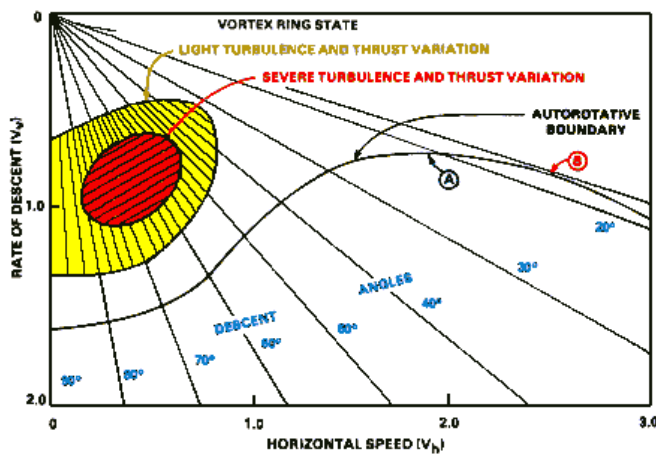
## 12.1 Autorotation

One system which is commonly used in rotorcraft is autorotation. During engine failure the main rotor(s) of the aircraft are disengaged from the engine shaft and rotate by the action of the air moving up through the rotor while the vehicle descends.

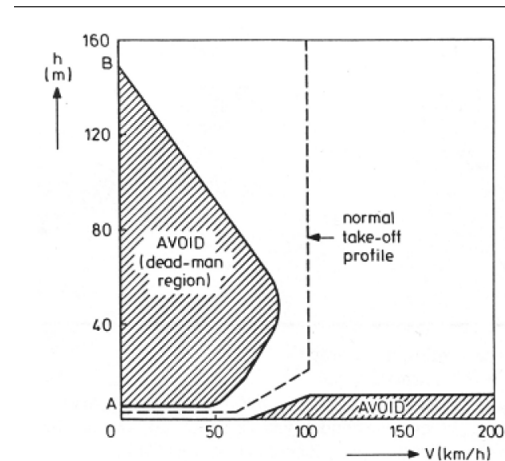
### 12.1.1 Autorotation Manoeuvre Principle

In autorotation a freewheeling unit in combination with the aerodynamics forces of the air passing through the rotor blades maintain the rotors angular velocity. The freewheeling unit can operate by a sprag clutch mechanism which disengages from the engine when the rotational velocity of the engine is lower than the rotor. In case of engine failure this results in a completely disengaged main rotor which allows it to rotate freely. At the instant of engine failure the vehicle is producing lift and thrust from its initial angle of attack and velocity. By lowering the attitude of the vehicle and rotors' blade pitch, lift and drag is reduced and the aircraft will start to descend which creates an upwards flow through the rotor. This creates a sufficient thrust to maintain the rotors rotational speed. Before touchdown the pitch is increased and collective blade pitch as well which uses the momentum of the blades to increase the lift and drag to ensure a soft landing.

The rate of descent is among other things dependent on density, gross weight and rotor rotational speed but can mainly be controlled by the airspeed. The descent rate is high at zero velocity and reaches a minimum at horizontal velocities around 20 and 35 m/s. Figure 12.2a shows this co-relation; the optimal velocity for a minimum descend rate is denoted by 'A' and the velocity for the shortest horizontal flight path is denoted by 'B'. The optimal glide angle is usually between 17° and 20° degrees. For helicopters even at a flight speed of zero the rotor is quite effective and has a drag coefficient of nearly the same as a parachute. The height which is required to perform an autorotation emergency manoeuvre can be seen in figure 12.2b. There are 2 regions in which it is dangerous for the aircraft and passengers to initiate auto rotation: There is a region at which the height is insufficient to provide enough forward movement to decrease the rate of descent and a region at low heights where the aircraft has too little time to perform a flare manoeuvre. Therefore during an ordinary take off procedure the aircraft first generates forward velocity after lift off and when a certain velocity is reached it starts to climb.



(a) descend rate vs. horizontal speed diagram of a typical helicopter



(b) Height vs velocity to safely perform autorotation

Figure 12.2: Optimal flight conditions for Autorotation

### 12.1.2 Autorotation for the HyDrone

Autorotation for the HyDrone will work with the same basic principles but differs in some aspects because of its multiple rotors and because they are coaxial as well. However, yaw control during autorotation is a separate issue. Normally, HyDrone controls its yaw by attempting to introduce a torque differential between the propellers. This is done by increasing the blade pitch of the propellers that rotate in the same direction. As a result of increasing the blade pitch of propeller blades rotating in the same direction produces this torque. However, during autorotation the rotors no longer provide torque to drive the main rotor but are driven by the airflow. The generated thrust is lower and differentiating the blade pitch is insufficient for yaw control. For helicopters this problem is counteracted with large vertical fins for directional stability which also are equipped with rudders to augment control. The rotor pitch of these helicopters are also directly connected to the pedals and can be operated without power. This however poses a problem for the fully autonomous HyDrone.

The chosen solution is a backup battery to provide power during failure of the main power source as mentioned in section 10.3.5. The backup battery provides power for the blade pitch control during autorotation. The required power for the autorotation manoeuvre is much lower because thrust is generated by the upwards airflow through the rotorblades. This provides the HyDrone with enough loiter time to find a suitable landing spot. In case of an engine failure, the control system stabilises the HyDrone with the other remaining functioning rotors which is described in section 11.4.2. The drag provided during autorotation is of the same order as the drag provided by a parachute. A parachute has the disadvantage that it requires more structural stiffness and therefore weight at the point where it is attached. Thus, autorotation is a much more desirable safety measurement than a parachute.

## 12.2 Navigation and Strobe Lighting

According to regulations of international authorities aircraft are required to have navigation lights; a red light on port side (left) and a green light on starboard (right) and a white light on the aft side (back). These lights indicate the flight direction of the aircraft. In fig. 12.3 the navigation light configuration of the HyDrone is shown. Number 1 and 2 represent the red and green light respectively, number 3 shows the rear lighting and at location number 4 (which is mounted at the centre at the top and bottom of the body) as well as on locations 1 to 3 strobe lights are present. The strobe lights send burst of high intensity light to help other pilots of manually operated aircraft to recognise the position of the aircraft during low visibility weather conditions. Also since the HyDrone operates in congested areas it is a good indication for the civilians where the HyDrone is in the sky during low visibility weather. During engine failure these lights can also be used as emergency lighting in combination with audible emergency equipment like an siren. In this manner people are notified early and have time react to a failing HyDrone.

## 12.3 Lightning Strike Protection

In order to prevent catastrophic effects from lightning strikes two things need to be taken in consideration. Firstly, the direct thermomechanical effects due to the high currents passing through the HyDrone can heat up

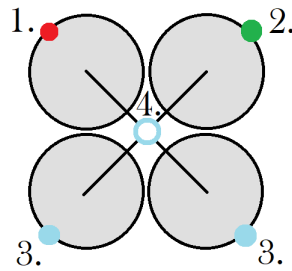


Figure 12.3: Navigation light location on the HyDrone

the materials which can cause catastrophic damage. Secondly, the indirect effect of the electrical equipment can be disrupted or damaged by the electromagnetic coupling between the electronic systems. In order to certified for lightning strike, rotorcraft have to comply with the regulations of FAR Parts 29 and 27[2] which describes test which should be completed successfully. Testing for the qualification of direct effects is done by injecting a current of a standard of 200 kA into the, to be tested, components. For example, the rotorblade or test specimens that are representative of components of the fuselage. These test are done at recognised certification agencies as HTIEP in China. To test indirect effects a small scale current is generated on the rotorcraft between 2 predefined points while measurements are taken on all system cabling which should be subject to certification. The measured peak impulses are then injected in a laboratory in the systems to test their robustness. If rotorcraft are tested and certified in both categories, then they can be operated safely although flying during a storm is not advised. Since 1976, across 64 million flight hours 113 cases have been reported of rotorcraft being struck by lightning from which only 1 accident occurred.<sup>1</sup> Thus for the HyDrone the components should be tested for direct and indirect effects of lightning strikes. If the components meet the certification requirements then it fair to assume that the HyDrone can be operated reliably during a lightning strike. The body is made of carbon composite, which is also electrically conductive, does not perform as well as a aluminium body. In order to be safely operable additional lightning protection is needed unlike aircraft which have a skin which is fully made of aluminium [68]. Lightning protection may include wire bundle shielding between the electrical subsystem components. The composite skin of the aircraft shall include metallic wiring or composite structure expanded foils to conduct the current of the lightning strike from the impact point trough the skin to the exit point.

## 12.4 Shrouds

The shrouds surrounding the propellers provide better propeller performance and reduced noise. However, the main advantage of a shrouded propeller configuration is the improvement of the overall safety of the aircraft design as described in section 7.4.1. They pertain to its functioning as an effective barrier during takeoff and landing for bystanders as well as to the passenger. In addition, the shrouds are designed to withstand impacts such as birdstrikes with the use of aramid reinforcement (see section 8.3.4). It goes to show that the inclusion of shrouds are good for safety.

The shrouds surrounding the propellers provide better propeller performance and reduced noise. However, the main advantage of a shrouded propeller configuration is the improvement of the overall safety of the aircraft design as described in section 7.4.1. The shroud functions as a safety barrier for bystanders during takeoff and landing as well as for the passenger.

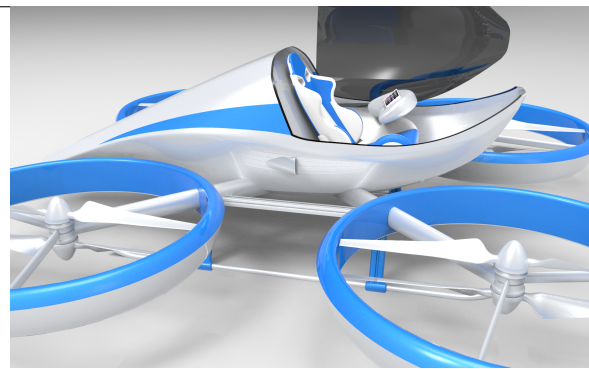
## 12.5 Recommendation

In this section the Safety Systems are stated which are (to be) implemented in the design which require further analysis in the development of the HyDrone. It consist of system which are already implemented in the design and which can be improved and system which are currently not integrated in the model but can prove to be beneficial for the overall design if further research has been performed. The systems are itemised below and are elaborated individually.

<sup>1</sup>[http://www.helicopters.airbus.com/website/en/ref/WHEN-LIGHTNING-STRIKES\\_133.html](http://www.helicopters.airbus.com/website/en/ref/WHEN-LIGHTNING-STRIKES_133.html)



(a) Design of the shroud



(b) Entrance to HyDrone

Figure 12.4: Design of the HyDrone

- Crash-Worthy Seats
- Maintenance System
- Cooling System
- Airbags
- Landing Gear Damping System
- Fire Handling
- Vehicle Entrance

### Crash-Worthy Seats

To guarantee the safety of the passenger crash-worthy seats are of importance. The HyDrone is most likely to crash in vertical direction (impact form hitting the ground) and thus unlike a car configuration the loads of the impact should be spread in this direction. This can be done with stroking seats which collapse under the weight of the occupant during impact, absorbing a large portion of the impact. The weight and costs of such a system should be further investigated in future work. A common problem during impact is the so called 'submarining' out of the shoulder harness and under the lap belt. Therefore a 5-point restraint belt should be implemented with a strap between the legs. A ejection seat has been considered as well but is not an options as is weighs a lot and cannot be used safely in the congested urban environment. During engine or power failure the HyDrone is still able to continue flight and land safely which would make an ejection seat obsolete.

### Maintenance System

A Maintenance system shall definitely be present in the HyDrone which constantly monitors all subsystems like the engines, fuel cell, altimeters, cooler etc. This system shall give updates on the performance of all sensors and actuator performance. In case of failure of a subsystem it shall determine the severity of the system loss and determine if the flight can be continued and after the nominal flight is completed maintenance can be done or that a emergency landing to the nearest landing sight shall be performed. The CPU for this system is already present as described in section 11.2. However further research shall be done on the system or equipment which is needed to check if all system are still operating properly. In future work the costs and masses of these components shall be further analysed.

### Cooling System

The cooling system for regulating the temperature of the power subsystem as well as the ambient temperature in the cockpit is accounted for in the design. The cooling system is overestimated in terms of costs and mass in the design as a safety factor because the precise mass was difficult to calculate before it was decided where the cooling system was positioned and thus were all vents should be placed. There is space within the 3D model of the design and in future work the geometry of the vents can be simulated and thus a better estimation of the mass and costs can be presented.

### Airbags

Airbags inside the cockpit of hovering aircraft are unnecessary as the impact of such a vehicle is in vertical direction. There are however rotorcraft with external airbags at or surrounding the landing gear. this increases the weight of the HyDrone significantly but might prove to be effective during impact with a pedestrian. This effect should be further analysed and a trade of should be made between the added mass and extra safety of such an airbag system.

### Landing Gear Damping System

the landing gear is placed underneath the HyDrone at a slight outward angle which allows for small elastic deformation of the skid when it positioned on the ground. This is more favourable than a straight configuration in which the load factor would be much higher. Further investigating should be done on the addition of a damping system in the form of a shock absorber. This can absorb a lot of impact during harsh landings at the

---

cost of increased weight. The effect, mass and costs of such a shock absorption system should be analysed in further development.

### **Fire Handling**

The power system and especially the hydrogen tank is a fireproof design as is described in section 10.4. It has multiple systems which guarantee the hydrogen tank with the flammable gas does not explode. Other Subsystems however might also be prone to fire. Implementing fire extinguishers in every engine or system is bad practice since it is a costly process and adds a extra mass and costs to the whole vehicle. In case of fire the HyDrone will perform an emergency landing as soon as a free landing sight allows for it. A much better solution is adding a fire wall between critical components which might ignite and the passenger which protects the occupant from the heat during an emergency landing. The costs and weight of such should be further analysed in future development of the HyDrone.

### **Vehicle Entrance**

The HyDrone is entered from the the starboard side where the step is attached at the skid. This allows for better entrance to he vehicle. However entering the vehicle could still be improved as the cockpit is still a distance from the ground which is hard to reach. Different systems have been considered were the landing platform has a stairs in order to enter the HyDrone but which minimises the available Landing sights to those who are equipped with this kind of measurements. Also more hinges in the HyDrone cockpit have been considered which increase weight. In the current configuration the HyDrone is entered from the side while the windshield is rotated around the rolling axis but there is still improvement left for the ease of entering the vehicle. The HyDrone during entrance is presented in fig. 12.4b.

## **12.6 Reliability, Availability, Maintainability, and Safety (RAMS)**

This section provides a short overview concerning the Reliability, Availability, Maintainability, and Safety characteristics of the design of the HyDrone. Reliability and Safety are an integral process which have been implemented throughout the whole design. Every subsystem is developed in a safe and reliable manner as is described in the safety sections of each subsystem chapter. The design philosophy behind this was to first design for reliability in the sense of mitigating the probability of failure with the aim of prevention. Critical subsystems have been designed in a redundant manner such that the during failure of a system the flight can be continued. Secondly safety measures were considered to mitigate the impact of a failure. The aim of the the safety systems was to prioritise the safety of the passenger and secondarily to reduce the damage of equipment or components of the HyDrone. Safety has also be taken in consideration in the sense of not harming the environment as the HyDrone is designed as an environmentally sustainable vehicle. Availability is also taken in consideration to guarantee that the subsystems can be kept in a functioning state. The subsystems which are implemented in the design and the materials used for the subsystems have been analysed by looking at their life cycles and operating conditions. The subsystems are designed to be operable in the environment they are exposed to during operation. During different failure modes the subsystems are design to be still operable as well to allow for a safe landing. The HyDrone is equipped with a maintenance system as described in section 12.5. This system monitors all the subsystems and checks if the function properly. In case a system fails which does not compromise the safety of the passenger during flight the flight is continued. If the failure of a system is critical the HyDrone will initiate an emergency landing at the nearest available landing sight. A maintenance report is also send to the ground station and if necessary, in case that the HyDrone cannot be repaired at the landing sight manually, a maintenance support unit is contacted to arrive at the landing sight. For scheduled maintenance the ground support team is given updates on the cycles flown and the overall performance of the subsystems which is monitored by the CPU. The prevent avoidable maintenance a pre-flight inspection is to be done before the first flight of the day the check if all the rotors are free and there are no object on the landing sight. When a certain amount of flight cycles (which is yet to be determined) is performed by the HyDrone a more thorough check is conducted by the maintenance support team. The data which is acquired during these checks is analysed and provides useful information for further development of the HyDrone.



---

# Chapter 13: Noise

This chapter first discusses the noise requirements in section 13.1. Then, the noise estimation model is presented and altered in section 13.2. Next, the results are presented in section 13.3 and are verified in section 13.4. After that, several observed quirks of the model are discussed in section 13.5. Finally, several improvement measures are suggested in section 13.6.

## 13.1 Requirements

As section 6.3 presented the noise limit requirements in EPNdB for predefined Takeoff, Flyover and Landing manoeuvres for Helicopters. The manoeuvres are quite dissimilar to those defined for the Hydrone. For example, the landing certification calls for measurements with the vehicle under a non-vertical approach angle at 120 *m* altitude. Also, for takeoff measurements are to be performed at a horizontal distance of 500 *m* and an altitude of 20 *m*. These are unique to the mission of a helicopter, rarely landing within cities except for emergencies. It is hypothesized that the horizontal distance is based on landing at remote landing zones or airports with ample of space, with the mission of the Hydrone calling for active operation in urban areas with high population densities. Nevertheless, the same requirement is assumed as EPNdB levels for this new mission have yet to be defined. Furthermore, as landing requirement the operational performance in hover at this same altitude of 120 *m* is taken. Finally, the Flyover manoeuvre is more similar and is evaluated at the original altitude of 150 *m* but at cruise velocity. For respectively takeoff, cruise and landing the sound levels are set to 86 *dB*, 84 *dB* and 89 *dB* according to EPNdB ratings.

Note that climb with constant velocity is not evaluated as takeoff (i.e. accelerating climb) is of higher propeller rpm and engine power at lower altitude and is therefore the more critical case.

To simplify the calculations, the performance and operational parameters of the flight phases are taken from the originally intended profiles as presented in chapter 9, but using the abovementioned distances solely for the flyover correction factor. It is stated in chapter 9 that these are critical for those particular flight phases. Therefore, this simplification results in an overall overestimation.

Beware that while the requirements are based on EPNdB-ratings set by the FAA, the model is based on maximum A-weighted levels (which is the recommended rating scheme proposed by the EPA [69]). EPNdB represents the integrated sum of loudness over the period within which the noise from the aircraft is within 10 *dB* of the maximum noise during a certain trajectory. CITE2 To contrast, maximum A-weighted noise levels represent the maximum noise as illustrated in fig. 13.1. From the definitions it can be deduced that maximum A-weighted noise levels are likely to overshoot EPNdB-ratings between 0 to 10 *dB*. The maximum A-weighted levels are to be equal to EPNdB *dB* levels with this margin on top.

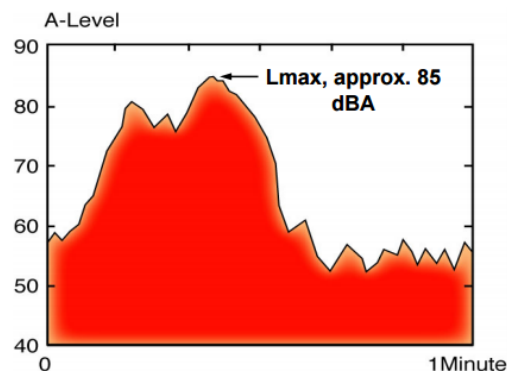


Figure 13.1: Illustration of Maximum A-weighted Noise Level [69]

## 13.2 Noise Model

The noise levels produced by the propulsion subsystem are estimated using a simple, semi-empirical model developed by the German Aerospace Center (DLR)[70] based on general physical principles of noise generation and radiation[21]. The estimation is conservative, providing a maximum noise level at ground level. The model was experimentally validated to an accuracy of 2*dB*. [21] This tool forms the basis of the noise analysis presented in this chapter.

For propeller-driven General Aviation aircraft the method is validated to an accuracy of  $2dB$ . As the aircraft class differs from the Hydrone, a set of additional assumptions is used. A brief literature study and extensive conversations with specialists on propeller noise within the Aerospace Engineering department of the TU Delft have yielded no suitable alternative for the scope of the DSE.

There are several limitations to this calculation method. For instance, it is based on a data set obtained from propeller noise calculations related to a reference constant blade geometry, a fixed radial blade loading distribution and typical blade lift and drag coefficients for General Aviation aircraft propeller. The blade geometry specifically pertains to the planform, the twist and the thickness at the 75% radial blade station which is 7% in this case.[21] In addition, the sound-attenuating effects of shrouds and the increased noise production due to the sets of counter rotating propellers are not taken into account. Therefore, an effort is made to account for these effects. As the aforementioned effects are absent in the model, the resulting estimate is believed to be conservative.

Several modifications are made to the model:

1. In the model the power is taken to be directly proportional to the propeller rpm based on maximum settings ( $P = P_{max} \cdot \frac{N}{N_{max}}$ ). Instead, the actual power determined in chapter 9 is used directly. At this point it is unclear whether this results in an over- or underestimation of the noise level. This will be evaluated in section 13.5.
2. While the model calls for the flight speed, the inlet velocity is taken as defined in chapter 9. Using the conditions for cruise, taking an inlet velocity of three times as much, yields a noise level increase of just 0.6 dB.
3. Flyover height  $H$  is redefined as the absolute distance to the point of measurement - not just the vertical distance to the observer. The author of the estimation method assumed the observer would be standing on the downward projection of the aircraft on the ground. The redefinition is required to evaluate the takeoff requirements.

### Calculation Method

The methodology aims to calculate the maximum overall A-weighted noise level by using an empirically-determined standard noise level  $L_A$  and subsequently include estimations of the influence thereon of a variety of parameters: Blade loading  $c_{P,B}$ , number of blades per propeller  $B$ , propeller rotational speed  $N$ , flyover height  $H$ , helical blade-tip Mach number  $M_H$  and number of propellers  $n$ . Additionally, a correction factor for the climb phase is included.

Unaltered, the model is valid for parameter levels defined in table 13.1. The Hydrone stays well within the boundaries, with engine powers ranging between 76.768 and 111.2 kW, propeller rotational velocity of 1790 and 3500 rpm, 2 blades per rotor, a propeller diameter of 1.9 m and blade-tip Mach numbers between 0.608 and 0.771.

Table 13.1: Parameter Values for which the Base Model as defined in [70] is valid [21].

Maximum engine power:	40-640 kW
Maximum propeller rpm:	1,500-4,000 x 1/min
Propeller blade number:	2-6
Propeller diameter	1.0-3.0 m
Helical blade-tip Mach number:	0.45-0.85

The input parameters are presented in table 13.2.

Table 13.2: Input Parameters to Noise Estimation Method

<i>Propeller design parameters</i>	<i>Operational parameters</i>	<i>Environmental parameters</i>
Number of propellers $n$ in –	Max Engine power $P_{max}$ in kW	Ambient temperature $T$ in K
Propeller diameter $D$ in m	Max Propeller rpm $N_{max}$ in 1/min	Ambient pressure $p$ in Pa
Number of blades $B$ in –	Flyover height $H$ in m	Ambient density $\rho$ in kg/m <sup>3</sup>

At first, several aerodynamic parameters are calculated, such as the ambient density, ambient speed of sound, helical blade-tip Mach number  $M_H$ , the propeller power and aerodynamic blade loading (i.e. power coefficient) per blade  $c_{P,B}$ .

$$a_0 = \sqrt{\gamma \cdot R \cdot T} \quad (13.1)$$

with adiabatic exponent  $\gamma = 1.4$  and specific gas constant  $R = 287.1 \frac{m^2}{s^2 K}$ .

$$M_H = \frac{\sqrt{U^2 + V^2}}{a_0} \quad (13.2)$$

$$P = P_{max} \cdot \frac{N}{N_{max}} \quad (13.3)$$

$$c_{P,B} = \frac{31,006 \cdot P}{\rho \cdot U^3 \cdot D^2 \cdot B} \quad (13.4)$$

Then, the summation of individual noise level contributions  $\Delta L_i$  in A-weighted decibels  $dB(A)$  incorporating an empirical factor of 108.6  $dB(A)$  yields the maximum A-weighted noise level  $L_{max}$ . Variables with subscript 'ref' are reference values and variables with capital 'E' are placeholders for other equations. Both are defined in the text. And the input variables were defined in table 13.2.

The noise level  $L_{max}$  is therefore calculated as thus:

$$L_{max} = 108.6 + \sum_{i=1}^7 \Delta L_i \quad (13.5)$$

What follow are the equations for accounting for parameter effects on noise. Firstly, the influence of blade loading:

$$\Delta L_1 = 10 \cdot \lg \left[ \frac{c_{P,B}}{c_{P,B,ref}} \right]^{E_1} \quad (13.6)$$

Secondly, the influence of number of blades:

$$\Delta L_2 = 10 \cdot \lg \left[ \frac{B}{B_{ref}} \right]^{E_2} \quad (13.7)$$

with  $B_{ref} = 2$  and  $E_2 = 1.00$  corresponding to  $B = 2$ .

Thirdly, the influence of propeller rotational speed:

$$\Delta L_3 = 10 \cdot \lg \left[ \frac{N}{N_{ref}} \right]^{E_3} \quad (13.8)$$

with  $N_{ref} = 1,000 \frac{1}{min}$  and  $E_3 = 3.39 - 1.75 \cdot M_H$ .

Fourthly, the influence of flyover height:

$$\Delta L_4 = 10 \cdot \lg \left[ \frac{D}{H} \right]^2 \quad (13.9)$$

Fifthly, the influence of helical blade-tip Mach number:

$$\Delta L_5 = 10 \cdot \lg \left[ \frac{M_H^{13.4}}{(1 - M_H)^{1.5}} \right] \quad (13.10)$$

Sixthly, there is also a term present to correct for higher noise production during climb conditions by adding the following constant term:

$$\Delta L_6 = 3 \quad (13.11)$$

with  $\Delta L_6 = 0dB$  for level flight. This extra term compensates for higher A-weighted noise on ground level due to the increased angle between the propellers and the horizon which is accompanied by higher sound levels (as illustrated in fig. 13.2a).

The final influence is that of the number of propellers:

$$\Delta L_7 = 10 \cdot \lg(n) \quad (13.12)$$

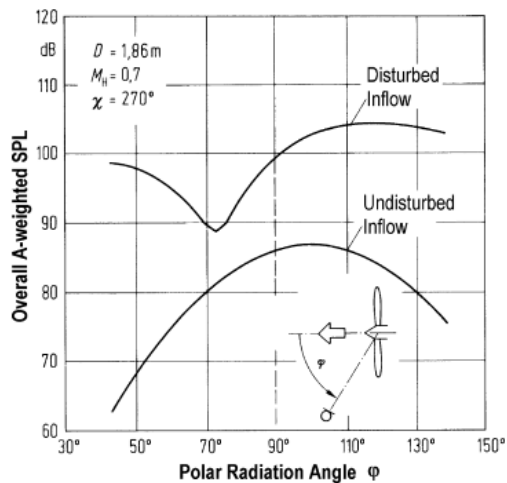
### Coaxial and other disturbance effects

Section 17.1.2.3 in[21] states that counter rotating Coaxial propellers can be interpreted as single rotation propellers in disturbed flow. Normally, this is the effect that would occur with fuselage interference in case of pushprop propeller aircraft and the presence of other (smaller bodies) interfering with the airflow. Disturbed inflow is also the condition of the airflow after the first set propeller disk and encounters the strut before moving into the second propeller disk.

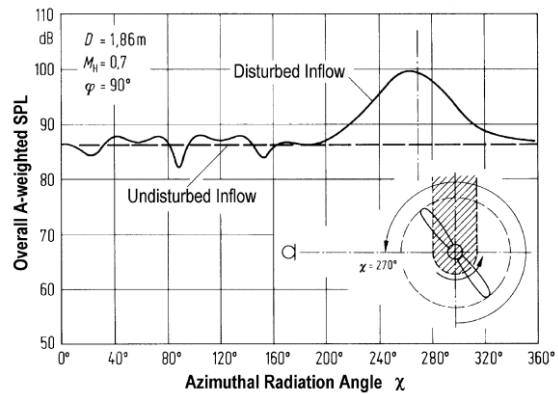
It can be observed that in the case of fig. 13.2c that the average noise level difference between disturbed and undisturbed inflow conditions of approximately 21  $dB$  and in the case of fig. 13.2a 14 – 23  $dB$  for a polar radiation angles of 90 – 130  $deg$ . For angles beyond this, the effect of disturbed flows is less known and the analogy with pull-propeller aircraft breaks apart. While the claim is highly disputable, the two figures do indicate that the effect of disturbed flow, and therefore counter rotating propellers, can be simplified to a constant value of  $\Delta L_8 = 20 dB$ . Thereby the implicit assumption is that disturbances by Coaxial rotors and the presence of struts disturbing the inflow yield a hundred times higher noise power levels and four times higher sound levels.

Figure 13.2b indicates that additional disturbances due to an object partially obscuring the airflow is highly directional. This observation is supported by what can be seen in fig. 13.2d. For propfans this also seems the case.

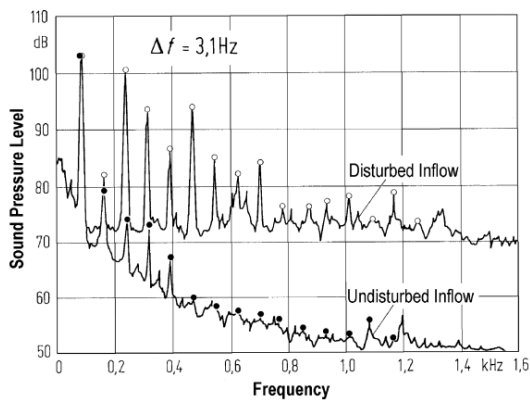
However, largely neglecting the directional variability of noise (which is exacerbated by the presence of shrouds) and the modelling of counter rotation and other disturbance effects as disturbed inflow demand more detailed modelling of the precise geometry. Also,  $\Delta L_8$  is taken 50 to 70  $dB$  and 85 to 115  $dB$ .



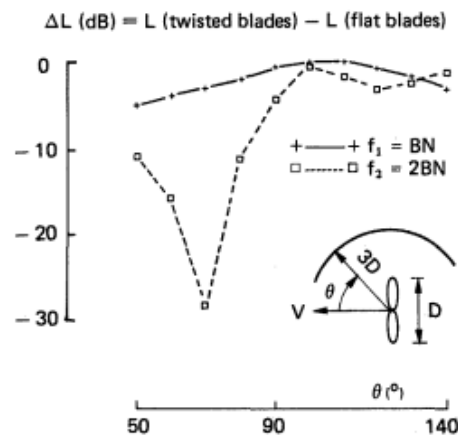
(a) Typical A-Weighted Propeller Noise Levels for Disturbed and Undisturbed Inflow Conditions as a Function of Polar Radiation Angles[21]



(b) Typical A-Weighted Propeller Noise Levels for Disturbed and Undisturbed Inflow Conditions as a Function of Azimuthal Radiation Angles[21]



(c) Effect of Disturbed Inflow Conditions on Noise for  $M_H = 0.5$ [21]



(d) Noise Directivity Profile [21]

Figure 13.2: Graphs retrieved from [21]

**Shrouds** From Figure 13.2a can also be observed that for typical propeller aircraft the largest A-Weighted noise levels are radiated in-plane or just beyond. For this source, a propeller with similar  $D$  and  $M_H$  was used. This observation is supported for single-rotor propfans (see fig. 13.2d) Assuming this then also holds for the lower inflow speed and for counter rotating propellers, it illustrates the relevance of impeding the sound waves in the same directions as where a shroud would be situated.

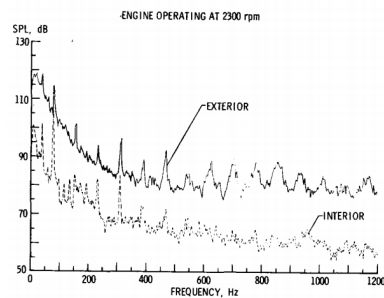


Figure 13.3: Exterior and Interior Noise Spectra[71]

If one were to believe that studies comparing exterior and interior noise levels are useful to indicate this effect, then fig. 13.3 gives an approximation of the attenuation in light aircraft. In this study, the exterior

microphone was placed about a meter from the fuselage wall and the interior at its centerline at head level. To be conservative and the fact that this discovery was at a late stage, this effect is not used in the estimations.

### 13.3 Results

Table 13.3 presents the maximum overall A-weighted noise levels and its individual contributions as calculated with the model using input parameters from the distinct flight phases. The input parameters are presented in table 9.3. The noise levels are evaluated for each flight condition (takeoff, cruise and landing - hover at altitude).

Table 13.3: Results from the Noise Model for Input Parameters Corresponding to Different Flight Phases (results rounded to 2 decimal)

Parameter	Unit	Takeoff	Cruise	Landing
Effect of blade loading	dB(A)	3.35	10.73	2.44
Effect of number of blades	dB(A)	0.00	0.00	0.00
Effect of propeller rotational speed	dB(A)	8.50	6.25	8.77
Effect of flyover height	dB(A)	-48.41	-37.95	-36.01
Effect of helical blade-tip Mach number	dB(A)	-7.62	-32.72	-0.04
Correction for climb-out conditions	dB(A)	0.00	0.00	0.00
Effect of number of propellers	dB(A)	9.03	9.03	9.03
Maximum overall A-weighted noise level	dB(A)	73.46	63.95	92.79
Maximum overall A-weighted noise level (disturbance factor included)	dB(A)	93.46	83.95	112.79
Requirement	dB(EPNL)	86.00	84.00	89.00

Based on the current the requirements, model and assumptions, the cruise noise production falls within limits for zero margin between dB(EPNL) and dB(A). For takeoff it can fall within limits if the margin approaches the upper limit as established in section 13.1. For landing the requirements are largely exceeded.

An interesting result is visible: The landing noise level appears to be more critical than that of takeoff. This can be explained by the fact that takeoff requirements are evaluated at a greater distance from the observer than for landing. As this is dependent on the interpretation of  $H$ , that assumption should be revisited in the future. Also, chapter 9 yields a propeller rpm higher than in takeoff and thereby the power is overestimated (see also table 13.4. As the calculations have been verified and are assumed correct, the noise produced during landing is overestimated.

It is hypothesised that the actual noise levels would be less during all flight conditions due to the effect of the shrouds. For one, the tip vorticity is becomes smaller, reducing the noise production for all flight conditions by expressly reducing the 'effect of helical blade-tip Mach number'. Furthermore, if the observer is located at the point of measurements that regulations dictated during landing, the Hydrone would be located at just 2.29 deg above the horizon. When looking at fig. 13.2a this would correspond to a radial angle of  $\phi = 92.29$  and not far off the highest noise direction. Considering that in this direction the noise emissions are blocked by the shroud, the actual observed noise levels could be lower. It is, however, unknown if and how much the shrouds influence the noise that is directed downwards.

To conclude, not all the noise requirements are reached in the current configuration. However, it was previously argued that the calculated noise levels - especially for landing - are likely overestimated by excluding the shrouds from the model. In addition, multitude factors have been introduced that add uncertainty to the final results, be it due to using propeller rpm instead of power directly, the definition of 'flyover height' in the requirements or the factor of 20 dB that was added to attempt to account for counter rotation and other inflow disturbances. Also, the helicopter requirements are adapted without explicit approval from or correspondence with the Federal Aviation Authorities in the United States.

### 13.4 Verification & Validation

Verification of the model was rather brief. After all, it is in effect a limited amount of equations that have to be evaluated sequentially and then added up. Also the number of inputs was limited. The procedures that were followed were twofold: Unit testing specific equations by entering input for which there is a predictable output. Then also system tests were performed where the total noise level was calculated both in spreadsheet software, EXCEL2013, and by hand.

The model is validated for propeller-driven General Aviation aircraft with input parameters in the ranges presented in table 13.1 to an accuracy of 2 dB(A). This accuracy level is - most likely - not maintained due to

the multitude of (additional) assumptions that have been made to accommodate a different aircraft class and propeller configuration. Even then, the noise-shielding effect of the shrouds have not been included.

Therefore, it is recommended to invest more resources into modifying existing models for the Hydrone’s specific aircraft configuration before performing any validation activities to define the effects of counter rotation propellers, shrouds and other disturbances. Subsequent preliminary validation can be performed by using the aeroacoustic prediction functionality of XROTOR and DFDC to include ducted-wall influences on the internal pressure distribution. However, as certain phenomena are neglected in such models (e.g. boundary-layer interaction, flow separation and turbulence) and to allow for geometry optimisation to a certain extent, a multi-objective optimisation could be used in conjunction with fluid solvers (CFD) and mesh generators.

Validation of the noise model and optimisation results would require experimental data from full-scale testing of the propulsion system with and without the shroud. Subsequently, flight testing can be used for validation of the noise generated by the passive components and validation of noise radiation profiles over differing polar and azimuthal angles in all flight conditions.

For certification testing, it is best to work with the regulation authorities to determine exactly which regulations the Hydrone is to follow, as its mission profile is in some ways dissimilar to helicopters.

## 13.5 Discussion

A notable observation from the results is that the effect of helical blade-tip Mach number on takeoff cruise noise is large. The reason for this is that the propeller rpm is  $N = 1790$  during cruise while  $N = 2568$  and  $2816$  during respectively accelerating climb and hover. Indeed, noise production is strongly tied to propeller rpm.

Furthermore, during cruise it is apparent that the effect of flyover height is substantial. It could, however, be argued that the effect of flyover height is inaccurate for low altitudes. For instance, as previously mentioned a  $\Delta L_4 = 0$  dB net effect is achieved for  $H = 1.95$  m. If then flyover height is plotted against its effect (see fig. 13.4), a much steeper gradient is present for  $1.95$  m  $< H < 35$  m than for higher altitudes. It could be argued as the model is independent of aircraft geometry, the model loses its accuracy for flyover heights not much larger than the geometry. Furthermore, as it is in fact the absolute distance from the observer to the aircraft which is important and that an observer is generally positioned at some horizontal distance away from the landing pad. If  $H = 30$  m is assumed, then a reduction is achieved of  $\Delta L_4 = -23.97$  dB.

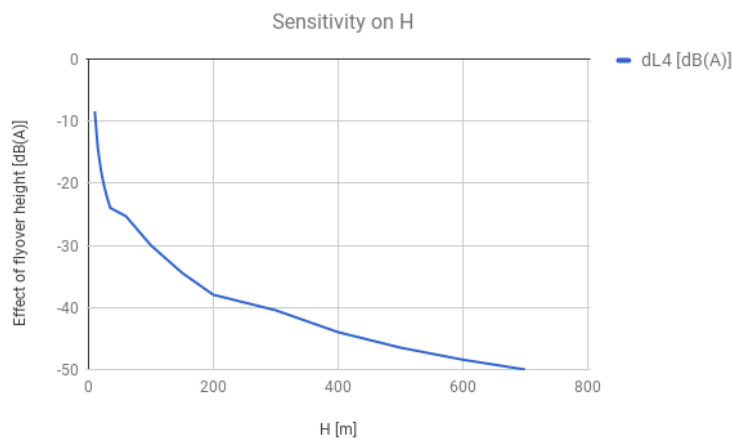


Figure 13.4: Sensitivity of flyover altitude on noise level

Also, the model dictates the propeller is defined from eq. (13.3) instead of using the more detailed calculated values for the flight phases in chapter 9. To evaluate the effect of using the more detailed, the values are compared in table 13.4. It seems that the model underreports the power. The effect of using the higher values, however, is relative. For example, for takeoff conditions using the 9.54 kW higher power value results in 0.68 dB higher result. Interestingly, the model overestimates the hover power due to the propeller rpm being relatively large. This results in an overestimation of the noise.

Table 13.4: Power estimation difference between detailed approach presented in chapter 9 and approach defined in eq. (13.3)

Power estimation	<i>Detailed [kW]</i>	<i>Power [kW]</i>	<i>Comparison [%]</i>
Takeoff	91.43	81.89	-10.44
Cruise	71.13	64.47	-9.36
Hover	76.77	89.79	16.96

## 13.6 Recommendations

Several options could be considered to improve noise performance with respect to model choice and implementation, and with respect to specific design choices.

- Improve the model as it can certainly be improved. At the moment a model is used for General Aviation propeller-driven aircraft, which does not entirely fit in the context of the Hydron. Therefore it is recommended to find a model that encapsulates more of the phenomena. Alternatively, it could be considered to set up a new model as the combination is quite unique. For this, a similar semi-empirical approach could be taken where relations for individual component effects are modelled from first-principles physics.
- Investigate the interior sound levels. This has not been considered (from a requirements nor a estimation standpoint) and certainly has to be taken into account. The earlier mentioned fig. 13.3 shows that fuselage noise level attenuation can be about 20 dB. Using this and still neglect the effect of shrouds, noise estimations reduce to interior noise levels found in cars[71]. Therefore, it appears that this is not a critical issue.
- Optimise the duct walls from an acoustics point of view, by incorporating (a) sound-absorbing liner on the inner duct, or (b) incorporating a double-shell design.[72][21] The former is proven to be effective in reducing noise emissions in turbomachinery by absorbing the ground frequency noise and emitting higher frequencies in return. This higher frequency sound is much more attenuated by the atmosphere.[73]
- As mentioned in section 7.7, it is recommended to lengthen the duct and increase the propeller pitch if the aerodynamic and mass penalties are not too large. The potential for noise improvement is large.
- As mentioned in section 7.7, increasing the duct allows for an increase in axial separation of the propellers.
- Reduce the aerodynamic loading of the downstream propeller through a (re)design of the propellers. Section 17.1.2.3 of [21] recommends this as an effective way to reduce the amplitudes of the unsteady airflow.
- Investigate the applicability flow type blade shapes. Incorporating a bow type blade shape would lower the helical blade tip mach number. [21]
- Investigate the effect of ground and building reflection, which may be important in urban environments. A starting point is the theory proposed in [21]. Further literature study and contact with regulation authorities is advised.
- Investigate the utility of empirical prediction methods of from turbomachinery[74] or fans.[75]
- Re-evaluate designing without coaxial counter-rotating propellers, as their contribution to noise is significant and it introduces needless design complexity.



---

# Chapter 14: Sustainability

In this chapter the the strategy for the sustainability of the design is explained. In section 14.1 and overview of the sustainability strategy determined in the midterm review is given. After this in section 14.2 a look into will be taken into the material choice and the recyclability of the materials. Then a method for the end-of-life plan of the batteries and stack is provided in section 14.3. The climate impact of the HyDrone is considered in section 14.4 and the remainder of sustainability aspects including operational cost, comfort and infrastructure are determined in section 14.5. For the future design and production process the ISO14001:2015 are explored in section 14.6 and finally recommendations with respect to sustainability are made in section 14.7.

## 14.1 Midterm Review

In the mid term report the aspects that involve sustainability were defined and targets were set up. These were categorised in targets imposed by the customer, self-imposed targets and targets that are set through standards. The targets set by the customer include zero-emission flight, 20% recyclable/recycled materials and an end-of-life plan for the batteries. An overview of the self-imposed targets is given in table 14.1. The standards that will be followed throughout the design process, production and operation are the ISO 14001:2015 standards.

Table 14.1: Self-Imposed Targets

Economic	Social	Environmental
Economic Efficiency	Comfort Noise Pollution	Air Pollution Climate Change Infrastructure Choice of Materials

Zero-emission flight was achieved by using the hydrogen fuel cell as a power source. As explained in chapter 10 the power generation only involves producing water.

The noise of the HyDrone was determined in chapter 13. For both takeoff, cruise and landing the noise falls within the requirements. As many assumptions are made to calculate the noise it is hard to determine whether the design contributes to sustainability with respect to noise.

It was chosen to use new materials for the HyDrone as they provide the required strength while minimising weight. So in order to comply with the recyclability requirement, 20% of the materials used in the HyDrone should be recyclable. As the total mass of the is 568.3 *kg* this results in a recyclable mass of approximately 114 *kg*. In the next section a method is provided to comply with this recyclability requirement.

## 14.2 Materials

For the choice of materials a trade-off was performed in chapter 8. From this it was decided to mainly use carbon fibre for the structure. The total carbon fibre mass of the drone is 289.5 *kg* which has an embodied energy, the energy needed to produce the material, of 76139 to 83955 *MJ*. The remainder of the manufacturing of the structure is for the skids. These weigh 21.5 *kg* and are made of aluminium. This gives an embodied energy of 3956 to 4386 *MJ*. As already discussed in section 8.1 the embodied energy of aluminium is smaller. Still a structure completely of aluminium would weigh more to provide the required strength which also increases the embodied energy. As the manufacturing of the materials itself does not contribute substantially to sustainability a in depth look is taken into recycling.

The components of the HyDrone that can potentially be recycled include the electrical wiring, body, shrouds, skids, propellers and beams. Most of these components are made of carbon fibre reinforced polymer (CFRP) for which the recycling process is explained in section 14.2.1. Exceptions include the skids and wiring which are made of aluminium. As stated by Miller et al. [76] aluminium has a high potential for recycling. This is because the recycling of aluminium only requires 5% of the energy that would be used to produce the aluminium in the conventional way. Furthermore the same properties as the parental material can be achieved<sup>1</sup>. Studies have shown that the losses for metal recycling are less than 2%<sup>2</sup>. Taking in to account any impurities that might be present in the material a conservative estimate that 90% of the aluminium can be recycled is made. So for the skids 19.35 *kg* and for the electrical wires 18.9 *kg* can be recycled.

<sup>1</sup><http://www.ecomena.org/recycling-aluminium/>[cited 23-06-2017]

<sup>2</sup><http://recycling.world-aluminium.org/review/recycling-indicators/>[cited 23-06-2017]

## 14.2.1 CFRP Recycling

The production of CFRP has high energy and environmental impact. By reusing or recycling CFRP, it can reduce the impact over its lifetime and decrease the landfilling and incineration of this valuable material. The CFRP used in the HyDrone will be recycled with a fluidised bed recycling process, which recovers the carbon fibres in an energy efficient way.

The first step to recover the CFRP is to strip the HyDrone from the parts that cannot be treated in the recycling process. They include the skids and electrical wiring which will be recycled separately. Furthermore, the battery, hydrogen fuel stack, furnishing, electronic components and climate system is taken out. The remainder of the material is shredded and then enters the fluidised bed reactor, where the epoxy resin is decomposed and oxidised to recover energy. After the fibres are removed, All non-organic material will remain in the bed, which is favourable for the assembled structure since it less labour intensive to remove all metal assembly parts before recycling. The removed fibres are now ready to be manufactured, the process is shown in fig. 14.1. The whole process of recovering carbon fibre only consumes  $6MJ/kg$  [77] where the processing of virgin fibre consumes at least  $198MJ/kg$  [78]

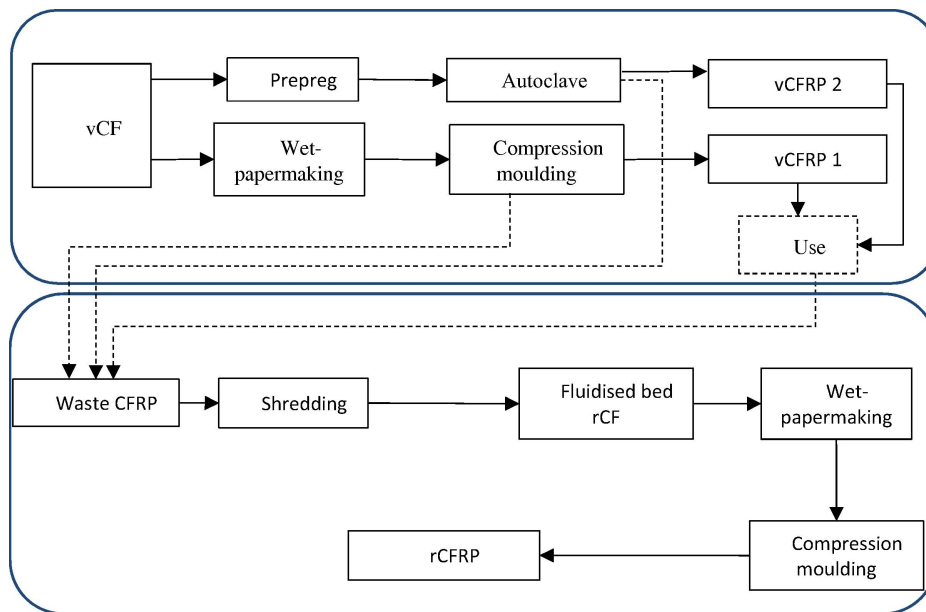


Figure 14.1: Overview of the Manufacturing and Recycling Process of CFRP [77]

## 14.2.2 Manufacturing and Mechanical Properties

Due to the size of the fibres, the recovered material is very suitable for the remanufacturing using wet paper making and compression moulding fig. 14.1. A comparison of virgin (vCFRP) and recycled CFRP (rCFRP) has been made by [77], based on similar materials with a mix of polyamide and carbon fibre, where the compression moulded part has a fibre volume fraction of 25%. As a third material vCFRP 2, a prepreg of epoxy and bi-axial woven vCF with a volume fraction of 50% is compared. This material is comparable with the CFRP used in the Hydrone, with a slightly lower tensile strength and slightly higher tensile modules. The comparison was made between materials with equivalent stiffness and strength. Results show that the mechanical properties of the virgin vCFRP are just slightly better than those of the recycled rCFRP and the energy needed for manufacturing is similar. However it should be noted that the recycled CFRP is inferior to the CFRP used in the HyDrone, both in mechanical properties and energy needed for manufacturing. An overview is shown in table 14.2.

Although the material properties of the recycled CFRP are inferior to the virgin CFRP used in the HyDrone it may be useful in a lot of application where lightweight structure is needed, which does not need to carry that much loading. Moreover the energy demanded and therefore the global warming potential for the production of a part in total is much lower. A comparison based on equivalent material stiffness and strength has been made by [77] as shown in fig. 14.2, comparing the rCFRP, vCFRP and vCFRP 2. CFRP used in the HyDrone and vCFRP are comparable regarding primary energy demand (PED) and global warming potential (GWP). The energy consumption of an equally sized material would be less for vCFRP 2 due to a lower fibre fraction, however this material would have a lower stiffness and strength. Resulting in comparable PED and GWP for equivalent stiffness and strength.

Table 14.2: Mechanical Material Properties and Total Manufacturing (Man.) Energy of vCFRP1, vCFRP2 and rCFRP [77]

	Tensile strength (MPa)	Tensile modulus (GPa)	Equivalent stiffness			Equivalent strength		
			Thickness ratio	Mass ratio	Total Man. Energy (MJ/kg)	Thickness ratio	Mass ratio	Total Man. Energy (MJ/kg)
vCFRP1	171.59 ± 6.6	19.74 ± 1.2	1.00	1.00	53,75	1.00	1.00	53,75
vCFRP2	570	70	0.66	0.75	34,57	0.55	0.62	34,57
rCFRP	148.56 ± 9.6	16.95 ± 0.5	1.05	1.05	51,73	1.07	1.07	50,79

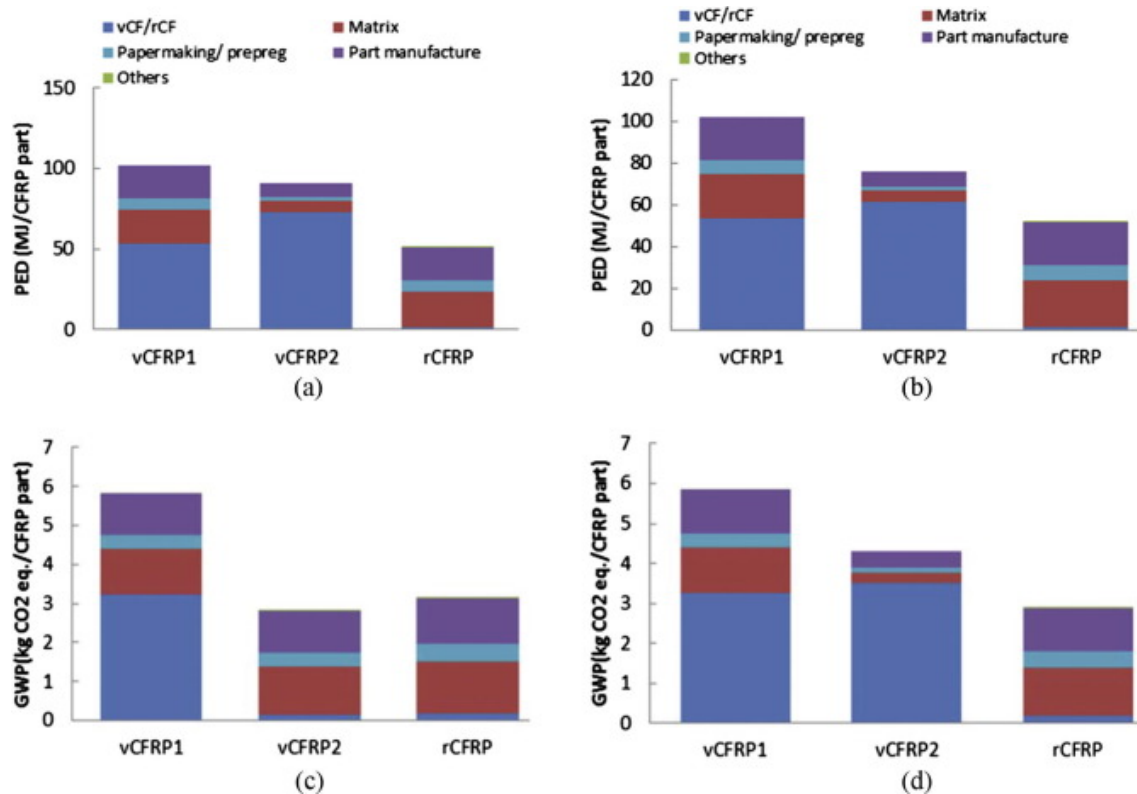


Figure 14.2: (a) Primary Energy Demand (PED), (c) Global Warming Potential (GWP) for vCFRP1, vCFRP2 and rCFRP under equivalent stiffness. (b) Primary Energy Demand (PED), (d) Global Warming Potential (GWP) for vCFRP1, vCFRP2 and rCFRP under equivalent strength. [77]

### 14.2.3 Results

As 65% of the CFRP used in the HyDrone consists of fibres it would be that part that can be recycled. The material produced can be used for structures that carry less loading. The main benefit using this process is that less PED and GWP is present in the recycling process than when the same type of CFRP is produced from scratch. Adding this to the recycled mass of aluminium the total recyclable mass can be determined. This is shown in table 14.3.

Table 14.3: Overview of the Recyclable Masses

Component	Recyclable Mass
Skids	19.5 kg
Wires	18.9 kg
Tanks	55.9 kg
Body	37.9 kg
Shrouds	40.6 kg
Propellers	35.6 kg
Beams	4.42 kg
Total	212.92 kg

---

The total recyclable mass is approximately 37.5% of the total mass so that the requirement for recyclable materials is amply met.

### 14.3 End-of-Life Plan

The final requirement set by the customer is an end-of-life plan for the batteries. As the HyDrone uses hydrogen as a power source it was decided that the end-of-life plan should include both the stack and the back up batteries. The stack is provided by a Swedish company called PowerCell. From email contact with this company it became clear that they provide a solution for when the stack is at the end of its life. The stack is taken back to the factory and the useful parts are taken out. The remaining parts are processed with a method that minimises the environmental impact.

For the end-of-life plan of the batteries an interesting technique called direct recycling is discussed in Gaines [79]. Here the battery materials are recovered so that they can be used in the manufacturing of new batteries with limited additional processing. The technique involves the discharged cells being placed in container to which  $CO_2$  is added. The  $CO_2$  temperature and pressure is raised above the supercritical point in order to extract the electrolyte from the cells. The electrolyte is then separated from the  $CO_2$  and after processing can be recycled if proven economic. The cells without the electrolyte are pulverised and the different materials are separated through techniques that exploit differences in electronic conductivity, density or other properties. The advantage of using this process is that almost all battery components are recovered and can be used for manufacturing new batteries. This reduces waste material that comes from the batteries and increases the recyclability.

### 14.4 Air Pollution & Climate Change

As the HyDrone will fly on hydrogen there will be no air pollution. Only water is produced. Still this water can have an influence on the climate which can be calculated using the average temperature response (ATR). For this a linear model as stated in Schwartz et al. [80] is used. This model is given by eq. (14.1).

$$ATR = Ue_i\mu_{ATR} \quad (14.1)$$

The unit ATR ( $\mu_{ATR}$ ) for water is  $5.77 \cdot 10^{-15} K/kg$  when the post-operation impacts are set equally important as the impacts during operation. Two different uses will be considered to calculate the temperature response. Firstly a look is taken into personal use. This will mean that the HyDrone will fly two cycles a day so that it needs to refuel each two days. It is assumed that the amount of working days in a year is approximately 220. This results in a refuelling of 110 times per year which is the  $U$  variable. When the tanks are emptied 39.4 kg water is produced which is the  $e_i$  variable. So this gives an ATR of  $2.5 \cdot 10^{-11} K$  for each HyDrone. Secondly a shared use scenario is explored. For this it is assumed that during the rush hours in the morning and afternoon the HyDrone is constantly operative. Assuming two rush hours in both the morning and afternoon this results in 15 cycles. It is assumed that for the remainder of the day the HyDrone flies five cycles so that it has to refuel five times in total each day. For 220 working days this results in an ATR of  $2.5 \cdot 10^{-10} K$ . Both these numbers are insignificant so that it can be concluded that the HyDrone has a negligible effect on the climate.

### 14.5 Operational Cost, Comfort and Infrastructure

The direct operational cost are a measure for the economic efficiency. A product which has a higher economic efficiency will contribute more to the gross domestic product, affordability and employment. The operational cost were calculated in section 19.1.3. The direct operational cost for the HyDrone is \$112.36 per hour. The Robinson R22 has a direct operating cost of \$145 per hour<sup>3</sup> so there is a substantial decrease.

Comfort will contribute to the accessibility of the drone and is expressed in seat space. The seat space in the HyDrone is 0.75m.

Finally the size of the required infrastructure was determined. A smaller required infrastructure means that less ground is required. This results in cost reduction but also gives the opportunity for development of more housing in urban areas. The length of the drone is 5 m and the width is 4.92 m. According to the U.S. Department of Transportation [81] the size of the landing place should be at least 1.5 times the length of the helicopter. Assuming the same rules hold for the HyDrone this results in a size of 7.5 by 7.5 m. The length of the Robinson R22 is 8.76 m<sup>4</sup> which results in a minimum required landing pad of 13.14 by 13.14 m.

---

<sup>3</sup><http://philip.greenspun.com/flying/robinson-r22>[cited 26-06-2017]

<sup>4</sup><https://robinsonheli.com/r22-specifications/>[cited 26-06-2017]

---

## 14.6 ISO Standards

As already stated throughout the design, production and operational time of the HyDrone the ISO14001:2015 standards will be used. The main benefits of using the ISO standards are<sup>5</sup>:

- Marketing advantage with respect to competitors
- Lowering the cost through reducing resource consumption and waste production
- Meeting environmental legal requirements
- Committing to social responsibilities and promoting a positive image with stakeholders, customers and employees

These standards provide a framework for the environmental management system (EMS) of the company. The EMS is a system consisting of related elements that organisations use to implement their environmental policy, achieve environmental objectives, meet the environmental compliance obligations, manage environmental aspects and address environmental risks and opportunities<sup>6</sup>. The stages that need to be followed to adhere to the ISO standards can be summarised as follows<sup>7</sup>.

1. Developing the environmental policy and planning the environmental management system (EMS)
2. Implementing the EMS
3. Checking and reviewing
4. Continuously improving the EMS

An elaboration on these stages is given here. The first step involves a setup of the environmental policy by the top level management which takes into account regulatory compliance, pollution prevention and continuous improvement. From this in the planning phase the environmental interactions and significant impacts and legal and other requirements are determined. Based on these environmental objectives and targets should be developed and programs designed to achieve them. For the HyDrone project these targets were identified in the above described sections with a method to assess them. From the implementing phase onwards these stages are regarded as post DSE activities. In the implementing phase the structure of the EMS need to be determined and the responsibilities need to be divided. Furthermore, the EMS need to be documented through policies. In the checking and reviewing phase the environmental interactions are monitored and corrective measures are taken. Finally the top level management reviews the environmental performance and recommends improvements so that the EMS is continuously updated.

In order to fully benefit from all aspects of the ISO standards one could pursue official certification. For this an external bureau should be contacted which does audits in order to assess whether you adhere to the requirements needed to get certification. One such bureau is the BSI group<sup>8</sup> but there are many other possible bureaus that can provide certification. The requirements one needs to adhere to are very extensively described in the official ISO documents. For brevity only the key requirements<sup>9</sup> are given here:

- Within the strategic direction of the organisation environmental management should play a major role
- Implementation of proactive initiatives to protect the environment from harm and degradation
- Focus on the complete life-cycle of the product considering environmental aspects from development to end-of-life
- Adding a stakeholder-focused communication strategy

To conclude the ISO standards show great benefits and are therefore implemented into the project. The largest part of setting up the EMS was already done by working out both the customer and self imposed targets. The remainder of the required stages for the ISO standards is left for post DSE activities. This includes the choice on whether official certification will be pursued or whether the ISO standards will only provide a guideline for efficient sustainable development.

## 14.7 Recommendations

In this chapter the different aspects of sustainability were identified and quantified. In the midterm review a method was established to give scores for the sustainability design. In order for this method to provide meaningful results reference aircraft are needed. This way the sustainability score of the HyDrone can be compared with the references. During the course of the final design it became clear that much of the information required to say something useful about a reference aircraft in terms of sustainability is unavailable. For the aspects where a reference is available this was given so that the scores can partly be compared. Given a total score in terms of sustainability and comparing with reference aircraft is left for future research. This also includes a more precise noise calculation as described in chapter 13

---

<sup>5</sup><http://www.iso14001.com.au/iso-14001-benefits.html>[cited 25-06-2017]

<sup>6</sup>[http://www.praxiom.com/iso-14001-definitions.htm#Environmental\\_management\\_system](http://www.praxiom.com/iso-14001-definitions.htm#Environmental_management_system)[25-06-2017]

<sup>7</sup><http://www.iso14001.com.au/iso-14001-requirements.html>[25-06-2017]

<sup>8</sup><https://www.bsigroup.com/en-GB/iso-14001-environmental-management/>[cited 25-06-2017]

<sup>9</sup>[https://www.iso.org/files/live/sites/isoorg/files/archive/pdf/en/introduction\\_to\\_iso\\_14001.pdf](https://www.iso.org/files/live/sites/isoorg/files/archive/pdf/en/introduction_to_iso_14001.pdf)[cited 25-06-2017]



# Chapter 15: Subsystem Interaction

In this chapter the interactions between subsystems themselves and with the user are presented. The interactions include abstract communication flows, holistic and electrical interaction between hardware components, and software and data handling.

## 15.1 Hardware Block Diagram

Figure 15.1 the Hardware Block Diagram of the HyDrone is shown in which the interaction of the different subsystems is shown. The hardware components are categorised by colours of which the legend can be found below.

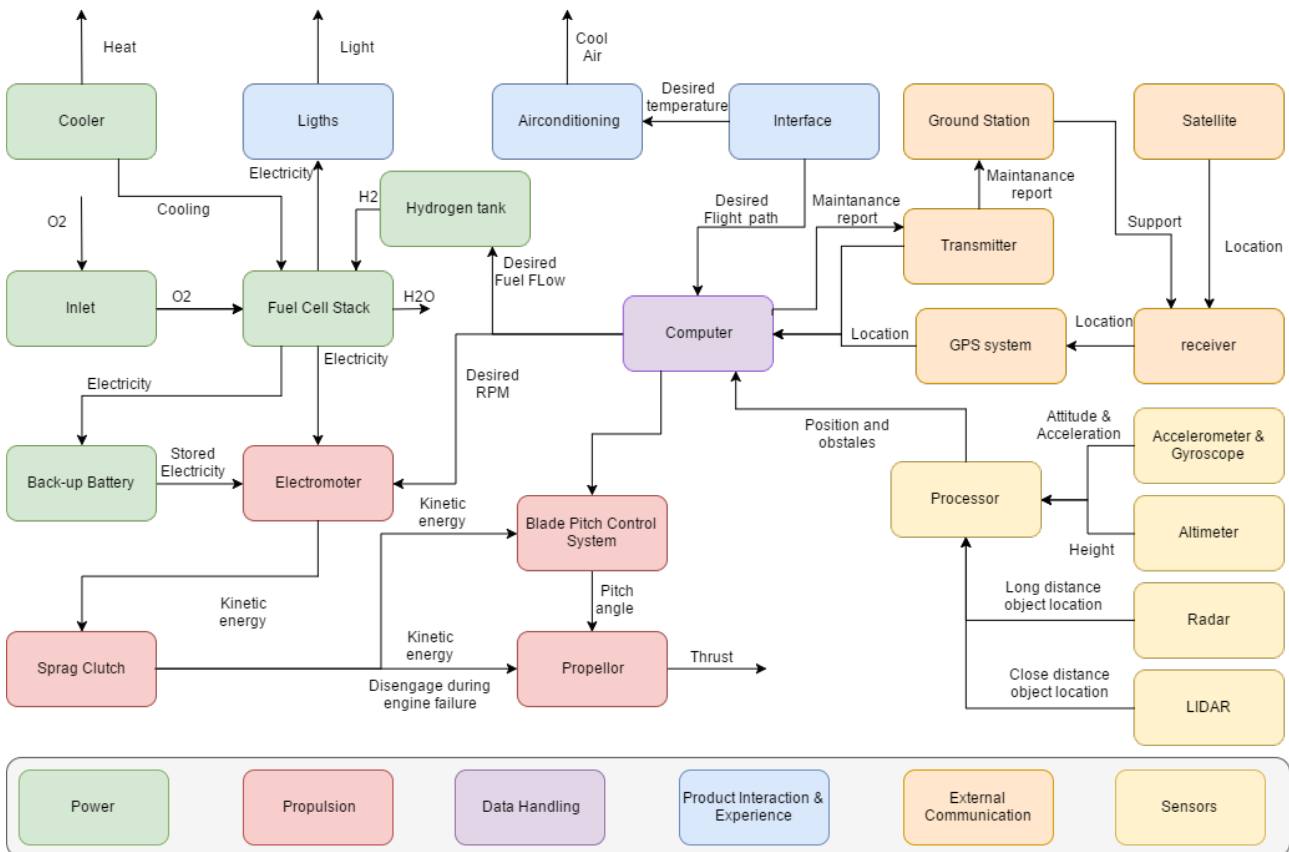


Figure 15.1: Hardware Block Diagram

## 15.2 Software Block Diagram

The Software Block Diagram is shown in fig. 15.2. The rectangles show the hardware systems which affect the software flow and the diamonds describe the checks, activities and manoeuvres which are performed during the software flow. Note that in the diagram not all the hardware components which influence the software are always shown for a more clear overview. The computer is present during all check points in the flow and the propeller is often an output of such a check. The emergency case is simplified in the top right corner. All the critical systems are monitored during the whole flight phase and in case of emergency the emergency lights and siren are always activated. Then the required safety system is activated for the specific emergency cases. The Emergency landing phase can differ in cases where the HyDrone still has time to find an appointed landing dock or where to nearest flat empty area is sought after in more critical cases. The pluses in fig. 15.2 represent the situation when the performed check gives a positive result and the minuses when the check gives a negative result.

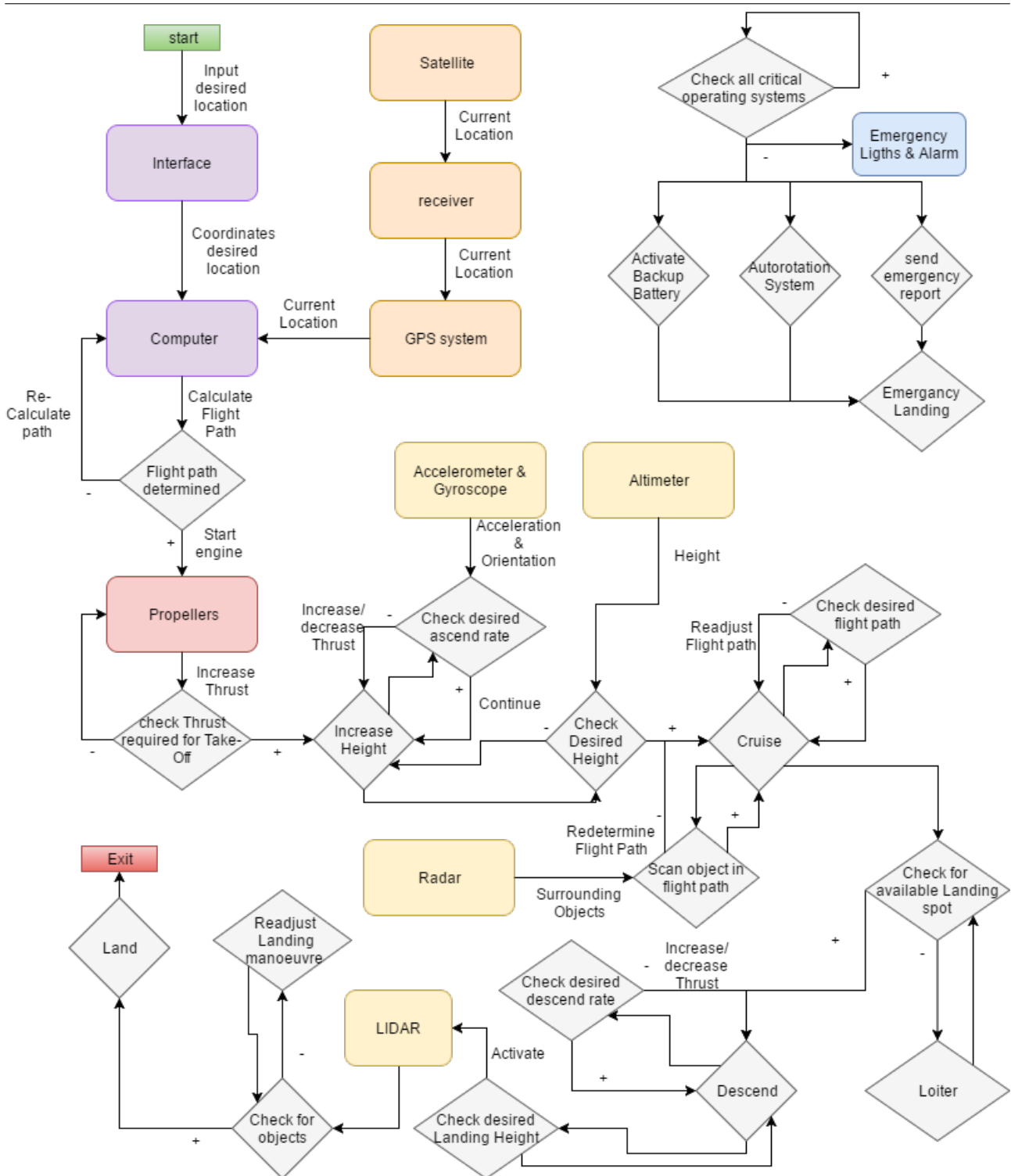


Figure 15.2: Software Block Diagram

### 15.3 Communication Flow and Data Block Handling Diagram

The data handling block diagram and communication flow diagram are merged into one diagram since they have a lot of similarities. fig. 15.3 depicts the internal flow of data as well as the external inputs during operation. As evident from fig. 15.3 the centralised data centre is the main source of information. Inputs such as maintenance and the position of other air vehicles will be collected here and send to the Hydrone. The data will first be encrypted such that it can not be altered by third parties.

The second key element is the on-board computer. It processes all incoming data and makes sure appropriate measures are taken to continue flight. The on-board computer assures the actual data of the Hydrone is fed back to the centralised data centre. One downside of the on-board computer is that it is crucial for flight. So

if it fails, the drone will probably crash. Therefore the system should be designed in a way that an emergency landing is performed in case of failure. There should also be an back-up computer which can perform the necessary calculations to land safely. Lastly, the software will be checked and updated regularly. This will be an automated process.

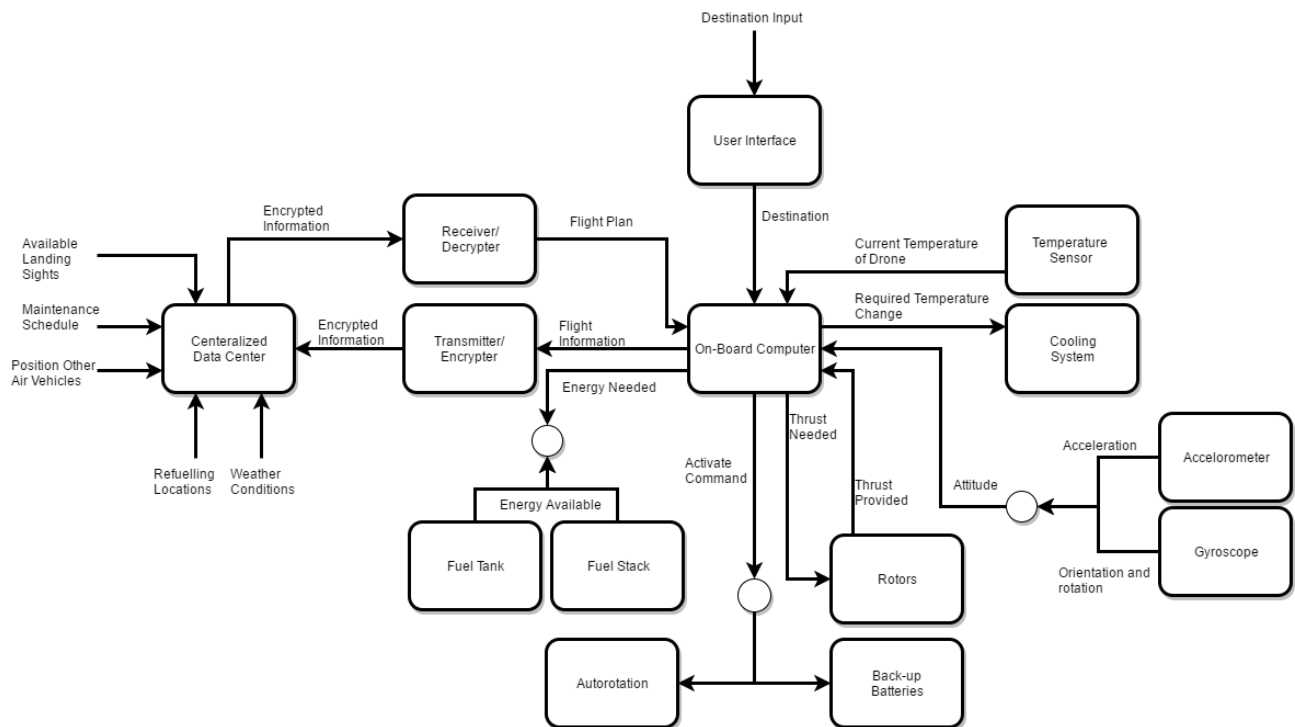


Figure 15.3: The Communication Flow and Data Handling Block Diagram



# Chapter 16: System Integration

In this chapter concludes the system design wherein the previously mentioned subsystems come together. Firstly, an overview of the final design is presented with drawings illustrating high level geometry and relative subsystem placement.

## 16.1 Design Overview

This section contains an overview of the design. First, the geometry is presented (see section 16.1.1). Next, a breakdown of the mass is given (see section 16.1.2). Finally, section 16.1.3 gives an overview of the power.

### 16.1.1 Geometry

Now that all subsystems have been designed, the overall dimensions can be given. These are represented in fig. 16.1. The dimensions are given in centimetres and the angles in degrees. Figure 16.2 clarifies the model by labelling the various subsystems.

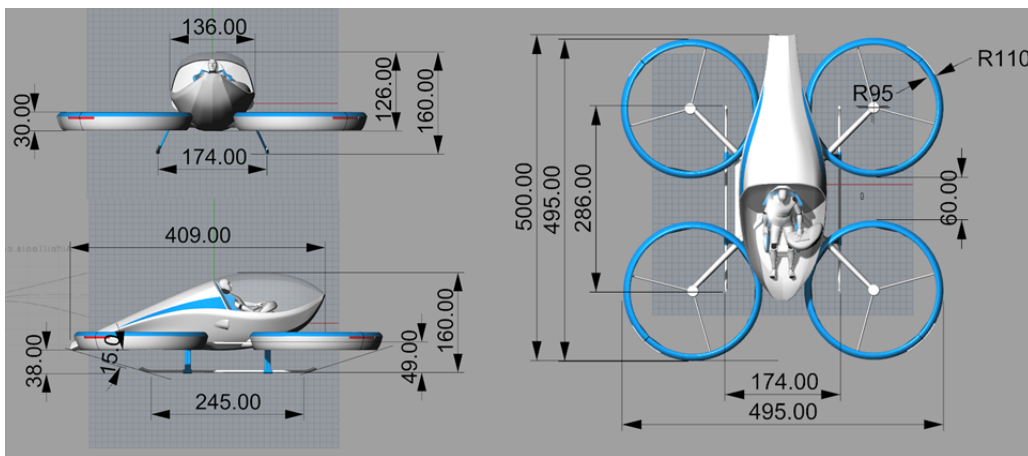


Figure 16.1: Geometry of the HyDrone

### 16.1.2 Mass Budget Allocation

Once all subsystems were designed the mass of the HyDrone could be calculated. All component masses were presented and added up in the mass budget table, table 16.1.

Table 16.1: Mass Budget

Component	Mass [kg]	Component	Mass [kg]	Component	Mass [kg]
<b>Structural</b>	149.0	<b>Power</b>	141.2	<b>Other</b>	49.0
Cockpit	58.3	Tanks (+H2)	86.0	Electronics	26.0
Skids	21.5	Stack	41.6	Climate System	10.0
Shrouds	62.4	Backup Battery	5.6	Furnishing	13.0
Beams	6.8	BoP + PCU	8.0	<b>Payload</b>	100.0
<b>Propulsion</b>	86.8	<b>Control</b>	20.0	<b>Contingency</b>	22.3
Propellers	54.8	Pitching System	12.8	<b>Total</b>	<b>568.3</b>
Motors	32.0	Sensors	7.2		

The structural and power subsystem mass are responsible for over half of the MTOW. 5% of the total mass excluding payload was budgeted for contingency. This makes the MTOW 568.3 kg. Please note that the fuel mass of 4.9 kg is included in the hydrogen fuel tank mass.

### 16.1.3 Power Budget Allocation

To assess whether enough power and energy is available to all components an energy and power budget breakdown is given in table 16.2. The table shows the maximum and average power draw of the individual components,

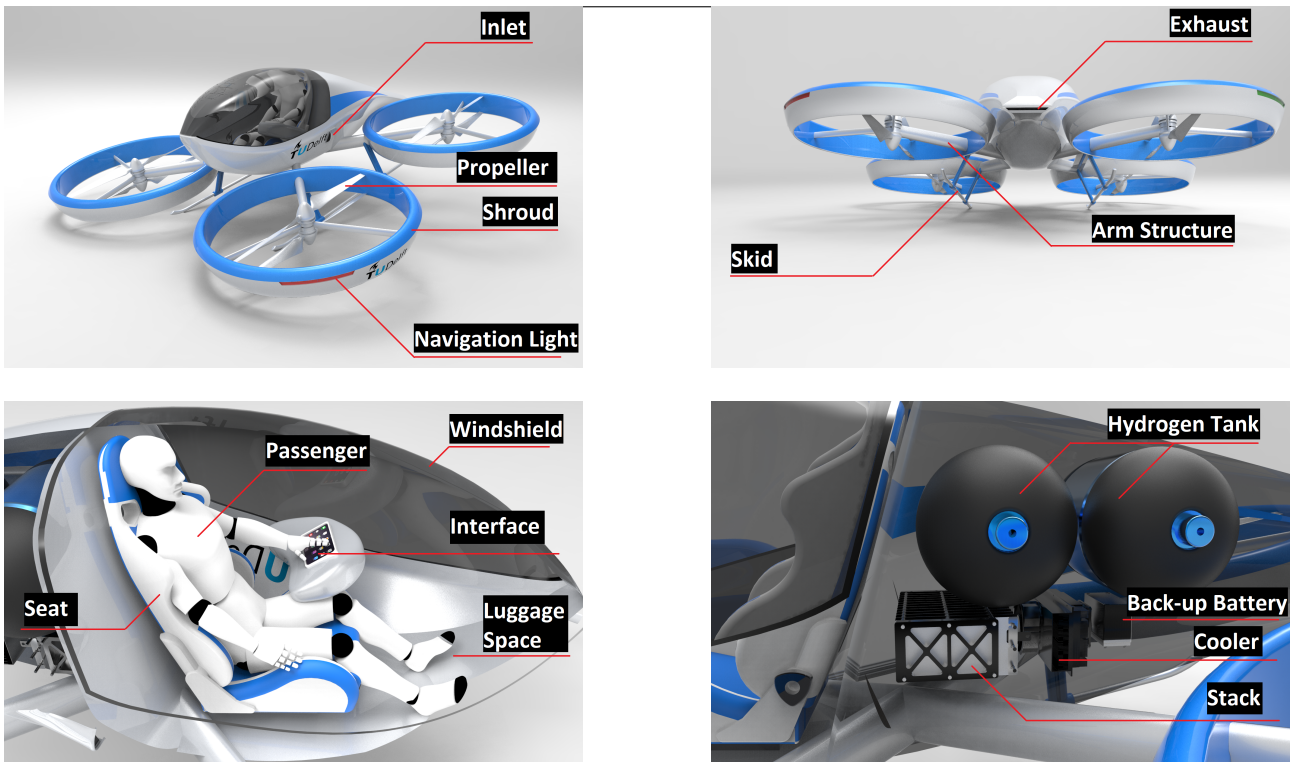


Figure 16.2: Labeled Subsystems

as well as the total amount of energy required for a duration of four flight cycles. The control component consists of all parts listed in table 11.1, excluding the pitch system, while taking into account that at any time only a limited amount of components is active. The other components are merely placed for redundancy. The actual power and energy drawn from the power subsystem is increased by the efficiency losses  $\eta$ . As shown, the contingency margin of 5% is generously satisfied.

Table 16.2: Energy and Power Budgets

Components	$P_{max}$ [W]	$P_{average}$ [W]	Energy [Wh]
Propulsion	91 400	72 350	75 365
Control	301.5	301.5	314.1
Lighting <sup>1</sup>	23.2	23.2	24.7
iPad Pro <sup>2</sup>	4.1	4.1	4.3
Air Conditioning	700	700	729.7
Pitch System	1600	400	416.7
Total	94 029	73 779	76 853
$\eta$	0.9	0.9	0.4423
Total/ $\eta$	104 476	81 976	173 773
Available	125 000	125 000	193 271
Contingency	19.6%	52.5%	11.2%

## 16.2 Performance Analysis

It is not only important what the HyDrone will look like. To give a clear overview of what the HyDrone can do, all performance characteristics were summed up in table 16.3. Apart from the table, the payload-range and climb performance were further worked out in section 16.2.1 and section 16.2.2.

<sup>1</sup><http://aeroleds.com/shop/category/faa-certified/>, [cited 26-06-2017]

<sup>2</sup><https://www.apple.com/ipad-pro/specs/>, [cited 26-06-2017]

Table 16.3: Performance Summary Table

Performance Parameter	Value	Performance Parameter	Value
Vertical Acceleration [ $m/s^2$ ]	1.18	Maximum Power Consumption [ $kW$ ]	104.5
Climb Velocity [ $m/s$ ]	11.8	Total Fuel Consumption [ $kgH2$ ]	4.41
Cruise Velocity [ $m/s$ ]	40	Energy Efficiency [%]	0.44
Cruise Drag Coefficient [-]	0.3	Maximum Noise Level [ $dB(A)$ ]	113
Cruise L/D [-]	0.36	Maximum Range (100 $kg$ Payload) [ $km$ ]	144
Take-off Thrust [ $kN$ ]	6.38	Maximum Manoeuvre Load [ $g$ ]	0.73

### 16.2.1 Payload-Range Performance

As not all passengers will have a mass equal to the maximum payload mass of 100  $kg$  and the HyDrone will also fly without payload, it is useful to analyse the differences in performance for these conditions. The payload-range diagram is an excellent tool for this analysis. This diagram is presented in fig. 16.3. The diagram was established by varying the payload mass between 0 and 100  $kg$  in steps of 33  $kg$ . The required thrust and powers for each of the four flight phases were calculated and used to determine the required energy and finally the maximum range that could be covered with this energy. This maximum range was based on the 171.6  $kWh$ , which is needed to fly four nominal, fully loaded cycles. It was simulated that this energy was used to power all subsystems besides propulsion, a single take-off and landing procedure and cruise flight.

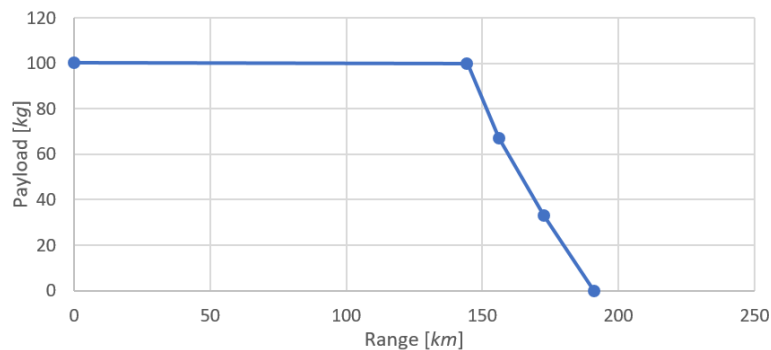


Figure 16.3: Payload-Range Diagram

No surprises were encountered. When the payload mass decreased the required thrust, power and energy of all flight phases decreased accordingly, with the result that the maximum range increased. At a payload mass of 0  $kg$  the HyDrone is almost 18% lighter than when fully loaded. For this difference in mass the maximum range increased by more than 32%. An empty drone could fly over 190  $km$  when fully filled up, without utilising its fuel reserves.

Please note that for payloads above 100  $kg$  the HyDrone is programmed not to take-off so the maximum range is set to zero.

### 16.2.2 Climb Performance

Another performance characteristic that was investigated is the climb performance. The maximum climb velocity gives an indication of how much faster the drone can ascent in the most optimal conditions. The nominal climb velocity is 11.8  $m/s$ . This required 87.3  $kW$  of power at 650  $m$  altitude. The maximum climb rate uses the full 111.6  $kW$  available for propulsion and was calculated to be 18.4  $m/s$ . However this value will most likely never be reached as there is no excess power to accelerate to this velocity. Even if this velocity is reached, it can not be maintained as the value is valid for sea level. At a lower air density the rotors require more power so a lower climb velocity will be reached at higher altitudes. There may however be a different climb velocity that can be reached and will result in a slightly lower energy consumption. To find this velocity the required power should be investigated at every instance in time instead of the average power for the four flight phases. This would require significantly more computation, which is recommended for the further development of this DSE.

## 16.3 Compliance Matrix

To assess whether the requirements stated in section 3.2 have been met in the final design a requirements compliance matrix has been set up. In this requirements matrix, which can be seen in table 16.4, a check mark  $\checkmark$  indicates the requirement is met. Requirements that have not been evaluated yet are denoted with 'tbd'

and will need to be evaluated in the post DSE phase. In case a requirement is not met it is marked with **X** and an explanation has been given below. For each requirement the reader is referred to the section where it is discussed.

Table 16.4: Requirements Compliance Matrix

Requirement		Reference	Requirement		Reference
POW1	tbd	PowerCell <sup>3</sup>	MS2	✓	chapter 8
POW2	✓	chapter 5	MS3	✓	chapter 8
POW3	✓	section 14.3	MS4	✓	section 16.1.1
POW4	tbd	PowerCell <sup>1</sup>	MS5	✓	section 16.1
POW5	✓	section 10.4	MS6	✓	section 16.1
SFT1	✓	chapter 12	AERO1	✓	section 7.4
SFT2	tbd		CONT1	✓	section 11.4.2
SFT3	✓	section 12.2	CONT2	✓	section 11.4.2
SFT4	tbd	section 12.3	COM1	✓	section 11.2.2
SFT5	✓	section 11.4	COM2	✓	section 11.2.2
SFT6	✓	section 11.4	COM3	✓	section 11.2.2
SFT7	tbd		COM4	<b>X</b>	section 11.2.2
SFT8	✓	chapter 8	PERF1	✓	section 16.2
SUS1	✓	section 14.4	PERF2	✓	section 16.2.1
SUS2	✓	section 14.2	PERF3	✓	section 16.2
SUS3	<b>X</b>	section 13.2	PERF4	✓	chapter 10
SOFT1	✓	section 15.3	PERF5	✓	section 16.2.1
SOFT2	✓	section 11.2.2	PERF6	✓	section 3.3
SOFT3	✓	section 15.3	PERF7	✓	section 11.4
SOFT4	✓	section 15.3	COST1	<b>X</b>	section 19.1.1
MS1	tbd		COST2	<b>X</b>	section 19.1.2

**SYS-TECH-POW1&4:** Data of the used fuel cell, which is still in its validation phase, is not yet available.

**SYS-TECH-SFT2:** While safety was of high priority during the design of the HyDrone a safety analysis of the integrated system is outside of the scope of the DSE project and left to the post-DSE phase.

**SYS-TECH-SFT7:** While the control system was not yet designed for jerk it is expected that more comprehensive control software would have no problems with limiting jerk.

**SYS-TECH-SUS3:** The noise during take-off and cruise is expected to fall within the stage 3 noise limits. However, during landing a maximum overall A-weighted noise level of  $92.79dB(A)$  is estimated. A closer look needs to be given to this during the post-DSE phase and mitigation measures should be investigated.

**SYS-TECH-MS1:** The material chosen in section 8.1.5 has an excellent resistance to water and a good resistance to UV-radiation[31]. However, the evaluation of weather resistance of the entire system has not yet been performed.

**SYS-TECH-COM4:** While the communications system as described in section 11.2.2 does not include equipment for the direct communication between the vehicle and air traffic control, the central HyDrone server will be able to reroute any communication.

**SYS-TECH-COST1:** The HyDrone is estimated to have a unit cost of US\$136 026, exceeding the required maximum of US\$112 000 (€100 000). This however includes the the US\$50 697 power subsystem which was excluded from the initial cost requirement by the customer. Taking this into account leads to a price of US\$85 329, which satisfies the requirement.

**SYS-TECH-COST2:** The expected development cost has been estimated at US\$23.6m, exceeding the US\$11.2m (€10.0m) requirement.

## 16.4 Sensitivity Analysis

In this section the sensitivity of the design will be investigated. Major design parameters were decreased and increased by 10% and the effect these variations had on the design outputs were documented. The six parameters that were varied are: The maximum take-off weight (MTOW), the frontal drag coefficient, the drag coefficient looking from the top (relevant for the vertical manoeuvres), the powertrain efficiency, the cruise velocity and the rotor radius. The four major outputs that were analysed are: the energy consumption per cycle in  $kWh$  of hydrogen, the maximum possible range in  $km$ , the fractional excess power and the fractional excess energy.

<sup>3</sup><http://www.powercell.se/wp-content/uploads/2017/05/S3-Fuel-Cell-Data-Sheet.pdf>, [cited 08-06-2017]

The last two outputs are based on the difference in available and required power. The changes in outputs are presented in table 16.5. Changes in outputs of more than 10% were considered sensitive and are printed in bold.

Table 16.5: Sensitivity Analysis

HyDrone	43.484	144.45	21.06	11.12	112.8
Variable	$E_{cycle}$ [kWh]	$R_{max}$ [km]	$P_{margin}$ [%]	$E_{margin}$ [%]	Max. Noise [dB(A)]
MTOW (-10%)	<b>-11.05</b>	<b>13.31</b>	7.22	<b>13.8</b>	-1.44
MTOW (+10%)	<b>14.83</b>	<b>-13.44</b>	<b>-23.6</b>	<b>-14.35</b>	<b>16.30</b>
$c_{d,front}$ (-10%)	-1.49	1.98	0	1.68	0
$c_{d,front}$ (+10%)	1.89	-2.40	0	-2.07	0
$c_{d,top}$ (-10%)	-0.08	0.02	0.46	0.08	0
$c_{d,top}$ (+10%)	0.08	-0.02	-0.36	-0.09	0
$\eta_{power}$ (-10%)	<b>11.11</b>	<b>-10.79</b>	<b>-12.56</b>	<b>-11.11</b>	0
$\eta_{power}$ (+10%)	-9.09	<b>10.78</b>	<b>12.1</b>	<b>11.11</b>	0
$v_{cruise}$ (-10%)	8.15	-9.55	0	-8.38	0
$v_{cruise}$ (+10%)	-2.34	3.09	0	2.66	0
$r_{rotor}$ (-10%)	<b>10.50</b>	-9.98	<b>-13.34</b>	<b>-10.56</b>	<b>27.20</b>
$r_{rotor}$ (+10%)	-6.48	7.25	<b>13.27</b>	7.69	-8.85

At first glance, the MTOW, the powertrain efficiency and rotor radius stand out and appear to be the sensitive parameters.

One of the largest differences is the difference in power margin for a 10% increase in MTOW. This increase in mass would make the required power higher than the 111.6 kW available for the propulsion system. Therefore the HyDrone would not be able to take-off and the mission would fail without changing other parameters. The energy consumption also increases significantly with the result that the margin on the energy decreases by an amount larger than the existing margin. So even if enough power would be available, the HyDrone would not be able to complete 4 cycles. The maximum range also decreases, but stays above the required 120 km. To operate the heavier drone, a higher rotational velocity of the rotors is required with as a consequence a far higher noise level. On the other hand a 10% decrease in mass, would make the drone much more effective and lightly less noisy.

The powertrain efficiency is another sensitive parameter. However, there are no real outliers. All variations are rather close to the 10% change in input. It is important to note, though, that for a 10% decrease in efficiency the reserve energy decreases to nearly zero. So if there are no other changes in parameters, the HyDrone would only just be able to complete its four cycle profile.

The last sensitive parameter is the rotor radius. Even though the outputs vary significantly, the margins in power and energy remain positive. The noise level does increase by a substantial amount for a smaller rotor radius. This is because the smaller rotors have to spin much faster to generate the same amount of lift.

Besides the sensitive parameters something else should be noted. For a 10% increase in velocity the energy consumption decreased and the range increased without negatively affecting other parameters. This indicates that the design has not been correctly optimised for cruise velocity. A quick analysis showed that the optimal velocity for the current configuration lies close to 44 m/s. Unfortunately, this value could not yet be implemented in the design. Determining an exact value and implementing it is a major recommendation for the future.

Furthermore, no unexpected results were encountered. All signs and order of magnitudes are in concordance with logic. It is for instance not surprising that a higher frontal drag coefficient does not influence the power margin as the maximum power is required at take-off. Also a slightly higher energy consumption is in agreement with a lower range and energy margin, while the maximum noise level remains unchanged as this value is reached during hover. The design was therefore considered robust.

If the optimal cruise velocity is applied and the mass and powertrain efficiency do not increase to much, the design of the HyDrone is regarded very feasible.



# Chapter 17: Manufacturing, Assembly & Integration Plan

In this chapter the production plan of the HyDrone is elaborated. It describes the Lean manufacturing and the Six Sigma methodology during the assembly process. Furthermore an overview will be given about how sustainability will be integrated into the assembly process.

## 17.1 Production plan

The production plan for the HyDrone will be in the scope of the Lean and Six Sigma methodology to find an efficient process for assembling the HyDrone. Lean manufacturing focuses on the manufacturing speed, reduces time between activities, events and cycles as well as reduction of waste and the elimination of bottlenecks, in order to save time and money. In addition Six Sigma reduces the number of errors in a process by use of the following 5 points itemised below.

- Define: Defining Problem and customer requirements
- Measure: Data collection of current process.
- Analyse: Identify the problem and investigate what causes it.
- Improve: Implement the solution that will solve the problem.
- Control: Maintain the improved results.

The purpose for the production plan for our HyDrone contains only the assembly process. The manufacturing of the materials and subsystems is done by external parties by subcontracting which is behind the scope of the HyDrones production plan. In the assembly process only one main assembly line is present which moves continuously forward and at specific moments is fed by sideways smaller assembly lines. These can be performed simultaneously to continuously feed the main assembly line.

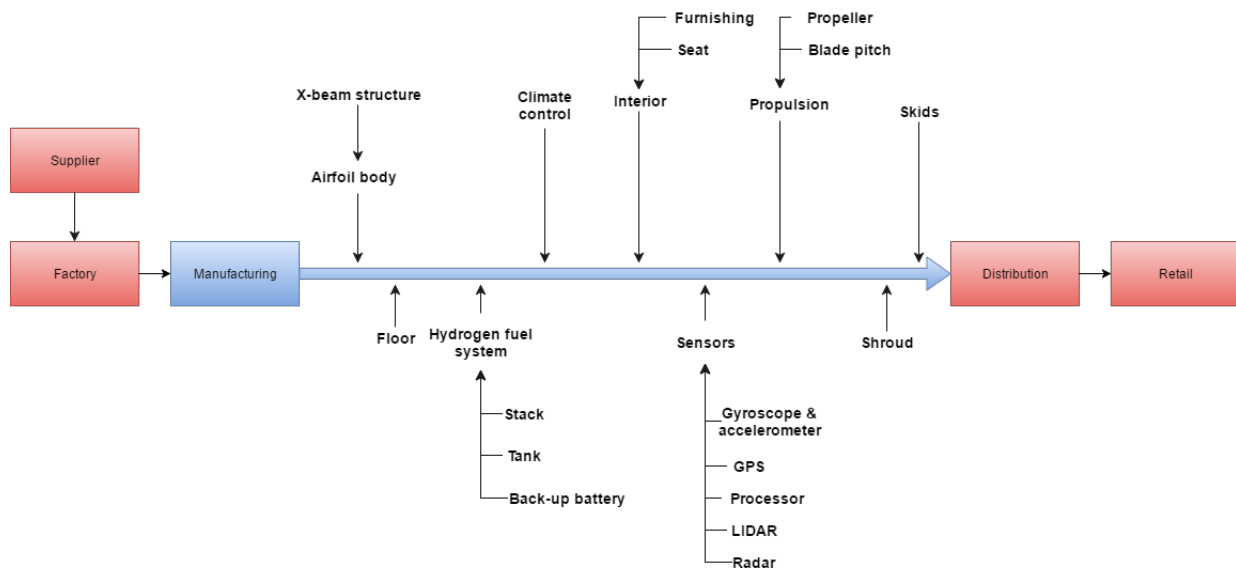


Figure 17.1: Assembly Line of the HyDrone

In fig. 17.1 it can be seen that the assembly line starts with assembling the core structure x-beam. Parallel to this assembly line the fuel system assembly is conducted. The time management between these two assembly lines should be executed in a way that when the base structure assembly is finished the fuel system assembly can be added immediately after that to the main assembly line. This process applies to the further assembly lines as well. As can be seen in fig. 17.1 the assembly line starts with placing the beams into the aerofoil body and firm them in a x-shape configuration. After that the floor is mounted on which the Hydrogen fuel system will be mounted. Then the climate control will be placed into the body followed by the interior. In this sideways assembly line the interior parts are mounted already together like the seats with the belts and the interface system. At the end when nothing will be more done in the interior the sensors will be placed carefully to prevent damaging them. After placing the sensors only things at the outer side of the body will be assembled as the

---

propellers, shrouds and skids. Which also are each assembled for a large part before they are mounted on the HyDrone in the main assembly line.

## 17.2 Sustainable Manufacturing

The lean manufacturing process as mentioned in section 17.1 reduces waste in the production process of the HyDrone that means that it has also an improving effect on sustainability. The benefits on sustainability will be now itemised.

- Preventing overproduction leads to less storage space and commuting to and from there. Also the chance of products product expiration or excess inventory.
- An efficient assembly line between the workstation in the factory prevents unnecessary transportation.
- Reducing time to correct errors or find them easier due to better checking procedures or technologies
- Hiring the right skilled people reduces the amount of people needed to complete the particular task.
- Poor human resource management which leads to not using or even missing opportunities.
- Efficient tooling of products to reduce the residual material after tooling.
- Using common tools to prevent in order to prevent unnecessary education for employees.
- Reducing processing of information, data and testing.
- Using ISO14001:2015 standards which specifies the requirements for an environmental management system that an organisation can use to improve its environmental performance.

---

# Chapter 18: Post DSE

This chapter details the design and development activities and respective timelines to be performed from publication of this report until market launch. They ought to be performed, as per the user requirements presented in section 3.2, within a time frame consistent with a time-to-market of 10 years.

## 18.1 Design and Development Logic

This section sets out to logically order all planned post DSE activities. The summary and conclusion of this section is captured in fig. 18.1. As can be seen in the figure the post DSE activities are divided into five stages: Starting in stage 1 and moving on to the next stage once the final activity in a stage has been performed. Notice that the development of the autonomous software plays through all five stages, as this is a very challenging aspect of the HyDrone. It is important that this software is developed in timely fashion. The following paragraphs provide stage by stage support and explanation of fig. 18.1.

**Stage 1:** The first task to be performed after the publication of this report is to come up with a detailed design. One could argue that the design presented in this report is also detailed, but activity 1.1 means to go into even further detail, using less simplifying assumptions and going all the way up to methods for assembly of parts. Next, a complete 3D model is produced which encompasses every single aspect of the design. After that parts of this model are analysed using FEM and CFD tools, subsequently the entire assembly of the model is also analysed through FEM and CFD. The results of these simulations are analysed and options for improvement are considered. The decision is then made to either confirm the current design or iterate and apply possibly improvements. Once the final design has been confirmed the autonomous software development is set in motion.

**Stage 2:** After the final design has been proven to work in theory an actual scaled prototype is produced. This prototype is used for wind-tunnel testing, to see how the aerodynamics work in reality, and is used for scaled flight test to investigate performance and stability of the HyDrone. From these tests results are gathered which are considered and iterated upon, when all improvements are made the prototype is confirmed and the next stage is entered.

**Stage 3:** Now that a real life check has been done on a scaled prototype, it is time to move on to 1:1 scaled tests. Structural- and performance tests are performed on parts and/or sub-systems (e.g. drop tests on the landing gear and performance tests on 1:1 scale propellers). Each part and/or sub-system is investigated and improved individually until they all comply with their desired behaviour. Lastly the parts/sub-systems are put through the certification process.

**Stage 4:** With every aspect of the entire vehicle working separately, a complete prototype is assembled. This prototype is first put through flight tests focusing on the flight envelope to see whether the finalised assembly meets performance requirements. From this analysis possible improvements are retrieved and implemented. At the same time the autonomous flight software is fine tuned for the actual vehicle (now that its final parameters are known). With the autonomous software fine tuned, flight tests can be performed to investigate whether or not the software works. If, at last, the vehicle appears to be fully functional, it is put through the certification process.

**Stage 5:** In this stage the development of the production line and acquisition of production facilities is set in motion, so that the HyDrone can actually produced on a larger and more efficient scale. Once all facilities are required, the production is started, resulting, finally, in the market launch of the HyDrone.

## 18.2 Timeline

With all the post DSE, or development process, activities established and put into logical order a time schedule had to be established. A total development time of 10 years has been specified for the HyDrone concept, the activities presented in section 18.1 have been divided over these 10 years. A clear overview to present such a time schedule is by means of a Gantt chart. The entire overview of the development process of the HyDrone is shown in fig. 18.2. Most of the presented elements of the Gantt chart should be self-evident, as the activities have already been described in the previous section. However, there are a few things which is further explained.

All the times required per stage are based upon what the HyDrone team thought to require in order to perform such a task. Some typical time indications are taken from flight magazines (e.g. often the first full-scale prototype of a concept is presented somewhat 3 years before the launch of the final product), but no estimations have been found based on technical articles and reports due to the lack of comparable information.

---

Please note that the activity 'Explore design improvements' (1.7, 2.4, 3.4 and 4.3) contains the iteration process described in the block diagram of fig. 18.1 i.e. 'Explore design improvements' encompasses the repetition of all the activities performed in the iteration process. Therefore, the 'Explore design improvements' typically takes just as long as all activities preceding it. This does not necessarily mean that it only contains one iteration, however. The assumption is made that every next iteration will not take as long as the previous one, since processes no longer have to be established from scratch.

What else is noticeable, although already shortly discussed in the previous section, is that the development of the autonomous software starts as soon as the first iteration of the final design has been confirmed through extensive 3D computer generated analysis. This is because the autonomous flight software plays a major role in the HyDrone concept and it has to work perfectly in order for the vehicle to be feasible.

The assumption is made that the production of the full-scale prototype will not take as long as the production of the prototypes for parts/sub-systems. This is because unexpected implications are likely to occur which will increase total time spent on an activity. Since these implications will occur during the part/sub-system production they will not happen again when the full prototype is assembled. Most likely, there will also be unexpected events during the assembly of all parts, but the delay caused by these events are assumed to be less than all the sum of all the delays occurring per part/sub-system.

Lastly, note how the establishment of manufacturing line for the vehicle already starts before finalising the full scale testing and certifying stage. This decision is made to prevent great unnecessary delay between finalising the vehicle and truly launching it. The manufacturing logistic stage does not start earlier to prevent attaining wrong tooling and facilities, as in the final stages of the design small things may still change which might in turn change the lay-out and components of the manufacturing line.

## DSE activities

### Post DSE activities

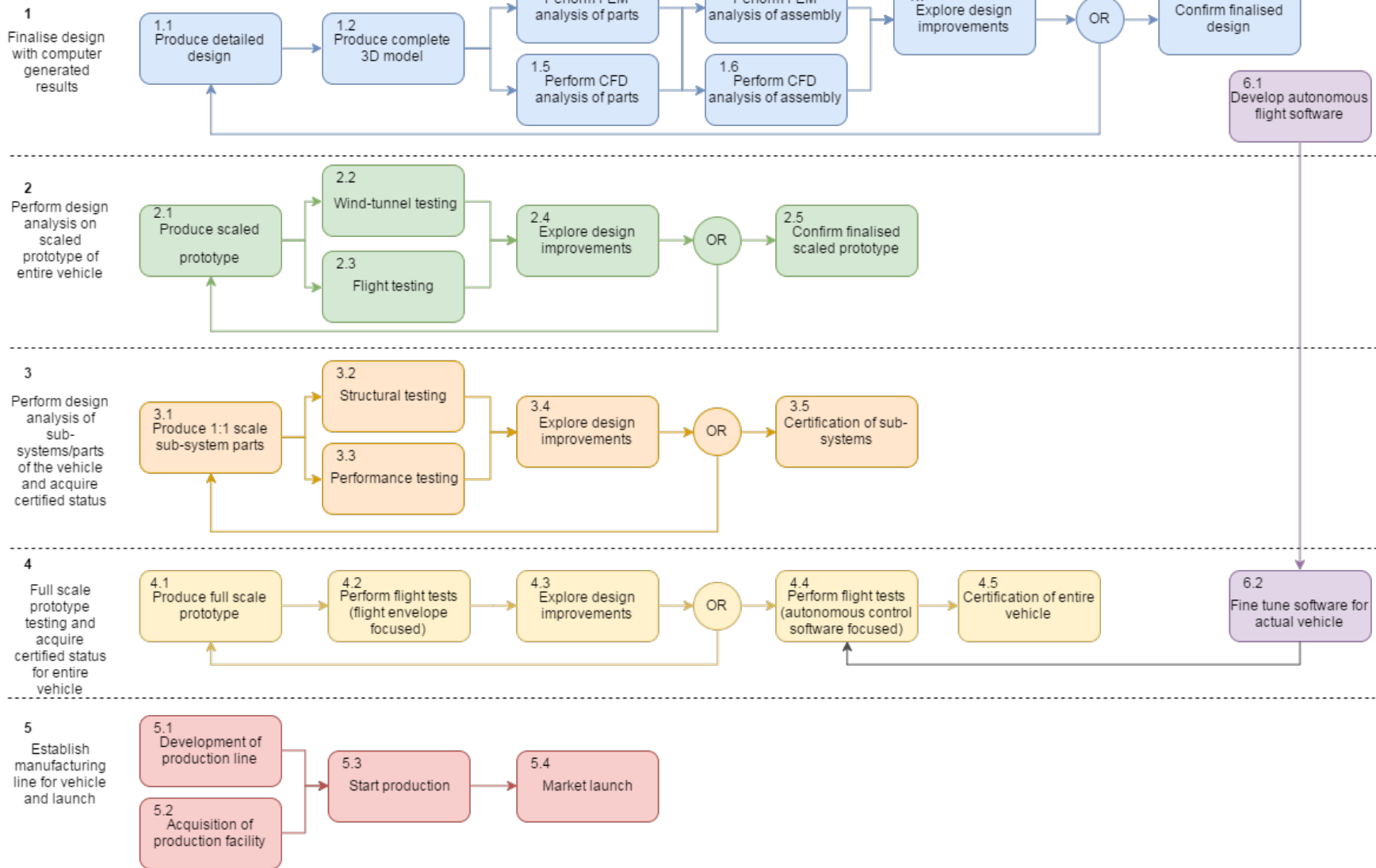


Figure 18.1: Project Design & Development Logic

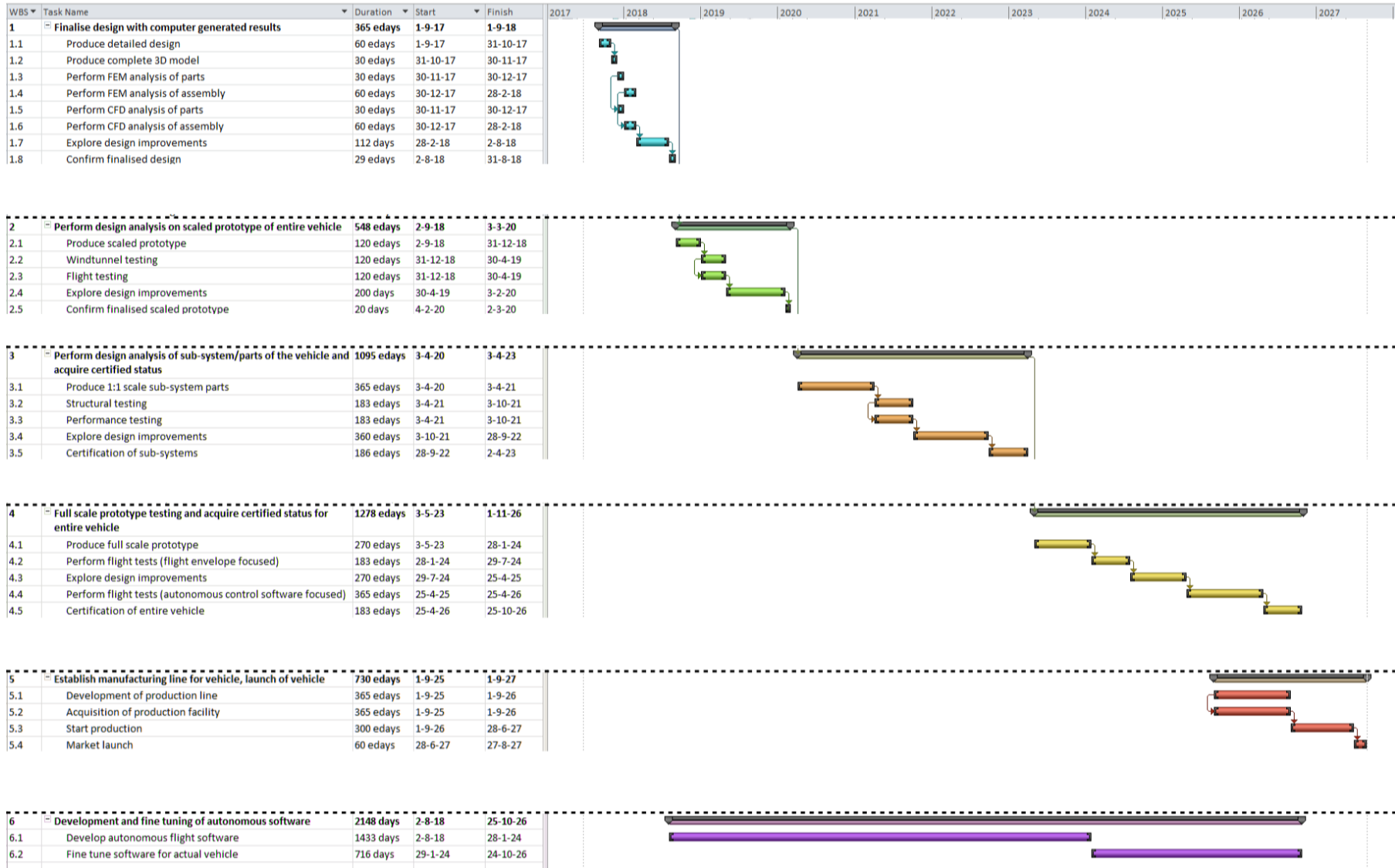


Figure 18.2: Project Gantt Chart

# Chapter 19: Business Plan

This chapter serves to disclose financial estimates from cost estimations to market analysis and return on investment (RoI).

## 19.1 Cost Estimations

The following section will include all the cost estimations performed on the HyDrone concept. First the unit production cost is estimated, followed by the total expected development cost related to the activities described in chapter 18. Lastly the operational costs are estimated, this is an aspect of a design concept which can easily be overlooked, but is of utmost important.

### 19.1.1 Unit Cost

The costs of each component within each subsystem have been estimated based on the sources given in table 19.1, where each value has been adjusted for inflation (US\$ 2017)<sup>1</sup>. Certain cost estimates have been based on the values quoted by online retailers, given that many of the components of the HyDrone are already widely available on the market. This is not the most substantial way to estimate the cost, given that other competitors may quote a different price for the same product, but does provide a general overview of how the budget can be affected.

Many of the components have been tailored to the HyDrone itself, such as the window and reinforcements. In this case, the fabrication costs of each material have been estimated based on the price-per-kilogramme rates from the *CES EduPack* database [31]. Using the cost distribution presented in fig. 19.1 allows one to estimate the labour costs based on the fabrication costs. Therefore, after determining the fabrication cost of a carbon fibre component, the total production cost can be obtained by dividing the fabrication cost by 0.14, since this its share of the total cost. It should be noted that the source from which fig. 19.1 was obtained is from 1975, which allows one to make a conservative estimation, given that the efficiency of the manufacturing process has likely improved ever since.

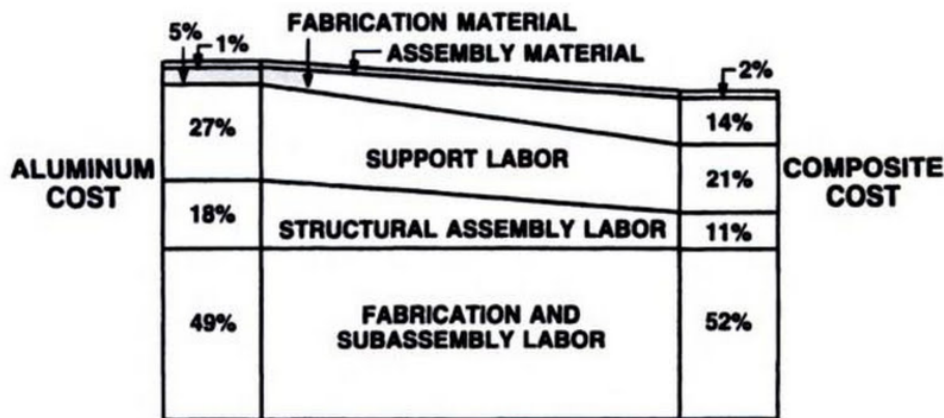


Figure 19.1: Structural Cost Breakdown [%] for the Vertical Fin of Lockheed L-1011 [82]

<sup>1</sup><http://www.usinflationcalculator.com/>

Table 19.1: Subsystem Cost Estimations (US\$ 2017)

	Number of Components	Cost of Single Component (US\$)	Combined Cost (US\$)	Notes/Sources
<b>Structures &amp; Materials</b>				
Beams	2	1036	2072	[31] [82]
Cockpit Reinforcement (front only)	1	2508.80	2508.80	[31] [82]
<i>Cockpit Assembly</i>	5	-	5272.96	Each component has a different price [31] [82]
Shrouds	4	2712.64	10850.56	[31] [82]
Shroud Reinforcements (front only)	2	6171.76	12343.52	[31] [82]
Skids	2	1111.60	2223.20	[31] [82]
Window	1	1070.72	1070.72	[31] [82]
<b>Propulsion &amp; Power</b>				
Battery (Reserve)	1	539.60	539.60	<sup>2</sup>
Cables	-	-	160	
Electric Motors	8	1195.71	9565.68	Adjusted for inflation (2011 prices) <sup>3</sup>
Fuel Cell Stack	1	39753.35	39753.35	Adjusted for inflation (2015 prices) <sup>4</sup>
Fuel Cell Tanks	2	5472.27	10944.54	Adjusted for inflation (2011 prices) <sup>5</sup>
Rotor Blades	16	1042.02	16672.32	[31] [82]
<b>Control &amp; Stability</b>				
4G Modems	2	99	198	<sup>6</sup>
GPS	2	380	760	<sup>7</sup>
Gyroscopes	2	27.26	54.52	<sup>8</sup>
LiDAR Sensors	5	500	2500	<sup>9</sup>
NVIDIA Processors	2	2500	5000	<sup>10</sup>
MESA Radar	5	1000	5000	<sup>11</sup>
Pitch Motors	8	800	6400	<sup>12</sup>
<b>Furnishing &amp; Equipment</b>				
Acoustic Foam	-	-	163.07	<sup>13</sup>
Air Conditioning	1	600	600	<sup>14</sup>
Ceiling Fabric	-	-	89.32	<sup>15</sup>
Seat	1	484	484	<sup>16</sup>
Tablet Interface (iPad Pro)	1	800	800	<sup>17</sup>
<b>Total Cost</b>			<b>136026.16</b>	

<sup>2</sup><https://electrek.co/2017/01/30/electric-vehicle-battery-cost-dropped-80-6-years-227kwh-tesla-190kwh/> [cited 23-06-2017]

<sup>3</sup><http://sustainableskies.org/the-joby-monarch-%E2%80%93-rising-above-it-all/> [cited 23-06-2017]

<sup>4</sup>[https://www.hydrogen.energy.gov/pdfs/15015\\_fuel\\_cell\\_system\\_cost\\_2015.pdf](https://www.hydrogen.energy.gov/pdfs/15015_fuel_cell_system_cost_2015.pdf) [cited 23-06-2017]

<sup>5</sup>[https://energy.gov/sites/prod/files/2016/09/f33/fcto\\_h2\\_storage\\_700bar\\_workshop\\_2\\_james.pdf](https://energy.gov/sites/prod/files/2016/09/f33/fcto_h2_storage_700bar_workshop_2_james.pdf) [cited 23-06-2017]

<sup>6</sup><https://www.4gltemall.com/huawei-e3372-4g-lte-cat4-usb-stick.html> [cited 23-06-2017]

<sup>7</sup><http://www.directionsmag.com/entry/finally-affordable-high-precision-gps-for-drones/470208> [cited 23-06-2017]

<sup>8</sup><http://uk.farnell.com/microchip/mm7150-ab0/3d-motion-module-i2c/dp/2474843> [cited 23-06-2017]

<sup>9</sup><http://news.techtime.co.il/2017/05/24/innoviz-lidar-sensor/> [cited 23-06-2017]

<sup>10</sup><https://www.fool.com/investing/2016/10/27/tesla-motors-inc-is-using-nvidia-corporations-driv.aspx> [cited 23-06-2017]

<sup>11</sup><http://echodyne.com/products/> [cited 23-06-2017]

<sup>12</sup><http://www.directindustry.com/prod/oriental-motor/product-15581-1850227.html> [cited 23-06-2017]

<sup>13</sup><https://www.zamro.nl/product/8817C/plaat-af-armaflex-af-13-8000x1000x13?gclid=CKSxZLqgOdQCFbMK0wodb6YPHQ> [cited 23-06-2017]

<sup>14</sup><http://www.ebay.com/itm/A-C-KIT-UNIVERSAL-UNDERDASH-EVAPORATOR-COMPRESSOR-2A-AIR-CONDITIONER-432-0-12V-/282083050516> [cited 23-06-2017]

<sup>15</sup>[http://www.schuimrubberbetaalbaar.nl/wand-en-plafondbekleding\\_114/hemel-bekleding-grijs-voor-auto-hemels-143-cm-breed-1988.html?gclid=CK\\_n9MqXOdQCFckV0wodQfAL2w](http://www.schuimrubberbetaalbaar.nl/wand-en-plafondbekleding_114/hemel-bekleding-grijs-voor-auto-hemels-143-cm-breed-1988.html?gclid=CK_n9MqXOdQCFckV0wodQfAL2w) [cited 23-06-2017]

<sup>16</sup><https://www.tillett.co.uk/shop/documents/downloads/B3.5%20Dimensions%202017.pdf> [cited 23-06-2017]

<sup>17</sup><https://www.apple.com/shop/buy-ipad/ipad-pro> [cited 23-06-2017]

The total unit cost estimate presented is that of the first produced HyDrone, as the scale of production increases the production cost per unit are likely to decrease. If the unit production cost would remain constant then the total production cost would simply follow from multiplying the amount of units produced by the cost related to the production of one unit. However, Larson & Wertz [83] found that the total production cost will not increase linearly with the production volume, instead the cost per unit will decrease to what is described as the 'learning curve'. This learning curve is a mathematical technique to account for economies of scale, set up time and human learning [83]. Equations eq. (19.1) to eq. (19.3) show this mathematical technique.

$$B = 1 - \frac{\ln(100\%/S)}{\ln(2)} \quad (19.1)$$

$$L = N^B \quad (19.2)$$

$$ProductionCost = TFU \cdot L \quad (19.3)$$

Here  $S$  is the learning curve slope,  $N$  is the number of units produced,  $L$  is the learning curve factor and  $TFU$  is the theoretical first unit cost. For aerospace industry the following relation between  $N$  and  $S$  is given:

- $N < 10 : S = 95\%$
- $10 > N < 50 : S = 90\%$
- $N \geq 50 : S = 85\%$

When dividing the total production cost again by the number of units produced one can see how the unit cost reduces as the amount of units produced increases. fig. 19.2 plots the unit cost versus the number of units produced for a  $S$  of 95% and a  $S$  of 85%. As is evident from the figure a learning curve of 85% greatly decreases the unit cost, however a reduction this extreme is not expected for the HyDrone as of the shelf singular components (like the fuel tanks) will not decrease in price this rapid. Looking at the  $S = 95\%$  curve one can see that even for a relatively slow learning process the unit cost already greatly decreases. From this analysis it can be concluded that a unit cost reduction can definitely be expected as the amount of produced HyDrones increases.

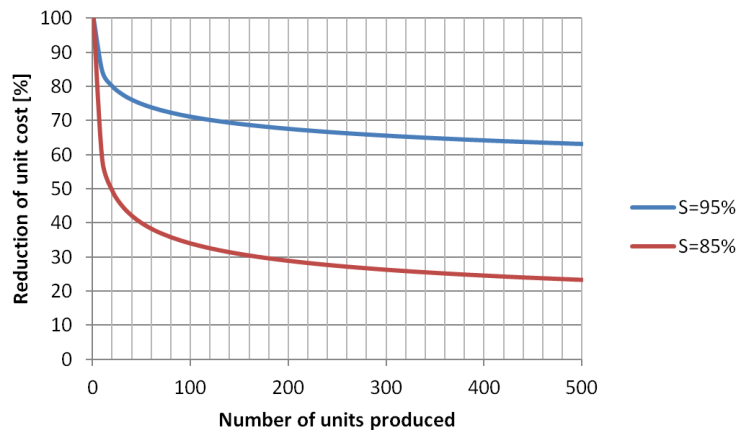


Figure 19.2: Unit Product Cost Decreases as Production Volume Increases

### 19.1.2 Development Costs

The development cost of the HyDrone is found by summing the estimated costs of all the activities presented in section 18.1. The final result of the development cost estimation and its subdivision over grouped activities is presented in fig. 19.3, a grant total development cost of roughly \$24M was estimated. The numbers in red indicate values which have been determined through 'educated guesses' due to lack of sources. The development cost of solely creating a functional final vehicle (so without certification and fabrication facilities) would be roughly \$10M. Please do note that the cost estimates established in this section are rough estimates and could greatly deviate in reality, the presented results are solely an indication of what development costs can be expected. A short explanation on how the different activities have been grouped is presented below:

- **A: Software.** These activities include software development and generation of computer generated simulations.
- **B: Prototype production.** This consists of building scaled/full-sized prototype parts/assemblies.
- **C: Tests.** The activities presented here encompass all the tests performed on parts and prototypes.
- **D: Designing.** These activities relate to all work performed to improve/confirm the design of the HyDrone.

- 
- **E: Certification.** This includes the certification process activities.
  - **F: Production logistics.** All activities involving the logistic setup to realise the HyDrone concept.

With the definition of each group in mind, the cost estimates could be established. The following paragraphs briefly explain how the cost estimations were performed per group of development activities.

**A:** The software costs were estimated by multiplying the amount of people working on a task times the amount of days that task is performed (as presented in section 18.2) times the average daily salary of a software engineer<sup>18</sup>. Assuming a team of five software developers this summed up to a total cost of roughly \$5.2M.

**B:** The prototype production costs were established as follows: for the scaled prototype costs it was assumed that these costs would equal half the costs of producing one unit (as found in section 19.1.1), the 1:1 scale sub-systems/parts were assumed to sum up to a total cost equal to that of producing one unit, lastly the full scale prototype was estimated to cost as much as one unit plus extra cost covering for unexpected implications and extra man hours required whilst producing the first prototype. The total sum of costs was estimated to be roughly \$0.38M. Note that the costs of having to create multiple prototypes after damage due to testing are not included here, but in C instead.

**C:** The wind-tunnel cost estimation was established by looking up daily costs of operating a reference wind-tunnel<sup>19</sup> and multiplying this by the amount of days required for testing (number of days specified in section 18.2). The performance testing cost was hard to quantify and thus estimated to be in the same order of magnitude as the wind-tunnel testing. For the scaled prototype flight testing the costs were estimated by assuming that the total damage caused by failed flights would equal three times the production costs of a single scaled prototype. All remaining tests costs were estimated using the same methodology as for the scaled flight test. A grant total of roughly \$2.2M was estimated to be spent on tests.

**D:** These costs were estimated using the same method as for A: multiply the average daily salary of single person times the amount of days spent times the amount of people working on an activity. This time the average salary of an aerospace engineer was used as a source<sup>20</sup>. Assuming a team of five aerospace engineers this added up to a total of roughly \$2.4M.

**E:** Due to a great lack of publicly available certification costs estimates for small helicopters no good estimate could be established here. A mere educated guess could be produced from past research performed. A total estimate of \$8.0M was established.

**F:** The same argumentation as for certification costs goes here: there is too little data available to make any reliable estimates. These costs also greatly depend on the scale of production and the type of tooling required, which complicates things even further. An educated guess of a total cost of \$5.5M was assumed.

---

<sup>18</sup><http://www.payscale.com/research/US/Job=SoftwareEngineer/Salary>

<sup>19</sup><https://www.aa.washington.edu/AERL/KWT/rateguide>

<sup>20</sup><http://www.payscale.com/research/US/Job=AerospaceEngineer/Salary>

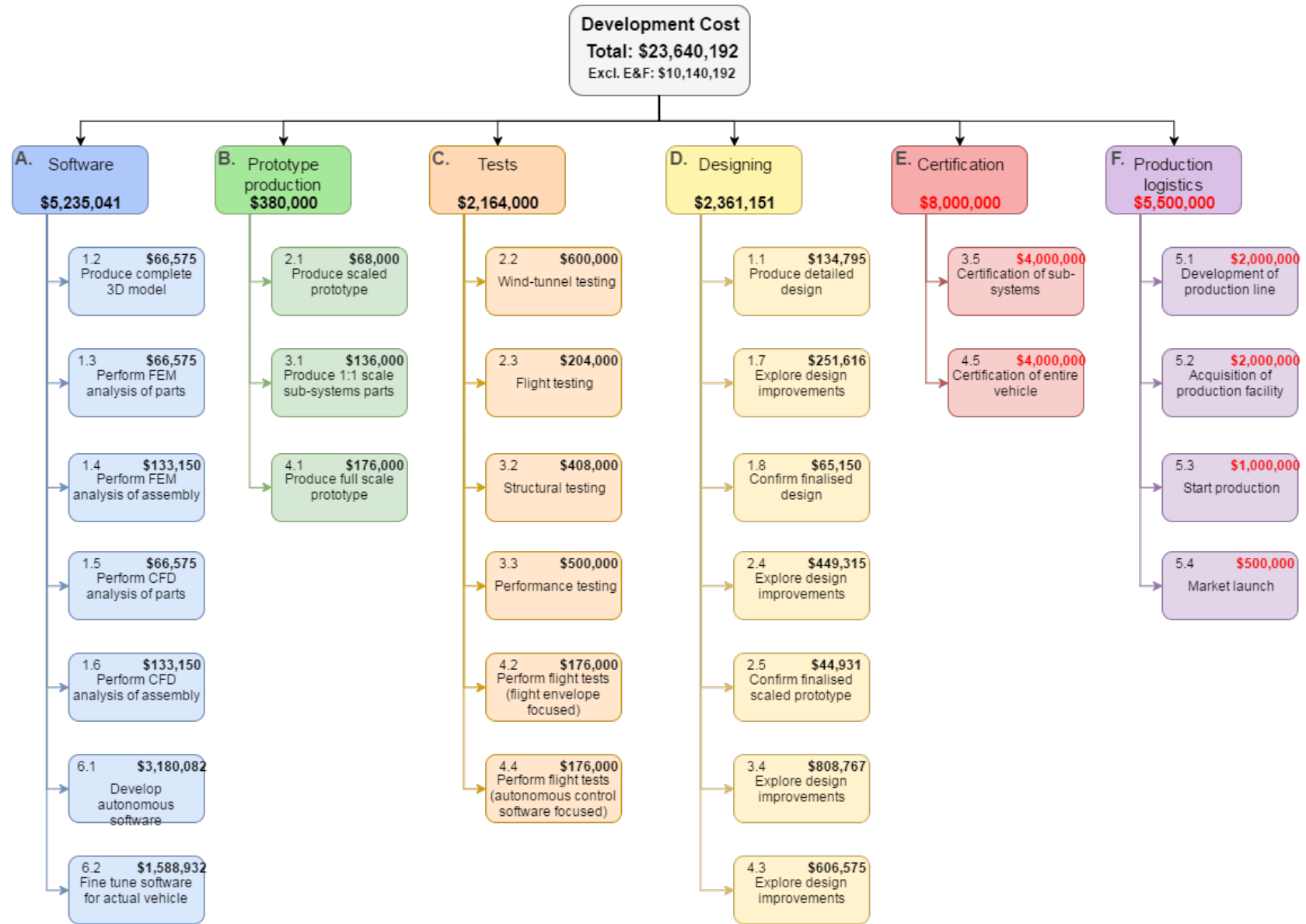


Figure 19.3: Cost Breakdown Structure

---

### 19.1.3 Operational Costs

It is found that for a system which developed for the long-term and multiple copies are produced, the operational and maintenance cost cover 60% of the total life cycle costs [84]. Since this is a significant part, it is important to make an estimation of these costs. The results are summarised in table 19.2. For the HyDrone the costs can be categorised as follows <sup>21</sup>

1. Variable Cost	2. Fixed Cost	3. Reserve for Overhaul
(a) Fuel	(a) Depreciation	(a) Engine Overhaul
(b) Maintenance	(b) Rentals	(b) Kit Overhaul
	(c) Insurance	
	(d) Other	

**1.a** The total amount of fuel used per mission is  $4.41\text{kg}$ , see section 10.1. The total duration of the mission is roughly 1 hours. This boils down to  $4.41\text{ kg}$  fuel per flight hour. The average price of hydrogen per gasoline gallon equivalent is \$14.10 [85]. Since  $0.997\text{ kg}$  hydrogen is equivalent to one gallon gasoline<sup>22</sup>, the total fuel cost per flight hour equal  $4.41 \cdot 0.997 \cdot 14.10 \approx \$62.2$ .

**1.b** The maintenance costs for the HyDrone are based on the Robinson R22 Helicopter. The R22 has an unscheduled maintenance cost of \$7.25 per flight hour. The maintenance labour costs per hour were estimated to be \$95.00 [86]. This means that for the R22 the flight hours to unscheduled maintenance hour ratio equals roughly 13.1 .

The scheduled periodic inspections also have a labor cost of \$ 95.00 per hour. The estimated scheduled inspection cost per flight hour is determined to be \$13.30. The flight hours to scheduled inspection cost per hour ratio is then equal to 7.1 . Summing up the scheduled and unscheduled maintenance costs, the average maintenance cost per flight hour equals \$20.55 for the R22.

It is expected that this will be roughly % 30 lower for the HyDrone[87][88]. Both sources indicate a cost saving of more that %35 when a electrical vehicle is compared to a vehicle with a combustion engine. To remain conservative, the value of % 30 was chosen. This results in a maintenance cost of \$ 14.38 per flight hour.

**2.a** Part of the fixed costs is the depreciation of the HyDrone. According to Conklin and de Decker the annual depreciation for rotorcraft equals to 5%<sup>23</sup>. With a selling price of \$260,000.00 this will cost  $0.05 \cdot 260,000 \approx \$13,000.00$  in the first year.

**2.b** The rentals category encompasses the landing and parking fees. It is assumed that the owners will use the HyDrone to travel between their homes and work. There are two options: Either let the HyDrone fly home again and park there or park at an hangar in the city. For the latter the parking costs are estimated to be \$100.00 if parked between 3 and 6 hours. \$120.00 if parked between 6 and 12 hours and a daily rate ( $\geq 12$  hours) of \$180.00. If parked shorter than 3 hours, no parking fee is charged. These fees and charges are handled at LAX<sup>24</sup>. The are assumed to be valid as an estimation since the initial market has much similarities with Los Angeles. For the former there will not be any parking fee. However, the HyDrone has to travel between the owners' home and work once more which costs more fuel. Besides the drone has to land one extra time on a heliport. This costs extra money as well. The landing fee is also taken from LAX and equals \$57.00.

**2.c** The insurance costs are estimated to be \$8000.00 a year. This value is based on the insurance cost of a Robinson R22 helicopter with an experienced pilot [86]. This low-weight helicopter is 1.5 time as expensive as the HyDrone and one would expect a lower insurance. However, the R22 has a long history of proven flight whereas the HyDrone still has to prove itself. Therefore it is assumed that the insurance costs will be approximately the same.

**2.d** The last category encompasses injuries, loss and damage which excesses the insurance recoveries. It also includes unforeseen expenses and professional/technical fees. For passenger air carriers these cost are roughly 0.1% of the operational costs [89]. To be conservative, a value of 1% is assumed for the HyDrone.

**3.a** Again the Robinson R22 to is taken as a reference. The R22 has an 2200 flight hour overhaul which costs \$29,000. However, the eight electrical engines of the HyDrone will cost \$9565.68 in total. Assuming that the maximum overhaul costs are equivalent to the price of eight new engines it is about 3 times as cheap as the R22 engine overhaul.

Furthermore an electric engine has few moving components whereas an combustion engine has a lot. This means that the electric engine is much less complex. Studies show that this results in % 35[87] to % 44[88] less maintenance intensive. Therefore it is assumed that the engine overhaul will take place every 2860 hour (2200

---

<sup>21</sup>[https://www.faa.gov/regulations\\_policies/policy\\_guidance/benefit\\_cost/media/econ-value-section-4-op-costs.pdf](https://www.faa.gov/regulations_policies/policy_guidance/benefit_cost/media/econ-value-section-4-op-costs.pdf)

<sup>22</sup><https://web.archive.org/web/20110608142250/http://ts.nist.gov/WeightsAndMeasures/upload/H2-Laws-and-Reg-Paper-USNWG-JUN2008.pdf>, [cited 24-6-2017]

<sup>23</sup><https://www.conklindd.com/t-threethoughtsonmarketdepreciation.aspx>, [cited 26-6-2017]

<sup>24</sup><http://www.lawa.org/uploadedFiles/AirOps/pdf/FY%202015-16%20Landing%20Fees%20at%20LAX.pdf> [cited 26-6-2017]

\* 1.3). This results in \$3.34 per flight hour for engine overhaul. This engine overhaul will take place in 125 labour hours of \$ 95 per hour[86].

Next, the overhaul of the fuel stack is to be determined. Because the PowerCell S3-335c is still being validated, not much data is provided. Therefore the following reasoning was done in order to come up with a number; Lately, ACAL Energy produced an hydrogen stack with an endurance of 10,000 hours. This is equivalent to 300.000 miles<sup>25</sup>. Furthermore, Toyota gives a 100,000 mile warranty for their fuel stack. Combining these two facts, results in a estimated 3333 hours of proper functioning. Therefore it is assumed that after 3333 hours, the fuel stack requires an overhaul. Of course, combining two facts of two different stacks and apply it to a third one is a very rough estimation. It is however still conservative since it is not likely that, after the warranty period is exceeded, the fuel stack will fail immediately. The result is an estimated  $\$39753.35 / 3333 = \$11.93$  per flight hour for stack overhaul.

**3.b** The HyDrone’s aircraft overhaul parts kit has many similarities with the R22’s kit. They both contain rotor blades, seats, belts, bearings, furnishing etc.<sup>26</sup>. It is therefore assumed that the time until overhaul of 2200 hours will be the same[86]. The total costs of the HyDrone’s kit is the sum of rotor blades and furnishing & equipment, as presented in table 19.1. This results in an extra  $\$18,808/2200 = \$8.55$  per flight hour for the overhaul kit. This is also estimated to costs 125 man hours.

The full overhaul (stack, engines, kit) will take 250 man hours [86] at an hourly rate of \$95. The average time until overhaul equals  $(2860+3333+2200)/3 = 2797$  hours. So the overhaul labour costs are  $(95*250)/2797 = \$8.49$  per flight hour.

Table 19.2: Operational Costs Table

Variable Costs		Fixed Costs	
Fuel	\$66.20 per flight hour	Depreciation	5% a year
Maintenance	\$14.39 per flight hour	Rentals: - Parking Costs - Landing Costs	\$180 a day \$59 per landing
Overhaul - Engine - Fuel Stack - Kit - Labour	\$3.34, \$11.93, \$8.55, \$8.49, per flight hour	Insurance	\$8000 a year
<i>Total</i>	\$112.36 per flight hour	Other	1% of total operational costs

The total variable costs per flight hour are \$112.36. In the future it is expected that this will decrease significantly. Firstly, hydrogen will become more and more accessible and therefore become cheaper. Secondly, fuel stacks will be mass produced and therefore the price will drop and the development will not stop as well. The latter will result in more efficient stacks. Lastly, electrical engines will become cheaper as well due to mass production.

## 19.2 Market Analysis

The following section presents a rough market analysis, based on statistical data and news articles. Section 19.2.1 identifies potential clients in certain target locations, whereas section 19.2.2 presents an estimate of the expected number of transactions for a given market price. Potential competitors have been identified in section 19.2.3, which also specifies how the civil helicopter industry can be challenged.

### 19.2.1 Target Audience

The target audience of the HyDrone are wealthy and environmentally conscious commuters in or near crowded cities. The HyDrone will be a viable solution for individuals with a relatively long commute, since traffic can be avoided and travel time will be reduced in an environmentally friendly manner. The fully autonomous capability of the HyDrone is meant to appeal to those without a pilot’s licence, thus further expanding the

<sup>25</sup><http://www.prnewswire.com/news-releases/hydrogen-fuel-cell-thats-as-durable-as-a-conventional-engine-213225731.html>

<sup>26</sup><http://rotorcorp.com/r22-overhaul-kits/>

potential market. It is expected that households with a yearly income of over \$400,000 will dominate the sales due to the estimated market price of \$260,000 (see section 19.2.2).

Sales will be concentrated in California, especially Los Angeles, San Francisco and San Jose, given that the infrastructure that makes hydrogen fuelled transport possible already exists in these cities, but only for cars<sup>27</sup>. These target cities are also highly congested during rush hour, with an average commute of 29.2 minutes in Los Angeles, 30.5 minutes in San Francisco and 25.9 minutes in San Jose<sup>28</sup>. The HyDrone can overcome ground level traffic congestion and will likely appeal to many who are looking to save time and improve their productivity.

## 19.2.2 Market Volume

The market volume is defined as the total amount of transactions observed within a specified time frame in a certain marketplace<sup>29</sup>. Estimating the market volume is complicated, given that one has to gauge the public's willingness to adapt to this new technology. The idea of travelling in a vehicle not controlled by a human operator is still quite concerning to some, especially when it comes to fully autonomous flight.

A survey by the University of Michigan Transportation Research Institute found that only 21.4% of American respondents would be 'very interested' in having their own self-driving vehicle, or lease one [90]. The same survey shows that the number of American respondents who are not willing to pay more for self-driving technology was 54.5%. This survey was limited to self-driving cars, but one can expect a drastic decrease in the number of respondents willing to purchase a fully autonomous passenger drone, mainly due to the novelty and lack of infrastructure to support it. Attitudes will likely change over time, as the technology advances and the necessary facilities become more readily available, thus making the public more familiar with the concept zero-emission autonomous flight.

It is therefore essential to make a conservative estimate, knowing that commercial deployment will likely occur in ten years. The *Ehang 184* is estimated to cost somewhere between \$200,000 and \$300,000<sup>30</sup>. In order to be competitive, the cost of the HyDrone should be somewhere within that range, which is why a market price of 260,000 has been established. Sales will be minimal during the development stage, where potential customers will have the chance to pre-order the HyDrone and receive it in 2027, which marks the beginning of full market deployment. The development stage will have to be funded by investors in order to make ends meet. After 2027, when the HyDrone is on the market, 200 units are expected to be sold within ten years. Assuming the market price stays constant throughout those ten years, a profit of around \$124,000 is expected per unit (\$260,000 - \$136,000), leading to a total expected profit of \$24.8 million between 2027 and 2037, which is just below the estimated development cost. This is of course a very rough estimate, given that the market price of the drone will likely change over time, especially if the number of clients exceeds expectations.

## 19.2.3 Market Share

The market share is the portion of a market that is controlled by a certain company or product over a specified time period<sup>31</sup>. The target audience established in section 19.2.1 is only a small fraction of the global market, thus allowing for further expansion when the service becomes more affordable in the future. However, when estimating the expected market share, one will have to consider potential competitors with a similar product or service. The potential market for an autonomous VTOL taxi service has already been explored by the likes of *Uber* and *Ehang*, where the former company aims to operate its vehicles at a price of \$1.38 per mile per passenger and establish a price of \$200,000 per vehicle when 5000 vehicles per year are produced<sup>32</sup>. Therefore, it is important to build a reputation for the HyDrone as an efficient and low cost alternative to other competitors.

Helicopters form the largest share of VTOL vehicles meant for private civilian use. The global production of civil helicopters was found to be 1110 in 2015<sup>33</sup>. The best selling private helicopter in 2015 was the Robinson R44 which had a list price of \$465,000<sup>34</sup> and sold 196 units<sup>35</sup>. A smaller version, the Robinson R22, comes at a price of \$292,000<sup>36</sup>, making it one of the more affordable civilian helicopters on the market<sup>37</sup>. With a market

<sup>27</sup><https://www.netinform.de/H2/H2Stations/H2Stations.aspx?Continent=NA&StationID=-1> [cited 23-06-2017]

<sup>28</sup><http://www.indexmundi.com/facts/united-states/quick-facts/california/average-commute-time/cities#chart> [cited 23-06-2017]

<sup>29</sup><http://www.businessdictionary.com/definition/market-volume.html> [cited 24-06-2017]

<sup>30</sup><http://www.dronethusiast.com/ehang-184-is-a-manned-uav-you-will-never-get-to-fly/>

<sup>31</sup><http://www.investopedia.com/terms/m/marketshare.asp> [cited 24-06-2017]

<sup>32</sup><https://www.uber.com/elevate.pdf> [cited 24-06-2017]

<sup>33</sup><https://www.theatlas.com/charts/HkcxY-qY> [cited 25-06-2017]

<sup>34</sup>[https://robinsonheli.com/wp-content/uploads/2015/06/r44\\_2\\_pricelist.pdf](https://robinsonheli.com/wp-content/uploads/2015/06/r44_2_pricelist.pdf) [cited 25-06-2017]

<sup>35</sup><https://robinsonheli.com/uncategorized/robinsons-r44-and-r66-helicopters-rank-number-one-in-sales-in-2015/> [cited 25-06-2017]

<sup>36</sup>[https://robinsonheli.com/wp-content/uploads/2016/03/r22\\_pricelist.pdf](https://robinsonheli.com/wp-content/uploads/2016/03/r22_pricelist.pdf) [cited 25-06-2017]

<sup>37</sup><https://owlcation.com/misc/How-much-does-a-Helicopter-cost> [cited 25-06-2017]

price of \$260,000, the HyDrone is a more affordable option that presents similar qualities with many added benefits, such as fully autonomous zero-emissions flight. Therefore, a significant share of the private helicopter market could be addressed.

The HyDrone could also be used as an alternative to public transportation, in the form of an autonomous taxi drone service. As explained in section 19.2.1, this idea is already being explored in Dubai, where the city aims to have a quarter of all journeys be autonomous by 2030. The city aims to meet this target by purchasing passenger drones from the *Ehang* company, which would be a major competitor if this potential market were to be further explored. Given that Dubai has a population of about 2.8 million residents as of June 2017<sup>38</sup>, which is expected to grow to 5 million by 2030<sup>39</sup>, the city will likely require services from other companies if it aims to meet its target and encourage competition.

### 19.2.4 Return on Investment

The return on investment (RoI) has been determined using eq. (19.4), where  $n$  is the number of units sold. The expected number of sales given in section 19.2.2 is expected to be within a ten year time span.

$$RoI = \frac{Market\ Price \times n - (Unit\ Cost \times n + Development\ Cost)}{Unit\ Cost \times n + Development\ Cost} = \frac{260,000 \cdot 200 - (136,000 \cdot 200 + 23.6 \cdot 10^6)}{136,000 \cdot 200 + 23.6 \cdot 10^6} \quad (19.4)$$

Therefore, an RoI of 2.36% is expected after ten years on the market.

Another interesting comparison is shown in fig. 19.4, here the expected cost, expected revenue and expected profit are plotted versus the amount of units sold. From this figure, the required amount of units sold to be 'break even' (total revenue equal to total cost) can easily be deducted and is found to be 191 units.

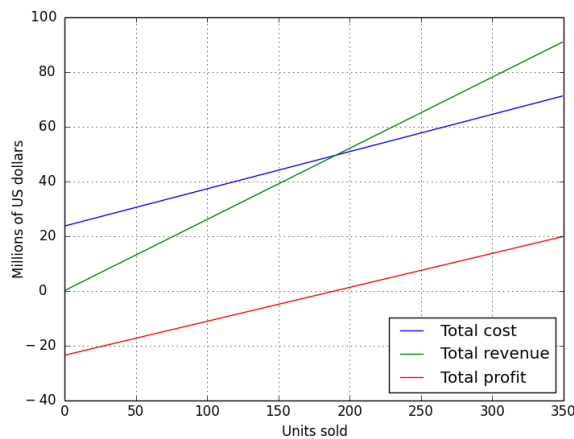


Figure 19.4: Expected Revenue, Cost and Profit Plotted vs amount of Units Sold

<sup>38</sup><http://www.dubai-online.com/essential/population/> [cited 25-06-2017]

<sup>39</sup><http://gulfbusiness.com/dubai-s-population-forecast-to-rise-to-five-million-by-2030/> [cited 25-06-2017]

---

## Chapter 20: Conclusion

The purpose of this report was to determine the final design of the HyDrone. The base for this was formed in the baseline and midterm report where a trade-off was made between the different concepts. Here it was chosen to use the multicopter concept for the final design. This concept uses a configuration with four low arms to which the rotors are attached. This concept was further worked out for the different subsystems. These subsystems include aerodynamics, structures and materials, propulsion, power, control and stability and safety.

For aerodynamics it was decided that the cockpit functions as a lifting body. This causes the required thrust, and thus power, in cruise becomes lower so that the HyDrone flies in a more efficient way. Furthermore, shrouds were added to the propellers in order to reduce noise and increase the safety.

In the structures department first the materials were selected taking into account the strength, cost, density and ecological footprint. Based on these criteria it was chosen to use quasi-isotropic carbon fibre for the cockpit, shrouds and load carrying structure. For the landing gear a more conventional material is used namely 7057-T6 aluminium. In order to cope with impacts the shrouds are reinforced with aramid fibre. Two crossed beams will be used to carry the loads of the propellers. The cockpit will only carry its own weight and the extra loads that are applied due to the lift that it generates. The shrouds were also designed to carry their own weight and aerodynamic forces. Finally the landing gear was designed. Its type was based on aerodynamic considerations while its dimensions were based on the maximum loads applied during landing.

For propulsion the choice was made to use a coaxial rotor system. This system is able to provide the required thrust and provides extra redundancy. The rotors were designed for the different flight phases. From this it became clear that a pitch system would be required in order to fly efficiently in all phases. This system was specifically designed for simplicity and thus low maintenance. The required power for the thrust is provided by a hydrogen fuel cell. This was sized so that it can provide both the maximum power needed during take-off and the required energy to fly four cycles.

In order for the drone to fly completely autonomously the required sensors needed to be selected. It was decided to use a LIDAR system to scan the ground for landing spots, a radar system to scan the environment around the drone for large distance and ultrasonic sensors, which scan the environment close to the HyDrone. Besides this an accelerometer, gyroscope and CORS GPS system are used to track the position and attitude. Finally the performance of the HyDrone was tested using a dynamic model and controllers were designed in order to ensure stable flight characteristics.

For safety the main aspect that was applied throughout the whole design of the drone is redundancy. This can for example be found in the coaxial configuration of the rotors which still provides safe landing capabilities when a rotor fails. Furthermore an autorotation mechanism was designed which ensures that even when all rotors fail the HyDrone can still land. Furthermore, possible safety weaknesses as lightning strikes and data hacking were considered and proper measures were taken to ensure complete safety.

Sustainability was taken into account for the whole design process. The material choices were based on the energy it cost to produce them and their recyclability capabilities. Furthermore, the shrouds were specifically designed to minimise the noise produced. The choice to use hydrogen was based on the fact that zero-emission flight was required which also contributes to sustainability. Finally an end-of-life plan for the batteries and stack was worked out to minimise environmental impact.

To conclude, the designs of departments were integrated to get the final design of the HyDrone. The final result is a four arm, low rotor, coaxial system with the cockpit acting as a lifting body. This design will provide an environmentally friendly solution to the growing traffic problems in highly urbanised cities.



---

## Chapter 21: Recommendations

Throughout the report for all the subsystems recommendations were made. A brief overview of these recommendations is given in this chapter. For a more detailed description the reader is referred to the chapter of the specific subsystem.

For aerodynamics the lifting body can be modelled in more detail using a CFD analysis. This would give more realistic results as the cockpit is now modelled as a wing which is much thicker than conventional aircraft wings. This also includes a more detailed noise analysis. For the shrouds a redesign might be done based on results from computer programs and CFD analysis. This might include a tilt-rotor design if complexity can be limited. It is also advised to consider fairing parts of the landing gear.

The design of the structure and the choice of materials can further be improved by implementing a FEM analysis to overcome the simplifications that were made. Furthermore, the dynamic load cases should be analysed in more detail which includes a deflection, vibration and fatigue analysis. Finally the assembly should be investigated together with the interior design and the influence of extreme weather needs to be taken into account. These all will lead to a more detailed structural analysis which could reduce weight as safety factors can be decreased.

In the design of the propulsion system a more advanced method as FVM could be used to provide more accurate results. Furthermore, the effect of the shrouds can be modelled in a more accurate way to provide more reliable results.

Using a hydrogen fuel cell to provide power is rather uncharted territory in aerospace applications. That is why a more detailed investigation in the BoP is required. Besides this the design of the electric circuit which contains components as the DC-DC converters but also the PCU should have more elaboration. Furthermore, the hydrogen technology shows a high growth potential and the developments should be closely followed. This might for example result in lighter tanks. Finally the cost of the power system is currently not very accurate and can be further specified.

For the control and stability section an in-depth look needs to be taken into the pitch system. As this is completely designed from scratch it is difficult to identify any possible weaknesses in the design. Furthermore, the choice for the type of gears and shaft has not yet been made. That is why a laboratory model needs to be made which tests the feasibility of the design. For the control system more investigation needs to be done in the tuning of the gains. If possible a method can be used to find the optimal combination of gains which can be used in multiple conditions.

In the safety system a look might be taken to a fire extinguishing system which can prevent all problems related to fire. Besides this a crash-seat can be designed which is specifically constructed for high loads to improve the safety of the passenger. Finally the landing gear might be expanded by adding a damper system. This increases both the comfort for the passenger and makes sure that the HyDrone can land with a higher velocity which increases the safety.



---

# Bibliography

- [1] Jenny Eriksson and Lars Svensson. Tuning for ride quality in autonomous vehicle. 2015.
- [2] *Code of Federal Regulations, Title 14, Aeronautics and Space*. National Archives and Records Administration, Office of the Federal Register, 2017.
- [3] Green Car Congress. Toyota fcv mirai launches in la; initial tfcs specs; 57,500or499 lease; leaning on prius analogy, november 2014.
- [4] Gina Willink Brett Glasner Carl Rusell, Jaewoo Jung. Wind tunnel and hover performance test results for multicopter uas vehicles.
- [5] Nicholas Willard. Multirotor aerodynamics.
- [6] Kenneth W. Liff Edwin J. Saltzman, K. Charles Wang. Aerodynamic assessment of flight-determined subsonic lift and drag characteristics of seven lifting-body and wing-body reentry vehicle configurations.
- [7] Wayne Johnson. *Helicopter Theory*. Dover Publications, New York, 1994.
- [8] Thomas F. Brooks Florence V. Hutcheson, Taylor B. Spalt. Airframe noise from a hybrid wing body aircraft configuration. National Aeronautic and Space Administration, 2016.
- [9] Mohammadreza Azimi Mofid Gorji-Bandpy. Airframe noise sources and reduction technologies in aircraft. Department of Mechanical Engineering, Babol Noshirvani University of Technology, 2012.
- [10] Geoff Wardle Stuart Macey. *H-Point*. Art Center College of Design, Pasadena CA, 2009.
- [11] John D. Anderson jr. *Aircraft Performance and Design*. WCB/McGraw-Hill, 1999.
- [12] John D. Anderson jr. *Introduction to FLight*. McGraw-Hill, 2008.
- [13] H.B. Helmbold. Der unverwundene ellipsenflugel als tragendi flache, 1942.
- [14] Sighard F. Hoerner. *Fluid-Dynamic Drag*. Sighard F. Hoerner, 1965.
- [15] Sighard F. Hoerner. Aerodynamic shape of wing tips, 1949.
- [16] Mark D. Moore. Nasa personal air transportation technologies.
- [17] H. Gounet and S. Lewy. Prediction of single-rotation prop-fan noise by frequency domain scheme. 1986.
- [18] Erdem D. Yilmaz, S. and M.S. Kavsaoglu. Effects of duct shape on a ducted propeller performance.
- [19] Yung Jian and Bo Zhang. Cfd study of a new annular lift fan configuration with high lift efficiency. 2017.
- [20] Kyrilian Dyer. Aerodynamic study f a small, ducted vtl aerial vehicle. Master's thesis, 2000.
- [21] Gerhard Muller and Michael Moser. *Handbook of Engineering Acoustics*. Springer, New York, 2013.
- [22] Elizabeth English John Holmes and Chris Letchford. Aerodynamic forces and moments on cubes and flat plates, with applications to wind-borne debris. 2004.
- [23] M. Dela. Xfoil, an analysis and design system for low reynolds number airfoils.
- [24] *Helicopter Flying Handbook*. U.S. Department of Transportation Federal Aviation Administration Flight Standards Service, 2012.
- [25] J.K. Sen. Advanced technology landing gear. Report, US Army Aviation Systems Command, 1990.
- [26] Grabowski A.M. McDermott W.J. Herr H.M. Kram R. McGowan, C.P. Leg stiffness of sprinters using running-specific prostheses. 2016.
- [27] M. Grawunder R. Ress and C. Breitsamter. Parasite drag reduction of a twin engine lightweight helicopter configuration. 2014.
- [28] M. Grawunder R. Ress and C. Breitsamter. Optimized skid-landing-gears for twin-engine light utility.
- [29] W. Khier. Navier-stokes prediction of the effect of the skids on the aerodynamics of the helipecter fuselage in forward flight.
- [30] Morits Grawunder Christian Breitsamter and Roman Ress. Aerodynamic design optimisation of a helicopter configuration including a rotating rotor head. 2014.
- [31] Granta Material Intelligence. Ces 2016 edupack, 2016.
- [32] National Research Council. *New Materials for Next-Generation Commercial Transports*. Washington, DC: The National Academies Press, 1996.
- [33] B. Irion D. van Heerden P. Kuiper H. de Wit Y. Yang, R. Boom. Recycling of composite materials. 2011.
- [34] Stanley T. Peters. *Composite Filament Winding*. ASM International, 2011.
- [35] T.H.G. Megson. *Aircraft Structures for Engineering Students*. Elsevier Aerospace Engineering Series. Elsevier Ltd., 2013.
- [36] Department of Physics New Mexico Tech. D'alembert's principle and applications.
- [37] Donald F. Young et al. *A Brief Introduction To Flud Mechanics*. Wiley, 2010.
- [38] L.H. Symes David Crist. Helicopter landing gear design and test criteria investigation, 1981.
- [39] TU Delft. Aerospace flight dynamics and simulation. BlackBoard Course.
- [40] M. Trudgeon. An overview of ngv cyliner safety standards, production and in-service requirements, 2005.
- [41] Justin Hale. Boeing 787 from the ground up, 2006.
- [42] Evonik Industries. Acrylite® acrylic sheet products for aircraft transparencies.
- [43] Phil Whyte. Helicopters get full composite treatment.

- [44] Timothy Edward Lee. Design and performance of a ducted coaxial rotor in hover and forward flight. Thesis, University of Maryland, College Park, 2010.
- [45] J. Gordon Leishman and Shreyas Ananthan. Aerodynamic optimization of a coaxial proprotor. American Helicopter Society, 2006.
- [46] Florent Lucas. Study of contra-rotating coaxial rotors in hover, a performance model based on blade element theory including swirl velocity.
- [47] R. Farrington and J. Rugh. Impact of vehicle airconditioning on fuel economy, tailpipe emissions, and electric vehicle range. Technical report, National Renewable Energy Laboratory.
- [48] A. Van Wijk, L. Verhoef. *Our Car as Power Plant*. IOS Press TU Delft, 2014.
- [49] Hexagon Composites. Hydrogen storage and transportation systems, 2017.
- [50] Dr. D Alciatore. Thin-walled pressure vessels. Technical report, Colorado State University, 2008.
- [51] Dominique Perreux. Hydrogen storage solutions, 2012.
- [52] B. D. James and C. Houchins. 700 bar type iv h2 pressure vessel cost projections. Technical report.
- [53] US Drive. Target explanation document: Onboard hydrogen storage for light-duty fuel cell vehicles, 2017.
- [54] Nuvera Fuel Cells. Alternative energy today. Technical report, Nuvera.
- [55] UTC Power Corporation. Model 120 puremotion system, 2012.
- [56] Ballard. Putting fuel cells to work, 2016.
- [57] Fuel Cell Technology Office. Multi-year research, development, and demonstration plan. Technical report.
- [58] Sunita Satyapal. Fuel cell system cost - 2015. Technical report.
- [59] Won Suh. Modeling, analysis and control of fuel cell hybrid power systems.
- [60] Green Car Congress. Panasonic develops new higher-capacity 18650 li-ion cells; application of silicon-based alloy in anode, december 2009.
- [61] Kiyotsugu Oba. Wiring harnesses for next generation automobiles. 2013.
- [62] B. C. Hennessey N. T. Nguyen. Status of nhtsa's hydrogen and fuel cell vehicle safety research program, 2007.
- [63] L.R. Gambone and J.Y. Wong. Fire protection strategy for compressed hydrogen-powered vehicles. Technical report, Powertech Labs Inc., 2008.
- [64] Tom Koehler. A green machine. may 2008.
- [65] Andrew Gibiansky. Quadcopter dynamics, simulation, and control. Description of quadcopter dynamics.
- [66] Teppo Luukkonen. Modelling and control of quadcopter. Technical report, 2011.
- [67] Zwe-Lee Gaing. A particle swarm optimization approach for optimum design of pid controller in avr system. *IEEE Transactions On Energy Conversion*, 19(2):384–391, May 2004.
- [68] Boeing. Lightning strikes: Protection, inspection, and repair, 2012.
- [69] Harris Miller Miller Hanson Inc. Basic aircraft noise terminology, 2012.
- [70] W Dobrzynski. Ermittlung von emissionskennwerten fur ur schallimmissionsrechnungen an landeplatzen, 1994.
- [71] Louis H. Williams James T. Howlett. Measurement, analysis, and prediction of aircraft interior noise. 1976.
- [72] B. Stuber and F. Lang. Schalldämmmaße von prozessofenwänden. 1983.
- [73] Kraft R. Molsigner R. Design and performance of duct acoustic treatment. 1991.
- [74] Sofrin T.G. Rice E.J. Gliebe P.R. Groeneweg, J.F.
- [75] title = Sources of noise in axial flow fans. year = 1964 Sharland, I.J.
- [76] Zhuang L. Bottema J. Wittebrood A.J. De Smet P. Haszler A. Vieregge A. Miller, W.S. Recent development in aluminium alloys for the automotive industry. *Materials Science and Engineering A*, 280(1), March 2000.
- [77] McKechnie T.A. Turner S.J. Pickering F. Meng, J. Energy and environmental assessment and reuse of fluidised bed recycled carbon fibres. may 2017.
- [78] T. Suzuki and J. Takahashi. Prediction of energy intensity of carbon fibre reinforced plastics for mass-produced passenger cars. May 2005.
- [79] Linda Gaines. The future of automotive lithium-ion battery recycling: Charting a sustainable course. *Sustainable Materials and Technologies*, 1-2, December 2014.
- [80] Ian A. Waitz Emily Schwartz, Ilan M. Kroo. Metric for comparing lifetime average climate impact of aircraft. *AIAA Journal*, 49(8):1600–1613, 2011.
- [81] U.S. Department of Aviation. Ac 150/5390-2c.
- [82] Robert M. Jones. *Mechanics Of Composite Materials*. Taylor & Francis, Inc., second edition edition, 1975.
- [83] J.R. Wertz W.J. Larson. *Space Mission Analysis and Design*. Kluwer Academic Publishers, third edition, 1999.
- [84] M.J.L. van Tooren R.J. Hamann. *Systems Engineering and Technical Management*. TU Delft, 2006.
- [85] U.S. Department of Energy. Clean cities alternative fuel price report, 2017.
- [86] Robinson Helicopter Company. R22 price list.
- [87] David Sung Jawad Arshad, Jawwad Zakaria.
- [88] Timothy E. Barder John W. Brennan.
- [89] Federal Aviation Administration. Aircraft operating costs.

- 
- [90] Brandon Schoettle & Michael Sivak. A survey of public opinion about autonomous and self-driving vehicles in the u.s., the u.k., and australia, 2014.

# Appendix A: Logbook

The logbook for this Final Report is presented below on subsection level. The authors (auth) are indicated by their initial as follows: LB (L. van Beek), PH (P. de Heer), MJ (M. de Jong), JK (J. Koelewijn), TK (T. Kuperus), FN (F. Nostheide), MS (M. Schouten), TV (T. van Veldhoven), SV (S. Vermeijlen) and JW (J. Watchorn).

Task	Auth	Cont	Task	Auth	Cont	Task	Auth	Cont	Task	Auth	Cont
1	JW		7.5.2	MJ	JK	10.2	SV		14.3	PH	
2	LB		7.5.3	JK		10.3	SV		14.4	PH	
2.1	LB		7.5.4	JK		10.3.1	SV		14.5	PH	
2.2	LB		7.6	LB	JK	10.3.2	SV		14.6	PH	
2.2.1	LB		7.7	LB	JK	10.3.3	SV		14.7	PH	
2.2.2	LB		8	MS		10.3.4	SV		15	TV	
2.2.3	LB		8.1	TK		10.3.5	SV		15.1	TV	
2.3	LB		8.1.1	TK		10.3.6	SV		15.2	TV	
2.3.1	LB	JK	8.1.2	TK		10.4	SV		15.3	LB	
2.3.2	LB		8.1.3	TK		10.5	SV		16	JK	
2.3.3	LB		8.1.4	TK		10.6	SV		16.1	JK	
2.3.4	LB		8.1.5	TK		11	PH		16.1.1	TV	
2.3.5	LB		8.2	MS		11.1	FN		16.1.2	SV	
2.3.6	LB		8.2.1	MS	MJ	11.2	FN	PH	16.1.3	MS	SV
2.4	LB		8.2.2	MS	MJ	11.2.1	FN	PH	16.2	SV	
3	MS		8.2.3	MS	TK	11.2.2	FN	PH	16.2.1	SV	MS
3.1	MS		8.2.4	MS		11.3	FN		16.2.2	SV	
3.2	MS		8.3	TK		11.4	PH		16.3	MS	
3.3	MS	SV	8.3.1	TK		11.4.1	PH	FN	16.4	SV	JK, MS
4	SV		8.3.2	TK		11.4.2	PH		17	FN	
4.1	PH	SV	8.3.3	TK		11.4.3	PH		17.1	FN	
4.2	SV	PH	8.3.4	TK		11.4.4	PH		17.2	FN	
5	FN		8.3.5	TK		11.5	FN	PH	18	MJ	
6	MJ		8.4	MJ		11.6	PH		18.1	MJ	JK
6.1	MJ	TV	8.4.1	MJ		12	TV		18.2	MJ	
6.2	MJ	TV	8.4.2	MJ		12.1	TV		19	MJ	
6.3	TV	MJ	8.4.3	MJ		12.1.1	TV		19.1	MJ	
6.4	TV	MJ	8.4.4	MJ		12.1.2	TV		19.1.1	MJ	JW
7	JK		8.4.5	MJ		12.2	TV		19.1.2	MJ	
7.1	JK		8.5	MJ		12.3	TV		19.1.3	LB	
7.2	LB	JK	8.5.1	MJ		12.4	TV	JK	19.2	JW	
7.3	LB		8.5.2	MJ		12.5	TV		19.2.1	JW	
7.3.1	LB		8.5.3	MJ		12.6	TV		19.2.2	JW	
7.3.2	LB		8.6	MS	TK, MJ	13	JK		19.2.3	JW	
7.3.3	LB		8.7	MJ	TK, MS	13.1	JK		19.2.4	JW	MJ
7.3.4	LB		8.8	TK	MJ, MS	13.2	JK		20	PH	
7.3.5	LB		8.9	TK	MJ, MS	13.3	JK		21	PH	
7.3.6	LB		9	JW		13.4	JK		Appendix A	MJ	SV
7.4	JK		9.1	JW		13.5	JK		Titlepage	MJ	
7.4.1	JK		9.2	JW		13.6	JK		Preface	JW	
7.4.2	JK		9.3	JW	SV	14	PH		Summary	JW	
7.4.3	JK		9.4	JW		14.1	PH		Nomenclature	SV	
7.4.4	JK		9.5	JW		14.2	TK		3D model	TV	
7.4.5	JK		9.6	JW		14.2.1	TK		Report Struc.	JK	MJ
7.5	JK		10	SV		14.2.2	TK				
7.5.1	MJ		10.1	SV		14.2.3	TK				